One-pot Synthesis of 2-bromopropionyl Esterified

Cellulose Nanofibrils as Versatile Coatings, Reactants and Macroinitiators

By
MENGZHE GUO
DISSERTATION

Submitted in partial satisfaction of the requirements for the degree of

DOCTOR OF PHILOSOPHY

in

Chemical Engineering

in the

OFFICE OF GRADUATE STUDIES

of the

UNIVERSITY OF CALIFORNIA

DAVIS

Approved:

You-Lo Hsieh, Chair

Roland Faller

Marjorie Longo

Committee in Charge

2022

Abstract

Nanocelluloses, the crystalline domains isolated from native cellulose, have gained increasing attention due to their uniquely ultra-high elastic modulus, low axial thermal expansion coefficient, and biocompatibility. All nanocelluloses in the market are hydrophilic and incompatible with most organic liquids and most synthesized polymers, limiting their applications which stated in the 1st chapter. In the 2nd chapter one-pot synthesis of 2-bromopropionyl esterified cellulose nanofibrils (Br-CNFs) coupled with *in-situ* disintegration by ultrasonication was developed and streamlined in processing and/or matrix media. This coupled functionalization and ultrasonication approach has been optimized to prepare Br-CNFs with tunable levels of esterification in high yields and imaged by atomic force microscopy (AFM) and transmission electron microscopy (TEM). The structures of Br-CNFs were further characterized by Fourier-transform infrared (FTIR) and liquid phase proton nuclear magnetic resonance (^{1}H NMR) spectroscopy. Thermal properties and crystallinity of Br-CNFs were characterized by thermogravimetric analysis (TGA) and X-ray diffraction (XRD), respectively. In the 3rd chapter, the organic compatibility and reactivity of these Br-CNFs have been demonstrated in their polyol role in replacing soft segment or as chain extender in synthesizing polyurethanes with significantly improved modulus (3x), strength (4x), and strain (1.5x) at merely 0.3 w% as polyol or 1.8 w% as extender. The Br bearing esters of these high specific surface Br-CNFs make them excellent macroinitiators for atom transfer radical polymerization (ATRP) of defined lengths of surface polymer grafts on crystalline cellulose, all described in 4th chapter. Br-CNF-g-PLMA from ATRP surface grafting of polylauryl methacrylate (PLMA) have shown to exhibit combined shear thinning behavior of Br-CNF proved by flow behavior index $n < 1$ and drag reducing effects of PLMA with up to 21071x increased viscosity. Moreover, in the 5th chapter Br-CNFs have shown

to be effective hydrophobic coatings on non-porous carbon and cellulose fabrics to respective water contact angles up to 105° and 88° as well as moderately improved the fabric's modulus (1.4x) and strength (1.2x). The multiple functionalities of these one-pot synthesized Br-CNFs have shown to be excellent surface modifiers (thin films, coatings), reactants or precursors for polyurethanes (polyols, crosslinkers), and ATRP macroinitiators for polymer sheath-nanocellulose core viscosity modifiers and drag reducers for diverse applications.

Acknowledgements

First and foremost, I would like to thank my major advisor, Prof. You-Lo Hsieh (Department of Biological and Agricultural Engineering), not only for supporting my PhD study but also for mentoring my personal life. Also, I appreciated the help and suggestions from committees of qualifying exam and dissertation, Prof. Roland Faller (Department of Chemical Engineering), Prof. Marjorie Longo (Department of Chemical Engineering), Prof. Adam Moulé (Department of Chemical Engineering), Prof. Gang Sun (Department of Biological and Agricultural Engineering), and Prof. Mark J Mascal (Department of Chemistry).

I am grateful to all colleagues in the lab, including but not limited to: Dr. Xiyu Song, Dr. Xingchen Liu, Dr. Juri Fukuda, Dr. Gabriel Patterson, Dr. Benjamin Pingrey, Dr. Jian Zhou, Dr. Xuezhu Xu, Dr. Lucas Messa, Dr. Maria Lucia Bianchi, Kaifang Fu, Jiahui Wei, Teresa Elena Lopez, Leilah-Marie Lockett, Holly Kathleen Allan, and Andrea M Harris. I am also thankful for Dr. Ping Yu, Dr. James Fettinger, Dr. Fei Guo, Bradley Shibata, and Leah Filardi for support of facility training.

Much appreciation goes to my wife, Yi Wang; my parents, Qiang Guo and Ming Meng, for their unconditional love and support.

Table of Contents

Chapter 1. Introduction

1.1. Cellulose introduction

As the most abundant natural polymer on earth, cellulose has been annually produced at approximately 75 to 100 billion tons.[1] Cellulose is an organic compound belonging to the category of polysaccharides made up of glucose subunits. It is found in cell walls of bacterial and plant cells. Although cellulose is widely used for thousands of years in forest products, paper, textiles, etc, it is still one of the most underutilized natural polymers. The renewable and sustainable resources for natural cellulose from plants, tunicates even bacteria verified its economic applicability meanwhile its biodegradable and low environmental impact nature proved the Green Chemistry concept. Cellulose content varies with 90% in cotton fiber[2], 40–70% in wood[3], 35-45% in corn stalks[4], 73% in sisal fibers[5], 45% in sugarcane bagasse[6], 30% in wheat straw[7] and approximately 62% in hemp[8]. **Table 1** display the chemical composition of different sources[9-17] on dry basis. Of all cellulose resources, rice straw is the largest crop residue globally and a significantly under-utilized, non-wood cellulose source from crop production by-product, containing cellulose (38.3%), hemicellulose (31.6%), lignin (11.8%) and silica ash (18.3%).[9] Pure cellulose was isolated from rice straw by a three-step isolation process[18] of toluene/ethanol extraction, acidified $NaClO_2$ delignification and alkaline hemicellulose dissolution to remove wax, lignin and hemicellulose in sequence.

Table 1.1 Dry composition of different plant sources. [9-17]

source	cellulose (%)	hemicellulose (%)	lignin (%)	silica,wax (%)
rice straw[9]	38.3	31.6	11.8	18.3
Pine (softwood)[10]	44	27	28	—
Yellow birch[10] (hardwood)	47	31	21	—
Jute[10]	73.2	13.6	13.4	—
Wheat straw[10]	48.8	35.4	17.1	—
Rice husk[10]	45	19	19.5	15
bagasse[11]	55.2	16.8	25.3	2.7
banana[12]	63-64	10	5	22
flax[12]	71	18.6-20.6	2.2	7.2
hemp[12]	70-74	17.9-22.4	3.7-5.7	3.2
mulberry barks[13]	37.4±2.3	25.3±2.5	10.0±0.8	27.3
galic straw[14]	41	18	6.3	34.7
carrot residual[15]	81	9	2.5	7.5
ground nut shell[16]	38.3	27.6	21.1	13
onion skin[17]	41.4±1.1	16.2±0.6	38.9±1.3	3.5

There are four polymorphs of cellulose: I, II, III, and IV[19]. Cellulose I found in nature consists of two allomorphs of Iα and Iβ[20]. Cellulose II is the most stable form of crystal emerged from aqueous sodium hydroxide treatment, which is also called regenerated cellulose[21]. The characteristic distinction between cellulose I and II is the layout of their atoms. In cellulose I chains are aligned in parallel direction, whereas it is found to be antiparallel in cellulose II.[22] Cellulose III obtained

from decomplexation of ammonia−cellulose I or ammonia−cellulose II is designated cellulose III_I or cellulose III_{II}, respectively, whereas, cellulose IV is derived from the glycerol modification of cellulose III.[19] Each cellulose molecule contains several crystalline and amorphous parts[23], making cellulose a semicrystalline polymer composed of ordered and disordered regions within a single microfibril.[24]

The chemical formula of cellulose is $(C_6H_{10}O_5)_n$, where n is the number of repeating glucose units or the degree of polymerization (DP). The repeating unit in cellulose consists of two glucose molecules known as one anhydroglucose unit. The DP of native cellulose ranging from 1500 to 3500[25] depending on the cellulose source and corresponding treatments. Native cellulose consists of long linear chains of D-glucose units joined by (1−4)-β-glycosidic bonds that are intermolecularly and intramolecularly hydrogen bonded. Crystalline cellulose from high plants has cellulose Iβ allomorph with a monoclinic two chain unit cell structure.[26, 27] In monoclinic unit cell, cellulose chains are aligned along c axis (001) direction and three major lattice planes $(110)_m$, $(1\bar{1}0)_m$, and $(200)_m$ have d-spacings of $d_{110} = 0.53$ nm, $d_{1\text{-}10} = 0.58$ nm and $d_{200} = 0.39$ nm, respectively.[28] Single cellulose chains in sheets perpendicular to (100) direction are hydrogen bonded[26], and the multiple sheets are held together mainly via van der Waals interactions[27]. The reducing end of the cellulose chain containing a hemiacetal group provide more functionality and directional asymmetry. The ubiquitous cellular hierarchical structure of cellulose lead to the extreme high mechanical strength. Cellulose has been used industrially as a raw material in products of paper[29], cellophane films[30], textiles[31], and dietary fibers[32]. To maintain uniformity and remove hierarchical structure associated defects, nanocelluloses have be extracted from macroscopic cellulose with as high performance materials.[33]

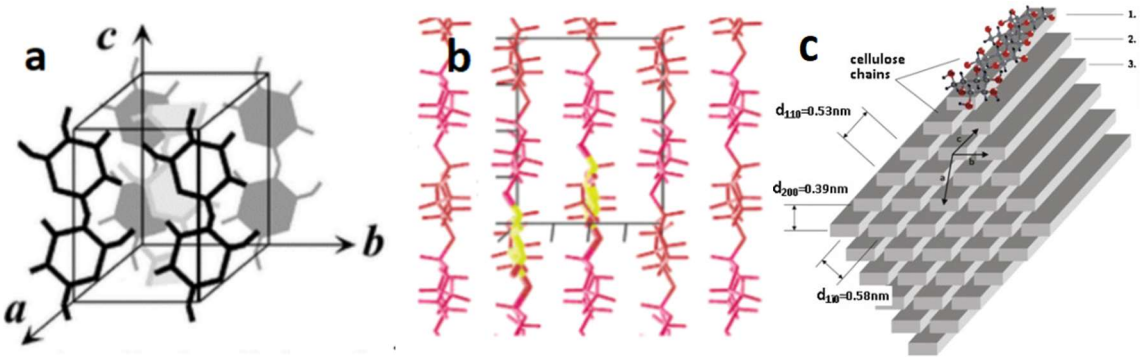

Figure 1.2. (a) Three dimensions view of cellulose Iβ monoclinic unit cell (a=0.801 nm, b= 0.817 nm, c= 1.036nm)[26], (b) Two dimensions view of I-β cellulose monoclinic unit cell (ac plane)[27], (c) Three dimensional view of I-β cellulose monoclinic crystal lattice with d_{110} = 0.53 nm, $d_{1\text{-}10}$ = 0.58 nm and d_{200} = 0.39 nm[28].

1.2. Nanocellulose

1.2.1 Definition and property

Nanocellulose that are ~3−20 nm wide and 100 nm to several micrometers long, generally referred to crystalline domains, can be separated by removing or breaking the extensive and strong inter-fibrillar hydrogen bonds in the non-crystalline regions. According to aspect ratio, nanocelluloses are classified to cellulose nanocrystals (CNC, aspect ratio < 100) and cellulose nanofibrils (CNF, aspect ratio > 100). Either CNC or CNF has gained increasing attention due to their reticulate three-dimensional (3D) web-shaped fibrous structure[34], high crystallinity[35], high elastic modulus (150 GPa for CNCs, 28 GPa for CNFs)[36, 37], low axial thermal expansion coefficient (10^{-7} K^{-1} for CNCs, 5×10^{-6} K^{-1} for CNFs)[38, 39], optical transparency,[40, 41] unique nanoscale lateral dimensions[42, 43] and high biocompability[44, 45]. Highly efficient top-down isolation methodology of nanocellulose from plant sources need to be investigated to meet large scale industrial applications.

1.2.2 Cellulose Nanocrystals

Cellulose nanocrystals (CNCs), the most used nanocellulose, were defibrillated from pure cellulose by removing the non-crystalline regions via acid hydrolysis[46-64]or mechanical treatment such as ball milling[65-67] and high-pressure homogenization[68, 69]. Sulfuric acid[47-55], phosphoric acid[59, 60] or oxalic acid[61-64] hydrolyze cellulose (1−4)-β-glycosidic bond and generates rod-like CNCs while esterify the hydroxyls to anionic sulfate, phosphate or oxalate groups to provide the necessary electrostatic repulsion to stabilize aqueous CNC suspensions.[46] In contrast, hydrochloric acid[56-58] only hydrolyzes (1−4)-β bond without introducing charged groups, causing potential agglomeration due to a lack of electrostatic repulsion between CNCs.[70] Common sulfuric acid hydrolysis results in low yield CNCs from 15 to 50 w%[46-55] due to disintegration of amorphous regions and degradation of crystalline parts[46]. Recently, non-toxic oxalic acid hydrolysis has been optimized to reach high yield of 71-93% with relative lower concentration of 0.5 w% [64] as compared to sulfuric acid hydrolyzed CNCs.

Among all mechanical treated CNCs, ball milling is the most promising and widely used methodology for CNCs isolation.[71] It is an environmentally sound and cost-effective technique compared to traditional acid hydrolysis using concentrated acid which is removed by centrifugation or dialysis, which is considered to be laborious process[65]. Without removing amorphous region as in hydrolysis, crystallinity of those ball milling CNCs was not higher than 70.3%[66] as reported and always lower than original fibers. Maximum thermal degradation temperature dropped ca. 80°C for sulfuric acid hydrolyzed CNCs[72] compared to original fiber, which was only ca. 20°C deduction for ball milling CNCs[67]. Modification of hydroxyls to sulfate groups on CNC surface through acid hydrolysis may prompt poor thermal stability in comparison to CNCs formed through a greener approach.[72]

1.2.3 Cellulose Nanofibrils

Compared to rod-like CNCs, high aspect ratio cellulose nanofibrils (CNFs) has been prepared via mechanical methods[43, 73-80] or combined of chemical modification and mechanical treatment[42, 81-89]. Homogenization[73, 74], grinding[75, 76], blending[43, 77], ultrasonication[78, 79] and aqueous counter collision[80] were used to help cellulose defibrillate into CNFs by opening (110) or (1-10) plane without modification of surface hydroxyls. High pressure homogenization (80 MPa, 30 cycles) produced 90 w% CNFs (10-20 nm width) from sugarcane bagasse with dramatically decreased crystallinity from 60 to 36 %.[73] Bleached and unbleached bamboo pulp has been grinded into 5-30 nm width CNFs but relative low crystallinity of 0.43 and 0.36, respectively.[75] A increased crystallinity of 72.2 to 81.5 % was observed for blended rice straw CNFs (2.70 ± 1.22 nm) at yield lower than 20 %.[43] Thick CNFs (ca. 68 nm width) has been isolated from pineapple leaf by ultrasonication with decreased crystallinity from 82.7 to 61.7 % and unreported yield.[78] Aqueous counter collision (ACC), which allows biobased materials to be downsized into nano-objects only using water jets, defibrillated homogenization pretreated bacterial cellulose into nearly 100% yield CNFs with slightly decreased crystallinity from 84 to 70 %.[80] It is obvious that optimization of mechanical methods for CNFs isolation is challenging, in which intensive conditions cause potential cellulose dissolution meanwhile weak conditions lead to low yield.

To allow CNFs defibrillation in mild conditions, surface hydroxyls could be modified into charged groups to decrease hydrogen bonding interactions among cellulose chains meanwhile provide the necessary electrostatic repulsion to stabilize in water. The most common chemical modifications aided cellulose defibrillation involves TEMPO (2,2,6,6-tetramethylpiperidin-1-yloxyl)-oxidation[42, 81-83], phosphorylation[84, 85], periodate-chlorite oxidation[86, 87] and sulfonation[88, 89]. TEMPO, a typical catalyst for the oxidation of primary hydroxyls, regio-selectively oxidizes

cellulose primary C6 hydroxyls to carboxylates[90], followed by mechanical blending to generate finer (1.5 nm thickness, 2.1 nm width) CNFs at high yield of 96.8%[42]. Sugarcane bagasse (SCB) phosphorylated CNFs after blending were prepared at 84.3% yield and extremely high charge of 2.56 mmol/g with three dimensions of W=3.84 nm, T=0.73 nm, and L=ca.500 nm.[85] Sequential periodate–chlorite (PC) oxidation followed by blending has been optimized to regioselectivity converted C2,C3 hydroxyls to carboxyl groups for preparation of CNFs (T=1.26 nm, W=3.28 nm) at yield of 98%.[86] A facile sulfation-disintegration approach combined direct sulfation with chlorosulfonic acid followed by blending has been established to generate sulfated CNF with tunable charge of 1.0-2.2 mmol/g and high yield up to 97%.[89]

To sum up, all those nanocelluloses either isolated by mechanical treatment[43, 73-80] or combined methods[42, 81-89] are all hydrophilic, some with anionic charges[42, 81-89], making them easily dispersible in aqueous media, but incompatible with less polar and non-polar organic liquids and most synthetic polymers. Thus, hydrophobic modification of CNCs and CNFs should be further investigated and broad their applications.

1.3. Hydrophobic Nanocellulose

1.3.1 Physical Methods

Nanocellulose exhibits superior structural characteristics than micro-size cellulose and capability of facile surface-modification for post application via different strategies. To render these hydrophilic nanocelluloses to be more compatible with organic media and polymers for broader applications, various physical[91-103] or chemical means[104-134] have been explored and reviewed[135]. Mechanical pretreatment such as ultrasonication to disperse nanocelluloses only limited in less polar polymer such as polyurethane (PU) [91-94], the compatibility issue to nonpolar media is still a challenge. Hydrophobic nanocellulose can also be obtained by physically absorbing cationic

surfactant[95-98] or quaternary ammonium salt[99-103]. Cationic surfactants with one end as long hydrophobic alkyl chain can be adsorbed on the anionic nanocellulose surface under the action of static electricity. As the cationic surfactant concentration increases, the chemical potential of the nanocellulose surface turns from positive to negative.[135] Sulfuric acid hydrolyzed CNC has been coated by absorbing cetyltrimethylammonium bromide (CTMAB) to enhance compatibility to hydrophobic anti-cancer drugs such as luteolin (LUT) and luteoloside (LUS).[96] Similarly to cationic ion, the hydrophobicity of the long chains on the quaternary ammonium salt will endow the nanocellulose with a hydrophobic surface[136] meanwhile either positive or negative ions on quaternary ammonium salt could bond to the hydroxyl or carboxyl groups on the surface of nanocellulose. Hydrophobic TEMPO-oxidized CNF (TEMPO-CNF) films with WCA of ~100° were prepared by casting and drying aqueous dispersions of TEMPO-CNF with quaternary alkylammoniums (QAs) as counterions for the surface carboxylate groups.[101] In addition, the hydrophobicity of the modified nanocellulose can be regulated by controlling the chain length of the quaternary ammonium salt.[137] To not only increase hydrophobicity but also introduce more functionality, chemical methods including esterification[104-118], silanation[119-122], amidation[123-126] and polymer grafting[112, 127-134] have been reported up to date on surface modification of hydrophilic nanocelluloses, in which most of them[104-114, 119-134, 138]are performed on already existing nanocelluloses.

1.3.2 Chemical Methods

Scheme 1.1. Hydrophobic nanocellulose modification involving (1) esterification[104], (2) silanation[121], (3) amidation[123], and (4) polymer grafting[112].

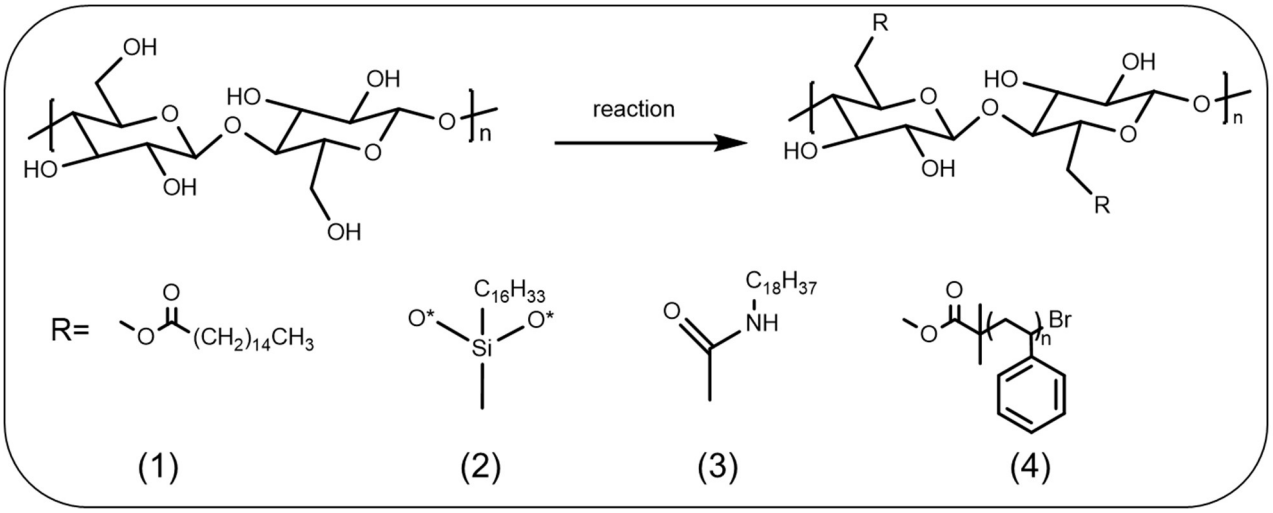

1.3.2.1 Esterification

The esterification reaction mainly converts nanocellulose surface hydroxyls to ester groups with one hydrophobic end. Hydrophobic cellulose nanopapers has been prepared by esterifying the hydroxyl groups on the surface of CNF using lactic acid during ultrasonication.[107] UV-shielded cinnamate groups were grafted onto the sulfuric acid hydrolyzed CNC surface through the esterification reaction between the hydroxyls and cinnamoyl chloride to increase hydrophobicity as well as exhibiting strong ultraviolet absorption and high visible light transmittance.[110] Those hydrophobic moieties were confirmed as a reinforcing nanofiller in a hydrophobic polymer matrix such as polystyrene.[110] Bromine esterification, a common reaction to introduce alkyl bromines to cellulose, has been performed on CNC[111]or CNF[112] to improve their respective solubility or dispersity in DMF[111] and anisole[112]. Sulfuric acid hydrolyzed CNCs[111] and TEMPO-oxidized and homogenized CNFs[112] were acylated with 2-bromoisobutyryl bromide (BIB) aided by 4-dimethylaminopyridine (DMAP) catalyst at ambient temperature to generate DMF dispersible CNFs to be polymerized with styrene.

It should be noted that esterification can be accomplished during the nanocellulose preparation in which a one-pot approach was achieved. For instance, hydrophobic CNF could be prepared by ball

milling of native cellulose in dimethylformamide (DMF) containing hexanoyl chloride, which could be homogeneously dispersed in non-polar organic solvents such as tetrahydrofuran, chloroform, and tertbutyl alcohol with unreported yield.[118] Esterification of cellulose with acetic anhydride followed by refining, cryo-crushing and homogenization has shown to generate ethanol and acetone suspensible cellulose and some 10-50 nm wide CNFs, but the extent unreported[115]. To diversify chemistry, quantify yield and simplify the disintegration process, one-pot synthesis of solventless telomerization of butadiene into 2,7-octadienyl ether (ODE), a 8-carbon diene, on cellulose followed by mechanical blending of aqueous ODE-cellulose suspensions to generate hydrophobic ODE-nanocellulose precipitates that were 27-41% dispersible in DMF, DMSO and chloroform.[116] Recently, 2-bromopropanoated nanofibrils (Br-CNF) have been facilely produced from one-pot esterification of cellulose with 2-bromopropionyl bromide (BPB) to 2-bromopropanoated cellulose (Br-cell) to be directly disintegrated by *in situ* ultrasonication in the same organic liquid, DMF.[117]

1.3.2.2 Silanation

Silane is a well-known chemical reagent that is widely used as a coupling agent between organic and inorganic materials. The silane reaction is hydrolysis and condensation in which the alkoxy groups in silane are able to be hydrolyzed with water to form silanol groups.[135] CNF was modified with hydrophobic alkoxysilane containing methyl (MTMS), propyl (PTMS), or aminopropyl (APTMS) functional groups to form silane-modified CNF (Si-CNF) and corresponding effects were investigated.[120] Crystallinity and structure of Si-CNF retained the same as original CNF with controllable degree of silanization and improved dispersity in chloroform, caused by coating with hydrophobic siloxane layer.[120] A two-step silanization using both silylation-modified linker (3-Glycidyloxypropyltrimethoxysilane) and reagent (dodecyltrimethoxysilane) was applied on

sulfuric acid hydrolyzed CNCs films to significantly increase water contact angle from 0° to about 140°, along with elevated initial thermal degradation temperatures from 186 to 215 °C.[121] A ultra-high absorption of TEMPO-CNF aerogels on non-polar chloroform (356 g per g) and decane (219 g per g) after silanization via chemical vapor deposition (CVD) was reported.[122]

1.3.2.3 Amidation

Amidation modification can also be used to hydrophobically modify nanocellulose by linking primary amine on the modifier to carboxylic acid on the surface of nanocellulose. Nanostarch films has been reinforced by the amidated CNCs with 230% tensile increase on strength along with 87.4% decrease of water vapor permeability and 25.6^ decrease of moisture absorption.[126] Electrostatic and covalent attachment of octadecylamine (ODA) to TEMPO-CNF surfaces can be easily achieved to disperse in DMSO, isopropanol and THF with slightly increased from 240 to 280°C.[123] CNF surface has been modified using alkenyl succinic anhydride (ASA) to increase hydrophobicity for preparation of reinforced CNF/Polypropylene nanocomposites.[124] Besides, CNF has been modified by linking 10-undecanoyl chloride to prepare a hydrophobically modified membrane after vacuum filtration, showing good moisture resistance, low surface roughness, and high tensile strength, suitable for packaging applications.[125]

1.3.2.4 Polymer grafting

Polymer grafting is to graft long-chain polymer or oligomers to the surface of nanocellulose via covalent bonds. Grafting side chains on nanocellulose backbone not only improve its hydrophobicity but also enhance entanglement at the polymer-cellulose interface[134], as well as introducing more targeted functionality[133]. Among all of grafting methods, "Grafting-from" method has been widely used in which initiators are immobilized followed by in-situ polymerization of monomers on the surface of nanocellulose.[132] N, N-dimethylamino-2-

methacrylic acid methyl ester (PDMAEMA) has been grafted on CNF aerogel surface with controllable surface wettability and WCA up to 130°, in presence of carbon dioxide.[131] Significantly WCA increase from 32° to 120° of CNC film surface was observed with increase of grafted length of alcohol from ethanol to 1-octanol using 2, 4-toluene diisocyanate (TDI) as crosslinker.[130] TEMPO oxidized CNC surface was grafted by polyethylene glycol (PEG) via ionic bonding to be homogeneously disperse in chloroform.[129] Multifunctional polymers have been grafted on nanocelluloses to increase their compatibility to hydrophobic nanocomposite.[112, 127, 128] Thermo-responsive poly(poly(ethylene glycol) methylacrylate)s has been grafted from sulfuric acid CNCs to generate low critical solution temperature tunable polymer hybrids.[127] Polystyrene was grafted on TEMPO-oxidized CNFs to significantly increase its combability to organic solvent and homogeneously dispersed in tetrahydrofuran (THF).[112] CNCs were grafted with polymethyl methacrylate (PMMA) to increase initial degradation temperature by 50 °C as well as improved compatibility to hydrophobic polystyrene.[128]

1.4. Nanocellulose Application

As a sustainable material, nanocellulose could be extracted from the disintegration of plant[50], synthesized by different microbial strains[139], and cell-free systems[140]. Current applications focus on functional paper[141, 142], dressing[143], textiles[144], food[145], comestics[146], antibacterial coatings[147], packaging[148-150], hydrogel/aerogel[122, 151-154], mechanically reinforced polymer composites[92, 155-167], tissue engineering[168, 169], bioprinting[170], optoelectronics[171], environmental remediation[172, 173], polymer grafting and so on, both alone and inside with other materials.

1.4.1 Packaging and coating

1.4.1.1 Methodology

Layer-by-Layer (LbL) assembly, electrospinning and film casting are the most common methods to prepare nanocelluloses as coating or packaging materials. LbL assembly has been investigated to deposit ultra-thin layers of functional substances onto surfaces until reaching sufficient thickness to provide gas barrier properties, mechanical properties, and wet-strength requirements.[173, 174] Electrostatic interaction can be exploited by alternating polyanionic and polycationic NCs layers to obtain denser and ultrathin layers for tailored physical properties.[149] Electrospinning is a remarkably simple method for generating nanofibers of polymers using electric force to draw charged threads of two polymer solutions followed by melting up to fiber diameters.[175] In the past years, cellulose-based materials have been successfully electrospun[176] with tunable thermal/mechanical properties and crystallinity with the alignment of the fibers. Film casting is a generic operation of evaporation of water or solvent from the NC at a controlled temperature to obtain dried films of neat or modified NC.[177] CNCs are more brittle than flexible CNFs and addition of the plasticizers like sorbitol and glycerol can mitigate the brittleness by reducing the intermolecular hydrogen bonding among CNCs.[178]

1.4.1.2 Application

Due to biodegradable and non-toxic nature, plant-based nanocelluloses with excellent mechanical, rheological and gas barrier properties have been investigated to replace oil-based plastics in variety of food packaging and coating application.[177] High strength lignin-based fibers were produced by electrospinning aqueous dispersions of lignin, poly(vinyl alcohol) (PVA), and cellulose nanocrystals (CNCs).[158] Cellulose nano-paper has been prepared from wood CNFs aqueous suspension (0.2%) by vacuum filtration to reach an extremely high strength to 214 MPa with 28%

porosity.[141] Highly stretchable graphene–nanocellulose composite nanopaper was made via vacuum filtration to achieve stretchability up to 100%.[142] A translucent light-diffusive translucent light diffuser consisting of TEMPO-oxidized woold pulp CNFs with tunable diffuse transmission of up to ~78% across the visible and near-infrared spectra.[171] TEMPO-oxidized CNF has been coated on polyethersulfone (PES) layer-by-layer to significantly enhanced antifouling and antibacterial properties with 49% less relative adhesion of bovine serum albumin (BSA).[147] Near CNF aqueous suspension has been coated on polylactic acid (PLA) surface to significantly enhanced the oxygen barrier with a decrease in oxygen permeability from 96-84%.[148] CNCs has been coated on paperboard with polylactic acid (PLA) layer by layer to reach both low oxygen (6 cm^3/m^2/day) and water vapor transmission rate (28 g/m^2/day) at 38°C and 90% relative humidity via extrusion coating.[150]

1.4.2 Hydrogel and aerogel

1.4.2.1 Methodology

Hydrogels of nanocelluloses are commonly prepared via addition of CNC/CNF to a polymer precursor solution followed chemical cross-linking of main polymer component to nanocellulose.[152] Freeze–thaw cycling, in which precursor material is rejected from growing ice-crystals (freeze) generated water-filled pores (thaw), could be used for preparation of strong hydrogel networks. Freeze-drying and supercritical drying,[169] in which aqueous gel phase is replaced with gas, are most used methods for preparation of nanocellulose aerogels. For anisotropic nanocellulose aerogel preparation, freeze casting method is used to apply a temperature gradient during the freezing process to allow ice crystallites grow directionally.[157]

1.4.2.2 Application

Nanocellulose based aerogels from freeze-drying have become a hot research topic due to their high absorbance ratio, surface area and amphiphilic behavior.[122] In situ-gelling nanocomposite hydrogels based on poly(oligoethylene glycol methacrylate) (POEGMA) and rigid rod-like cellulose nanocrystals (CNCs) has been prepared to reach 35-fold increase in the gel shear storage modulus at 4.95 w% gel addition.[151] 50 w% TEMPO-oxidized CNF aerogel was used as loading matrix with PEDOT: PSS as stretchable sensor with increased the conductivity from 0.05 to 0.12 S m^{-1}.[153] Ultra-light (1.7 to 8.1 mg cm^{-3}) and ultra-porous (99.5 to 99.9%) aerogels have been assembled from Tempo-CNFs with amphiphilic behavior.[122] CNC based aerogel was also prepared through supercritical CO_2 drying to reach high surface area (605 m^2 g^{-1}).[154]

1.4.3 Polymer composites

1.4.3.1 Methodology

Because of native crystallinity and high strength, cellulose nanocrystals (CNCs) and cellulose nanofibrils (CNFs) have been extensively studied as reinforcements to produce cost-effective, highly durable nanocomposite materials.[165] Nanocelluloses can interact with polymer matrixes by either physical mixing or covalent bonding. Physical mixing method take advantage of weak secondary forces such as hydrogen bonding, dipole-dipole interactions and van der Waals forces[166] between nanocellulose and doped polymer. Thus, potentially low the stiffness of nanocellulose polymer matrixes should be anticipated.[156] Covalent bonding interactions between nanocellulose and compatible polymer via crosslinking potential provide high strength composite. Especially for CNFs, high-aspect-ratio fibers can impose efficient entrapment effects on the chains of the matrix polymer and cause a sort of chain confinement to increase the stress-transfer capacity relative to that of short fibers.[167]

1.4.3.2 Application

Thermoplastic block copolymer elastomers have been widely used because it combines the high extensibility of vulcanized rubbers and the energy-saving processing recyclable nature of thermoplastics.[179] For simply physical mixing nanocellulose composites, CNCs were utilized as reinforcement to increase stiffness of shape memory polyurethane composites.[92] Cellulose-nanofibril-film-reinforced polycarbonate composite was synthesized by compression molding with modulus of 11 GPa.[159] Thermoplastic starch (TPS) was mixed with cotton linter CNFs to make high strength nanocomposite via solution casting method.[160] Sulfuric acid CNFs[155] and carboxymethyl CNFs[156] were doped as filler in commercial waterborne polyurethane to enhance mechanical strength 4 or 8-fold with a drop of tensile strain from 700% and 396% to 429% and 6.4%, respectively. In the case of polyester based thermoplastic polyurethane (TPU), mixing up to 1 %[92] or 30 %[161] CNC with the aid of ultrasonication in DMF did not improve tensile strength or strain significantly, likely due the incompatibility between the hydrophilic CNC and hydrophobic TPU matrix

For nanocellulose covalent bonded composite, one of the representative examples is nanocelluloses as reactive polyol in-situ synthesis of polyurethane (PU). Dispersing aqueous CNCs (0.5 w%) in PTMEG (M_n :1,000 *Da*) by homogenization and water evaporation followed by sequential reactions to MDI and 1,4-BD improved tensile strength of PU composite by 40 %[162]. Additional pretreatments of either freeze-drying CNC[91] or sequential solvent exchanging CNC[163] and CNF[164] via acetone to DMF, then ultrasonicated with PTMEG[91, 164] or hydroxylated soybean oil[163] have shown to improve some of the tensile modulus[91, 163], strength[91, 163, 164], and strain[91, 164], all optimized at 1 w% addition. Specially, a facilely synthesized 2-bromopropionyl bromide esterified cellulose nanofibrils (Br-CNF) has been used as polyol in-situ polymerization of TPU

with enhanced strength (3.2x), stretchability (3.9x) and modulus (1.5x) at merely 0.3 w% addition in chapter 3.

1.4.4 Polymer Grafting

1.4.4.1 Methodology

There are two main approaches for grafting polymer brushes on nanocelluloses (NC) surface (i) "grafting-to" method, including both covalent and non-covalent interactions and (ii) "grafting-from" approach, mainly from surface initiated atom transfer radical polymerization (SI-ATRP).[180] The "grafting to" approach has the advantage of introducing a already synthesized and well-defined polymer on the surface through peptide coupling, epoxy ring-opening, click chemistry or adsorption approaches to form (non-)ionic or electrostatic interactions.[167] "Grafting from" approach involves two sequential steps a) immobilization of initiators and b) polymerization,[181] making it possible to achieve a high-density grafting of brushes and enable of good control of grafted polymer length. Thus, "grafting from" is more commonly applied in the literature for both hydrophilic and hydrophobic polymers grafted on NC substrates.[182] The most common used "grafted from" method is atom transfer radical polymerization (ATRP), which is one of the most robust and widely used control radical polymerization techniques because of the simple experimental setup, precise molecular weight control, available initiators and catalysts used in a large range of solvents and reaction conditions.[183]

1.4.4.2 Application

Esterified nanocelluloses with alkyl bromines are suitable macroinitiators for ATRP of chain polymers to synthesize NCs-centered star-like block copolymer matrix. Surface initiated (SI)-ATRP has previously been applied to graft controllable length of functional polymer brush on CNCs[128, 184-203] or CNFs[112, 204-206] to behave as entire stimuli-responsive material[184-187, 207, 208],

hydrophobic reinforcement filler[112, 128, 188-195, 204], gold nanoparticles stabilizer[196], anionic moiety binder[197, 198], thermoplastic elastomer[199] or for characterizations[200-203, 205, 206]. Poly(N-isopropylacrylamide) (PNiPAAm) was grafted from the surface of CNCs by SI-ATRP to prepare CNCs based temperature sensitive film.[207] TEMPO-CNFs/PNiPAAM aerogel was synthesized via free radical polymerization and lyophilization to obtain hydrophilicity/hydrophobicity thermal switchable properties.[208] Alkyl bromine immobilization, mostly involving reacting 2-bromoisobutyryl bromide (2-BIB) [112, 128, 184-186, 188-203, 206] on freeze-dried[128, 184, 185, 188-202, 206] or DMF solvent exchanged[112, 186, 203] nanocelluloses, was necessary to prepare macroinitiators dispersible in DMF[184-186, 191, 194-203, 206], DMSO[188, 192], toluene[189, 193] or anisole[112, 128, 190] for surface grafting. Additionally, aqueous dispersible macroinitiators were prepared by reacting 2-bromopropionic acid on CNC slurry (11.5 w %) in presence of toluenesulfonic acid (12 w/v% in acetic acid) followed by dialysis and freeze-drying.[187] Br content, or degree of substitution (DS) for OHs converted to Br esters, were determined to be extremely low to 1.4 [192], 3.5 [193], 7.44[200] and 9.5[190] Br % by elementary analysis (EA), or 26 %[186] by ^{13}C NMR integration both on CNC-Br. Freeze-dried homogenized CNFs were modified by 2-BIB in sequential chemical vapor deposition (CVD) and solution state acylation for a high DS up to 43 % by ^{1}H NMR.[206] Complex initiator immobilization process and unattainable high grafting density limited surface grafting application on nanocelluloses as backbone macroinitiators.

Although up to several hundred degree of polymerization (DP) for chain length could be controlled by varying reaction time or monomer concentrations, less than 35 %[184, 192, 194] conversion for SI-ATRP on CNC-Br[184, 192, 194] still need to be improved. One possible reason for low conversion was the less accessibility of immobilized Br initiators on nanocelluloses surfaces compared to free initiators. Thus, sacrificial initiator such as ethyl 2-bromoisobutyrate (EBIB)[188-191, 193, 195-197, 199-

[201, 203] or 2-hydroxyethyl 2-bromoisobutyrate (HEBIB) [112, 205] were added accompanied with macroinitiators to significant increase conversion up to 92 %[188] for CNC-Br and 70 %[112] for CNF-Br, both with narrow polydispersity Index (PDI) up to 1.1[188] and 1.17[112] determined by gel permeation chromatography (GPC). Also, use of sacrificial initiator helped to gather chain length information and distribution without cleaving polymer chains from the macroinitiator surface. However, those assumptions of equal accessibility and reactivity for both sacrificial and immobilized initiator were unreasonable, causing inaccurate estimation of surface chain length. Compared to more publications on rigid and short CNCs[128, 184-203], surface grafting of polymer brush on flexible and high aspect ratio CNFs is even more scarce and need to be investigated.

1.5. Challenge and Limitation

Nanocellulose exhibits superior structural characteristics than micro-size cellulose and capability of facile surface-modification for post application via different strategies.[135] Scientific researchers have been working on expanding NCs market in which full potential is still not reached. Among those challenges for NCs application, design[209], characterization[210], and environmental concern[211] are the three main causes to limit industrial demands.

1.5.1 Design

Engineering design process for NCs application includes materials selection, usage or content of product, quality and durability of final product, and total cost.[212, 213] NCs are source and process dependent materials[214] with uncertainty of performance, for which better investigation and proper selection of their most appropriate merits are required to achieve more reliable and better design data.[215] In most cases, the structure of NCs can be affected, or even destroyed during modification, resulting in the partial loss of the initial excellent properties (i.e. crystallinity[35], thermal stability[72]). When NCs are used as reinforcements in composite, filler loading and exfoliation of NCs, as well

as the intermolecular covalent bonding can significantly alter the characteristics of the bulk polymers.[216, 217] NCs can be either mixed with melt-processed polymer or in-situ polymerization as reinforcements. In both scenarios those heterogeneous fibers and matrix structure along with in-between incompatibility suppressed production of reinforced cellulose nano-polymeric composites.[209] Small filler content is typically desired because of its infinitesimal volume and the large interfacial area compared to bulky polymer. Other parameters such as fiber size, geometry and orientation, NaOH surface treatment, processing temperature are also important parameters for nanocomposite optimization.[218-221] Uncountable combinations of material, process and homogenizing selections really increase workload of researchers and limit NCs commercialized application.

1.5.2 Characterization

One of the main factors hindering the commercial development of nanomaterials is the absence of fast and robust characterizations methods to perform an efficient process and quality control along the production chain.[210] However, current NCs characterization methods, including atomic force microscopy (AFM), transmission electron microscopy (TEM), scanning electron microscopy (SEM), and etc, are all based on off-line measurements carried out in laboratory facilities that require high capital investment, time-consuming analysis and highly qualified personnel.[222] The lack of real-time characterization at accessible speed and reliability delay information gathering during NCs production processes. Although rheology of CNFs has been widely used to determine concentration[223], aspect ratio[224] and surface functional group density[225], the fitting parameters for CNFs are still highly dependent on sources and processing method. NC products are always in aqueous suspension form except aerogel to be stored in refrigerator with addition of bactericide to prevent microbial growth[226]. Especially for sulfuric acid hydrolyzed CNCs, low temperature is

mandatory to reduce the self-catalyzed desulfation.[227] NCs strong intermolecular interactions[228] also limited production of highly concentrated aqueous dispersions, which further increased the shipping and storage cost.

1.5.3 Environmental concern

High water usage is one environmental issue limiting large scale NCs production.[211] Most of the current modification methods for NCs isolation involve hazardous and costly chemicals. For instance, acid hydrolysis method generate large amount of acidic wastewater during long processing time, which may also cause equipment corrosion, and the formation of inhibitors.[229] Mechanical treatments, such as high-intensity ultrasonication[230], cryocrushing[231], grinding[232] and high-pressure homogenization[233], all use extensive energy to disintegrate highly ordered hydrogen bonds and dense network structure of cellulose[234].

Several emerging technologies in nanocellulose production such as microwaves irradiation[235], enzymatic method[236], electron beam irradiation[237] and cold plasma[238] has been recently investigated for NCs isolation to save energy. Microwaves-assisted (300 W, 10 or 30 min) dilute acid pretreatment was used to prepare CNC from pure microcrystalline cellulose to significantly increased yield to 84.4% after sulfuric acid hydroxysis.[235] An increase of yield from 61% to 82% for cellulase enzyme treated followed by sulfuric acid hydrolyzed cotton linter CNC was observed compared to non-enzyme treated CNC.[236] A high CNC yield of 67.4% was produced from pulp cellulose via electron beam irradiation followed by high-pressure homogenization.[237] A green facile two-phase air plasma/mild alkaline pretreatment approach was developed for efficient production of 73.4% carboxyl- and 97.6% amino-functionalized nanofibrillated cellulose with 90.4% energy reduction compared to baseline process.[238] Thus, those novel technologies in

developing sustainable, cost-effective, and eco-friendly methodologies is the future trend in NCs production.

1.6 Conclusion

In this chapter, a review of cellulose, nanocelluloses (CNCs and CNFs), hydrophobic nanocelluloses modification, application and limitations is provided. Production of two types of nanocellulose (CNF and CNC) from various feedstocks using physical or chemical methodologies have been reported. Hydrophobic modification of nanocelluloses involving esterification, silanation, amidation and polymer grafting were introduced. Nanocelluloses applications were classified to four categories including film coating, aerogel/hydrogel, composite and polymer grafting. Thus, researchers are continuously looking for the most efficient, sustainable, economically viable, and environmentally friendly production technologies to fulfil its growing demand. Some novel technologies such as microwaves irradiation, enzymatic processing, cold plasma, electron beam irradiation have been developed to decrease processing time, energy consumption for preparation of large-scale nanocelluloses at high yield. To sum up, this chapter introduce the sequential processes for nanocelluloses preparation and application from variety of plant sources.

1.7 Reference:

1. Chen, L.; Zhu, J.; Baez, C.; Kitin, P.; Elder, T., Highly thermal-stable and functional cellulose nanocrystals and nanofibrils produced using fully recyclable organic acids. *Green Chemistry* **2016,** *18* (13), 3835-3843.
2. Britannica, E., Cellulose. *Retrieved May* **2008,** *23*, 2008.
3. Genet, M.; Stokes, A.; Salin, F.; Mickovski, S. B.; Fourcaud, T.; Dumail, J.-F.; Van Beek, R., The influence of cellulose content on tensile strength in tree roots. *Plant and soil* **2005,** *278* (1), 1-9.

4. Qu, T.; Guo, W.; Shen, L.; Xiao, J.; Zhao, K., Experimental study of biomass pyrolysis based on three major components: hemicellulose, cellulose, and lignin. *Industrial & engineering chemistry research* **2011,** *50* (18), 10424-10433.
5. Mwaikambo, L. Y.; Ansell, M. P., Chemical modification of hemp, sisal, jute, and kapok fibers by alkalization. *Journal of applied polymer science* **2002,** *84* (12), 2222-2234.
6. Viera, R. G.; Rodrigues Filho, G.; de Assunção, R. M.; Meireles, C. d. S.; Vieira, J. G.; de Oliveira, G. S., Synthesis and characterization of methylcellulose from sugar cane bagasse cellulose. *Carbohydrate Polymers* **2007,** *67* (2), 182-189.
7. Hon, D. N.-S., *Chemical modification of cellulose*. Marcel Dekker: New York, Basel, Hong Kong: 1996.
8. Ouajai, S.; Shanks, R., Composition, structure and thermal degradation of hemp cellulose after chemical treatments. *Polymer degradation and stability* **2005,** *89* (2), 327-335.
9. El-Taraboulsi, M., A Modified of Nitric Acid Pulping of Bagasse. *Cellule. Chem. Technol* **1980,** *14* (1), 29-36.
10. Martí-Ferrer, F.; Vilaplana, F.; Ribes-Greus, A.; Benedito-Borrás, A.; Sanz-Box, C., Flour rice husk as filler in block copolymer polypropylene: Effect of different coupling agents. *Journal of Applied Polymer Science* **2006,** *99* (4), 1823-1831.
11. Hoareau, W.; Trindade, W. G.; Siegmund, B.; Castellan, A.; Frollini, E., Sugar cane bagasse and curaua lignins oxidized by chlorine dioxide and reacted with furfuryl alcohol: characterization and stability. *Polymer Degradation and Stability* **2004,** *86* (3), 567-576.
12. Mohanty, A. K.; Misra, M.; Drzal, L. T., *Natural fibers, biopolymers, and biocomposites*. CRC press: 2005.
13. Li, R.; Fei, J.; Cai, Y.; Li, Y.; Feng, J.; Yao, J., Cellulose whiskers extracted from mulberry: A novel biomass production. *Carbohydrate polymers* **2009,** *76* (1), 94-99.
14. Kallel, F.; Bettaieb, F.; Khiari, R.; García, A.; Bras, J.; Chaabouni, S. E., Isolation and structural characterization of cellulose nanocrystals extracted from garlic straw residues. *Industrial Crops and Products* **2016,** *87*, 287-296.
15. Siqueira, G.; Oksman, K.; Tadokoro, S. K.; Mathew, A. P., Re-dispersible carrot nanofibers with high mechanical properties and reinforcing capacity for use in composite materials. *Composites Science and Technology* **2016,** *123*, 49-56.
16. Bano, S.; Negi, Y. S., Studies on cellulose nanocrystals isolated from groundnut shells. *Carbohydrate polymers* **2017,** *157*, 1041-1049.
17. Rhim, J.-W.; Reddy, J. P.; Luo, X., Isolation of cellulose nanocrystals from onion skin and their utilization for the preparation of agar-based bio-nanocomposites films. *Cellulose* **2015,** *22* (1), 407-420.
18. Lu, P.; Hsieh, Y.-L., Preparation and characterization of cellulose nanocrystals from rice straw. *Carbohydrate Polymers* **2012,** *87* (1), 564-573.
19. Lavoine, N.; Desloges, I.; Dufresne, A.; Bras, J., Microfibrillated cellulose–Its barrier properties and applications in cellulosic materials: A review. *Carbohydrate polymers* **2012,** *90* (2), 735-764.
20. Kumar, R.; Mago, G.; Balan, V.; Wyman, C. E., Physical and chemical characterizations of corn stover and poplar solids resulting from leading pretreatment technologies. *Bioresource technology* **2009,** *100* (17), 3948-3962.
21. Siqueira, G.; Bras, J.; Dufresne, A., Cellulosic bionanocomposites: a review of preparation, properties and applications. *Polymers* **2010,** *2* (4), 728-765.

22. Aulin, C.; Ahola, S.; Josefsson, P.; Nishino, T.; Hirose, Y.; Osterberg, M.; Wagberg, L., Nanoscale Cellulose Films with Different Crystallinities and Mesostructures□ Their Surface Properties and Interaction with Water. *Langmuir* **2009,** *25* (13), 7675-7685.
23. Shmulsky, R.; Jones, P. D., Forest products and wood science: an introduction. **2019**.
24. Nasir, M.; Hashim, R.; Sulaiman, O.; Asim, M., Nanocellulose: Preparation methods and applications. In *Cellulose-reinforced nanofibre composites*, Elsevier: 2017; pp 261-276.
25. Nechyporchuk, O.; Belgacem, M. N.; Bras, J., Production of cellulose nanofibrils: A review of recent advances. *Industrial Crops and Products* **2016,** *93*, 2-25.
26. Toba, K.; Yamamoto, H.; Yoshida, M., On the mechanical interaction between cellulose microfibrils and matrix substances in wood cell walls: effects of chemical pretreatment and subsequent repeated dry-and-wet treatment. *Journal of wood science* **2013,** *59* (5), 359-366.
27. Nishiyama, Y.; Sugiyama, J.; Chanzy, H.; Langan, P., Crystal structure and hydrogen bonding system in cellulose Iα from synchrotron X-ray and neutron fiber diffraction. *Journal of the American Chemical Society* **2003,** *125* (47), 14300-14306.
28. Ju, X.; Bowden, M.; Brown, E. E.; Zhang, X., An improved X-ray diffraction method for cellulose crystallinity measurement. *Carbohydrate polymers* **2015,** *123*, 476-481.
29. Eichhorn, S.; Sirichaisit, J.; Young, R., Deformation mechanisms in cellulose fibres, paper and wood. *Journal of Materials Science* **2001,** *36* (13), 3129-3135.
30. Yang, Q.; Fukuzumi, H.; Saito, T.; Isogai, A.; Zhang, L., Transparent cellulose films with high gas barrier properties fabricated from aqueous alkali/urea solutions. *Biomacromolecules* **2011,** *12* (7), 2766-2771.
31. Dall'Acqua, L.; Tonin, C.; Peila, R.; Ferrero, F.; Catellani, M., Performances and properties of intrinsic conductive cellulose–polypyrrole textiles. *Synthetic Metals* **2004,** *146* (2), 213-221.
32. Mikkelsen, D.; Gidley, M. J.; Williams, B. A., In vitro fermentation of bacterial cellulose composites as model dietary fibers. *Journal of agricultural and food chemistry* **2011,** *59* (8), 4025-4032.
33. Moon, R. J.; Martini, A.; Nairn, J.; Simonsen, J.; Youngblood, J., Cellulose nanomaterials review: structure, properties and nanocomposites. *Chemical Society Reviews* **2011,** *40* (7), 3941-3994.
34. Islam, S. U.; Ul-Islam, M.; Ahsan, H.; Ahmed, M. B.; Shehzad, A.; Fatima, A.; Sonn, J. K.; Lee, Y. S., Potential applications of bacterial cellulose and its composites for cancer treatment. *International Journal of Biological Macromolecules* **2021,** *168*, 301-309.
35. Daicho, K.; Saito, T.; Fujisawa, S.; Isogai, A., The crystallinity of nanocellulose: dispersion-induced disordering of the grain boundary in biologically structured cellulose. *ACS Applied Nano Materials* **2018,** *1* (10), 5774-5785.
36. Iwamoto, S.; Kai, W.; Isogai, A.; Iwata, T., Elastic modulus of single cellulose microfibrils from tunicate measured by atomic force microscopy. *Biomacromolecules* **2009,** *10* (9), 2571-2576.
37. Fukuzumi, H.; Saito, T.; Isogai, A., Influence of TEMPO-oxidized cellulose nanofibril length on film properties. *Carbohydrate Polymers* **2013,** *93* (1), 172-177.
38. Diaz, J. A.; Wu, X.; Martini, A.; Youngblood, J. P.; Moon, R. J., Thermal expansion of self-organized and shear-oriented cellulose nanocrystal films. *Biomacromolecules* **2013,** *14* (8), 2900-2908.

39. Puangsin, B.; Yang, Q.; Saito, T.; Isogai, A., Comparative characterization of TEMPO-oxidized cellulose nanofibril films prepared from non-wood resources. *International journal of biological macromolecules* **2013,** *59*, 208-213.
40. Zhao, M.; Ansari, F.; Takeuchi, M.; Shimizu, M.; Saito, T.; Berglund, L.; Isogai, A., Nematic structuring of transparent and multifunctional nanocellulose papers. *Nanoscale Horizons* **2018,** *3* (1), 28-34.
41. Haywood, A. D.; Davis, V. A., Effects of liquid crystalline and shear alignment on the optical properties of cellulose nanocrystal films. *Cellulose* **2017,** *24* (2), 705-716.
42. Jiang, F.; Han, S.; Hsieh, Y.-L., Controlled defibrillation of rice straw cellulose and self-assembly of cellulose nanofibrils into highly crystalline fibrous materials. *Rsc Advances* **2013,** *3* (30), 12366-12375.
43. Jiang, F.; Hsieh, Y.-L., Chemically and mechanically isolated nanocellulose and their self-assembled structures. *Carbohydrate Polymers* **2013,** *95* (1), 32-40.
44. Pääkkö, M.; Ankerfors, M.; Kosonen, H.; Nykänen, A.; Ahola, S.; Österberg, M.; Ruokolainen, J.; Laine, J.; Larsson, P. T.; Ikkala, O., Enzymatic hydrolysis combined with mechanical shearing and high-pressure homogenization for nanoscale cellulose fibrils and strong gels. *Biomacromolecules* **2007,** *8* (6), 1934-1941.
45. Ye, Y.-S.; Zeng, H.-X.; Wu, J.; Dong, L.-Y.; Zhu, J.-T.; Xue, Z.-G.; Zhou, X.-P.; Xie, X.-L.; Mai, Y.-W., Biocompatible reduced graphene oxide sheets with superior water dispersibility stabilized by cellulose nanocrystals and their polyethylene oxide composites. *Green Chemistry* **2016,** *18* (6), 1674-1683.
46. Sèbe, G.; Ham-Pichavant, F. d. r.; Ibarboure, E.; Koffi, A. L. C.; Tingaut, P., Supramolecular structure characterization of cellulose II nanowhiskers produced by acid hydrolysis of cellulose I substrates. *Biomacromolecules* **2012,** *13* (2), 570-578.
47. Habibi, Y.; Lucia, L. A.; Rojas, O. J., Cellulose nanocrystals: chemistry, self-assembly, and applications. *Chemical reviews* **2010,** *110* (6), 3479-3500.
48. Bondeson, D.; Mathew, A.; Oksman, K., Optimization of the isolation of nanocrystals from microcrystalline cellulose by acid hydrolysis. *Cellulose* **2006,** *13* (2), 171.
49. Elazzouzi-Hafraoui, S.; Nishiyama, Y.; Putaux, J.-L.; Heux, L.; Dubreuil, F.; Rochas, C., The shape and size distribution of crystalline nanoparticles prepared by acid hydrolysis of native cellulose. *Biomacromolecules* **2007,** *9* (1), 57-65.
50. Dufresne, A., Nanocellulose: a new ageless bionanomaterial. *Materials today* **2013,** *16* (6), 220-227.
51. Hafemann, E.; Battisti, R.; Bresolin, D.; Marangoni, C.; Machado, R. A. F., Enhancing chlorine-free purification routes of rice husk biomass waste to obtain cellulose nanocrystals. *Waste and Biomass Valorization* **2020,** *11* (12), 6595-6611.
52. Nang An, V.; Nhan, C.; Thuc, H.; Tap, T. D.; Van, T. T. T.; Van Viet, P.; Van Hieu, L., Extraction of high crystalline nanocellulose from biorenewable sources of Vietnamese agricultural wastes. *Journal of Polymers and the Environment* **2020,** *28* (5), 1465-1474.
53. Wu, C.; Zhang, X.; Wang, X.; Gao, Q.; Li, X., Surface modification of cellulose nanocrystal using succinic anhydride and its effects on poly (butylene succinate) based composites. *Cellulose* **2019,** *26* (5), 3167-3181.
54. Dufresne, A., *Nanocellulose: from nature to high performance tailored materials*. Walter de Gruyter GmbH & Co KG: 2017.
55. Bai, W.; Holbery, J.; Li, K., A technique for production of nanocrystalline cellulose with a narrow size distribution. *Cellulose* **2009,** *16* (3), 455-465.

56. Cheng, M.; Qin, Z.; Chen, Y.; Hu, S.; Ren, Z.; Zhu, M., Efficient extraction of cellulose nanocrystals through hydrochloric acid hydrolysis catalyzed by inorganic chlorides under hydrothermal conditions. *ACS Sustainable Chemistry & Engineering* **2017,** *5* (6), 4656-4664.
57. Shang, Z.; An, X.; Seta, F. T.; Ma, M.; Shen, M.; Dai, L.; Liu, H.; Ni, Y., Improving dispersion stability of hydrochloric acid hydrolyzed cellulose nano-crystals. *Carbohydrate polymers* **2019,** *222*, 115037.
58. Yu, H.-Y.; Qin, Z.-Y.; Liu, L.; Yang, X.-G.; Zhou, Y.; Yao, J.-M., Comparison of the reinforcing effects for cellulose nanocrystals obtained by sulfuric and hydrochloric acid hydrolysis on the mechanical and thermal properties of bacterial polyester. *Composites Science and Technology* **2013,** *87*, 22-28.
59. Gan, I.; Chow, W. S., Synthesis of phosphoric acid-treated sugarcane bagasse cellulose nanocrystal and its thermal properties enhancement for poly (lactic acid) nanocomposites. *Journal of Thermoplastic Composite Materials* **2019,** *32* (5), 619-634.
60. Vanderfleet, O. M.; Osorio, D. A.; Cranston, E. D., Optimization of cellulose nanocrystal length and surface charge density through phosphoric acid hydrolysis. *Philosophical Transactions of the Royal Society A: Mathematical, Physical and Engineering Sciences* **2018,** *376* (2112), 20170041.
61. Wang, W.; Sun, N.; Cai, Z.; Sun, K.; Gu, F.; Jin, Y.; Xiao, H., Sustainable high yield production of cellulose nanomaterials for easy-cleaning surfaces of cellulose-based materials. *BioResources* **2020,** *15* (1), 1014-1025.
62. Li, D.; Henschen, J.; Ek, M., Esterification and hydrolysis of cellulose using oxalic acid dihydrate in a solvent-free reaction suitable for preparation of surface-functionalised cellulose nanocrystals with high yield. *Green Chemistry* **2017,** *19* (23), 5564-5567.
63. Xu, W.; Grénman, H.; Liu, J.; Kronlund, D.; Li, B.; Backman, P.; Peltonen, J.; Willför, S.; Sundberg, A.; Xu, C., Mild Oxalic-Acid-Catalyzed Hydrolysis as a Novel Approach to Prepare Cellulose Nanocrystals. *ChemNanoMat* **2017,** *3* (2), 109-119.
64. Jia, W.; Liu, Y., Two characteristic cellulose nanocrystals (CNCs) obtained from oxalic acid and sulfuric acid processing. *Cellulose* **2019,** *26* (15), 8351-8365.
65. Kang, X.; Kuga, S.; Wang, C.; Zhao, Y.; Wu, M.; Huang, Y., Green preparation of cellulose nanocrystal and its application. *ACS Sustainable Chemistry & Engineering* **2018,** *6* (3), 2954-2960.
66. Song, K.; Ji, Y.; Wang, L.; Wei, Y.; Yu, Z., A green and environmental benign method to extract cellulose nanocrystal by ball mill assisted solid acid hydrolysis. *Journal of Cleaner Production* **2018,** *196*, 1169-1175.
67. Hernández-Varela, J. D.; Chanona-Pérez, J. J.; Benavides, H. A. C.; Sodi, F. C.; Vicente-Flores, M., Effect of ball milling on cellulose nanoparticles structure obtained from garlic and agave waste. *Carbohydrate Polymers* **2021,** *255*, 117347.
68. Park, N.-M.; Choi, S.; Oh, J. E.; Hwang, D. Y., Facile extraction of cellulose nanocrystals. *Carbohydrate Polymers* **2019,** *223*, 115114.
69. Yue, Y.; Zhou, C.; French, A. D.; Xia, G.; Han, G.; Wang, Q.; Wu, Q., Comparative properties of cellulose nano-crystals from native and mercerized cotton fibers. *Cellulose* **2012,** *19* (4), 1173-1187.
70. Gopi, S.; Balakrishnan, P.; Chandradhara, D.; Poovathankandy, D.; Thomas, S., General scenarios of cellulose and its use in the biomedical field. *Materials Today Chemistry* **2019,** *13*, 59-78.

71. Rana, A. K.; Frollini, E.; Thakur, V. K., Cellulose nanocrystals: Pretreatments, preparation strategies, and surface functionalization. *International Journal of Biological Macromolecules* **2021,** *182*, 1554-1581.
72. Rosa, M.; Medeiros, E.; Malmonge, J.; Gregorski, K.; Wood, D.; Mattoso, L.; Glenn, G.; Orts, W.; Imam, S., Cellulose nanowhiskers from coconut husk fibers: Effect of preparation conditions on their thermal and morphological behavior. *Carbohydrate polymers* **2010,** *81* (1), 83-92.
73. Li, J.; Wei, X.; Wang, Q.; Chen, J.; Chang, G.; Kong, L.; Su, J.; Liu, Y., Homogeneous isolation of nanocellulose from sugarcane bagasse by high pressure homogenization. *Carbohydrate polymers* **2012,** *90* (4), 1609-1613.
74. Taheri, H.; Samyn, P., Effect of homogenization (microfluidization) process parameters in mechanical production of micro-and nanofibrillated cellulose on its rheological and morphological properties. *Cellulose* **2016,** *23* (2), 1221-1238.
75. Correia, V. d. C.; dos Santos, V.; Sain, M.; Santos, S. F.; Leao, A. L.; Savastano Junior, H., Grinding process for the production of nanofibrillated cellulose based on unbleached and bleached bamboo organosolv pulp. *Cellulose* **2016,** *23* (5), 2971-2987.
76. Abe, K.; Iwamoto, S.; Yano, H., Obtaining cellulose nanofibers with a uniform width of 15 nm from wood. *Biomacromolecules* **2007,** *8* (10), 3276-3278.
77. Uetani, K.; Yano, H., Nanofibrillation of wood pulp using a high-speed blender. *Biomacromolecules* **2011,** *12* (2), 348-353.
78. Mahardika, M.; Abral, H.; Kasim, A.; Arief, S.; Asrofi, M., Production of nanocellulose from pineapple leaf fibers via high-shear homogenization and ultrasonication. *Fibers* **2018,** *6* (2), 28.
79. Wang, S.; Cheng, Q., A novel process to isolate fibrils from cellulose fibers by high-intensity ultrasonication, Part 1: Process optimization. *Journal of applied polymer science* **2009,** *113* (2), 1270-1275.
80. Kose, R.; Mitani, I.; Kasai, W.; Kondo, T., "Nanocellulose" as a single nanofiber prepared from pellicle secreted by Gluconacetobacter xylinus using aqueous counter collision. *Biomacromolecules* **2011,** *12* (3), 716-720.
81. Saito, T.; Nishiyama, Y.; Putaux, J.-L.; Vignon, M.; Isogai, A., Homogeneous suspensions of individualized microfibrils from TEMPO-catalyzed oxidation of native cellulose. *Biomacromolecules* **2006,** *7* (6), 1687-1691.
82. Isogai, A.; Saito, T.; Fukuzumi, H., TEMPO-oxidized cellulose nanofibers. *nanoscale* **2011,** *3* (1), 71-85.
83. Jiang, F.; Hsieh, Y.-L., Self-assembling of TEMPO oxidized cellulose nanofibrils as affected by protonation of surface carboxyls and drying methods. *ACS Sustainable Chemistry & Engineering* **2016,** *4* (3), 1041-1049.
84. Ghanadpour, M.; Carosio, F.; Larsson, P. T.; Wågberg, L., Phosphorylated cellulose nanofibrils: a renewable nanomaterial for the preparation of intrinsically flame-retardant materials. *Biomacromolecules* **2015,** *16* (10), 3399-3410.
85. Messa, L. L.; Faez, R.; Hsieh, Y.-L., Phosphorylated cellulose nanofibrils from sugarcane bagasse with pH tunable gelation. *Carbohydrate Polymer Technologies and Applications* **2021,** *2*, 100085.
86. Patterson, G.; Hsieh, Y.-L., Tunable dialdehyde/dicarboxylate nanocelluloses by stoichiometrically optimized sequential periodate–chlorite oxidation for tough and wet shape recoverable aerogels. *Nanoscale Advances* **2020,** *2* (12), 5623-5634.

87. Liimatainen, H.; Visanko, M.; Sirviö, J. A.; Hormi, O. E.; Niinimaki, J., Enhancement of the nanofibrillation of wood cellulose through sequential periodate–chlorite oxidation. *Biomacromolecules* **2012,** *13* (5), 1592-1597.
88. Liimatainen, H.; Visanko, M.; Sirviö, J.; Hormi, O.; Niinimäki, J., Sulfonated cellulose nanofibrils obtained from wood pulp through regioselective oxidative bisulfite pre-treatment. *Cellulose* **2013,** *20* (2), 741-749.
89. Pingrey, B.; Hsieh, Y.-L., Sulfated Cellulose Nanofibrils from Chlorosulfonic Acid Treatment and Their Wet Spinning into High-Strength Fibers. *Biomacromolecules* **2022,** *23* (3), 1269-1277.
90. Saito, T.; Nishiyama, Y.; Putaux, J.-L.; Vignon, M.; Isogai, A. J. B., Homogeneous suspensions of individualized microfibrils from TEMPO-catalyzed oxidation of native cellulose. *Biomacromolecules* **2006,** *7* (6), 1687-1691.
91. Pei, A.; Malho, J.-M.; Ruokolainen, J.; Zhou, Q.; Berglund, L. A., Strong nanocomposite reinforcement effects in polyurethane elastomer with low volume fraction of cellulose nanocrystals. *Macromolecules* **2011,** *44* (11), 4422-4427.
92. Auad, M. L.; Contos, V. S.; Nutt, S.; Aranguren, M. I.; Marcovich, N. E., Characterization of nanocellulose-reinforced shape memory polyurethanes. *Polymer International* **2008,** *57* (4), 651-659.
93. Viet, D.; Beck-Candanedo, S.; Gray, D. G., Dispersion of cellulose nanocrystals in polar organic solvents. *Cellulose* **2007,** *14* (2), 109-113.
94. Fujisawa, S.; Ikeuchi, T.; Takeuchi, M.; Saito, T.; Isogai, A., Superior reinforcement effect of TEMPO-oxidized cellulose nanofibrils in polystyrene matrix: optical, thermal, and mechanical studies. *Biomacromolecules* **2012,** *13* (7), 2188-2194.
95. Dai, L.; Zhu, W.; Lu, J.; Kong, F.; Si, C.; Ni, Y., A lignin-containing cellulose hydrogel for lignin fractionation. *Green Chemistry* **2019,** *21* (19), 5222-5230.
96. Qing, W.; Wang, Y.; Wang, Y.; Zhao, D.; Liu, X.; Zhu, J., The modified nanocrystalline cellulose for hydrophobic drug delivery. *Applied Surface Science* **2016,** *366*, 404-409.
97. Prathapan, R.; Thapa, R.; Garnier, G.; Tabor, R. F., Modulating the zeta potential of cellulose nanocrystals using salts and surfactants. *Colloids and Surfaces A: Physicochemical and Engineering Aspects* **2016,** *509*, 11-18.
98. Pan, Y.; Xiao, H.; Cai, P.; Colpitts, M., Cellulose fibers modified with nano-sized antimicrobial polymer latex for pathogen deactivation. *Carbohydrate polymers* **2016,** *135*, 94-100.
99. Yin, Y.; Hong, Z.; Tian, X.; Zhu, Q.; Jiang, X.; Wang, H.; Gao, W., Cellulose nanocrystals modified with quaternary ammonium salts and its reinforcement of polystyrene. *Polymer Bulletin* **2018,** *75* (5), 2151-2166.
100. Salajková, M.; Berglund, L. A.; Zhou, Q., Hydrophobic cellulose nanocrystals modified with quaternary ammonium salts. *Journal of Materials Chemistry* **2012,** *22* (37), 19798-19805.
101. Shimizu, M.; Saito, T.; Fukuzumi, H.; Isogai, A., Hydrophobic, ductile, and transparent nanocellulose films with quaternary alkylammonium carboxylates on nanofibril surfaces. *Biomacromolecules* **2014,** *15* (11), 4320-4325.
102. Kaldéus, T.; Träger, A.; Berglund, L. A.; Malmström, E.; Lo Re, G., Molecular engineering of the cellulose-poly (caprolactone) bio-nanocomposite interface by reactive amphiphilic copolymer nanoparticles. *ACS nano* **2019,** *13* (6), 6409-6420.

103. Sakakibara, K.; Yano, H.; Tsujii, Y., Surface engineering of cellulose nanofiber by adsorption of diblock copolymer dispersant for green nanocomposite materials. *ACS applied materials & interfaces* **2016,** *8* (37), 24893-24900.
104. Fumagalli, M.; Sanchez, F.; Molina-Boisseau, S.; Heux, L., Surface-restricted modification of nanocellulose aerogels in gas-phase esterification by di-functional fatty acid reagents. *Cellulose* **2015,** *22* (3), 1451-1457.
105. Wang, Y.; Wang, X.; Xie, Y.; Zhang, K., Functional nanomaterials through esterification of cellulose: a review of chemistry and application. *Cellulose* **2018,** *25* (7), 3703-3731.
106. Kang, X.; Sun, P.; Kuga, S.; Wang, C.; Zhao, Y.; Wu, M.; Huang, Y., Thin cellulose nanofiber from corncob cellulose and its performance in transparent nanopaper. *ACS Sustainable Chemistry & Engineering* **2017,** *5* (3), 2529-2534.
107. Sethi, J.; Farooq, M.; Sain, S.; Sain, M.; Sirviö, J. A.; Illikainen, M.; Oksman, K., Water resistant nanopapers prepared by lactic acid modified cellulose nanofibers. *Cellulose* **2018,** *25* (1), 259-268.
108. Geng, S.; Wei, J.; Aitomäki, Y.; Noël, M.; Oksman, K., Well-dispersed cellulose nanocrystals in hydrophobic polymers by in situ polymerization for synthesizing highly reinforced bio-nanocomposites. *Nanoscale* **2018,** *10* (25), 11797-11807.
109. Germiniani, L. G.; da Silva, L. C.; Plivelic, T. S.; Gonçalves, M. C., Poly (ε-caprolactone)/cellulose nanocrystal nanocomposite mechanical reinforcement and morphology: the role of nanocrystal pre-dispersion. *Journal of Materials Science* **2019,** *54* (1), 414-426.
110. Zhang, Z.; Zhang, B.; Grishkewich, N.; Berry, R.; Tam, K. C., Cinnamate-functionalized cellulose nanocrystals as UV-shielding nanofillers in sunscreen and transparent polymer films. *Advanced Sustainable Systems* **2019,** *3* (4), 1800156.
111. Morandi, G.; Heath, L.; Thielemans, W. J. L., Cellulose nanocrystals grafted with polystyrene chains through surface-initiated atom transfer radical polymerization (SI-ATRP). *Langmuir* **2009,** *25* (14), 8280-8286.
112. Huang, C.-F.; Chen, J.-K.; Tsai, T.-Y.; Hsieh, Y.-A.; Lin, K.-Y. A., Dual-functionalized cellulose nanofibrils prepared through TEMPO-mediated oxidation and surface-initiated ATRP. *Polymer* **2015,** *72*, 395-405.
113. Ashori, A.; Babaee, M.; Jonoobi, M.; Hamzeh, Y., Solvent-free acetylation of cellulose nanofibers for improving compatibility and dispersion. *Carbohydrate polymers* **2014,** *102*, 369-375.
114. Tripathi, A.; Ago, M.; Khan, S. A.; Rojas, O. J., Heterogeneous acetylation of plant fibers into micro-and nanocelluloses for the synthesis of highly stretchable, tough, and water-resistant co-continuous filaments via wet-spinning. *ACS applied materials & interfaces* **2018,** *10* (51), 44776-44786.
115. Jonoobi, M.; Harun, J.; Mathew, A. P.; Hussein, M. Z. B.; Oksman, K., Preparation of cellulose nanofibers with hydrophobic surface characteristics. *Cellulose* **2010,** *17* (2), 299-307.
116. Fukuda, J.; Hsieh, Y.-L., Hydrophobic 2, 7-Octadienyl Ether-Cellulose Nanofibrils Using Butadiene Sulfone as the Dual Reagent and Medium. *ACS Sustainable Chemistry & Engineering* **2021,** *9* (18), 6489-6498.
117. Guo, M.; Hsieh, Y.-L., One-pot synthesis of 2-bromopropionyl esterified cellulose nanofibrils as hydrophobic coating and film. *RSC Advances* **2022,** *12* (24), 15070-15082.
118. Huang, P.; Wu, M.; Kuga, S.; Wang, D.; Wu, D.; Huang, Y., One-step dispersion of cellulose nanofibers by mechanochemical esterification in an organic solvent. *ChemSusChem* **2012,** *5* (12), 2319-2322.

119. Valdebenito, F.; García, R.; Cruces, K.; Ciudad, G.; Chinga-Carrasco, G.; Habibi, Y., CO2 adsorption of surface-modified cellulose nanofibril films derived from agricultural wastes. *ACS Sustainable Chemistry & Engineering* **2018,** *6* (10), 12603-12612.
120. Frank, B. P.; Durkin, D. P.; Caudill, E. R.; Zhu, L.; White, D. H.; Curry, M. L.; Pedersen, J. A.; Fairbrother, D. H., Impact of silanization on the structure, dispersion properties, and biodegradability of nanocellulose as a nanocomposite filler. *ACS Applied Nano Materials* **2018,** *1* (12), 7025-7038.
121. Lin, W.; Hu, X.; You, X.; Sun, Y.; Wen, Y.; Yang, W.; Zhang, X.; Li, Y.; Chen, H., Hydrophobic modification of nanocellulose via a two-step silanation method. *Polymers* **2018,** *10* (9), 1035.
122. Jiang, F.; Hsieh, Y.-L., Amphiphilic superabsorbent cellulose nanofibril aerogels. *Journal of Materials Chemistry A* **2014,** *2* (18), 6337-6342.
123. Johnson, R. K.; Zink-Sharp, A.; Glasser, W. G., Preparation and characterization of hydrophobic derivatives of TEMPO-oxidized nanocelluloses. *Cellulose* **2011,** *18* (6), 1599-1609.
124. Wang, L.; Okada, K.; Sodenaga, M.; Hikima, Y.; Ohshima, M.; Sekiguchi, T.; Yano, H., Effect of surface modification on the dispersion, rheological behavior, crystallization kinetics, and foaming ability of polypropylene/cellulose nanofiber nanocomposites. *Composites Science and Technology* **2018,** *168*, 412-419.
125. Li, W.; Wang, S.; Wang, W.; Qin, C.; Wu, M., Facile preparation of reactive hydrophobic cellulose nanofibril film for reducing water vapor permeability (WVP) in packaging applications. *Cellulose* **2019,** *26* (5), 3271-3284.
126. Navarro, J. R.; Bergström, L., Labelling of N-hydroxysuccinimide-modified rhodamine B on cellulose nanofibrils by the amidation reaction. *Rsc Advances* **2014,** *4* (105), 60757-60761.
127. Zhang, X.; Zhang, J.; Dong, L.; Ren, S.; Wu, Q.; Lei, T. J. C., Thermoresponsive poly (poly (ethylene glycol) methylacrylate) s grafted cellulose nanocrystals through SI-ATRP polymerization. *Cellulose* **2017,** *24* (10), 4189-4203.
128. Yin, Y.; Tian, X.; Jiang, X.; Wang, H.; Gao, W., Modification of cellulose nanocrystal via SI-ATRP of styrene and the mechanism of its reinforcement of polymethylmethacrylate. *Carbohydrate polymers* **2016,** *142*, 206-212.
129. Pal, N.; Banerjee, S.; Roy, P.; Pal, K., Reduced graphene oxide and PEG-grafted TEMPO-oxidized cellulose nanocrystal reinforced poly-lactic acid nanocomposite film for biomedical application. *Materials Science and Engineering: C* **2019,** *104*, 109956.
130. Abushammala, H., Nano-Brushes of alcohols grafted onto cellulose nanocrystals for reinforcing poly (Butylene succinate): Impact of Alcohol chain length on interfacial adhesion. *Polymers* **2020,** *12* (1), 95.
131. Li, Y.; Zhu, L.; Grishkewich, N.; Tam, K. C.; Yuan, J.; Mao, Z.; Sui, X., CO2-responsive cellulose nanofibers aerogels for switchable oil–water separation. *ACS applied materials & interfaces* **2019,** *11* (9), 9367-9373.
132. Kim, M.; Schmitt, S. K.; Choi, J. W.; Krutty, J. D.; Gopalan, P., From self-assembled monolayers to coatings: Advances in the synthesis and nanobio applications of polymer brushes. *Polymers* **2015,** *7* (7), 1346-1378.
133. Syverud, K.; Xhanari, K.; Chinga-Carrasco, G.; Yu, Y.; Stenius, P., Films made of cellulose nanofibrils: surface modification by adsorption of a cationic surfactant and characterization by computer-assisted electron microscopy. *Journal of Nanoparticle Research* **2011,** *13* (2), 773-782.

134. Yang, X.; Xie, H.; Du, H.; Zhang, X.; Zou, Z.; Zou, Y.; Liu, W.; Lan, H.; Zhang, X.; Si, C., Facile extraction of thermally stable and dispersible cellulose nanocrystals with high yield via a green and recyclable FeCl3-catalyzed deep eutectic solvent system. *ACS Sustainable Chemistry & Engineering* **2019,** *7* (7), 7200-7208.
135. Sun, L.; Zhang, X.; Liu, H.; Liu, K.; Du, H.; Kumar, A.; Sharma, G.; Si, C., Recent Advances in Hydrophobic Modification of Nanocellulose. *Current Organic Chemistry* **2021,** *25* (3), 417-436.
136. Wang, H.; Xie, H.; Du, H.; Wang, X.; Liu, W.; Duan, Y.; Zhang, X.; Sun, L.; Zhang, X.; Si, C., Highly efficient preparation of functional and thermostable cellulose nanocrystals via H2SO4 intensified acetic acid hydrolysis. *Carbohydrate Polymers* **2020,** *239*, 116233.
137. Huang, D.; Yang, Q.; Jin, S.; Deng, Q.; Zhou, P., Self-assembly of cellulose nanoparticles as electrolyte additive for capillary electrophoresis separation. *Journal of Chromatography A* **2014,** *1367*, 148-153.
138. Samantaray, P. K.; Baloda, S.; Madras, G.; Bose, S., Interlocked Dithi-Magnetospheres–Decorated MoS2 Nanosheets as Molecular Sieves and Traps for Heavy Metal Ions. *Advanced Sustainable Systems* **2019,** *3* (6), 1800153.
139. Ullah, M. W.; Ul Islam, M.; Khan, S.; Shah, N.; Park, J. K., Recent advancements in bioreactions of cellular and cell-free systems: a study of bacterial cellulose as a model. *Korean Journal of Chemical Engineering* **2017,** *34* (6), 1591-1599.
140. Ullah, M. W.; Ul-Islam, M.; Khan, S.; Kim, Y.; Park, J. K., Innovative production of bio-cellulose using a cell-free system derived from a single cell line. *Carbohydrate polymers* **2015,** *132*, 286-294.
141. Henriksson, M.; Berglund, L. A.; Isaksson, P.; Lindström, T.; Nishino, T., Cellulose nanopaper structures of high toughness. *Biomacromolecules* **2008,** *9* (6), 1579-1585.
142. Yan, C.; Wang, J.; Kang, W.; Cui, M.; Wang, X.; Foo, C. Y.; Chee, K. J.; Lee, P. S., Highly stretchable piezoresistive graphene–nanocellulose nanopaper for strain sensors. *Advanced materials* **2014,** *26* (13), 2022-2027.
143. Czaja, W.; Krystynowicz, A.; Bielecki, S.; Brown Jr, R. M., Microbial cellulose—the natural power to heal wounds. *Biomaterials* **2006,** *27* (2), 145-151.
144. Liyanapathiranage, A.; Peña, M. J.; Sharma, S.; Minko, S., Nanocellulose-based sustainable dyeing of cotton textiles with minimized water pollution. *ACS omega* **2020,** *5* (16), 9196-9203.
145. Azeredo, H. M.; Rosa, M. F.; Mattoso, L. H. C., Nanocellulose in bio-based food packaging applications. *Industrial Crops and Products* **2017,** *97*, 664-671.
146. Almeida, T.; Silvestre, A. J.; Vilela, C.; Freire, C. S., Bacterial nanocellulose toward green cosmetics: Recent progresses and challenges. *International Journal of Molecular Sciences* **2021,** *22* (6), 2836.
147. Aguilar-Sanchez, A.; Jalvo, B.; Mautner, A.; Nameer, S.; Pöhler, T.; Tammelin, T.; Mathew, A. P., Waterborne nanocellulose coatings for improving the antifouling and antibacterial properties of polyethersulfone membranes. *Journal of Membrane Science* **2021,** *620*, 118842.
148. Le Gars, M.; Dhuiège, B.; Delvart, A.; Belgacem, M. N.; Missoum, K.; Bras, J., High-Barrier and Antioxidant Poly (lactic acid)/Nanocellulose Multilayered Materials for Packaging. *ACS omega* **2020,** *5* (36), 22816-22826.

149. Martin, C.; Jean, B., Nanocellulose/polymer multilayered thin films: tunable architectures towards tailored physical properties. *Nordic Pulp & Paper Research Journal* **2014,** *29* (1), 19-30.
150. Koppolu, R.; Lahti, J.; Abitbol, T.; Swerin, A.; Kuusipalo, J.; Toivakka, M., Continuous Processing of Nanocellulose and Polylactic Acid into Multilayer Barrier Coatings. *ACS applied materials & interfaces* **2019,** *11* (12), 11920-11927.
151. De France, K. J.; Chan, K. J.; Cranston, E. D.; Hoare, T., Enhanced mechanical properties in cellulose nanocrystal–poly (oligoethylene glycol methacrylate) injectable nanocomposite hydrogels through control of physical and chemical cross-linking. *Biomacromolecules* **2016,** *17* (2), 649-660.
152. De France, K. J.; Hoare, T.; Cranston, E. D., Review of hydrogels and aerogels containing nanocellulose. *Chemistry of Materials* **2017,** *29* (11), 4609-4631.
153. Zhou, J.; Hsieh, Y.-L., Conductive polymer protonated nanocellulose aerogels for tunable and linearly responsive strain sensors. *ACS applied materials & interfaces* **2018,** *10* (33), 27902-27910.
154. Heath, L.; Thielemans, W., Cellulose nanowhisker aerogels. *Green Chemistry* **2010,** *12* (8), 1448-1453.
155. Pursula, P.; Kiri, K.; Mc Caffrey, C.; Sandberg, H.; Vartiainen, J.; Flak, J.; Lahtinen, P., Nanocellulose–polyurethane substrate material with tunable mechanical properties for wearable electronics. *Flexible and Printed Electronics* **2018,** *3* (4), 045002.
156 Cheng, D.; Wei, P.; Zhang, L.; Cai, J., New Approach for the Fabrication of Carboxymethyl Cellulose Nanofibrils and the Reinforcement Effect in Water-Borne Polyurethane. *ACS Sustainable Chemistry & Engineering* **2019,** *7* (13), 11850-11860.
157. Donius, A. E.; Liu, A.; Berglund, L. A.; Wegst, U. G., Superior mechanical performance of highly porous, anisotropic nanocellulose–montmorillonite aerogels prepared by freeze casting. *Journal of the mechanical behavior of biomedical materials* **2014,** *37*, 88-99.
158. Ago, M.; Okajima, K.; Jakes, J. E.; Park, S.; Rojas, O. J., Lignin-based electrospun nanofibers reinforced with cellulose nanocrystals. *Biomacromolecules* **2012,** *13* (3), 918-926.
159. Panthapulakkal, S.; Sain, M., Preparation and characterization of cellulose nanofibril films from wood fibre and their thermoplastic polycarbonate composites. *International Journal of Polymer Science* **2012,** *2012*.
160. Savadekar, N.; Mhaske, S., Synthesis of nano cellulose fibers and effect on thermoplastics starch based films. *Carbohydrate Polymers* **2012,** *89* (1), 146-151.
161. Rueda, L.; Saralegui, A.; d'Arlas, B. F.; Zhou, Q.; Berglund, L. A.; Corcuera, M.; Mondragon, I.; Eceiza, A., Cellulose nanocrystals/polyurethane nanocomposites. Study from the viewpoint of microphase separated structure. *Carbohydrate polymers* **2013,** *92* (1), 751-757.
162. Amin, K. N. M.; Amiralian, N.; Annamalai, P. K.; Edwards, G.; Chaleat, C.; Martin, D. J., Scalable processing of thermoplastic polyurethane nanocomposites toughened with nanocellulose. *Chemical Engineering Journal* **2016,** *302*, 406-416.
163. Ivdre, A.; Mucci, V.; Stefani, P.; Aranguren, M.; Cabulis, U. In *Nanocellulose reinforced polyurethane obtained from hydroxylated soybean oil*, IOP Conference Series: Materials Science and Engineering, IOP Publishing: 2016; p 012011.
164. Lee, M.; Heo, M. H.; Lee, H.-H.; Kim, Y.-W.; Shin, J., Tunable softening and toughening of individualized cellulose nanofibers-polyurethane urea elastomer composites. *Carbohydrate polymers* **2017,** *159*, 125-135.

165. Abitbol, T.; Rivkin, A.; Cao, Y.; Nevo, Y.; Abraham, E.; Ben-Shalom, T.; Lapidot, S.; Shoseyov, O., Nanocellulose, a tiny fiber with huge applications. *Current opinion in biotechnology* **2016,** *39*, 76-88.
166. Chen, J.; Gao, Q.; Zhou, G.; Xu, X., Interactions between the protein-epigallocatechin gallate complex and nanocrystalline cellulose: A systematic study. *Food Chemistry* **2022,** *387*, 132791.
167. Kargarzadeh, H.; Mariano, M.; Huang, J.; Lin, N.; Ahmad, I.; Dufresne, A.; Thomas, S., Recent developments on nanocellulose reinforced polymer nanocomposites: A review. *Polymer* **2017,** *132*, 368-393.
168. Markstedt, K.; Mantas, A.; Tournier, I.; Martínez Ávila, H.; Hagg, D.; Gatenholm, P., 3D bioprinting human chondrocytes with nanocellulose–alginate bioink for cartilage tissue engineering applications. *Biomacromolecules* **2015,** *16* (5), 1489-1496.
169. Manzocco, L.; Plazzotta, S.; Powell, J.; de Vries, A.; Rousseau, D.; Calligaris, S., Structural characterisation and sorption capability of whey protein aerogels obtained by freeze-drying or supercritical drying. *Food Hydrocolloids* **2022,** *122*, 107117.
170. Piras, C. C.; Fernández-Prieto, S.; De Borggraeve, W. M., Nanocellulosic materials as bioinks for 3D bioprinting. *Biomaterials science* **2017,** *5* (10), 1988-1992.
171. Wu, W.; Tassi, N. G.; Zhu, H.; Fang, Z.; Hu, L., Nanocellulose-based translucent diffuser for optoelectronic device applications with dramatic improvement of light coupling. *ACS applied materials & interfaces* **2015,** *7* (48), 26860-26864.
172. Reshmy, R.; Philip, E.; Madhavan, A.; Pugazhendhi, A.; Sindhu, R.; Sirohi, R.; Awasthi, M. K.; Pandey, A.; Binod, P., Nanocellulose as green material for remediation of hazardous heavy metal contaminants. *Journal of Hazardous Materials* **2022,** *424*, 127516.
173. Aulin, C.; Karabulut, E.; Tran, A.; Wågberg, L.; Lindström, T., Transparent nanocellulosic multilayer thin films on polylactic acid with tunable gas barrier properties. *ACS applied materials & interfaces* **2013,** *5* (15), 7352-7359.
174. Ankerfors, M.; Lindström, T.; Nordmark, G. G., Multilayer assembly onto pulp fibres using oppositely charged microfibrillated celluloses, starches, and wetstrength resins− Effect on mechanical properties of CTMP-sheets. *Nordic Pulp & Paper Research Journal* **2016,** *31* (1), 135-141.
175. Li, D.; McCann, J. T.; Xia, Y.; Marquez, M., Electrospinning: a simple and versatile technique for producing ceramic nanofibers and nanotubes. *Journal of the American Ceramic Society* **2006,** *89* (6), 1861-1869.
176. Bhardwaj, N.; Kundu, S. C., Electrospinning: a fascinating fiber fabrication technique. *Biotechnology advances* **2010,** *28* (3), 325-347.
177. Fotie, G.; Limbo, S.; Piergiovanni, L., Manufacturing of food packaging based on nanocellulose: Current advances and challenges. *Nanomaterials* **2020,** *10* (9), 1726.
178. Foster, E. J.; Moon, R. J.; Agarwal, U. P.; Bortner, M. J.; Bras, J.; Camarero-Espinosa, S.; Chan, K. J.; Clift, M. J.; Cranston, E. D.; Eichhorn, S. J., Current characterization methods for cellulose nanomaterials. *Chemical Society Reviews* **2018,** *47* (8), 2609-2679.
179. Luo, Y.; Wang, X.; Zhu, Y.; Li, B.-G.; Zhu, S., Polystyrene-block-poly (n-butyl acrylate)-block-polystyrene triblock copolymer thermoplastic elastomer synthesized via RAFT emulsion polymerization. *Macromolecules* **2010,** *43* (18), 7472-7481.
180. Yu, J.; Lu, C.; Wang, C.; Wang, J.; Fan, Y.; Chu, F., Sustainable thermoplastic elastomers derived from cellulose, fatty acid and furfural via ATRP and click chemistry. *Carbohydrate polymers* **2017,** *176*, 83-90.

181. Zhao, B.; Brittain, W. J., Polymer brushes: surface-immobilized macromolecules. *Progress in Polymer Science* **2000,** *25* (5), 677-710.
182. Rol, F.; Belgacem, M. N.; Gandini, A.; Bras, J., Recent advances in surface-modified cellulose nanofibrils. *Progress in Polymer Science* **2019,** *88*, 241-264.
183. Khabibullin, A.; Mastan, E.; Matyjaszewski, K.; Zhu, S., Surface-initiated atom transfer radical polymerization. In *Controlled Radical Polymerization at and from Solid Surfaces*, Springer: 2015; pp 29-76.
184. Zhang, X.; Zhang, J.; Dong, L.; Ren, S.; Wu, Q.; Lei, T., Thermoresponsive poly (poly (ethylene glycol) methylacrylate) s grafted cellulose nanocrystals through SI-ATRP polymerization. *Cellulose* **2017,** *24* (10), 4189-4203.
185. Yuan, W.; Wang, C.; Lei, S.; Chen, J.; Lei, S.; Li, Z., Ultraviolet light-, temperature-and pH-responsive fluorescent sensors based on cellulose nanocrystals. *Polymer Chemistry* **2018,** *9* (22), 3098-3107.
186. Zhang, J.; Wu, Q.; Li, M.-C.; Song, K.; Sun, X.; Lee, S.-Y.; Lei, T., Thermoresponsive copolymer poly (N-Vinylcaprolactam) grafted cellulose nanocrystals: synthesis, structure, and properties. *ACS Sustainable Chemistry & Engineering* **2017,** *5* (8), 7439-7447.
187. Risteen, B.; McBride, M.; Gonzalez, M.; Khau, B.; Zhang, G.; Reichmanis, E., Functionalized cellulose nanocrystal-mediated conjugated polymer aggregation. *ACS Applied Materials & Interfaces* **2019,** *11* (28), 25338-25350.
188. Hatton, F. L.; Kedzior, S. A.; Cranston, E. D.; Carlmark, A., Grafting-from cellulose nanocrystals via photoinduced Cu-mediated reversible-deactivation radical polymerization. *Carbohydrate polymers* **2017,** *157*, 1033-1040.
189. Boujemaoui, A.; Mongkhontreerat, S.; Malmström, E.; Carlmark, A., Preparation and characterization of functionalized cellulose nanocrystals. *Carbohydrate Polymers* **2015,** *115*, 457-464.
190. Morandi, G.; Heath, L.; Thielemans, W., Cellulose nanocrystals grafted with polystyrene chains through surface-initiated atom transfer radical polymerization (SI-ATRP). *Langmuir* **2009,** *25* (14), 8280-8286.
191. Zhang, Z.; Tam, K. C.; Sèbe, G.; Wang, X., Convenient characterization of polymers grafted on cellulose nanocrystals via SI-ATRP without chain cleavage. *Carbohydrate polymers* **2018,** *199*, 603-609.
192. Wang, H. D.; Roeder, R. D.; Whitney, R. A.; Champagne, P.; Cunningham, M. F., Graft modification of crystalline nanocellulose by Cu (0)-mediated SET living radical polymerization. *Journal of Polymer Science Part A: Polymer Chemistry* **2015,** *53* (24), 2800-2808.
193. Kedzior, S. A.; Kiriakou, M.; Niinivaara, E.; Dube, M. A.; Fraschini, C.; Berry, R. M.; Cranston, E. D., Incorporating cellulose nanocrystals into the core of polymer latex particles via polymer grafting. *ACS Macro Letters* **2018,** *7* (8), 990-996.
194. Zhang, Z.; Sèbe, G.; Wang, X.; Tam, K. C., UV-absorbing cellulose nanocrystals as functional reinforcing fillers in poly (vinyl chloride) films. *ACS Applied Nano Materials* **2018,** *1* (2), 632-641.
195. Le Gars, M.; Bras, J.; Salmi-Mani, H.; Ji, M.; Dragoe, D.; Faraj, H.; Domenek, S.; Belgacem, N.; Roger, P., Polymerization of glycidyl methacrylate from the surface of cellulose nanocrystals for the elaboration of PLA-based nanocomposites. *Carbohydrate Polymers* **2020,** *234*, 115899.

196. Zhang, Z.; Sèbe, G.; Wang, X.; Tam, K. C., Gold nanoparticles stabilized by poly (4-vinylpyridine) grafted cellulose nanocrystals as efficient and recyclable catalysts. *Carbohydrate Polymers* **2018,** *182*, 61-68.
197. Rosilo, H.; McKee, J. R.; Kontturi, E.; Koho, T.; Hytönen, V. P.; Ikkala, O.; Kostiainen, M. A., Cationic polymer brush-modified cellulose nanocrystals for high-affinity virus binding. *Nanoscale* **2014,** *6* (20), 11871-11881.
198. Abousalman-Rezvani, Z.; Eskandari, P.; Roghani-Mamaqani, H.; Mardani, H.; Salami-Kalajahi, M., Grafting light-, temperature, and CO2-responsive copolymers from cellulose nanocrystals by atom transfer radical polymerization for adsorption of nitrate ions. *Polymer* **2019,** *182*, 121830.
199. Yu, J.; Wang, C.; Wang, J.; Chu, F., In situ development of self-reinforced cellulose nanocrystals based thermoplastic elastomers by atom transfer radical polymerization. *Carbohydrate polymers* **2016,** *141*, 143-150.
200. Kiriakou, M. V.; Berry, R. M.; Hoare, T.; Cranston, E. D., Effect of Reaction Media on Grafting Hydrophobic Polymers from Cellulose Nanocrystals via Surface-Initiated Atom-Transfer Radical Polymerization. *Biomacromolecules* **2021,** *22* (8), 3601-3612.
201. Majoinen, J.; Walther, A.; McKee, J. R.; Kontturi, E.; Aseyev, V.; Malho, J. M.; Ruokolainen, J.; Ikkala, O., Polyelectrolyte brushes grafted from cellulose nanocrystals using Cu-mediated surface-initiated controlled radical polymerization. *Biomacromolecules* **2011,** *12* (8), 2997-3006.
202. Morits, M.; Hynninen, V.; Niederberger, A.; Ikkala, O.; Gröschel, A. H.; Müllner, M., Polymer brush guided templating on well-defined rod-like cellulose nanocrystals. *Polymer Chemistry* **2018,** *9* (13), 1650-1657.
203. Zhang, Z.; Wang, X.; Tam, K. C.; Sebe, G., A comparative study on grafting polymers from cellulose nanocrystals via surface-initiated atom transfer radical polymerization (ATRP) and activator re-generated by electron transfer ATRP. *Carbohydrate polymers* **2019,** *205*, 322-329.
204. Navarro, J. R.; Edlund, U., Surface-initiated controlled radical polymerization approach to enhance nanocomposite integration of cellulose nanofibrils. *Biomacromolecules* **2017,** *18* (6), 1947-1955.
205. Chen, J.-K.; Huang, H.-Y.; Tu, C.-W.; Lee, L.-T.; Jamnongkan, T.; Huang, C.-F., SI ATRP for the Surface Modifications of Optically Transparent Paper Films Made by TEMPO-Oxidized Cellulose Nanofibers. *Polymers* **2022,** *14* (5), 946.
206. Morits, M.; McKee, J. R.; Majoinen, J.; Malho, J.-M.; Houbenov, N.; Seitsonen, J.; Laine, J.; Gröschel, A. H.; Ikkala, O., Polymer brushes on cellulose nanofibers: modification, SI-ATRP, and unexpected degradation processes. *ACS Sustainable Chemistry & Engineering* **2017,** *5* (9), 7642-7650.
207. Hemraz, U. D.; Lu, A.; Sunasee, R.; Boluk, Y. J. J. o. c.; science, i., Structure of poly (N-isopropylacrylamide) brushes and steric stability of their grafted cellulose nanocrystal dispersions. *Journal of colloid and interface science* **2014,** *430*, 157-165.
208. Zhang, X.; Wang, Y.; Zhao, J.; Xiao, M.; Zhang, W.; Lu, C.; Engineering, Mechanically strong and thermally responsive cellulose nanofibers/poly (N-isopropylacrylamide) composite aerogels. *ACS Sustainable Chemistry & Engineering* **2016,** *4* (8), 4321-4327.
209. AL-Oqla, F. M.; Rababah, M., Challenges in design of nanocellulose and its composites for different applications. In *Cellulose-reinforced nanofibre composites*, Elsevier: 2017; pp 113-127.

210. Balea, A.; Blanco, A.; Delgado-Aguilar, M.; Monte, M. C.; Tarres, Q.; Mutjé, P.; Negro, C., Nanocellulose Characterization Challenges. *BioResources* **2021,** *16* (2).
211. Pradhan, D.; Jaiswal, A. K.; Jaiswal, S., Emerging technologies for the production of nanocellulose from lignocellulosic biomass. *Carbohydrate Polymers* **2022**, 119258.
212. Dweiri, F.; Al-Oqla, F. M., Material selection using analytical hierarchy process. *International journal of computer applications in technology* **2006,** *26* (4), 182-189.
213. Ashby, M. F.; Johnson, K., *Materials and design: the art and science of material selection in product design*. Butterworth-Heinemann: 2013.
214. Thomas, B.; Raj, M. C.; Joy, J.; Moores, A.; Drisko, G. L.; Sanchez, C., Nanocellulose, a versatile green platform: from biosources to materials and their applications. *Chemical reviews* **2018,** *118* (24), 11575-11625.
215. Al-Oqla, F. M.; Sapuan, M. S.; Ishak, M. R.; Aziz, N. A., Combined multi-criteria evaluation stage technique as an agro waste evaluation indicator for polymeric composites: date palm fibers as a case study. *BioResources* **2014,** *9* (3), 4608-4621.
216. AL-Oqla, F. M.; Sapuan, S.; Jawaid, M., Integrated mechanical-economic–environmental quality of performance for natural fibers for polymeric-based composite materials. *Journal of Natural Fibers* **2016,** *13* (6), 651-659.
217. Al-Oqla, F. M.; Sapuan, S., Polymer selection approach for commonly and uncommonly used natural fibers under uncertainty environments. *Jom* **2015,** *67* (10), 2450-2463.
218. Sapuan, S.; Pua, F.-l.; El-Shekeil, Y.; AL-Oqla, F. M., Mechanical properties of soil buried kenaf fibre reinforced thermoplastic polyurethane composites. *Materials & Design* **2013,** *50*, 467-470.
219. Al-Oqla, F. M.; Sapuan, S.; Anwer, T.; Jawaid, M.; Hoque, M., Natural fiber reinforced conductive polymer composites as functional materials: A review. *Synthetic Metals* **2015,** *206*, 42-54.
220. George, G.; Joseph, K.; Nagarajan, E.; Jose, E. T.; George, K., Dielectric behaviour of PP/jute yarn commingled composites: Effect of fibre content, chemical treatments, temperature and moisture. *Composites Part A: Applied Science and Manufacturing* **2013,** *47*, 12-21.
221. Satyanarayana, K. G.; Arizaga, G. G.; Wypych, F., Biodegradable composites based on lignocellulosic fibers—An overview. *Progress in polymer science* **2009,** *34* (9), 982-1021.
222. Pennells, J.; Heuberger, B.; Chaléat, C.; Martin, D. J., Assessing cellulose micro/nanofibre morphology using a high throughput fibre analysis device to predict nanopaper performance. *Cellulose* **2022,** *29* (4), 2599-2616.
223. Jowkarderis, L.; van de Ven, T. G., Intrinsic viscosity of aqueous suspensions of cellulose nanofibrils. *Cellulose* **2014,** *21* (4), 2511-2517.
224. Li, M.-C.; Wu, Q.; Song, K.; Lee, S.; Qing, Y.; Wu, Y., Cellulose nanoparticles: structure–morphology–rheology relationships. *ACS Sustainable Chemistry & Engineering* **2015,** *3* (5), 821-832.
225. Colson, J.; Bauer, W.; Mayr, M.; Fischer, W.; Gindl-Altmutter, W., Morphology and rheology of cellulose nanofibrils derived from mixtures of pulp fibres and papermaking fines. *Cellulose* **2016,** *23* (4), 2439-2448.
226. Nguyen, H.-L.; Jo, Y. K.; Cha, M.; Cha, Y. J.; Yoon, D. K.; Sanandiya, N. D.; Prajatelistia, E.; Oh, D. X.; Hwang, D. S., Mussel-inspired anisotropic nanocellulose and silver nanoparticle composite with improved mechanical properties, electrical conductivity and antibacterial activity. *Polymers* **2016,** *8* (3), 102.

227. Beck, S.; Bouchard, J., Auto-catalyzed acidic desulfation of cellulose nanocrystals. *Nordic Pulp & Paper Research Journal* **2014,** *29* (1), 6-14.
228. Deepa, B.; Abraham, E.; Cordeiro, N.; Mozetic, M.; Mathew, A. P.; Oksman, K.; Faria, M.; Thomas, S.; Pothan, L. A., Utilization of various lignocellulosic biomass for the production of nanocellulose: a comparative study. *Cellulose* **2015,** *22* (2), 1075-1090.
229. Teo, H. L.; Wahab, R. A., Towards an eco-friendly deconstruction of agro-industrial biomass and preparation of renewable cellulose nanomaterials: A review. *International journal of biological macromolecules* **2020,** *161*, 1414-1430.
230. Dilamian, M.; Noroozi, B., A combined homogenization-high intensity ultrasonication process for individualizaion of cellulose micro-nano fibers from rice straw. *Cellulose* **2019,** *26* (10), 5831-5849.
231. Alemdar, A.; Sain, M., Isolation and characterization of nanofibers from agricultural residues–Wheat straw and soy hulls. *Bioresource technology* **2008,** *99* (6), 1664-1671.
232. Berglund, L.; Noël, M.; Aitomäki, Y.; Öman, T.; Oksman, K., Production potential of cellulose nanofibers from industrial residues: Efficiency and nanofiber characteristics. *Industrial Crops and Products* **2016,** *92*, 84-92.
233. Hongrattanavichit, I.; Aht-Ong, D., Nanofibrillation and characterization of sugarcane bagasse agro-waste using water-based steam explosion and high-pressure homogenization. *Journal of Cleaner Production* **2020,** *277*, 123471.
234. Yan, M.; Tian, C.; Wu, T.; Huang, X.; Zhong, Y.; Yang, P.; Zhang, L.; Ma, J.; Lu, H.; Zhou, X., Insights into structure and properties of cellulose nanofibrils (CNFs) prepared by screw extrusion and deep eutectic solvent permeation. *International Journal of Biological Macromolecules* **2021,** *191*, 422-431.
235. Qian, M.; Lei, H.; Villota, E.; Zhao, Y.; Wang, C.; Huo, E.; Zhang, Q.; Mateo, W.; Lin, X., High yield production of nanocrystalline cellulose by microwave-assisted dilute-acid pretreatment combined with enzymatic hydrolysis. *Chemical Engineering and Processing-Process Intensification* **2021,** *160*, 108292.
236. Beltramino, F.; Roncero, M. B.; Vidal, T.; Valls, C., A novel enzymatic approach to nanocrystalline cellulose preparation. *Carbohydrate polymers* **2018,** *189*, 39-47.
237. Lee, M.; Heo, M. H.; Lee, H.; Lee, H.-H.; Jeong, H.; Kim, Y.-W.; Shin, J., Facile and eco-friendly extraction of cellulose nanocrystals via electron beam irradiation followed by high-pressure homogenization. *Green Chemistry* **2018,** *20* (11), 2596-2610.
238. Shaghaleh, H.; Wang, S.; Xu, X.; Guo, L.; Dong, F.; Hamoud, Y. A.; Liu, H.; Li, P.; Zhang, S., Innovative two-phase air plasma activation approach for green and efficient functionalization of nanofibrillated cellulose surfaces from wheat straw. *Journal of Cleaner Production* **2021,** *297*, 126664.

Chapter 2. One-pot Synthesis of Bromine Esterified Cellulose Nanofibrils as Hydrophobic Coating and Film

Published on RSC Advances, May 17, 2022

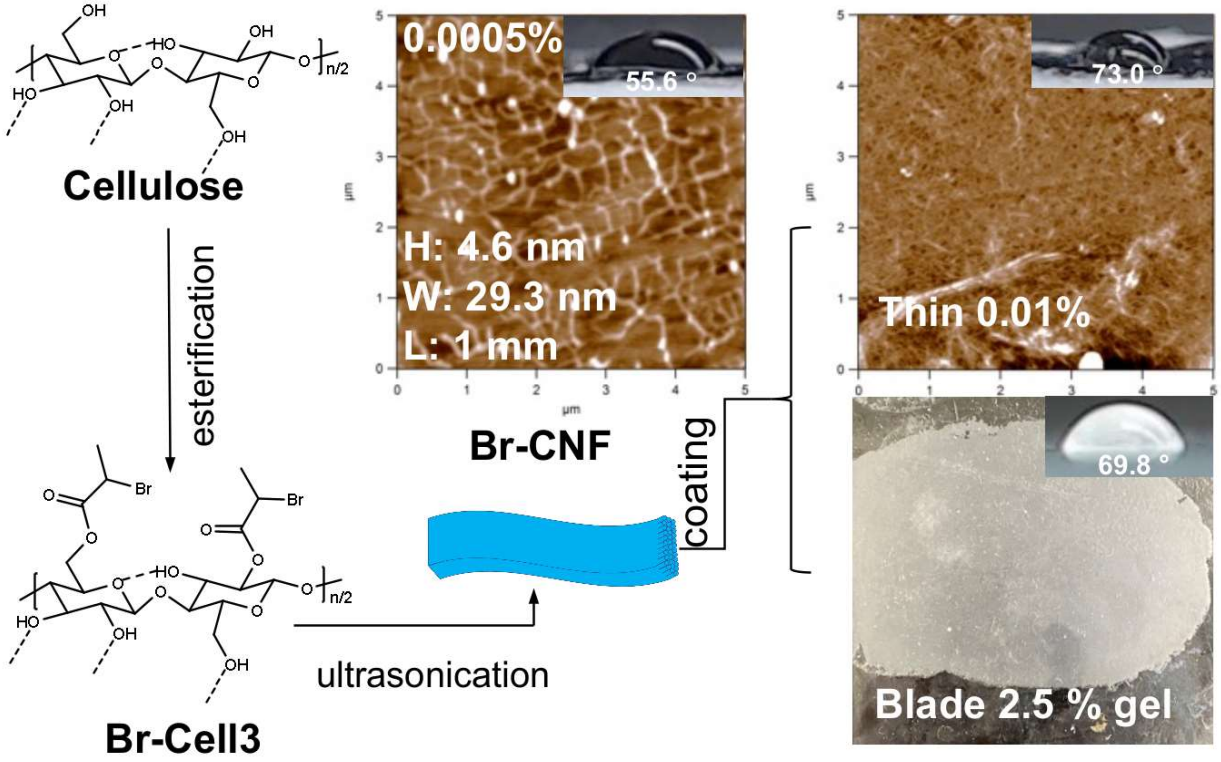

Abstract

Hydrophobic bromine esterified cellulose nanofibrils (Br-CNFs) have been facilely produced via one-pot esterification of cellulose with 2-bromopropionyl bromide (BPB) then directly disintegrated in DMF by ultrasonication. Br-CNFs optimally produced by this streamlined Br-esterification-ultrasonication approach, i.e., 5:1 BPB to anhydroglucose AGU molar ratio, 23 °C, 6 h and ultrasonication (50% amplitude, 30 min), were 4.6 nm thick, 29.3 nm wide, and 1 µm long in 70.9% yield and 47.8% crystallinity. Successful cellulose hydroxyl to bromine ester conversion was confirmed by the presence of Br ester by FTIR and ^{1}H NMR. The degree of substitution (DS) of hydroxyl to ester was determined to be between the underestimated 0.53 (DS_s) based on XRD and Br-CNF dimensions and the overestimated 0.56 (DS_{NMR}) from solution-state ^{1}H NMR. Br-

CNF dispersions in DMF exhibited Newtonian behavior at concentrations below and shear thinning behavior above 0.5%, enabling homogeneous deposition at dilute concentrations up to 0.01% into few nm ultra-thin layers as well blade coating of gel into ca. 100 μm thick film, all similarly hydrophobic with surface WCAs in the range of 70-75°. The ultra-high modulus and strength film from gel coating further shows the potential for dual high-strength and hydrophobic applications.

2.1 Introduction

Cellulose is not only the most abundant natural polymer on earth with renewable annual production of 75 to 100 billion tons,[1] but also the most chemically homogeneous and intrinsically semi-crystalline. The crystalline domains can be isolated as a few to tens nm wide and hundreds nm long rod-like cellulose nanocrystals (CNCs) or thinner and longer cellulose nanofibrils (CNFs). These so called nanocelluloses have gained increasing attention due to their ultra-high elastic modulus (150 GPa for CNCs, 28 GPa for CNFs)[2, 3], low axial thermal expansion coefficient (10^{-7} K^{-1} for CNCs, 5×10^{-6} K^{-1} for CNFs)[4, 5] and biocompatibility[6, 7]. CNCs and CNFs have been most commonly produced by either removing the non-crystalline regions via acid hydrolysis[8-12], modifying them by oxidation[12-18], or disintegrated by mechanical forces[12-17, 19-22], or a combination of the latter two[13-17]. These nanocelluloses[8-22] are all hydrophilic, some with anionic charges, making them easily dispersible in aqueous media, but incompatible with less polar and non-polar organic liquids and most synthetic polymers.

To render these hydrophilic nanocelluloses to be more compatible with organic media and polymers for broader applications, various physical or chemical means have been explored[23-33]and reviewed[34]. CNCs were freeze-dried then ultrasonicated[23-25] and CNFs were acetone exchanged

then homogenized[26] to be dispersible in DMF. Chemical reactions, such as esterification[27-29], acetylation[30, 31], silanation[32], and amidation[33] have also been applied to convert the hydrophilic hydroxyls[27-32] and carboxyls[33] of CNCs[27-29] and CNFs[30-33] to more hydrophobic long alkyl chains[27-29, 32, 33] or acetyl groups[30, 31]. Bromine esterification, a common reaction to introduce Br esters to cellulose, has been performed on sulfuric acid hydrolyzed CNC[35] and TEMPO-oxidized and homogenized CNF[36] using 2-bromoisobutyryl bromide (BIB) aided by 4-dimethylaminopyridine (DMAP) catalyst to improve their respective dispersity in DMF[35] and anisole[36]. To date, efforts to generated hydrophobic nanocelluloses have been limited and mainly from modification of already fabricated nanocelluloses[27-36].

Although esterification[37] or acetylation[38] have been reported to alter nanocelluloses' product such as CNC casted[37] and CNF vacuum filtrated[38] nanopapers to be hydrophobic, producing dispersible hydrophobic nanocelluloses from modification of cellulose is more scarce. Esterification of cellulose with acetic anhydride followed by refining, cryo-crushing and homogenization has shown to generate ethanol and acetone suspensible cellulose and 10-50 nm wide CNFs, but the extent of CNFs was not reported[39]. To diversify chemistry, we have successfully established the one-pot solventless telomerization of 1,3-butadiene on cellulose to introduce 2,7-octadienyl ether (ODE), a 8-carbon diene, then mechanical blending of aqueous ODE-cellulose suspensions to generate hydrophobic ODE-nanocellulose in the precipitates that were 27-41% dispersible in DMF, DMSO, and chloroform[40]. To advance this direct functionalization-disintegration of cellulose approach to produce hydrophobic nanocelluloses, one-pot synthesis of hydrophobic cellulose followed by direct disintegration in organic media into hydrophobic nanocelluloses would further simplify the process.

Herein, a one-pot synthesis of hydrophobic cellulose coupled with direct disintegration in an organic liquid was developed and streamlined. First and foremost, rationally designed bromine esterification was applied to convert the accessible cellulose C2, C3 and C6 hydroxyls into organic compatible bromine esters. While both 2-bromopropionyl bromide (BPB)[41] and 2-bromoisobutyryl bromide (BIB)[42] were effective in acylating ionic liquid dissolved wood pulp cellulose to become DMF soluble, the more chemically stable BPB with secondary carbon as relatively poor nucleophile was selected to be the bromine provider for the direct esterification of cellulose solids. The extent of bromine esterification of cellulose necessary to allow disintegration in organic media was studied by sequentially varying bromine provider BPB quantity to anhydroglucose unit (AGU) from 1:1 to 10:1 BPB:AGU molar ratios, reaction times (1-12 h), then temperatures (23-90°C). DMF, a common solvent for cellulose ester[43, 44], was used as the reaction as well as dispersing media for disintegrating bromine esterified cellulose (Br-Cell) into bromine esterified nanocelluloses (Br-NCs) by ultrasonication. Ultrasonication that has shown to be effective to disintegrate TEMPO-oxidized wood cellulose (0.01 w/v%) in aqueous media into 3.6 (±0.3) nm wide CNF with ca. 100 length-to-width ratio[45] was carried out in varying amplitudes and lengths of time to provide a range of power. The optimal bromine esterification reaction and ultrasonication power were determined by evaluating the quantities and qualities of DMF-dispersible Br-NCs imaged by atom force microscopy (AFM) and transmission electron microscopy (TEM). The structures of Br-CNFs were further characterized by Fourier-transform infrared (FTIR) and liquid phase proton nuclear magnetic resonance (^{1}H NMR) spectroscopy. Thermal properties and crystallinity of Br-CNFs were characterized by thermogravimetric analysis (TGA) and X-ray diffraction (XRD), respectively. Moreover, the viscosity and wetting behaviors

of thin layer hydrophobic Br-NCs on HOPG or blade coated film on glass were evaluated by water contact angle (WCA) measurement for potential surface modification and coating applications.

2.2 Experimental section

2.2.1 Materials. Cellulose was isolated from rice straw (Calrose variety) by a previously reported three-step 2:1 v/v toluene/ethanol extraction, acidified $NaClO_2$ (1.4%, pH 3-4, 70 °C, 5 h) delignification, and alkaline hemicellulose dissolution (5% KOH, 90 °C, 2 h) process and lyophilized (Labconco Lyophilizer)[46]. 2-Bromopropionyl bromide (BPB, 97%, Alfa Aesar), 4-Dimethylaminopyridine (DMAP, 99%, Acros Organics), potassium bromide (KBr, 99.9+%, Fisher Scientific), acetone (histological grade, Fisher Scientific), N,N-dimethylformamide (DMF, certified grade, Fisher Scientific) and trifluoroacetic acid (99%, Sigma Aldrich) were used as received without further purification. All water used was purified by Milli-Q Advantage water purification system (Millipore Corporate, Billerica, MA). For AFM imaging, mica (highest-grade V1 mica discs, 10 mm, Ted Pella, Inc. Redding, CA) and highly oriented pyrolytic graphite (HOPG, grade ZYB) were used. For TEM, carbon grids (300-mesh copper, formvar−carbon, Ted Pella Inc.) were used. For UV−vis spectrophotometry, 1 mm UV-vis standard cell quartz cuvettes (Fisher Scientific) were used.

2.2.2 Synthesis of Bromine Esterified Cellulose (Br-Cell). Bromine esterification of cellulose was performed at varying BPB to anhydroglucose unit (AGU) ratios (1:1 to 10:1 BPB:AGU), reaction times (1 to 12 h), and temperatures (23 to 90°C) (**Scheme 2.1**). The crystallinity of rice straw cellulose is estimated as 0.67 from the average 0.618[46] and 0.722[12] by XRD. Amorphous AGU or OHs was 2.04 or 6.17 mmol per gram of cellulose.[40] Freeze-dried cellulose (0.50 g, 3.1 mmol AGU) was added to DMF (30 mL) and stirred until homogeneously dispersed. Bromine

provider BPB (3.33 g, 15.4 mmol, 5-times AGU or amorphous OHs) and DMAP (0.05 g, 0.4 mmol) catalyst were dissolved in DMF (10 mL) in an ice bath under constant vortexing, then added to the cellulose dispersion to start the reaction and stopped by vacuum filtration. The reacted cellulose solids were rinsed with acetone three times to remove residual BPB, DMAP and DMF, then dried at 55 °C overnight to obtain dry bromine esterified cellulose (Br-Cell). The extent of reaction in Br-Cell was determined by mass gain and expressed as Br content (σ, mmol/g):

$$\sigma = \frac{m_2 - m_1}{135 \times m_1} \tag{2.1}$$

where m_1 is the initial cellulose mass (g), m_2 is the dry Br-Cell mass (g), and 135 (g/mmol) is the molecular mass gain from hydroxyl to bromine ester.

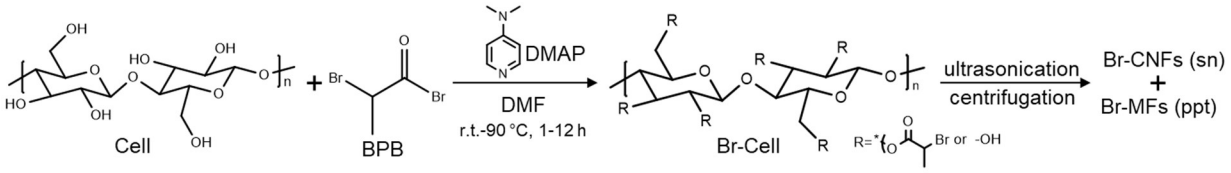

Scheme 2.1. Bromine esterification reaction of cellulose and ultrasonication to generate hydrophobic Br-CNFs in the supernatant and Br-Cell microfibrils in the precipitate.

2.2.3 Generation of Bromine Esterified Nanocelluloses (Br-NCs) by Ultrasonication. Br-Cell (0.1 g) was resuspended in 100 mL DMF at 0.1 w/v% and ultrasonicated (Qsonica Q700, 50/60 Hz) at varied amplitudes (25-100 %) and times (10-120 min) in an ice bath and 10-minute time intervals to disintegrate the microfibers. All ultrasonicated dispersions were centrifuged (Eppendorf 5804R, 5k rpm, 10 min) to collect the clear Br-esterified nanocellulose (Br-NC) containing supernatants and Br-Cell precipitates for further characterization. Mass of air-dried Br-Cell precipitates were determined gravimetrically and subtracted from initial Br-Cell mass to derive the Br-NC quantities in supernatants. The Br-NC as percentage of the initial Br-Cell was reported.

2.2.4 Characterizations. The morphologies of dried Br-Cells were imaged by optical microscopy (Leica DM2500). Br-Cell was redispersed at 0.1 w/v% in DMF and 10 μL droplets were deposited on glass slides to measure the width and length (n > 100) of microfibers. Their averages and standard deviations were reported. Br-NCs in DMF dispersions were imaged by AFM and TEM on different substrates. Br-NCs (10 μL, 0.0005 w/v %) were deposited on freshly cleaved hydrophilic mica or relatively hydrophobic highly oriented pyrophoric graphite (HOPG), then air-dried in fume hood for 6 h and profiled by AFM in the tapping mode with scan size and rate set to 5μm × 5μm and 512 Hz. Br-NCs (10 μL, 0.0005 w/v %) were deposited onto both glow and non-glow discharged carbon-coated TEM grids, and excess liquid was removed after 5 min by blotting with a filter paper. The specimens were negatively stained with 2 w/v% aqueous uranyl acetate and blotted to remove excess solution with filter paper, repeated five times then dried under the ambient condition for 15 min. The samples were observed using a Philip CM12 transmission electron microscope at a 100 kV accelerating voltage. The lengths and widths of CNFs were measured and calculated using ImageJ Analyzer (ImageJ, NIH, USA).

For ^{1}H NMR, 40 mL acetone was added into Br-CNF3 in DMF dispersions (10 mL, 0.50 w/v%) followed by centrifugation (5k rpm, 10 min) to decant the supernatant, repeated three times to prepare Br-CNF3 acetone gel. Br-CNF3 acetone gel (ca. 5 mg) was added into 1 mL DMSO-d_6, then sonicated (10 min, Branson 2510) and vacuumed at 50°C or 80°C for 1 h, and repeated three times to remove residual acetone. After centrifugation (5k rpm, 10 min), Br-CNF3 in DMSO-d_6 supernatant (ca. 0.2 w/v%) was collected for ^{1}H NMR (Bruker AVIII 800 MHz ^{1}H NMR spectrometer) characterization. Around 1 mL supernatant was placed in one NMR tube with 50 μL trifluoroacetic acid added to shift all OHs peak downfield to above 4.5 ppm.

Transparent FTIR pellets were prepared by mixing 3 mg of oven dried Br-Cell, Br-CNF3 and Br-Cell3 precipitates with 300 mg of spectroscopic grade (99.9+%) potassium bromide (KBr) after 1 min pressurization under 800 MPa barrel chamber, then scanned by Thermo Nicolet 6700 spectrometer under ambient conditions from an accumulation of 64 scans at a 4 cm^{-1} resolution from 4000 to 400 cm^{-1}. TGA were performed on a TGA-50 thermogravimetric analyzer (Shimadzu, Japan) by heating 5 mg dry sample at 10 °C/min from 25 to 500 °C under purging N_2 (50 mL/min). The crystalline structures were determined by XRD using a PANalytical X'pert Pro powder diffractometer with a Ni-filtered Cu Kα radiation (λ = 1.5406 Å) at 45 kV anode voltage and 40 mA current. Br-Cell3 powder was rinsed three times with acetone and oven-dried (55°C) overnight. Br-CNF3 film was generated from 0.5 w/v% DMF dispersions by evaporating DMF in fume hood for 7 d. The samples were fixed on stage by double-sided tape, then diffractograms were recorded from 5 to 40° at a scan rate of 2°/min. Crystallinity index (CrI) was calculated using the intensity of the 200 peak (I_{200}, 2θ =22.5°) and the intensity minimum between the peaks at 200 and 110 (I_{am}, 2θ = 19.0°) as follows[47]

$$\mathrm{CrI} = \frac{\mathrm{I_{200}} - \mathrm{I_{am}}}{\mathrm{I_{200}}} \tag{2.2}$$

The crystallite dimensions were calculated using the Scherrer equation[48]

$$\mathrm{D_{hkl}} = \frac{0.9\,\lambda}{\beta_{1/2}\cos\theta} \tag{2.3}$$

where D_{hkl} is the crystallite dimension in the direction normal to the (h k l) lattice planes, λ is the X-ray radiation wavelength (1.5406 Å), $\beta_{1/2}$ is the full width at half-maximum of the diffraction peak in radius calculated using peak fitting software (Fityk, 1.3.1).

Br-CNF3 at concentrations of 0.0005 to 0.01 w/v% were deposited on freshly exfoliated graphite and allowed to air-dry for 6 h. 0.5 w/v% Br-CNF3 DMF dispersion was concentrated to 2.5 w/v% Br-CNF3 organogel by ambient drying in fume hood for 4 d, then 5 mL gel (1 mm thickness) was

coated on glass using a Doctor-Blade film coater (INTSUPERMAI Adjustable Film Applicator Coater KTQ-II) as one hundred μm thick film after ambient drying overnight. Water contact angles (WCAs) of sessile drops (5 μL) on fresh mica, exfoliated graphite, carbon, glow-discharged carbon and film coated glass, as well as single and double deposited Br-CNF3 on graphite were measured using the ImageJ Analyzer and the average values were calculated from both sides of a sessile drop reported in total of 5 images for each (n=5). The root mean square (RMS) of Br-CNF deposited graphite surfaces were measured from microscopic peaks and valleys of AFM images.

Br-CNF3 in DMF dispersions were serial diluted from 0.5 w/v% to 0.25, 0.13 and 0.06 w/v% then scanned by UV-vis spectroscopy (Thermo Scientific, Evolution 600) from 325 to 800 cm^{-1} at 4 cm^{-1}/s. Viscosities of Br-CNF3 DMF dispersions were measured at 25°C with shear rates from 1 to 220 s^{-1} using a Brookfield DV3T rheometer.

2.3 Results and discussion

2.3.1 Bromine Esterification of Cellulose. Cellulose was isolated from rice straw at 35.0±3.3% (n=10) yield, comparable to previous reported value[46], and freeze-dried to a white fluffy mass. Bromine esterification of cellulose was conducted under varying BPB:AGU molar ratios (1:1 to 10:1), reaction times (1-12 h), and temperatures (23-90°C) to evaluate their effects on the extent of hydroxyl to bromine ester conversion or Br content (σ, mmol/g) (**Scheme 2.1**). At 23°C for 12 h, a 5 time increase of BPB:AGU ratio from 1:1 to 5:1 led to a 12 time increase in the Br content (σ) from 0.6-6.0 mmol/g while further doubling the ratio only increase σ by another 20% to 7.2 mmol/g (**Figure 2.1a**). The optimal 5:1 BPB:AGU ratio was selected to vary the length of reaction at 23°C. Br content (σ) increased from 3.4 to 5.7 mmol/g, showing close to linear relationship with reaction time from 1 to 6 h, then to 6.0 mmol/g at 12 h essentially unaffected (**Figure 2.1b**). Under

the optimal 5:1 BPB:AGU ratio and 6 h time, increasing temperatures from 23-70 C° improved Br content (σ) from 5.7 to 8.7 mmol/g, but further increase to 90°C lowered the σ to 3.4 mmol/g (**Figure 1c**). The significantly reduced σ from Br-esterification at 90°C suggested possible dissolution of the excessively Br-esterified cellulose. Overall, Br-Cell with 0.6 to 8.7 mmol/g σ has been facilely produced and easily controlled by the esterification conditions, i.e., 1:1 to 5:1 BPB:AGU ratios, 1-6 h, and 23-70 °C. The highest 8.7 mmol/g Br content was achieved by Br esterification conducted at 5:1 BPB:AGU ratio and 70 °C for 6 h.

The DMF dispersibility of 1% Br-Cells with four Br ester levels, i.e., Br-Cell1 (0.6 mmol/g), Br-Cell2 (3.4 mmol/g), Br-Cell3 (5.7 mmol/g), and Br-Cell4 (8.7 mmol/g), was then observed. The least Br-esterified Br-Cell1 did not disperse and remained settled even at a lower 0.1 % whereas those more esterified Br-Cell2, 3 and 4 were dispersible in DMF to different degrees (**Figure 1d**). The Br-Cell2 and Br-Cell3 DMF dispersions appeared homogeneous and translucent, but Br-Cell4 phase separated immediately (t=0). After 10 min, Br-Cell3 also settled similarly to Br-Cell4 while Br-Cell2 remained somewhat dispersed. Optical microscopic observation showed all four Br-Cells to be microfibers in similar 4-5 mm widths while their lengths reduced by nearly 30% from 221 to ca. 158 mm compared to the original cellulose for all except for the significantly shorter 36 mm long Br-Cell4. While no change in microfiber width nor evidence of dissolution, the 84% reduction in their length of Br-Cell4 (**Figure S1**) with the highest σ (8.7 mmol/g) suggested this more extensive Br esterification condition may be close to the onset of chain scission with potential cellulose dissolution. One control reaction at 23°C for 6 h without adding BPB was performed to induce only 1.1% mass loss, indicating no significant mass loss during filtration and evaporation process. Thus, eqn. 1 is applicable to estimate Br content from mass gain % of cellulose.

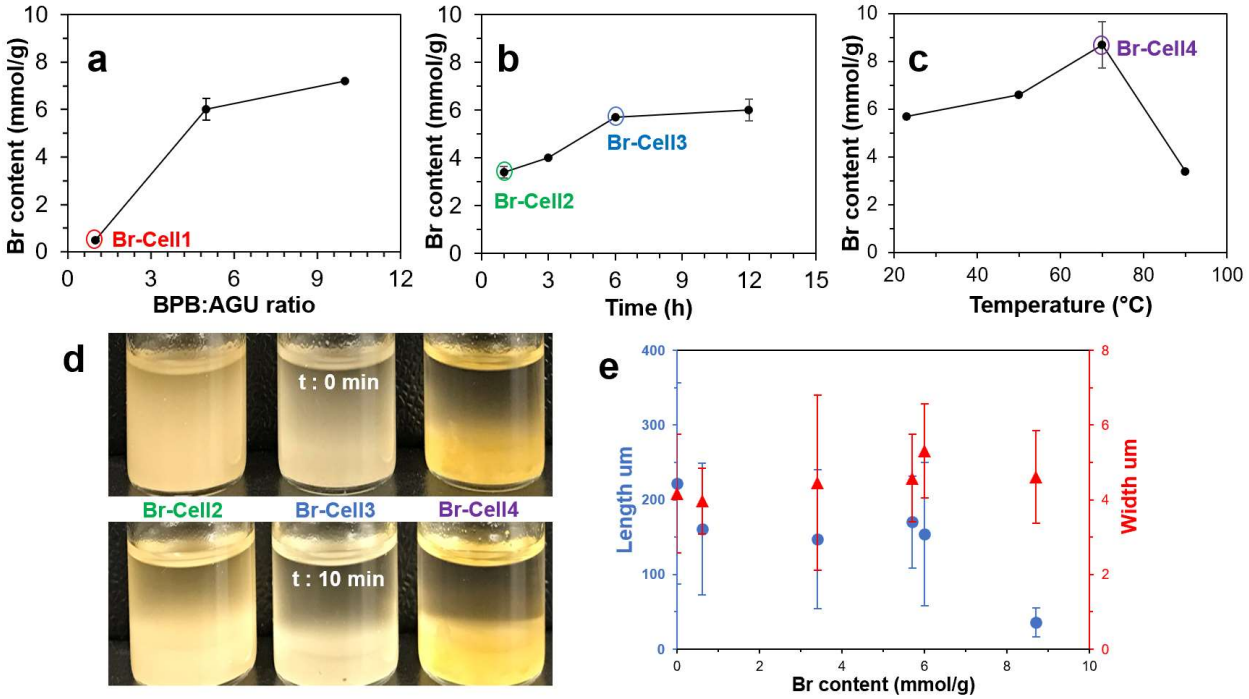

Figure 2.1. Br content (σ) in Br-Cell as affect by reaction conditions: (a) BPB:AGU molar ratio (23°C, 12 h); (b) reaction time (5:1 BPB:AGU, 23°C); and (c) temperature (5:1 BPB:AGU, 6 h); (d) 1% DMF dispersion immediate and 10 min after vortexing; (e) microfiber dimensions.

2.3.2 Br-NCs by Ultrasonication. Four Br-Cells with σ from 0.6 to 8.7 mmol/g were ultrasonicated in DMF (0.1 w/v%) at 25-100 % amplitudes for 10-120 min to collect the Br-NC containing supernatants. Upon ultrasonication at 50% amplitude for 30 min, the least esterified Br-Cell1 (σ from 0.6 mmol/g) produced only 10.6% Br-NCs, essentially the same as the 10.4% NCs from unmodified cellulose under the same ultrasonication condition (**Figure S2.2)**, indicating Br acetylation at 0.6 mmol/g to be insufficient to facilitate disintegration and/or dispersion. The NCs from unmodified cellulose appeared as few larger and thicker (5-20 nm) nanoparticles (NPs) on mica but numerous much smaller and thinner (3 nm) NPs on graphite, indicative of their more hydrophobic surfaces. Among the three more esterified Br-Cells, more Br-NCs were produced

with increasing ultrasonication amplitudes from 25-100% at 60 min, with the highest 97.3% yield for Br-Cell3 (5.7 mmol/g) compared to the modest 56.9 and 73.1% from either the respective less esterified Br-Cell2 (3.4 mmol/g) and the more esterified Br-Cell4 (8.7 mmol/g) (**Figure S2.3)**. Since a very close second highest yield of 93.8% was produced from Br-Cell3 at half of the amplitude, the effect of ultrasonication time (10-120 min) on the morphology of Br-NCs generated from Br-Cell2-4 was observed at 50% amplitude to conserve energy (**Figure 2.2)**. Br-NC yields increased with longer ultrasonication (50% amplitude) for all three Br-Cells; Br-NC yields from Br-Cell3 (5.7 mmol/g) was highest and most time-dependent, ranging from 38.2% to 97.3%, followed by slight time-dependent and modest 29.3 to 49.3% Br-NC yields for Br-Cell4 (8.7 mmol/g) and the least time-dependent and lowest 19.0 to 25.8% Br-NC yields for Br-Cell2 (3.4 mmol/g). However, not all Br-NCs were fibrillar. For the most DMF dispersible Br-Cell2 (**Figure 2.1d**), nearly all Br-NCs were fibrillar, from entangled to more individualized in reducing thickness of 6.5 to 1.2 nm, but in low yields. The most esterified Br-Cell4 was disintegrated into mostly Br-NPs, also in decreasing sizes, with only few fibrils from longer ultrasonication. Ultrasonication of Br-Cell3 produced 38.2% Br-NCs in the forms of both Br-CNFs and Br-NPs at 10 min, 70.9% Br-CNFs at 30 min, and 93.8% at 60 min all as Br-NPs. As expected, ultrasonication transfers sound energy to disintegrate Br-Cell microfibers into Br-NCs with increasing effects by either higher amplitudes or longer time. The forms and sizes of NCs, however, were found highly dependent on the extent of Br-esterified cellulose. The less esterified (3.4 mmol/g) produced all Br-CNFs but at low yields (19.0 to 25.8%) whereas the most esterified (8.7 mmol/g) produced majority of Br-NPs at modest yields (29.3 to 49.3%). Therefore, Br-Cell3 was deemed optimally esterified (5.7 mmol/g) with sufficient Br esters to be disintegrated by ultrasonication (50%, 30 min) into mostly Br-CNF in 70.9% yield, and 4.6 nm average thickness.

Noteworthy, longer ultrasonication of the optimally esterified Br-Cell3 produced 93.8% and 97.0% bromine esterified NPs at respective 1 h and 2 h. Those Br-NPs were potentially attributed to reassembling of dissolved cellulose during sonication and would cause decrease of Br-CNFs crystallinity. Therefore, this esterification-ultrasonication approach to functionalize cellulose and disintegrate in functionalize nanocelluloses are highly effective and can be tuned to produce either Br-CNFs or Br-NPs efficiently.

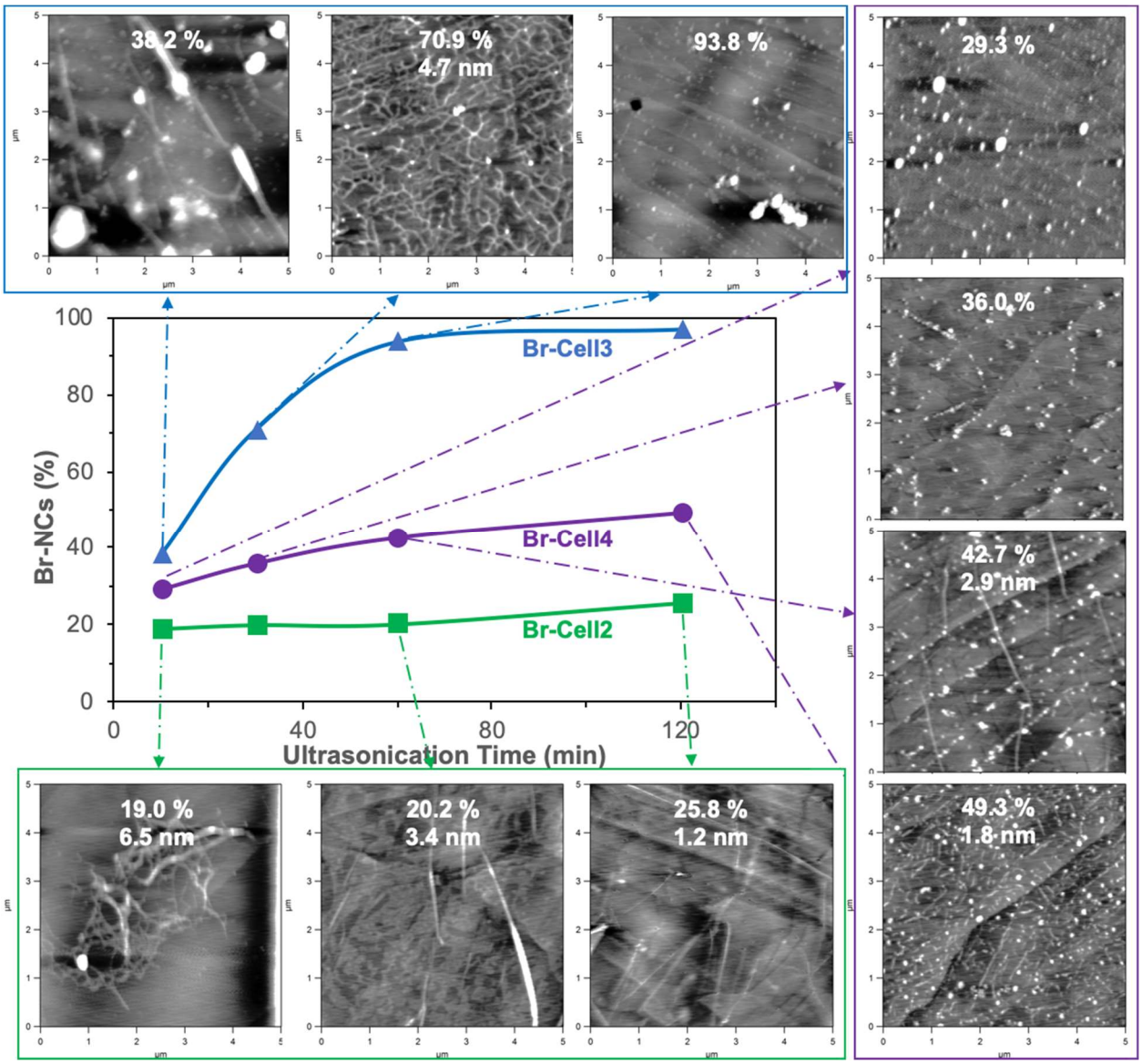

Figure 2.2. Yields and morphology of Br-NCs (5k rpm, 10 min) from ultrasonication (50% amplitude, 10-120 min) of Br-Cell2 (3.4 mmol/g), Br-Cell3 (5.7 mmol/g), and Br-Cell4 (8.7 mmol/g). AFM were imaged on highly oriented pyrophoric graphite (HOPG) with corresponding yield and Br-CNF thickness.

2.3.3 Br-CNF3 Morphology Characterized by AFM and TEM. Br-CNF3 were further imaged by AFM on freshly exfoliated graphite and by TEM on glow discharged carbon grid to display interconnecting nanofibrils with 4.6 nm average thickness (**Figure 2.3a**), 29.2 nm average width, and varying lengths in the order around 1 μm (**Figure 2.3b**). The irregular widths under TEM may be due to the reassociation of the more Br-esterified surface chains along Br-CNF surfaces. Also, under both AFM and TEM, the inter-connecting fibrillar network left few isolated fibrils**,** making differentiating fibril ends difficult and causing inaccurate estimation of Br-CNF3 length. Similar inter-connecting fibrillar structures were also observed at much more diluted 0.0001 and 0.00005 w/v% concentrations (**Figure S2.3a-c)**, confirming the inter-connecting fibrillar structures to be independent of concentrations and seemingly mono-layer. The inter-connecting fibrillar network dried from the most concentrated Br-CNF (0.0005 w/v%, on graphite) appeared thinner and more fragmented after exposing to air for 24 h (**Figure S2.4d**), possibly due to degradation of CNF caused by reactions between Br esters and moisture in the air.

To further elucidate the interaction among Br-CNFs, a second Br-CNF3 droplet was placed on top of the completed dry first (10 μL, 0.0005 w/v%) (**Figure S2.5**). More heterogenous, condensed and inter-connecting CNFs were observed at the center than near the edge of the first dried droplet (**Figure S2.5b-d**). The significant association among Br-CNFs from second deposition (**Figure S2.5b)** as compared to isolated fibrils from the initial single droplet gave evidence to preferential and stronger association among Br-CNFs over affinity of Br-CNF to graphite surface. Association

among Br-CNFs may include dipole-dipole interactions between surface esters, hydrogen bonding among unsubstituted surface hydroxyls, and potential chemical reaction between Br esters and remaining hydroxyls in preference to adhesion to the graphite surface from the sequential deposition.

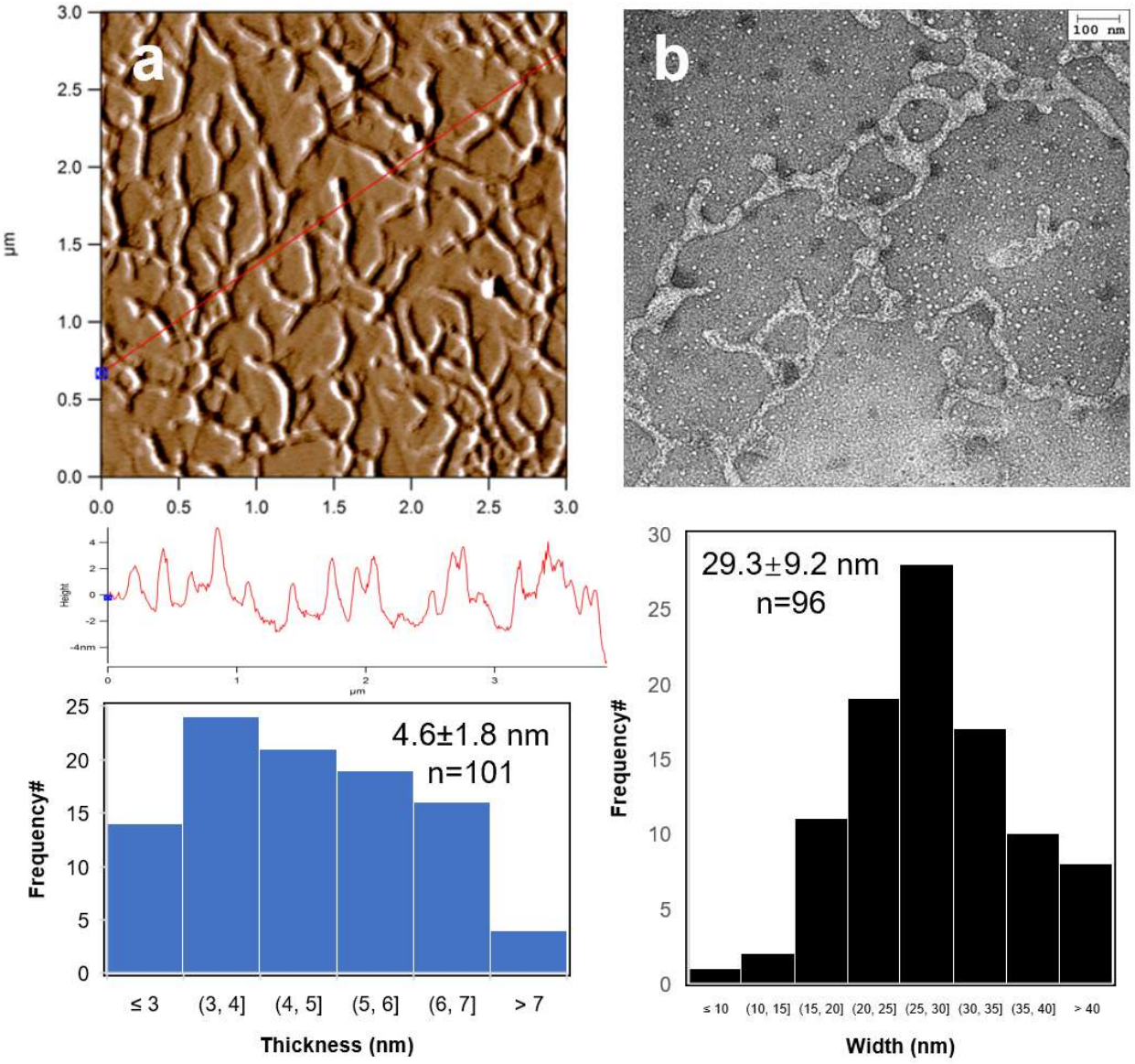

Figure 2.3 Morphology of Br-CNF3 (0.0005 w/v%, 10 mL) supernatant (5k rpm, 10 min) from ultrasonication (50% amplitude, 30 min): (a) AFM image on graphite, height profile, and height distribution; (b) TEM images on glow-discharged carbon grid with width distribution.

2.3.4 FTIR Spectroscopy and Thermal Analysis of Br-Cell, Br-CNF3 and Br-Cell3 Precipitates. The presence of the new 2-bromopropionyl carbonyl peak at 1740 cm^{-1} in the FTIR spectra of all four Br-Cells confirmed the successful conversion of cellulose hydroxyls to 2-bromopropionyl group (**Figure 2.4a**). The carbonyl peak (1740 cm^{-1}) intensities increased whereas the cellulose C-H stretching peak (2900 cm^{-1}) reduced in intensities with the increasing Br content (σ) from 0.6-8.7 mmol/g. The bromine ester sp^3 C-C stretching at 2780 cm^{-1} appeared for Br-Cell2 and increased with increasing σ, while the most esterified Br-Cell4 also showed intense bromine ester sp^2 C-C stretching at 2970 cm^{-1}. The carbonyl peak (1740 cm^{-1}) on Br-CNF3 remained unchanged from Br-Cell3, indicating no side reaction or degradation to the Br esters by ultrasonication. The stronger carbonyl peak (1740 cm^{-1}) in Br-CNF3 compared to Br-Cell3 precipitates indicated that Br-CNF3 in supernatant represented the more Br esterified fraction (70.9%) whereas the less Br esterified could be disintegrated by ultrasonication and remained in the precipitate. The persistent cellulose crystalline peak (1430 cm^{-1}) in both Br-Cell and Br-CNFs suggested that the bulk of cellulose crystalline domains was not affected by esterification and ultrasonication. The lowered intensity of the absorbed moisture peak (1632 cm^{-1}) for the highly esterified Br-Cell4 was also expected. Furthermore, weaker hydrogen bonding O-H stretching peak (3100-3800 cm^{-1}) in all Br-Cells than underivatized cellulose supported the successful cellulose hydroxyl conversion to bromine esters. The reduced hydrogen bonding interactions

between cellulose chains could also aid the opening of (110) or (1-10) planes in Br-cell via ultrasonication to generate more Br-NCs.

With increasing Br-esterification levels, moisture absorption of Br-Cell reduced from 6.08% to 0.02% (**Figure 2.4b)** which was consistent with effect of converting hydrophilic hydroxyls to Br-ester (**Figure 2.4a)**. The underivatized cellulose was stable at up to 260 °C and rapidly lost significant mass to give 2.6% char at 500 °C. With the increase of Br content from 0 to 8.7 mmol/g, both the onset and max degradation temperatures lowered for Br-Cell1, 2 and 3, then slightly increased for Br-Cell4 (**Figure 2.4c**). The lowered onset and max degradation temperatures may be due to the insertion of less thermal stable bromine esters; while the opposite increasing onset and max degradation temperatures of Br-Cell4 may be explained by the highly substituted Br esters behaved as vapor-phase flame-retardant moieties to suppress decomposition of cellulose, a potential worthy of further study in the future. The significantly higher moisture contents of Br-CNF3 (8.5%) and Br-Cell3 precipitate (4.5%) than that of precursor Br-Cell3 (0.65%) gave evidence to generation of new hydrophilic surfaces due to the opening of cellulose (110) and (1-10) planes from ultrasonication. The lower onset and max degradation temperatures of Br-CNF3 (205 and 234°C) than its precursor Br-Cell3 (219 and 241°C) could be due to the three order of magnitude smaller fiber dimensions (4.7 nm thickness) and much higher specific surfaces.

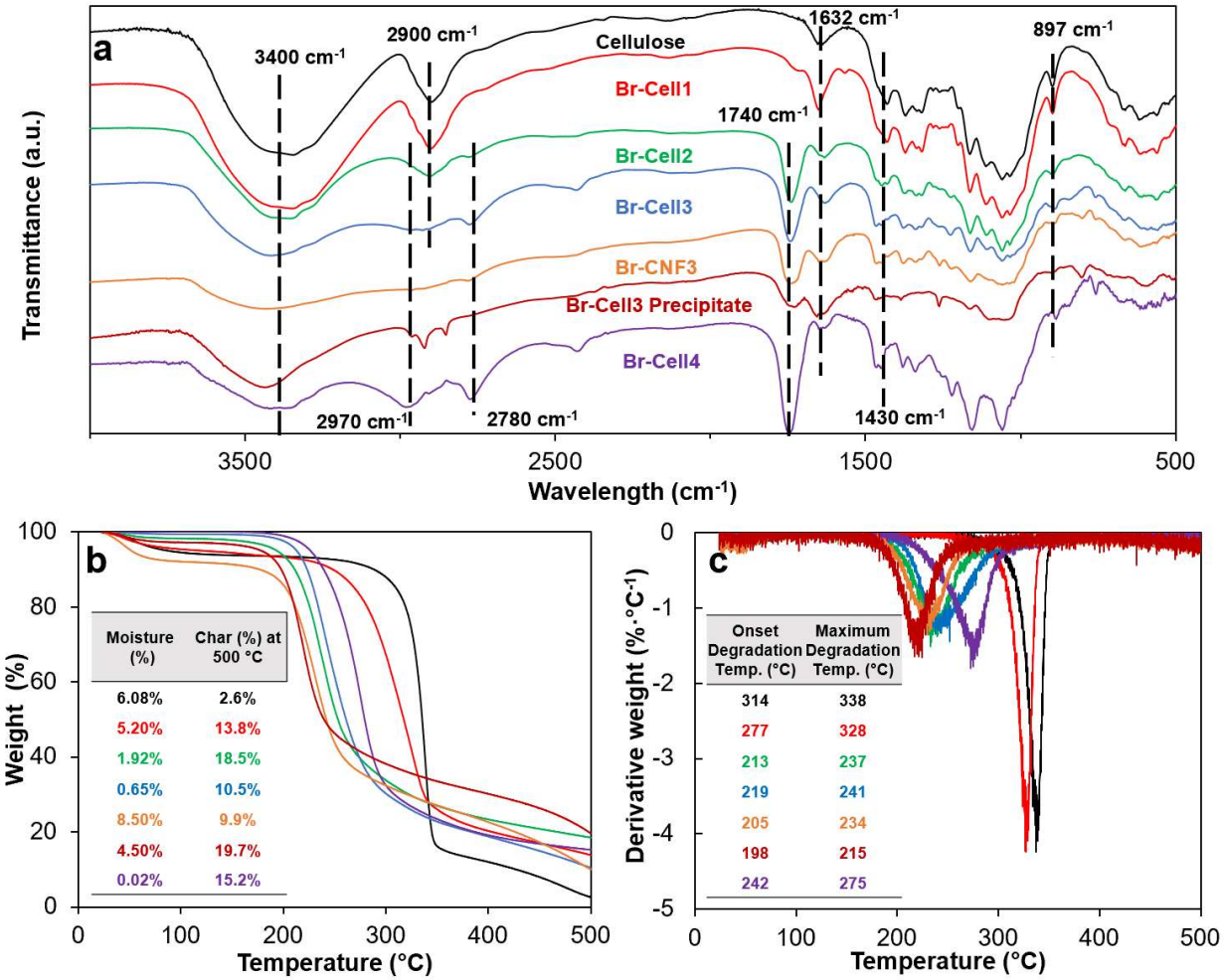

Figure 2.4 Characterizations of cellulose, Br-Cell1-4, Br-CNF3 and Br-Cell3 precipitate: (a) FT-IR spectra; (b) TGA; and (c) DTGA curves. Moisture (%) was the mass loss at 140 °C.

2.3.5 Degree of substitution of surface OH by Solution-State ^{1}H-NMR and Model Simulation.

Solution-state ^{1}H NMR of 50°C or 80°C pretreated Br-CNF3 in three times acetone evaporation process showed cellulosic protons with characteristic methyl proton (Ha) or methylene proton (Hb) peaks of the alkyl bromide groups (**Figure 2.5**). For both spectra, the furthest downfield peak at δ 4.20-4.52 and δ 4.53 are assigned to the cellulosic anomeric proton (H1) similar to the chemical

shift at δ 4.5 reported in dissolved cellulose[49]. The H6 and H6' peaks for 50°C treated Br-CNF3 appeared at δ3.71-4.06 whereas two clear peaks appeared at δ 3.97 and δ 3.83 for 80°C treated Br-CNF3. Both ranges were relatively downfield due to esters' de-shielding effect, but comparable to those in δ 3.65-3.88 range for dissolved MCC in NaOD/D_2O[50]. Multiple overlapping peaks between δ 3.29-3.70 and δ 3.42-3.57 were assigned to H3, H4 and H5, matching those at δ 3.34-3.66 of TEMPO-CNF in D_2O[51]. The furthest upfield cellulosic peak at δ 3.16 and δ 3.04 coincided with the chemical shift of H2 at δ 3.29 for cellulose/NaOD/D_2O[49] and δ 3.05 for cellulose dissolved in DMA-d_9/LiCl[52]. Doublet methyl proton peaks (Ha) at δ 2.12 and δ 1.29 were both comparable to δ 1.6[41] of soluble Br-esterified cellulose. Most significantly, both doublet methyl (Ha) and quartet methylene proton (Hb) peaks at δ 4.53-4.87 and δ 4.11 indicated the successful insertion of Br ester esters.

The degree of substitution of surface hydroxyls to Br esters (DS_{NMR}) were quantified based on the assumption that all anomeric protons and all Ha and Hb protons of amorphous and crystalline surface AGUs of Br-CNF3 are detectable by ^{1}H NMR. The cellulose anomeric proton was the sum of the integrated areas for all anomeric H1 to H6' proton peaks averaged by 7 then normalized by reference methylene proton Hb. Br esters could be estimated by integration of the areas of methyl Ha or methylene Hb divided by their respective 3 and 1 protons. The ratio of Br esterified C2, C3 and C6 OHs per surface AGU could be determined mathematically by the area ratio of Br ester calculated from Ha or Hb over normalized anomic proton. Since each AGU has 3 OHs, DS_{Ha} and DS_{Hb}, representing the fraction of OH substituted by Br-ester determined by proton Ha or Hb, could be calculated by dividing ratio of Br esterified OHs per surface AGU by 3 according to eqn. 2.4 or 2.5.

$$DS_{Ha} = \frac{1}{3} \times \frac{\text{integral of methyl protons (Ha, doublet)}/3}{\sum_1^{6'} \text{integral of anomeric protons (H}^i\text{)}/7} \quad (2.4)$$

$$DS_{Hb} = \frac{1}{3} \times \frac{\text{integral of methylene protons (Hb,quartet)}}{\sum_1^{6'} \text{integral of anomeric protons } (H^i)/7} \quad (2.5)$$

For 80°C treated Br-CNF3, majority of Br-CNF3 were in precipitates at bottom of DMSO-d_6 suspension after centrifugation and decanted, causing relative lower proton signal compared to 50°C treated Br-CNF3 (**Figure 2.5c, d**). Those Br-CNFs interconnected by potential endothermic[53] interfibrillar N-substitution between alkyl bromide and OHs would precipitate at 80°C with only small portion of dissolved cellulose still in DMSO-d_6. Thus, 80°C treated spectra showed more distinguishable anomic proton peaks with inconsistency between 0.75 DS_{Ha} and 0.57 DS_{Hb} which could induced to unreliable 0.66 DS_{NMR}. The relatively upfield Ha proton peak at δ 1.29 compared to δ 2.12 at 50°C indicated the decreased de-shielding effect of Br ester caused by releasing HBr during N-substitution. In addition, the cellulose dissolution could also be observed from the significant lower integral values (**Figure 2.5b**) of H1(0.04), H2 (0.06), H6 (0.13) and H6'(0.08) compared to H3,4,5 (3.81). In comparison, 0.53 DS_{Ha} and 0.58 DS_{Hb} calculated from 50°C treated Br-CNF3 spectra within the 2σ range of total 7.4% benchtop NMR uncertainty[54] were averaged to be 0.56 DS_{NMR}. In preparing Br-CNF3 in DMSO-d_6 for ^{1}H NMR, Br-CNF3 was first solvent exchanged from DMF to acetone where the more hydrophilic or less Br-esterified may be left in DMF, thus not included for ^{1}H NMR. Therefore, the 0.56 DS_{NMR} derived may represent the more hydrophobic or more highly Br esterified CNF, thus higher than the DS of overall Br-CNF3 population.

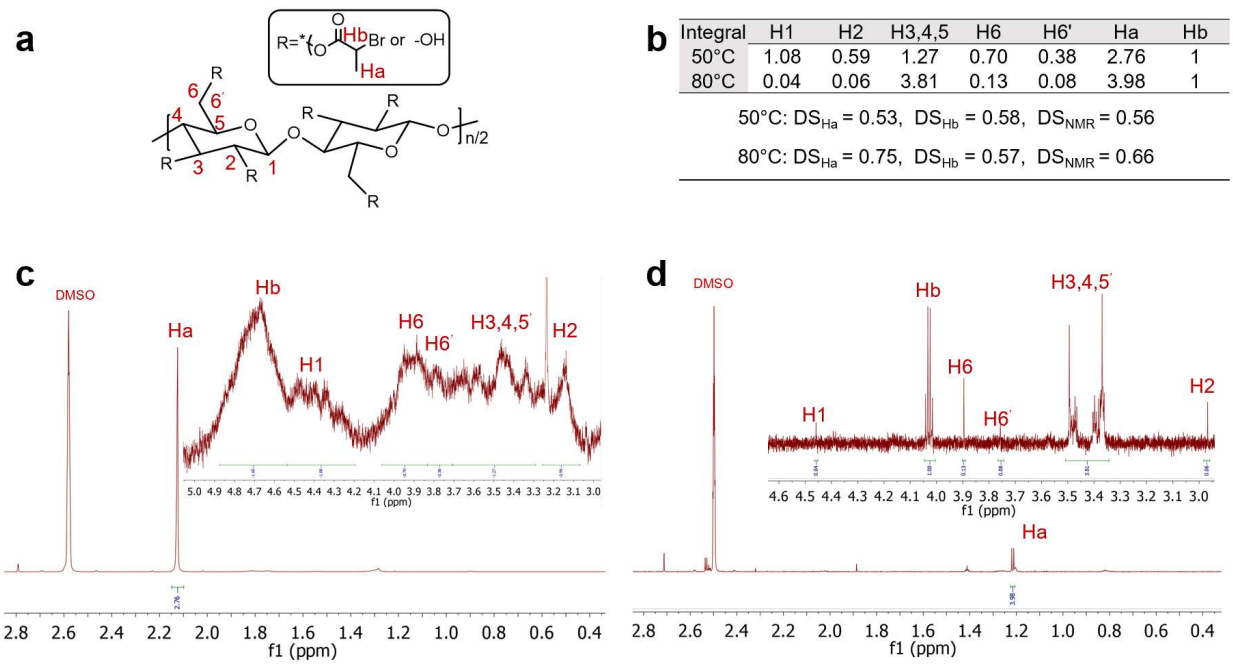

Integral	H1	H2	H3,4,5	H6	H6'	Ha	Hb
50°C	1.08	0.59	1.27	0.70	0.38	2.76	1
80°C	0.04	0.06	3.81	0.13	0.08	3.98	1

50°C: DS_{Ha} = 0.53, DS_{Hb} = 0.58, DS_{NMR} = 0.56

80°C: DS_{Ha} = 0.75, DS_{Hb} = 0.57, DS_{NMR} = 0.66

Figure 2.5. (a) Structure and proton assignment of Br-CNF3; (b) Integral values of H1-6', Ha and Hb with corresponding DS_{Ha}, DS_{Hb} and DS_{NMR}; Br-CNF3 (ca. 0.2 wt%) ^{1}H NMR spectra in DMSO-d_6 via solvent exchange from acetone evaporated at (c) 50°C and (d) 80°C vacuum chamber. DS_{Ha} and DS_{Hb} were calculated using eqn. 4 and eqn. 5 whereas DS_{NMR} was their average.

Both Br-Cell3 and Br-CNF3 displayed 2θ peaks at 14.6, 16.5, and 22.5° corresponding to the respective (1-10) (110) (200) monoclinic Iβ lattice planes of cellulose (**Figure 2.6a**). The lowered 50.0% CrI of Br-Cell3 compared to original cellulose (69.1%) without size reduction (**Figure S2.1a, c**) gave evidence to bromine esterification of more exposed cellulose chains on crystalline surfaces (**Figure 2.6b**). The 47.8% CrI of Br-CNF3 was only very slightly lower than the 50.0% of Br-Cell3. The crystalline size, calculated via Scherrer eqn. 3, of Br-CNF3 (1.45 nm) was significantly lowered to only one third of Br-Cell (4.77 nm), indicating disintegration of crystalline regions in Br-Cell into smaller domains by ultrasonication without affecting overall crystallinity.

The much higher absorbed moisture (8.5%) in Br-CNF3 than that in Br-Cell3 microfibers (0.65%) (**Figure 2.4b)** supported the notion that additional hydrophilic surfaces may be produced from ultrasonication.

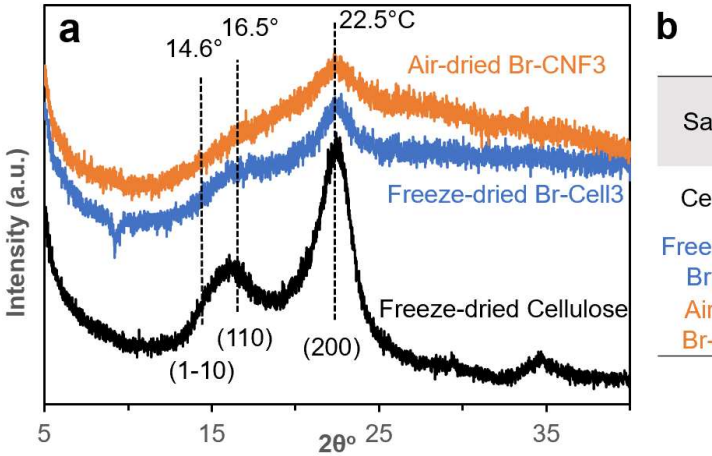

b

Samples	CrI(%)	FWHM (degree)	$\beta_{1/2}$ (rad)	D_{hkl} (nm)
Cellulose	69.1	1.9	0.03316	4.27
Freeze-dried Br-Cell3	50.0	1.7	0.02967	4.77
Air-dried Br-CNF3	47.8	5.6	0.09774	1.45

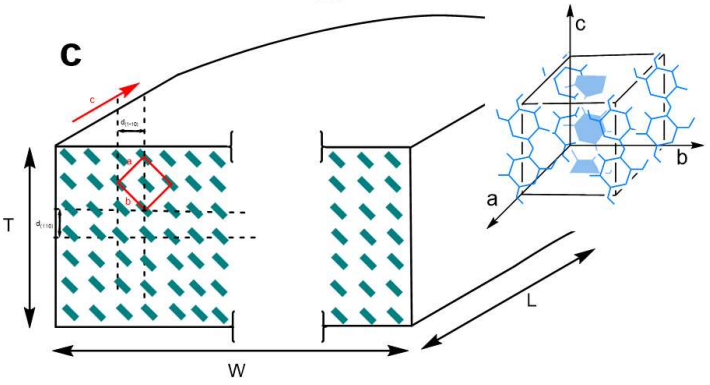

d

Dimension (nm)		Rc	Rm	R_{OH}
T	4.6	0.36	3	1.74
W	29.3	$DS_\sigma = 0.53$		

Figure 2.6 Crystalline structure of cellulose, Br-Cell and Br-CNF3: (a) XRD spectra; (b) crystallinity (CrI) and crystal parameters calculated by the Scherrer equation; (c) Br-CNF cross-section with cellulose chains represented by green rectangles, Br-esterified (1-10) (110) plane surfaces and thickness (T), width (W), and length (L) indicated; inset shows cellulose Iβ monoclinic unit cell; (d) Degree of substitution DS_s calculated from Br-CNF dimensions based on the cross-section shown in c.

A model representing the lateral cross-section of individual Br-CNF with hydrophilic (110) and (1-10) planes as surfaces was thus used (**Figure 2.6c**), displaying thickness (T), width (W), and

length (L) and the cellulose Iβ monoclinic unit cell dimensions along the (100) and (010) planes as a and b, respectively. The number of total cellulose chains N_t in the crystalline cross-section and the number of surface cellulose chains N_s are expressed respectively as

$$\mathrm{N}_t = \left(\frac{\mathrm{T}}{\mathrm{d}_{110}} + 1\right)\left(\frac{\mathrm{W}}{\mathrm{d}_{1-10}} + 1\right) \tag{2.6}$$

$$\mathrm{N}_s = 2\left(\left(\frac{\mathrm{T}}{\mathrm{d}_{110}} + 1\right) + \left(\frac{\mathrm{W}}{\mathrm{d}_{1-10}} + 1\right)\right) - 4 = 2\left(\frac{\mathrm{T}}{\mathrm{d}_{110}} + \frac{\mathrm{W}}{\mathrm{d}_{1-1}}\right) \tag{2.7}$$

where "2" is for the two width and thickness sides; "-4" is for the four double counted corner chains; d_{110} and d_{1-10} are d-spacings of (110) and (1-10) planes. Since only half of the crystalline surface chains, or only 1.5 OHs per crystalline surface AGU would expose, the ratio of crystalline surface OHs per AGU (Rc) is

$$\mathrm{Rc} = \frac{1.5\mathrm{N}_s}{\mathrm{N}_t} = \frac{3\left(\frac{\mathrm{T}}{\mathrm{d}_{110}} + \frac{\mathrm{W}}{\mathrm{d}_{1-10}}\right)}{\left(\frac{\mathrm{T}}{\mathrm{d}_{110}} + 1\right)\left(\frac{\mathrm{W}}{\mathrm{d}_{1-10}} + 1\right)} \tag{2.8}$$

Both amorphous and crystalline surfaces OHs should be counted as part of CNF surface OHs. Since all OHs in amorphous regions are exposed, the amorphous OHs per AGU (Rm) is 3 OHs/AGU. The ratio of total available OHs per AGU (R_{OH}) is the weight average of those on the crystalline surfaces (Rc) and on amorphous region (Rm) expressed as

$$\mathrm{R}_{\mathrm{OH}} = \mathrm{Rc} \times \mathrm{CrI} + \mathrm{Rm} \times (1 - \mathrm{CrI}) \tag{2.9}$$

where the crystallinity CrI of Br-CNF3 is 0.478 (**Figure 2.6b**). The degree of substitution (DS_σ) or mol % surface OHs esterified is as follows

$$\mathrm{DS}_\sigma = \frac{\sigma \times \mathrm{mw}_{\mathrm{AGU}}}{\mathrm{R}_{\mathrm{OH}}} \tag{2.10}$$

Where σ is 5.7 mmol/g for both Br-Cell3 and Br-CNF3 and $\mathrm{mw}_{\mathrm{AGU}}$ is the molecule mass of AGU (0.162 g/mmol). The d spacings were calculated according to the Bragg's law using 16.5° and 14.6° 2θ peaks derived from deconvolution of cellulose XRD spectra to be 0.534 and 0.606 nm

for d_{110} and d_{1-10}, respectively (**Figure S2.6)**. Using the measured 4.7 nm T and 29.3 nm W values, Rc and R_{OH} were calculated to be 0.36 OHs/AGU and 1.74 OHs/AGU, respectively. The DS_{σ} was determined to be 0.53 by eqn. 10 (**Figure 2.6d**). Using the overall Br content of 5.7 mmol/g for both the precursor Br-Cell3 and Br-CNF3 may underestimated DS_{σ} of Br-CNF in the supernatant whereas the less substituted fraction is likely the micro-size cellulose in the precipitates. Nevertheless, the potential overestimated 0.56 DS_{NMR} and underestimated 0.53DS_{σ} showed good consistency of actual DS to be in-between 0.53 and 0.56. The reliability of the solvent-exchanging method to prepare ^{1}H NMR sample and the cross-sectional model with hydrophilic plane surfaces were both validated.

2.3.6 Interfacial and surface properties of Br-CNF3

The interfacial interactions among Br-CNF3 and four substrates with varied hydrophilicity/hydrophobicity in a range of concentrations (0.0005 to 0.01 w/v%) were observed. The substrates using in AFM and TEM imaging and their water contact angles (WCAs) were mica (16.8°), freshly exfoliated graphite (71.8°), glow discharged carbon grid (68.2°), and carbon grid (115.3°) (**Figure 2.7a**). On hydrophilic mica, most Br-CNF3 appeared as either loosely or extensively agglomerated short fibrils in 1.2 nm average thickness (**Figure 2.7b**). On the moderately hydrophobic graphite and glow discharged carbon grid, inter-connecting fibrillar network was prevalent (**Figure 2.7c, d)** as noted earlier (**Figure 2.3a-c**) whereas only large NPs were observed on the hydrophobic carbon grid (**Figure 2.7e)**. These observations indicated Br-CNF3 in the supernatant were mostly moderately hydrophobic with better compatibility to graphite and glow discharged carbon, appearing as 4.6 nm thick and 29.3 nm wide fibrils. Meanwhile some Br-CNF3 were sufficiently hydrophilic to be partially dispersed as thin fibrils on mica while none was as hydrophobic as carbon. Both higher moisture absorption of Br-CNF3 than Br-Cell3 (**Figure**

2.4b) and thinner hydrophilic CNFs (**Figure 2.7b**) are consistent with the opening of hydrophilic (110) planes as new surfaces from ultrasonication of Br-cell into Br-CNF. These observations also further supported the hydrophilic model for Br-CNF (**Figure 2.6c)**. Moreover, the presence of Br-CNF as large NPs on carbon grid may be due to their aggregation via hydrogen bonding of surface OHs and dipole-diploe interactions of newly surface functionalized esters.

With increasing Br-CNF3 concentrations from 0.0005 to 0.01 w/v%, WCAs on Br-CNF3 deposited graphite increased from 55.6 ° to 73.0 ° (**Figure 2.7f-i**). Br-CNF3 appeared as inter-connecting fibrils at the lower 0.0005 and 0.001 w/v% and as entangled fibrillar networks with few particulates at higher 0.005 and 0.01 w/v%. The initial deposition of 0.0005 w/v% Br-CNF3 dispersion partially covered the graphite to increase its hydrophilicity, lowering WCA from 71.8° (**Figure 2.7b**) to 55.6° (**Figure 2.7f**). The hydrophilicity decreased slightly with increasingly coverage at 0.001 w/v% (60.8° WCA) and further when nearly full coverage at 0.005 w/v% (75.4° WCA) (**Figure 7k**), with slightly increased surface roughness. Further increased Br-CNF3 to 0.01 w/v% did not alter WCA, but slightly reduced the surface roughness as expected with fuller coverage. Therefore, diluted Br-CNF3 deposited at concentrations from 0.0005 to 0.01 w/v% is capable of monolayer to few layers to alter surface wettability and may be used in potentially surface coating and super-thin film applications.

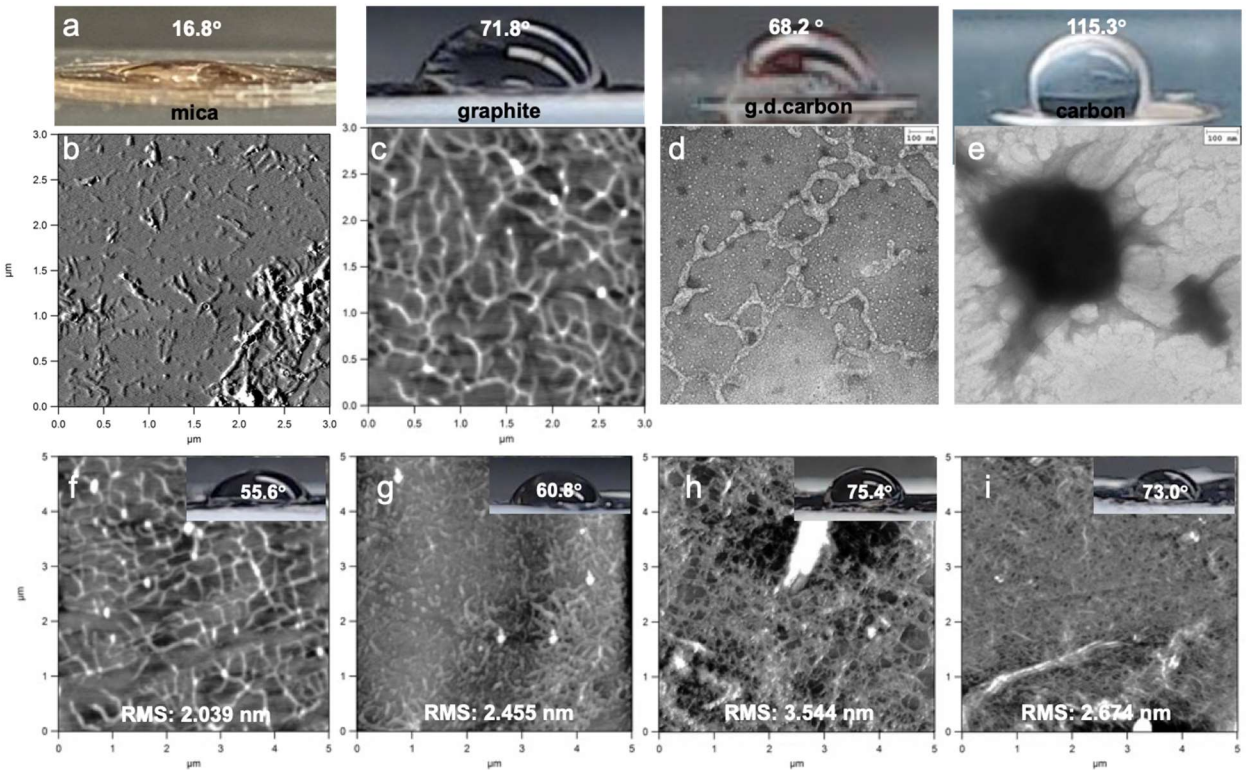

Figure 2.7. Br-CNF3 on substrates: (a) individual substrates with WCAs indicated; AFM (b,c) and TEM (d,e) images of Br-CNF3 (10 µL, 0.0005 w/v%) on corresponding substrates above; (f-i) AFM images and WCAs of Br-CNF3 air-dried on graphite at: (f) 0.0005 w/v%, (g) 0.001 w/v %, (h) 0.005 w/v%, and (i) 0.01 w/v% concentrations.

2.3.7 Dispersing Behaviors and Rheology of Br-CNF3. Dispersing behaviors of Br-CNF3 and their corresponding rheology at higher concentrations were investigated for additional potential formulation and application. First, disintegration of Br-Cell3 in DMF by ultrasonication (50%, 30 min) was scaled up by ten times from 0.1 to 1.0 w/v%. With increasing Br-Cell3, the resulting Br-CNF3 concentrations in the supernatants increased from 0.07 to 0.5 w/v%, while the Br-Cell3 to Br-CNF3 conversion or the yield reduced from 70.9 to 50.7% (**Figure 2.8a**). All Br-CNF dispersions up to 0.5 w/v% appeared relatively transparent (**Figure 2.8b, c**). The Br-CNF dispersions from 0.06 to 0.25 w/v% exhibited Newtonian behaviors, i.e., their viscosities were

independent of shear rates (**Figure 2.8d**). At 0.5 w/v%, Br-CNF3 dispersion exhibited a shear thinning region at low shear rates below 150 s^{-1} and a Newtonian region above. This implied that strong inter-fibrillar interaction of Br-CNF3 at 0.5 w/v% leads to higher viscosity in the low shear region below 150 s^{-1}. With increasing shear rates, fibrillar Br-CNF3 became more oriented in the direction of shear flow until reached the Newtonian region. The highest concentration that Br-CNF3 can be directly and homogeneously dispersed into DMF was 0.5 w/v%, above which Br-CNF3 formed gels that contained crystalline micro-fibers (**Figure 2.8e**). Br-CNF3 (0.5 w/v%) DMF dispersion was further concentrated to 2.5 w/v% gel by evaporation (ambient temperature, 4 d), then blade coated as 1 mm thick gel on glass and air-dried overnight to ca. 100 μm thick film. The WCA of the coated Br-CNF3 film was 69.8° (**Figure 2.8f**), close to the WCAs of thin layers deposited from 0.005 w/v% (75.4°, **Figure 2.7h**) and 0.01 w/v% (73.0 °, **Figure 2.7i**)**.** Similar WCAs for thin layers and thick blade coated film implied the surface organization of Br-CNF3 to be independent of thickness from several nm to one hundred μm and may applied as hydrophobic coating in either manner. Furthermore, the coated thin film had an impressively high modulus of 198 MPa, as well as 6.7 MPa tensile stress and 10.7% strain-to-failure (**Figure S2.7**). Therefore, not only the Br-CNF3 dispersion's shear-thinning behavior above 0.5 w/v% demonstrate its potential as a rheology modifier in organic formulation, but the ultra-high modulus and strength of its thin film also present its potential as strength enhancement additive in coating and film applications.

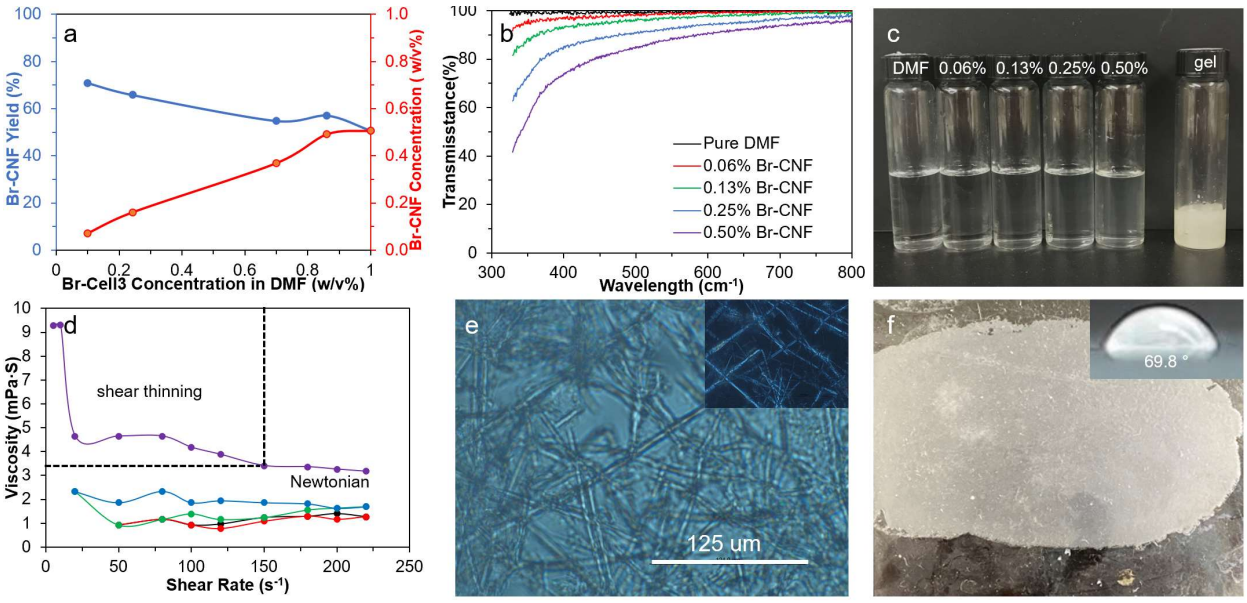

Figure 2.8. Scaled up generation of Br-CNF3 from ultrasonication (50% amplitude, 30 min) and their viscosity and gel characteristics: (a) Br-CNF yields and supernatant concentrations as related to initial Br-Cell3 concentrations in DMF; (b) UV-vis spectra; (c) images of Br-CNF supernatants and gel at above 0.5 w/v%; (d) viscosity at varied shear rates; (e) optical microscopy of 0.5 w/v% Br-CNF gel; (f) WCA of film by blade coating 1 mm Br-CNF3 (2.5 w/v%) gel on glass, and air dried.

2.4 Conclusions

This study proofs the concept for facile one-pot functionalization of cellulose and direct disintegration of functionalized cellulose by ultrasonication in organic liquids into hydrophobic nanocelluloses. Organic compatible Br-esterified cellulose nanofibrils (Br-CNFs) have been successfully synthesized via rationally designed bromine esterification of cellulose, followed by direct ultrasonication. This bromine esterification-ultrasonication approach can be tuned to produce either Br-CNFs or Br-NPs efficiently. The optimally esterified Br-Cell3 (5:1 BPB:AGU

ratio, 23°C, 6 h) contained 5.7 mmol/g Br esters to be disintegrated by ultrasonication (50% amplitude, 30 min) to yield 70.9% Br-CNF3 in average 4.6 nm thickness, 29.3 nm width, up to 1 μm length, and 47.8% crystallinity. While Br esterification lowered the overall crystallinity (69.1% to 50.0%), ultrasonication reduced the crystalline size (from 4.77 nm to 1.45 nm) in Br-CNF and exposed more (110) and (1-10) hydrophilic planes as evident by the increased moisture absorption (0.65% to 8.5%). The successful conversion of surface OHs to Br esters was confirmed by the presence of C=O at 1740 cm^{-1} in FTIR and chemical shifts for methyl proton (Ha) and methylene proton (Hb) at δ 2.12 and δ 4.53-4.87 in ^{1}H NMR, respectively. The degree of substitution was determined to be between the underestimated 0.53 DS_{σ} based on CrI and Br-CNF dimensions in cross-sectional model and overestimated 0.56 DS_{NMR} from solution-state ^{1}H NMR. Dilute dispersions (0.005-0.01 w/v%) of Br-CNF3 dispersions exhibited Newtonian behaviors at concentrations below and shear thinning behaviors at above 0.5 w/v% and could be homogeneously deposited as few nm ultra-thin layers to exhibit WCAs in the range of 73-75°. Moreover, blade coating of gel (2.5 w/v%) could also dried to one hundred μm thick hydrophobic (70° WCA) film, showing hydrophobicity irrespective of thickness. All were similarly hydrophobic as cellulose acetates and polyesters. The shear-thinning behavior of Br-CNF dispersions demonstrate their potential application as viscosity modifiers in variety of mechanical fluids. The ultra-high modulus and strength film from gel coating further shows the potential for dual high-strength and hydrophobic applications.

2.5. Supplemental information

Figure S2.1. Optical images of (a) cellulose, (b) Br-Cell1, (c) Br-Cell3 and (d) Br-Cell4 at 0.1 w/v% in DMF.

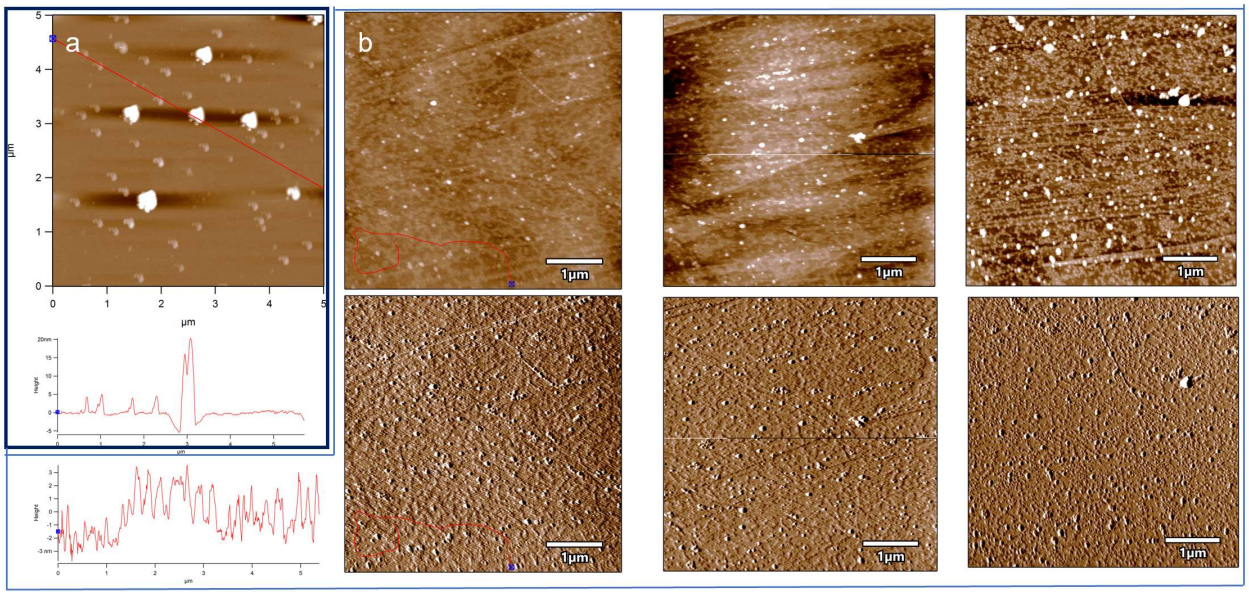

Figure S2.2. AFM images with height profiles of NCs at (0.001 w/v % in DMF) from unmodified cellulose supernatant after ultrasonication (50% amplitude, 30 min) and centrifugation (5k rpm, 10 min) on: (a) mica; (b) graphite.

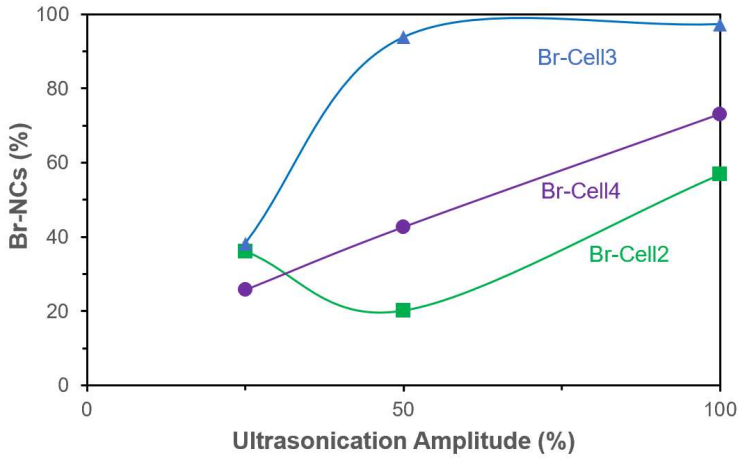

Figure S2.3. Effect of ultrasonication amplitude (60 min) on Br-NCs in the supernatant (centrifugation 5000 rpm, 10 min) from Br-Cell2 (3.4 mmol/g), Br-Cell3 (5.7 mmol/g), and Br-Cell4 (8.7 mmol/g).

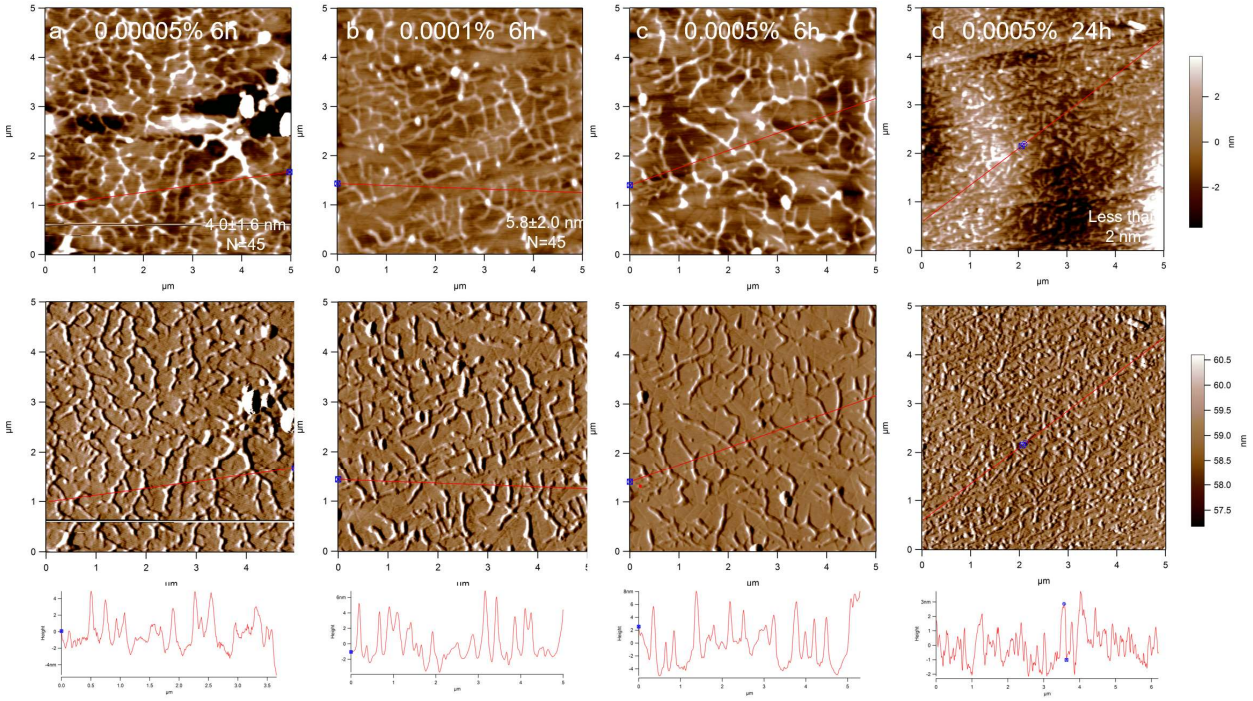

Figure S2.4. AFM images and height profiles of Br-CNF3 (on graphite) from varied concentrations and time: (a) 0.00005%, 6h; (b) 0.0001%, 6h; (c) 0.0005%, 6h; (d) 0.0005%, 24h.

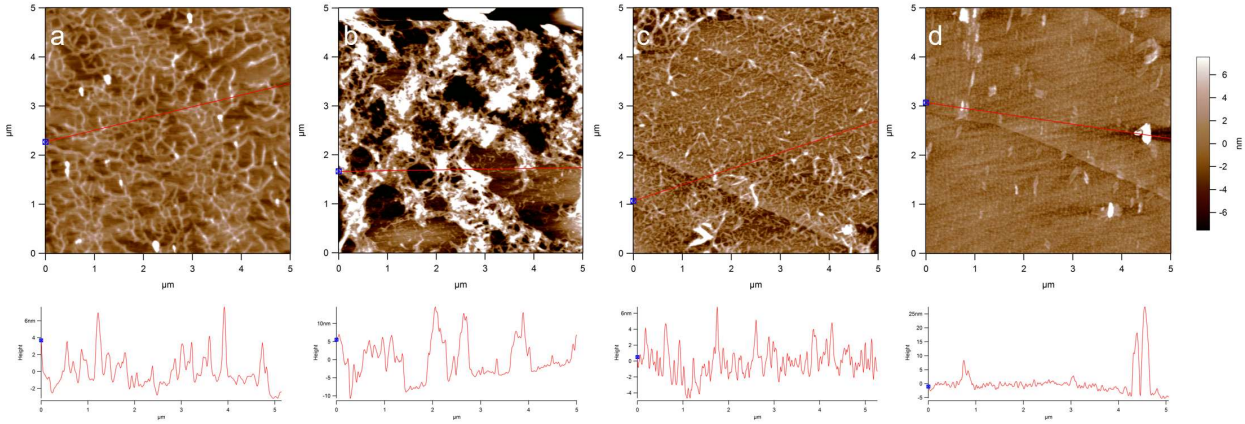

Figure S2.5. AFM images and corresponding height profiles of Br-CNF3 (10 uL, 0.0005 w/v%) on graphite: (a) single droplet (air-dried, 3 h); (b-d) two sequential depositions (air-dried, 3 h for each), showing center of droplet in b, area between center and edge in c, and near edge of droplet in c.

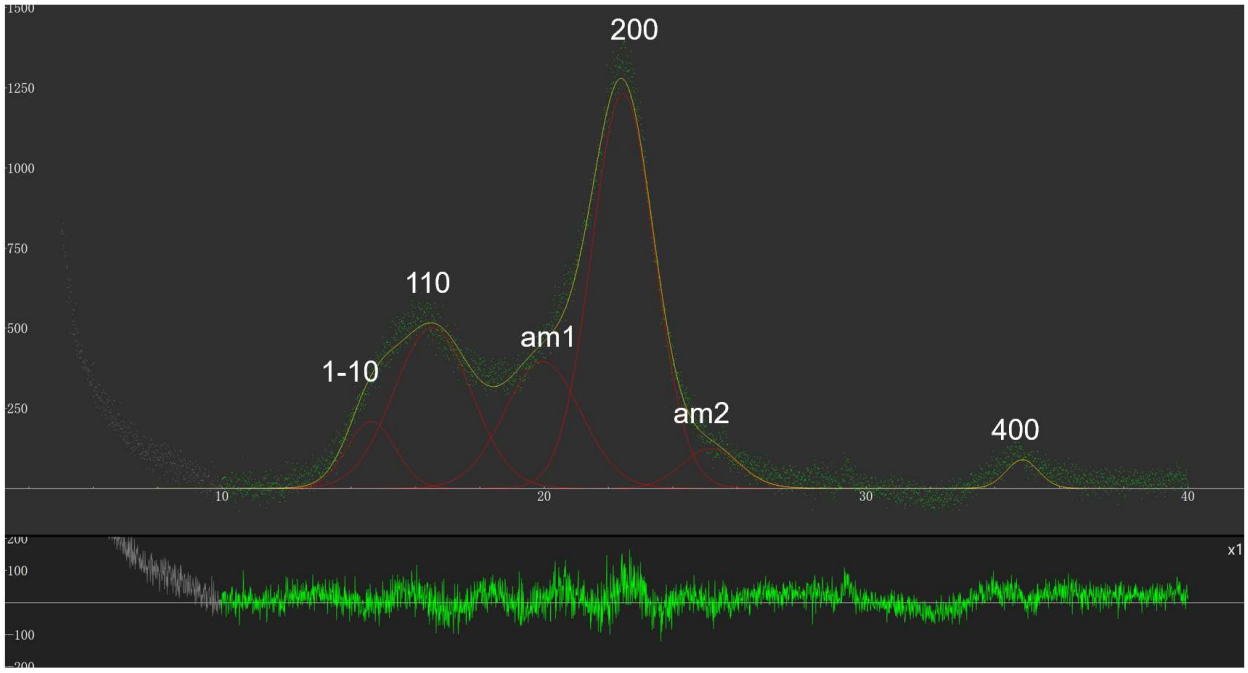

Figure S2.6. Deconvolution (VoigtA fitting method) of cellulose XRD spectra with (1-10), (110) and (200) planes at corresponding 2θ of 14.6, 16.5 and 22.5°.

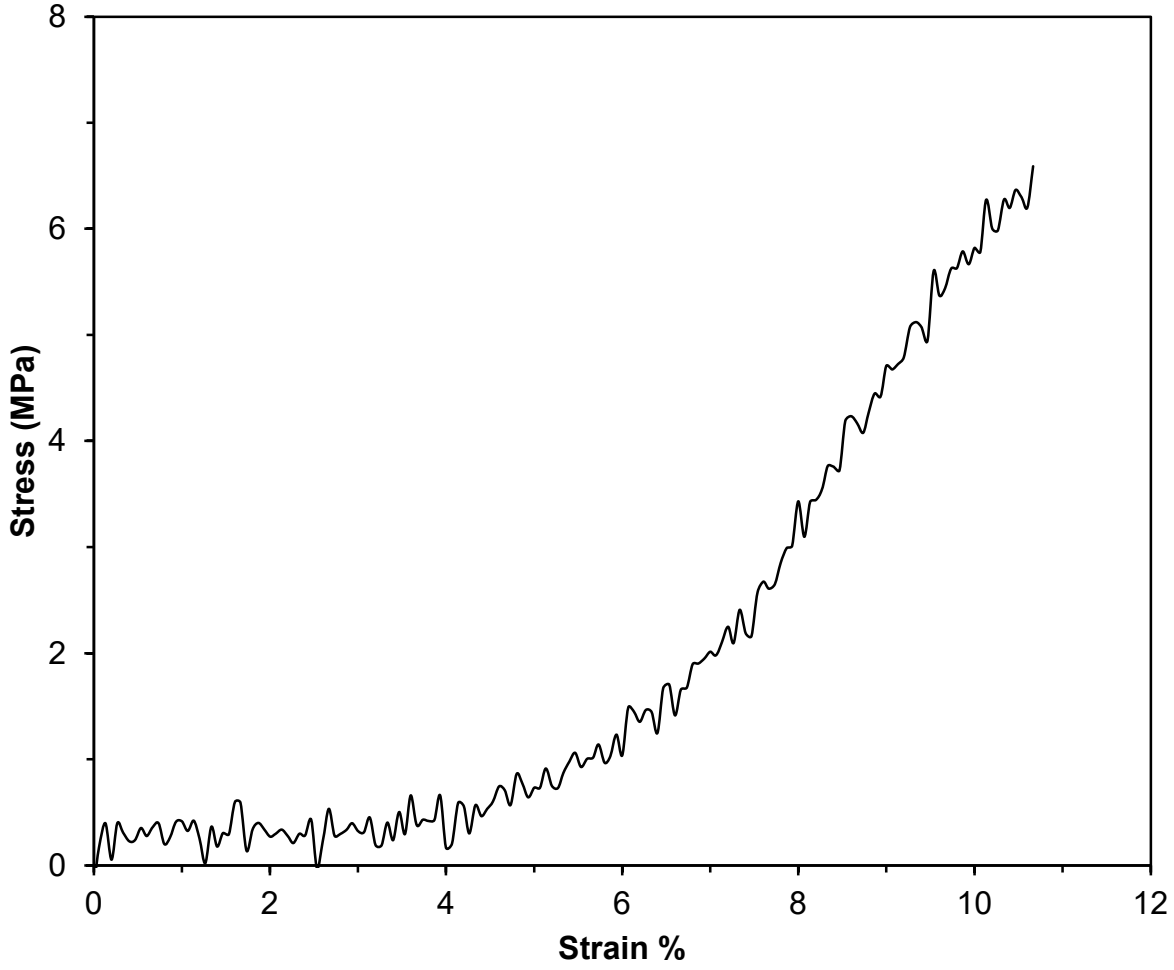

Figure S2.7. Engineering stress-strain curves for blade coating CNF films.

2.6. Reference

1. Chen, L.; Zhu, J.; Baez, C.; Kitin, P.; Elder, T., Highly thermal-stable and functional cellulose nanocrystals and nanofibrils produced using fully recyclable organic acids. *Green Chemistry* **2016,** *18* (13), 3835-3843.
2. Iwamoto, S.; Kai, W.; Isogai, A.; Iwata, T., Elastic modulus of single cellulose microfibrils from tunicate measured by atomic force microscopy. *Biomacromolecules* **2009,** *10* (9), 2571-2576.
3. Fukuzumi, H.; Saito, T.; Isogai, A., Influence of TEMPO-oxidized cellulose nanofibril length on film properties. *Carbohydrate Polymers* **2013,** *93* (1), 172-177.
4. Diaz, J. A.; Wu, X.; Martini, A.; Youngblood, J. P.; Moon, R. J., Thermal expansion of self-organized and shear-oriented cellulose nanocrystal films. *Biomacromolecules* **2013,** *14* (8), 2900-2908.

5. Puangsin, B.; Yang, Q.; Saito, T.; Isogai, A., Comparative characterization of TEMPO-oxidized cellulose nanofibril films prepared from non-wood resources. *International journal of biological macromolecules* **2013,** *59*, 208-213.
6. Ye, Y.-S.; Zeng, H.-X.; Wu, J.; Dong, L.-Y.; Zhu, J.-T.; Xue, Z.-G.; Zhou, X.-P.; Xie, X.-L.; Mai, Y.-W., Biocompatible reduced graphene oxide sheets with superior water dispersibility stabilized by cellulose nanocrystals and their polyethylene oxide composites. *Green Chemistry* **2016,** *18* (6), 1674-1683.
7. Thomas, B.; Raj, M. C.; Joy, J.; Moores, A.; Drisko, G. L.; Sanchez, C., Nanocellulose, a versatile green platform: from biosources to materials and their applications. *Chemical reviews* **2018,** *118* (24), 11575-11625.
8. Habibi, Y.; Lucia, L. A.; Rojas, O. J., Cellulose nanocrystals: chemistry, self-assembly, and applications. *Chemical reviews* **2010,** *110* (6), 3479-3500.
9. Bondeson, D.; Mathew, A.; Oksman, K., Optimization of the isolation of nanocrystals from microcrystalline cellulose by acid hydrolysis. *Cellulose* **2006,** *13* (2), 171.
10. Elazzouzi-Hafraoui, S.; Nishiyama, Y.; Putaux, J.-L.; Heux, L.; Dubreuil, F.; Rochas, C., The shape and size distribution of crystalline nanoparticles prepared by acid hydrolysis of native cellulose. *Biomacromolecules* **2007,** *9* (1), 57-65.
11. Dufresne, A., Nanocellulose: a new ageless bionanomaterial. *Materials today* **2013,** *16* (6), 220-227.
12. Jiang, F.; Hsieh, Y.-L., Chemically and mechanically isolated nanocellulose and their self-assembled structures. *Carbohydrate Polymers* **2013,** *95* (1), 32-40.
13. Saito, T.; Nishiyama, Y.; Putaux, J.-L.; Vignon, M.; Isogai, A., Homogeneous suspensions of individualized microfibrils from TEMPO-catalyzed oxidation of native cellulose. *Biomacromolecules* **2006,** *7* (6), 1687-1691.
14. Isogai, A.; Saito, T.; Fukuzumi, H., TEMPO-oxidized cellulose nanofibers. *nanoscale* **2011,** *3* (1), 71-85.
15. Wang, M. S.; Jiang, F.; Hsieh, Y.-L.; Nitin, N., Cellulose nanofibrils improve dispersibility and stability of silver nanoparticles and induce production of bacterial extracellular polysaccharides. *Journal of Materials Chemistry B* **2014,** *2* (37), 6226-6235.
16. Jiang, F.; Han, S.; Hsieh, Y.-L., Controlled defibrillation of rice straw cellulose and self-assembly of cellulose nanofibrils into highly crystalline fibrous materials. *Rsc Advances* **2013,** *3* (30), 12366-12375.
17. Jiang, F.; Hsieh, Y.-L., Self-assembling of TEMPO oxidized cellulose nanofibrils as affected by protonation of surface carboxyls and drying methods. *ACS Sustainable Chemistry & Engineering* **2016,** *4* (3), 1041-1049.
18. Saito, T.; Isogai, A., TEMPO-mediated oxidation of native cellulose. The effect of oxidation conditions on chemical and crystal structures of the water-insoluble fractions. *Biomacromolecules* **2004,** *5* (5), 1983-1989.
19. Li, J.; Wei, X.; Wang, Q.; Chen, J.; Chang, G.; Kong, L.; Su, J.; Liu, Y., Homogeneous isolation of nanocellulose from sugarcane bagasse by high pressure homogenization. *Carbohydrate polymers* **2012,** *90* (4), 1609-1613.
20. Pääkkö, M.; Ankerfors, M.; Kosonen, H.; Nykänen, A.; Ahola, S.; Österberg, M.; Ruokolainen, J.; Laine, J.; Larsson, P. T.; Ikkala, O., Enzymatic hydrolysis combined with mechanical shearing and high-pressure homogenization for nanoscale cellulose fibrils and strong gels. *Biomacromolecules* **2007,** *8* (6), 1934-1941.

21. Wågberg, L.; Decher, G.; Norgren, M.; Lindström, T.; Ankerfors, M.; Axnäs, K., The build-up of polyelectrolyte multilayers of microfibrillated cellulose and cationic polyelectrolytes. *Langmuir* **2008,** *24* (3), 784-795.
22. Aulin, C.; Johansson, E.; Wågberg, L.; Lindström, T., Self-organized films from cellulose I nanofibrils using the layer-by-layer technique. *Biomacromolecules* **2010,** *11* (4), 872-882.
23. Pei, A.; Malho, J.-M.; Ruokolainen, J.; Zhou, Q.; Berglund, L. A., Strong nanocomposite reinforcement effects in polyurethane elastomer with low volume fraction of cellulose nanocrystals. *Macromolecules* **2011,** *44* (11), 4422-4427.
24. Auad, M. L.; Contos, V. S.; Nutt, S.; Aranguren, M. I.; Marcovich, N. E., Characterization of nanocellulose-reinforced shape memory polyurethanes. *Polymer International* **2008,** *57* (4), 651-659.
25. Viet, D.; Beck-Candanedo, S.; Gray, D. G., Dispersion of cellulose nanocrystals in polar organic solvents. *Cellulose* **2007,** *14* (2), 109-113.
26. Fujisawa, S.; Ikeuchi, T.; Takeuchi, M.; Saito, T.; Isogai, A., Superior reinforcement effect of TEMPO-oxidized cellulose nanofibrils in polystyrene matrix: optical, thermal, and mechanical studies. *Biomacromolecules* **2012,** *13* (7), 2188-2194.
27. Fumagalli, M.; Sanchez, F.; Molina-Boisseau, S.; Heux, L., Surface-restricted modification of nanocellulose aerogels in gas-phase esterification by di-functional fatty acid reagents. *Cellulose* **2015,** *22* (3), 1451-1457.
28. Wang, Y.; Wang, X.; Xie, Y.; Zhang, K., Functional nanomaterials through esterification of cellulose: a review of chemistry and application. *Cellulose* **2018,** *25* (7), 3703-3731.
29. Kang, X.; Sun, P.; Kuga, S.; Wang, C.; Zhao, Y.; Wu, M.; Huang, Y., Thin cellulose nanofiber from corncob cellulose and its performance in transparent nanopaper. *ACS Sustainable Chemistry & Engineering* **2017,** *5* (3), 2529-2534.
30. Ashori, A.; Babaee, M.; Jonoobi, M.; Hamzeh, Y., Solvent-free acetylation of cellulose nanofibers for improving compatibility and dispersion. *Carbohydrate polymers* **2014,** *102*, 369-375.
31. Tripathi, A.; Ago, M.; Khan, S. A.; Rojas, O. J., Heterogeneous acetylation of plant fibers into micro-and nanocelluloses for the synthesis of highly stretchable, tough, and water-resistant co-continuous filaments via wet-spinning. *ACS applied materials & interfaces* **2018,** *10* (51), 44776-44786.
32. Valdebenito, F.; García, R.; Cruces, K.; Ciudad, G.; Chinga-Carrasco, G.; Habibi, Y., CO2 adsorption of surface-modified cellulose nanofibril films derived from agricultural wastes. *ACS Sustainable Chemistry & Engineering* **2018,** *6* (10), 12603-12612.
33. Johnson, R. K.; Zink-Sharp, A.; Glasser, W. G., Preparation and characterization of hydrophobic derivatives of TEMPO-oxidized nanocelluloses. *Cellulose* **2011,** *18* (6), 1599-1609.
34. Sun, L.; Zhang, X.; Liu, H.; Liu, K.; Du, H.; Kumar, A.; Sharma, G.; Si, C., Recent Advances in Hydrophobic Modification of Nanocellulose. *Current Organic Chemistry* **2021,** *25* (3), 417-436.
35. Morandi, G.; Heath, L.; Thielemans, W. J. L., Cellulose nanocrystals grafted with polystyrene chains through surface-initiated atom transfer radical polymerization (SI-ATRP). *Langmuir* **2009,** *25* (14), 8280-8286.
36. Huang, C.-F.; Chen, J.-K.; Tsai, T.-Y.; Hsieh, Y.-A.; Lin, K.-Y. A., Dual-functionalized cellulose nanofibrils prepared through TEMPO-mediated oxidation and surface-initiated ATRP. *Polymer* **2015,** *72*, 395-405.

37. Operamolla, A.; Casalini, S.; Console, D.; Capodieci, L.; Di Benedetto, F.; Bianco, G. V.; Babudri, F., Tailoring water stability of cellulose nanopaper by surface functionalization. *Soft Matter* **2018,** *14* (36), 7390-7400.
38. Cunha, A. G.; Zhou, Q.; Larsson, P. T.; Berglund, L. A., Topochemical acetylation of cellulose nanopaper structures for biocomposites: mechanisms for reduced water vapour sorption. *Cellulose* **2014,** *21* (4), 2773-2787.
39. Jonoobi, M.; Harun, J.; Mathew, A. P.; Hussein, M. Z. B.; Oksman, K., Preparation of cellulose nanofibers with hydrophobic surface characteristics. *Cellulose* **2010,** *17* (2), 299-307.
40. Fukuda, J.; Hsieh, Y.-L., Hydrophobic 2, 7-Octadienyl Ether-Cellulose Nanofibrils Using Butadiene Sulfone as the Dual Reagent and Medium. *ACS Sustainable Chemistry & Engineering* **2021,** *9* (18), 6489-6498.
41. Sui, X.; Yuan, J.; Zhou, M.; Zhang, J.; Yang, H.; Yuan, W.; Wei, Y.; Pan, C., Synthesis of cellulose-graft-poly (N, N-dimethylamino-2-ethyl methacrylate) copolymers via homogeneous ATRP and their aggregates in aqueous media. *Biomacromolecules* **2008,** *9* (10), 2615-2620.
42. Chmielarz, P. J. E. P. L., Cellulose-based graft copolymers prepared by simplified electrochemically mediated ATRP. *Express Polymer Letters* **2017,** *11* (2), 140.
43. Yang, T.; Xiao, P.; Zhang, J.; Jia, R.; Nawaz, H.; Chen, Z.; Zhang, J., Multifunctional cellulose ester containing hindered phenol groups with free-radical-scavenging and UV-resistant activities. *ACS applied materials & interfaces* **2018,** *11* (4), 4302-4310.
44. Cao, X.; Sun, S.; Peng, X.; Zhong, L.; Sun, R.; Jiang, D., Rapid synthesis of cellulose esters by transesterification of cellulose with vinyl esters under the catalysis of NaOH or KOH in DMSO. *Journal of agricultural and food chemistry* **2013,** *61* (10), 2489-2495.
45. Saito, T.; Kuramae, R.; Wohlert, J.; Berglund, L. A.; Isogai, A., An ultrastrong nanofibrillar biomaterial: the strength of single cellulose nanofibrils revealed via sonication-induced fragmentation. *Biomacromolecules* **2013,** *14* (1), 248-253.
46. Lu, P.; Hsieh, Y.-L., Preparation and characterization of cellulose nanocrystals from rice straw. *Carbohydrate Polymers* **2012,** *87* (1), 564-573.
47. Segal, L.; Creely, J. J.; Martin Jr, A.; Conrad, C., An empirical method for estimating the degree of crystallinity of native cellulose using the X-ray diffractometer. *Textile research journal* **1959,** *29* (10), 786-794.
48. Scherrer, P., Estimation of the size and internal structure of colloidal particles by means of röntgen. *Nachr. Ges. Wiss. Göttingen* **1918,** *2*, 96-100.
49. Kowsaka, K.; Okajima, K.; Kamide, K., Two-dimensional nuclear magnetic resonance spectra of cellulose and cellulose triacetate. *Polymer journal* **1988,** *20* (12), 1091-1099.
50. Isogai, A., NMR analysis of cellulose dissolved in aqueous NaOH solutions. *Cellulose* **1997,** *4* (2), 99-107.
51. Jiang, F.; Dallas, J. L.; Ahn, B. K.; Hsieh, Y.-L., 1D and 2D NMR of nanocellulose in aqueous colloidal suspensions. *Carbohydrate polymers* **2014,** *110*, 360-366.
52. Nardin, R.; Vincendon, M., Homo-and heteronuclear two-dimensional correlated nuclear magnetic resonance spectra of cellulose. *Macromolecules* **1986,** *19* (9), 2452-2454.
53. Roberts, J. D.; Caserio, M. C., *Basic principles of organic chemistry*. WA Benjamin, Inc.: 1977.
54. Lee, Y.; Matviychuk, Y.; Holland, D. J., Quantitative analysis using external standards with a benchtop NMR spectrometer. *Journal of Magnetic Resonance* **2020,** *320*, 106826.

Chapter 3. 2-Bromopropionyl Esterified Cellulose Nanofibrils as Chain Extender or Polyol in Stoichiometrically Optimized Syntheses of High Strength Polyurethanes

Published on Biomacromolecules, October 6, 2022

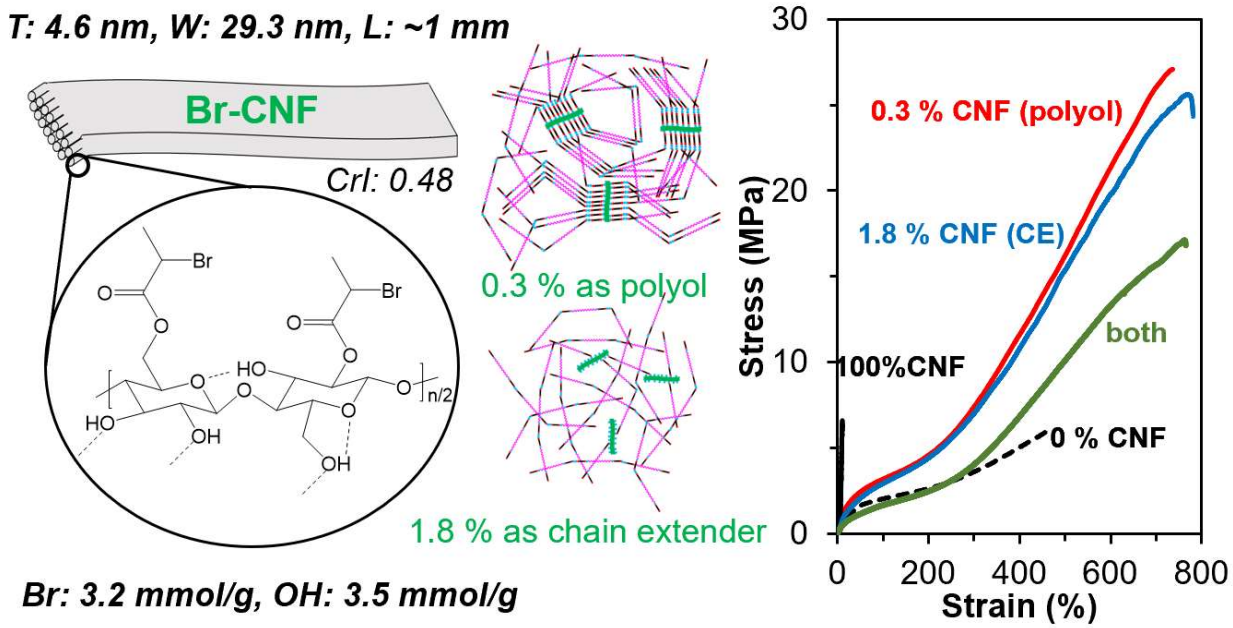

Abstract

2-Bromopropionyl bromide esterified cellulose nanofibrils (Br-CNF) facilely synthesized from one-pot esterification of cellulose and *in situ* ultrasonication have exhibited excellent DMF dispersibility and reactivity to serve as either chain extender or polyol in the synthesis of polyurethanes (PUs). The tensile modulus, strength, and stain of PU optimally polymerized with Br-CNF replacing 11 mol% of chain extender OHs or 1.8 mol% of soft segment OHs, i.e., equivalent of 1.5 w% or 0.3 w% of Br-CNF in PUs, were significantly enhanced to over three times, nearly four times, and 50%, respectively. In either role, the experimental modulus exceeding those predicted by the Halpin-Tsai model gave evidence to the stoichiometrically optimized covalent bonding with Br-CNF while the improved strain-to-failure was attributed to increased hydrogen bonding interactions between Br-CNF and soft segment. These new Br-CNF

offer novel synthetic strategies to not only streamline polyurethane synthesis but also maximize their reinforcing effect to demonstrate their potential applications to the synthesis of other polymers.

3.1. Introduction

Cellulose nanocrystals (CNCs) and cellulose nanofibrils (CNFs) are attractive one-dimensional nanofillers to reinforce polymer matrixes due to their intrinsically high surface area[1], high Young's modulus (150 GPa for CNCs, 28 GPa for CNFs)[2, 3], and very low coefficient of thermal expansion (10^{-7} K^{-1} for CNCs, 5×10^{-6} K^{-1} for CNFs)[4, 5]. CNCs are most commonly obtained by removing the non-crystalline domains in cellulose by sulfuric acid hydrolysis[6-10], whereas CNFs are derived by separating along the less crystalline domains by mechanical forces[10-19], or chemical reactions, such as (2,2,6,6-Tetramethylpiperidin-1-yl)oxyl (TEMPO) oxidation[10-15, 20], or a combination of both[10-15]. All these processes produce hydrophilic and, in many cases, anionically charged nanocelluloses[6-20] that are easily aqueously dispersed and miscible with water-soluble polymers. For instance, mixing CNC[21, 22] and CNF[23, 24] with waterborne polyurethane (WPU) has produced 3.5[21] or 4-fold[23] stronger films, but with considerably reduced strain at ca. 80 and 40 %, respectively. The poor corrosion resistance[25] and relative low strength[26] of WPU along with very high loadings of 30 % CNC[21] and 20 % CNF[23], however, limit their use. In the case of polyester based thermoplastic polyurethane (TPU), mixing up to 1 %[27] or 30 %[28] CNC with the aid of ultrasonication in DMF did not improve tensile strength or strain significantly, likely due the incompatibility between the hydrophilic CNC and hydrophobic TPU matrix.

Incorporating micrometer-scale microcrystalline[29] or microfibrillated cellulose[30] with polytetramethylene ether glycol (PTMEG, M_n:1,000 *Da*) in the reaction with methylene diphenyl diisocyanate (MDI) then chain extended with 1,4-butadienol (1,4-BD) was effective in increasing

the tensile strength of the resulting TPUs by 3[29] or 4.5[30] times, respectively (Table 3.1). However, dispersing aqueous CNCs (0.5 w%) in PTMEG (M_n: 1,000 *Da*) by homogenization and water evaporation followed by sequential reactions to MDI and 1,4-BD only improved tensile strength by 40 %[31]. Additional pretreatments of either freeze-drying CNC[32] or sequential solvent exchanging CNC[33] and CNF[34] via acetone to DMF, then ultrasonicated with PTMEG[32, 34] or hydroxylated soybean oil[33] have shown to improve some of the tensile modulus[32, 33], strength[32-34], and strain[32, 34], all optimized at 1 w% addition. In all above cases, a constant 2:1 NCO (MDI) to OH (PTMEG)[29-32, 34] or 1.2:1 NCO (MDI) to OH (hydroxylated soybean oil)[33] molar ratio were used without considering cellulose hydroxyls. In addition, the shear force employed in mixing, such as homogenization[31] and ultrasonication[35], can potentially reduce cellulose crystallinity by 40 and 20 % as reported on sugarcane bagasse and apple pomace[35], respectively.

Table 3.1. Summary of micro-scale celluloses and nanocelluloses in PU synthesis with 2:1 MDI: PTMEG and chain extended with 1,4-BD[29-32,34], except for one with 20 mol% excess MDI and no chain extender[33]. Tensile property improvement was indicated by times of increases (x).

Micro/Nano Cellulose	Cell (w%)	Cell OH content (mmol/g)	Preparation	Media	Dispersing Method	Prepolymer Precursor	Modulus (MPa)	Strength (MPa)	Strain (%)	Optimal Cell cotent (w%)	MDI (w%) of PU
MCC[29]	1-10	NA	none	DMF (0.3 wt% LiCl)	none	PTMEG (1000)	4.9-21.1 4.3x	8.0-24.0 3x	390-970 2.5x	5	31.5
MFC[30]	0.5-5	1.25	none	DMF	none	PTMEG (1000)	1.2-27.7 23x	5.8-26.3 4.5x	761-1387 1.8x	1	31.5
CNC[31]	0.5 (0-3 mol % excess MDI)	NA	none	PTMEG (1000)	homogenization (rotor–stator homogeniser, 1	PTMEG (1000)	16.6-16.1 1x	41.7-58.3 1.4x	1096-1011 0.9x	0.5	35.8
CNC[32]	0.5-5	2.8	freeze-drying	DMF	sonication*	PTMEG (1000)	8.2-44.9 5.5x	7.5-61.5 8.2x	751-994 1.3x	1	31.5
CNC[33]	0.5-2	NA	solvent exchange to acetone	hydroxylated soybean oil (Agrol 3.6)	sonication (IKA T 18 Basic Ultra-Turrax)	hydroxylated soybean oil (Agrol 3.6)	11.3-45 4x	2.5-5.3 2.1x	N/A	1	35.0
TEMPO-CNF[34]	0.5-2	NA	solvent exchange to acetone	DMF	sonication (VCX 500 Ultrasonic Processors, 300 W, 1 min)	PTMEG (2000)	8.7-4.9 0.6x	4.5-39.8 8.8x	419-2344 5.6x	1	19.5

CNCs[36-59] and CNFs[60-62] have been esterified to convert the cellulose OHs to alkyl bromines to improve their dispersity in organic liquids, such as DMF[36-49, 59], DMSO[50, 51, 62], THF[52, 53, 61], anisole[54-57, 60], and toluene[58, 59, 62]. Recently, 2-bromopropanoated nanofibrils (Br-CNF) have been directly produced by facile one-pot esterification of cellulose with 2-bromopropionyl bromide (BPB) to 2-bromopropanoated cellulose (Br-cell) to enable disintegration by *in situ* ultrasonication in the same organic liquid, DMF.[63] The 2-bromopropionyl esters on the surfaces of Br-CNF makes them compatible to DMF meanwhile the remaining surface OHs are available for reaction, making Br-CNF dual and even multi-functional from the perspective of organic reaction polymer synthesis. In the synthesis of PU, the residual surface OHs on Br-CNF present multiple hydroxyl groups as in polyols to potentially replace diols for chain extension of diisocyanate capped prepolymer or to replace some of the diols in prepolymer synthesis. These reaction-based incorporation of Br-CNF in the synthesis of PU is expected to achieve the highest reinforcing effect by maximizing covalent bonding.

In this study, Br-CNFs were incorporated in the synthesis of PU in two roles. As chain extenders, Br-CNFs were added to replace some of 1,4-BD to react with MDI-capped PTMEG prepolymers. The reinforcement effects of Br-CNF as chain extender were investigated by replacing up to 35 mol% OHs in 1,4-BD with the surface OHs from Br-CNF, which is equivalent up to 5.4 w% Br-CNF in the PU/CNF composites. As polyols, Br-CNFs were incorporated to partially replace equal OH from PTMEG diols, both capped by MDI then extended by 1,4-BD. The multiple surface OHs on Br-CNFs, along with their crystalline core, justify their low up to 0.5 w% quantities. A higher molecular weight PTMEG (M_n: 2,900 *Da*), nearly up to three times of the most commonly reported (M_n: 1,000[29, 30, 32] or 2,000[34] *Da*), was selected as soft segment to effectively lower the quantity of

diisocyanate, the most toxic constituent in PU syntheses. Furthermore, MDI, with one three hundredth vapor pressure than the more volatile toluene diisocyanate (TDI)[64], was used as hard segment to minimize inhalation exposure. Most significantly, not only the polyurethane reaction stoichiometry of $OH_{diol+Br\text{-}CNF}$:NCO_{MDI}:$OH_{diol+Br\text{-}CNF}$ was rationalized, but the surface OHs of Br-CNFs were also fully accounted for, to optimize both prepolymer syntheses and chain extension reactions. The effective role of Br-CNF, their molar or mass compositions, and the optimal reaction conditions, were evaluated by their effects on the elastic modulus, tensile stress, and stain-to-failure of the synthesized PU/CNF composites. The formation of urethane link was verified by attenuated total reflection (ATR). Thermal properties, such as glass transition temperature (T_g) and melting temperature (T_m), of the synthesized PU/CNF film were characterized by differential scanning calorimetry (DSC). The bulk morphology and organization of Br-CNFs in PU matrix were observed by optical microscopy under cross-polar.

3.2. Experimental

3.2.1. Materials. Cellulose was isolated from rice straw (Calrose variety) by a previously reported three-step process of 2:1 v/v toluene/ethanol extraction, acidified $NaClO_2$ (1.4 %, pH 3-4, 70 °C, 5 h) delignification, and alkaline hemicellulose dissolution (5 % KOH, 90 °C, 2 h)[65]. 2-Bromopropionyl bromide (BPB, 97%, Alfa Aesar), 4-dimethylaminopyridine (DMAP, 99%, Acros Organics), polytetramethylene ether glycol (PTMEG, M_n:1,000 and 2,900 *Da*, Sigma Aldrich), methylene diisocyanate (MDI, 97 %, Sigma Aldrich), 1,4-butanediol (1,4-BD, 99 %, Alfa Aesar), N,N-dimethylformamide (DMF, certified grade, Fisher Scientific), and acetone (histological grade, Fisher Scientific) were used as received without further purification. All

nanocellulose concentrations in DMF were denoted in weight/volume percent (w/v%) whereas all PU/CNF compositions were designated in weight/weight percent (w%).

3.2.2. Synthesis and Characterization of Br-CNFs. Br-CNFs were produced from rice straw cellulose by one-pot esterification with 2-bromopropionyl (5:1 BPB to anhydroglucose or AGU molar ratio, 23 °C, 6 h) and *in situ* ultrasonication (Qsonica Q700, 50/60 Hz, 50 % amplitude, 30 min) in DMF.[63] For imaging by atomic force microscopy (AFM, Asylum-Research MFP-3D), Br-CNF DMF dispersion was diluted (10 μL, 0.0005 w/v%) and deposited on freshly cleaved highly oriented pyrophoric graphite (HOPG), then air-dried in fume hood for 6 h. The heights of Br-CNFs (n : 100) were profiled in the tapping mode with a 5 μm × 5 μm scan size and a 512 Hz scan rate. For imaging by transmission electron microscopy (TEM, Philip CM12), Br-CNF dispersion (10 μL, 0.01 %) was deposited onto glow-discharged carbon-coated TEM grids (300-mesh copper, Formvar-carbon, Ted Pella Inc., Redding, CA), blotted with a filter paper after 5 min to remove excess dispersion, negatively stained with aqueous uranyl acetate (2 w/v %) for 5 min, and blotted again to remove excess liquid. This staining-blotting process was repeated five times, dried under the ambient condition for 15 min, then imaged at a 100 kV accelerating voltage. The widths and lengths of over 100 Br-CNFs for each sample were calculated using ImageJ Analyzer (ImageJ, NIH, USA). Crystallinity and domain size of air-dried Br-CNF film were determined using X ray diffraction (XRD) as described[10, 63, 66] previously.

The Br content of Br-CNF (σ_{Br}, mmol/g) was determined by the mass gain of 2-bromopropionyl esterified cellulose in which the C2, C3 and C6 OHs were converted to 2-bromopropionyl ester:

$$\sigma_{Br} = \frac{m_{Br-c} - m_{cell}}{135 \times m_{Br-cell}} \quad (3.1)$$

where m_{cell} is the initial cellulose mass (g), $m_{Br-cell}$ is the dry mass (g) of 2-bromopropionyl esterified cellulose, and 135 (g/mol) is the molecular mass difference between 2-bromopropionyl ester and hydroxyl. The substitution of surface OHs to 2-bromopropionyl, described as fraction of converted OHs (ρ), was estimated via solution phase ^{1}H NMR (Bruker AVIII 800 MHz ^{1}H NMR spectrometer) following the previously established method[63] briefly described in Supporting Information. Surface OH content (σ_{OH}, mmol/g) of Br-CNF was calculated by multiplying Br content (σ_{Br}, mmol/g) by available OH (1- ρ) then divided by converted OH (ρ):

$$\sigma_{\text{OH}} = \sigma_{\text{Br}} \times \frac{1-\rho}{\rho} \tag{3.2}$$

3.2.3. Polyurethane Synthesis. The polyurethane control was prepared by dissolving MDI (1.90 mmol, 0.47 g) and PTMEG (Mn:2,900 Da, 0.86 mmol, 2.5 g) in DMF (20 mL), degassed (Branson 2510) for 1 min, purged with N2 for 10 min, then reacted at 90 °C in an oil bath under stirring for 3 h to form prepolymer. Chain extender 1,4-BD (0.86 mmol, 0.078 g) was added to react at 90 °C for another 3 h, then quenched in ice bath to end the reaction.

3.2.4. Br-CNF as Extender. To prepare PU/CNF composites using Br-CNF as part of extender at a fixed 2.2:1:1 NCO_{MDI}:OH_{PTMEG}:$OH_{1,4\text{-}BD+Br\text{-}CNF}$ molar ratio (Scheme 3.1a), PTMEG (M_n:2,900 *Da*, 1.72 mmol OHs, 2.5 g) was reacted with MDI (3.80 mmol NCOs, 0.47 g) in 15 mL DMF, degassed (Branson 2510) for 1 min, purged with N_2 for 10 min, then sealed and heated to 90 °C with stirring for 3 h to form prepolymer. Br-CNF (0.5 w/v% in DMF) was added at 1.8 or 5.4 w%, i.e., 11 mL or 35 mL (0.19 and 0.61 mmol available OHs), to pre-dissolved 1,4-BD (0.069 and 0.051 g, 1.54 and 1.12 mmol OHs), degassed for 1 min, then to the prepolymer under constant stirring at 90 °C for another 3 h, finally quenched in ice bath to stop the reaction. Without any 1,4-

BD, PU/CNF with Br-CNF (0.5 w/v %, 0.61 mmol available OHs, 35 mL) as the lone extender was also synthesized at a fixed 2.2:1:0.35 NCO_{MDI}: OH_{PTMEG}: $OH_{Br\text{-}CNF}$ molar ratio for comparison.

3.2.5. Br-CNF as Polyol. The PU/CNF composites with Br-CNF serving in the role as polyol (Scheme 3.1b) were prepared at varying Br-CNF contents (0-0.5 w%) at a fixed 2.2:1:1 NCO_{MDI}: $OH_{PTMEG+Br\text{-}CNF}$: $OH_{1,4\text{-}BD}$. Br-CNF dispersions were diluted with DMF to 20 mL in 0.0075, 0.015, 0.03, 0.045, and 0.075 w/v%, degassed (Branson 2510) for 1 min and purged N_2 for 10 min. PTMEG (M_n:2,900 *Da*, 1.72 mmol OHs, 2.5 g) and MDI (3.8-3.92 mmol NCOs, 0.47-0.49 g) were added into each dispersion in high vacuum silicone grease sealed 50 mL round bottom flask at 90°C oil bath under stirring to react for 3 h to form prepolymer. 1,4-BD (0.86 mmol, 0.078 g) was added to reacted for another 3 h, then quenched to end reaction. Reactions were repeated with 1.8 mL Br-CNF (0.5 w/v %) at 2.1:1:1 and 2:1:1 NCO_{MDI}: $OH_{PTMEG+Br\text{-}CNF}$:$OH_{1,4\text{-}BD}$ molar ratios to investigate excess MDI effects. Lower molecular weight PTMEG (M_n:1,000 *Da*) was used with 1.8 mL Br-CNF (0.5 w/v %) at 2.2:1:1 NCO_{MDI}: $OH_{PTMEG+Br\text{-}CNF}$:$OH_{1,4\text{-}BD}$ molar ratio. Films were cast from various viscous reaction mixtures of various PU/CNF compositions as well as Br-CNF alone in glass petri dishes and dried at 60 °C oven for 2 d. Volume of circular films were calculated from thickness and diameter measured by micrometers and graduated scale to estimate densities.

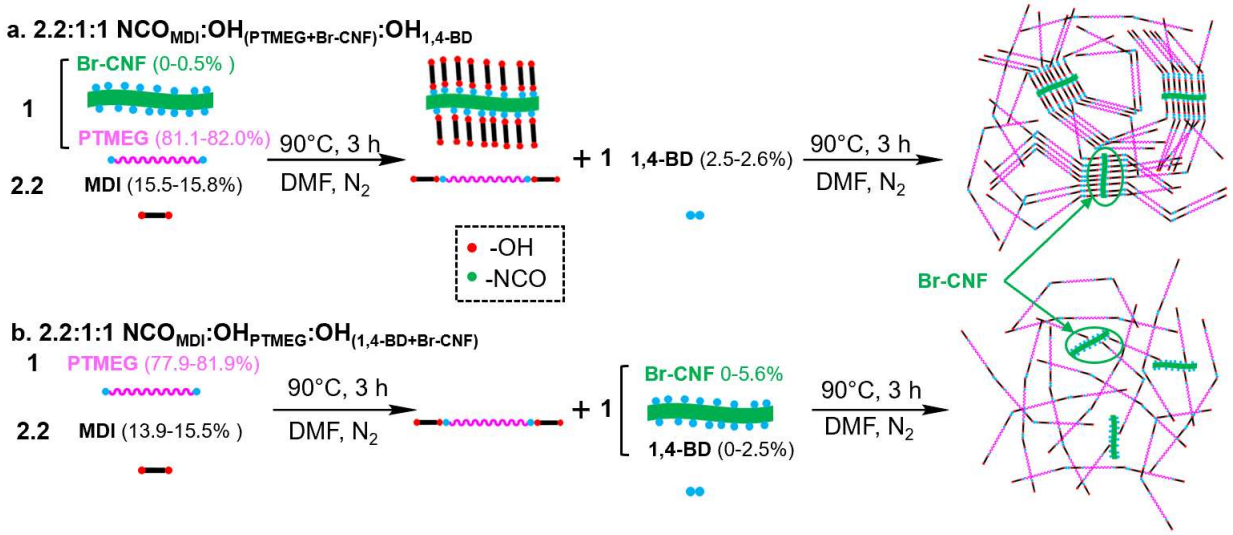

Scheme 3.1. Scheme for polyurethane synthesis with Br-CNFs serving as: (a) chain extender, (b) polyol; at the same 2.2:1:1 NCO_{MDI}: $OH_{PTMEG+Br-CNF}$: $OH_{1,4-BD+Br-CNF}$ molar ratio.

3.2.6. Characterization of PU/CNF film. The morphology of PU/CNF film was imaged by optical microscopy (Leica DM2500) in transmission mode and under cross-polars. For attenuated total reflectance (ATR) Fourier transformed infrared spectroscopy, each PU film was scanned by Thermo Nicolet 6700 spectrometer under ambient conditions from an accumulation of 128 scans at a 4 cm^{-1} resolution from 4000 to 400 cm^{-1}. To determine glass transition (T_g) and melting (T_m) temperatures of PU/CNF film, each ca. 10 mg sample was cooled by liquid nitrogen to -100 °C and scanned at 10 °C/min to 50 °C by differential scanning calorimetry (DSC, DSC-60 Shimadzu). The tensile properties of films (40×14×0.4 mm) were measured using an Instron 5566 tensile tester with a static 5 kN load cell, ca. 20 mm gauge length and 20 mm/min crosshead speed to break and to 400 % strain in cyclic mode. For each data point, at least three films were tested with the average value and standard deviation reported. The modulus was determined by the initial slope of strain-stress curve. Engineering stress (σ) was calculated from F/A_0, where F was applied load (N) and

A_0 is the initial cross-sectional area (m^3). Engineering strain (Ɛ) was calculated by $\Delta L/L_0$, where ΔL was the extension (mm) of the sample and L_0 was initial sample gauge length (mm).

3.3. Results and discussion

3.3.1. Characteristics of Br-CNFs. Br-CNFs were optimally synthesized by one-pot 2-bromopropionyl esterification of rice straw cellulose (5:1 BPB to AGU molar ratio, 23 °C, 6 h) and *in situ* ultrasonication (50 % amplitude, 30 min) in DMF[63] to be ribbon-like with 4.6 ± 1.8 nm thickness (T), 29.3 ± 9.2 nm width (W), and ca. 1 μm length (L) (**Figure S3.1a** and **b**). The Br-CNF geometries are uniquely anisotropic, showing over 6 W/T and 213 L/T ratios. 2-bromopropionyl esterification converts the OHs in the less ordered region of cellulose to 2-bromopropionyl esters to endow organic compatibility and to facilitate the direct disintegration by ultrasonication of 2-bromopropionyl esterified cellulose into homogeneously dispersed Br-CNFs, all in the same organic media DMF. The level of substitution (ρ) quantified by ^{1}H NMR (**Figure S3.2**) was 0.48, showing nearly half of the surface OHs were converted to 2-bromopropionyl esters. The remaining 52% surface OHs, equivalent to 3.5 mmol OHs/g Br-CNF by eqn. (2), remained available to react with MDI. The XRD of Br-CNFs displayed 2θ peaks at 14.6, 16.5, and 22.5°, corresponding to the respective (1-10) (110) (200) monoclinic Iβ lattice planes of cellulose (**Figure S3.3**). The 0.48 CrI of Br-CNF showed retention of 69 % crystallinity of the original cellulose (CrI:0.69).

Table 3.2. CNF Characteristics: dimensions, crystallinity, Br content/degree of substitution, available OHs content.

Thickness (nm)	Width (nm)	Length (nm)	Crystallite Dimension (nm)	CrI	Br content (mmol/g)	Level of substitution	OHs content (mmol/g)
4.6	29.3	ca. 1000	1.45	0.48	3.2	0.48	3.5

Br-CNFs have similar in thickness (T=4.6 nm) as another highly hydrophobic ODE-CNF (T = 4.4 nm, W = 4.1 nm, L = 1.7 μm)[66], both are thicker than hydrophilic TEMPO-CNF (T = 1.5 nm, W = 2.1 nm, up to 1 μm long)[13], all ca/ 1 μm or longer and derived from the same rice straw cellulose. Br-CNF (W=29.3 nm) is, however, considerably wider than those respective ODE-CNF and TEMPO-CNF, i.e., by 7 and 14 times. The 6 W/T ratio of the cross-section gives Br-CNF highly anisotropic lateral dimensions than the near isotropic W/T ratios of ODE-CNF and TEMPO-CNF, both the latter two disintegrated by high-speed blending in water. These lateral dimensional and aspect ratio differences indicated the specific ultrasonication applied to be less intensive to disintegrate 2-bromopropionyl esterified cellulose in the less ordered domains into CNFs compared to aqueous high-speed blending of either hydrophobic ODE-cellulose or hydrophilic TEMPO-cellulose. Br-CNFs (CrI:0.48) (**Figure S3.3**) is slightly less crystalline than ODE-CNF (CrI:0.52)[66] but clearly less crystalline than TEMPO-CNF (CrI:0.63)[13]. The reduced crystallinity of Br-CNF was attributed mainly to the chemical reaction of cellulose, i.e., 2-bromopropionyl esterification reduced crystallinity of cellulose (CrI:0.69) to Br-cell (CrI:0.50)[63] to signify the more robust 2-bromopropionyl esterification in DMF in comparison to lesser effects on crystallinity from the less intensive telomerization[66] or TEMPO-oxidation[13]. The significantly retained crystallinity (CrI:0.48) and largely available surface OHs (3.5 mmol/g) made Br-CNF uniquely

surface-reactive polyols with crystalline core as potential covalent bonded reinforcement in TPU synthesis.

3.3.2. Br-CNF as chain extender in PU synthesis at 2.2:1:1 NCO: OH: OH. Br-CNF was incorporated as chain extender to partially replace 11 and 35 mol% OH in 1,4-BD or 1.8 and 5.4 w% Br-CNF in PU syntheses at a fixed 2.2:1:1 NCO_{MDI}:OH_{PTMEG}:$OH_{1,4\text{-}BD+Br\text{-}CNF}$ molar ratio (**Scheme 3.1a**, **Figure 3.1**). Br-CNF was also incorporated as the only chain extender at 5.6 w%, equivalent to 35 mol% OHs of 1,4-BD, for comparison. Upon replacing 11 mol% OHs of 1,4-BD with 1.8 w% Br-CNF (**Figure 3.1b** and **c**), the elastic modulus, tensile strength and strain-to-failure significantly increased from 2.6 to 8.3 MPa, 5.4 to 26.7 MPa and 490 to 883%, respectively. Replacing over three times of 1,4-BD OHs (35 mol%) with Br-CNF (5.4 w%) further doubled the modulus to 16.5 MPa but lowered the strength by 30 % to 18.8 MPa and stain by 22 % to 684 %. The enhanced elastic modulus and tensile stress were attributed to linking the MDI-capped soft segments with multiple OHs of Br-CNF like crosslinkers, instead of the short 4-C extender. The increased strain-to-failure was attributed to the strengthened soft domains from hydrogen bonding between the remaining unreacted OH on Br-CNF and PTMEG. That modulus increase essentially linearly with Br-CNF contents further signifies the contribution of multiply crosslinked Br-CNF with MDI-capped soft segments. The more heterogeneous appearance of films with 5.4 w% Br-CNF suggest possible agglomeration and/or phase separation of Br-CNF to lead to lowered tensile stress and strain-to-failure (**Figure 3.1a**). Furthermore, using 5.6 w% Br-CNF (equivalent to 35 mol% OHs of 1,4-BD) as the only extender, the modulus drastically increased from 16.5 to 173 MPa while the strain significantly reduced from 684 to 46 %, but only slightly decreased tensile stress from 18.8 to 17.0 MPa. As the lone chain extender, 5.6 w% Br-CNF only provided 35 mol%

OHs of 1,4-BD, insufficient to link all the MDI-capped soft segments to turn the elastomeric PU to high modulus plastic.

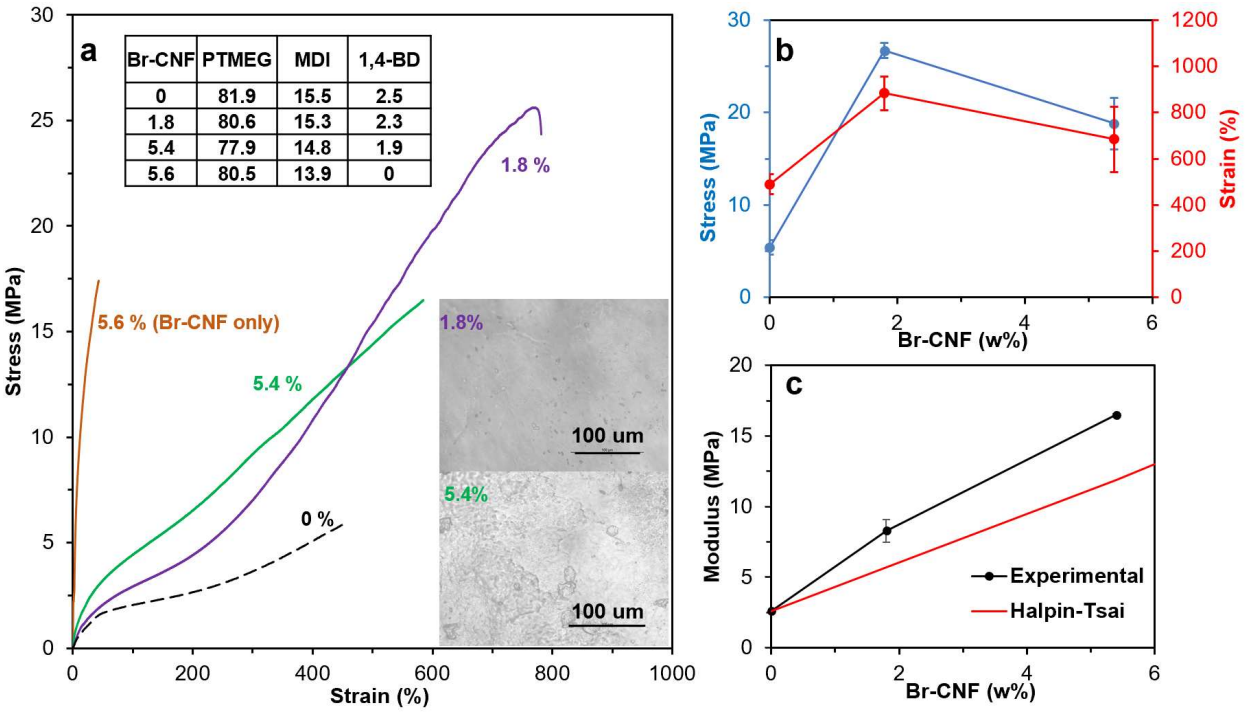

Figure 3.1. Tensile properties of PU synthesized with Br-CNF as chain extender to replace 11 and 30 mol% of 1,4-BD hydroxyls at 2.2:1:1 NCO_{MDI}: OH_{PTMEG}:$OH_{1,4\text{-}BD+Br\text{-}CNF}$: (a) representative stress-strain curves for PU/CNF films (n≥3) with Br-CNF (w%) compositions and photographic images of PU/CNF films; (b) tensile stress and strain-to-failure; (c) Experimental and Halpin-Tsai simulated elastic modulus (MPa) (n≥3).

The Halpin-Tsai model that predicts the modulus of short fiber reinforced composites with perfectly aligned, homogeneously mixed, and constant fiber volume fraction in a continuous matrix[67] was used to compare with the experimental values. The predicted modulus from the Halpin-Tsai model is expressed as

$$E = E_m\left(\frac{1+\zeta\eta V_f}{1-\eta V_f}\right) \tag{3.3}$$

$$\eta = \frac{E_f/E_m - 1}{E_f/E_m + \zeta} \tag{3.4}$$

where E is the longitudinal modulus of the unidirectional composite; V_f is the fiber volume fraction based on mass fraction of Br-CNF in PU with their respective estimated densities of 1.2 g/cm^3 and 1.1 g/cm^3; E_m and E_f are the respective matrix and fiber modulus; ζ is a shape factor for Br-CNF and defined[68] as

$$\zeta = (0.5L/D)^{1.8} \tag{3.5}$$

where L is the 1 μm length of Br-CNF and D is the diameter or the geometrical mean (11.7 nm) of Br-CNF thickness (4.6 nm) and width (29.3 nm).

From Halpin-Tsai model simulation[67, 68], elastic modulus for PU with 1.8 % and 5.4 % Br-CNF were 5.7 and 11.9 MPa, ca. 30 % lower than the respective experimental values of 8.3 and 16.5 MPa. The higher experimental modulus than predicted by the Halpin-Tsai model supports the presence of new covalent bonding between Br-CNF and MDI when applied as extender. As a chain extender, the optimal Br-CNF content was 1.8 w% to significantly improve all three tensile properties, i.e., to over 3 times in modulus, nearly 4 times in strength, and 80 % increase in strain. Similarly, the overall toughness also reached highest at 1.8 w%.

3.3.3. Br-CNF as polyol in PU synthesis. Br-CNF with 3.5 mmol OHs/g was also used as polyol to replace 0.3, 0.6, 1.2, 1.8 and 3.1 mol% OHs of PTMEG diols to synthesize pre-polymer with 10 mol% excess of MDI, i.e., 2.2:1:1 NCO_{MDI}:$OH_{PTMEG+Br\text{-}CNF}$:$OH_{1,4\text{-}BD}$ mole ratio, to ensure capping all Br-CNF surface OHs. These partial replacement of diol with Br-CNF polyol represent 0.05, 0.1, 0.2, 0.3, and 0.5 w% of Br-CNF in the PU/CNF composites. The colorless PU turned yellowish

with increasing Br-CNF contents and into golden color with 0.5 w% Br-CNF (**Figure 3.3.2a**). With up to 0.3 w% Br-CNF, the elastic modulus increased by over three times from 2.6 to 8.3 MPa and the tensile strength by nearly four times from 5.4 to 21.1 MPa, while the strain also increased by 54% from 490 to 755 % (**Figure 3.2b, c**). However, with further increased Br-CNF content to 0.5 w%, all tensile modulus, strength, and strain reduced to respective 6.0 MPa, 15.7 MPa, and 539 %, i.e., levels near or below those with 0.1 w% Br-CNF. The increases in all three mechanical properties were attributed to improved dispersion due to 2-bromopropionyl esters functionalized Br-CNF surfaces and covalent bonding between Br-CNF surface OHs and MDI. The outstanding reinforcement effects on modulus and tensile strength were attributed to the crystalline core of Br-CNF and surface OHs covalent bonded with MDI, serving as additional and new kind of hard segments. Meanwhile replacing diol with Br-CNF polyol in the soft segments could also enhance hydrogen bonding interactions between unreacted Br-CNF surface OHs and PTMEG to increase stretchability. In addition, the ability of Br-CNF to realign along the loading direction may be another reason for increased tensile strength and stretchability. That much reduced tensile stress, strain-to-failure and elastic modulus with 0.5 w% Br-CNF may be due to inter Br-CNF association, reducing their reaction with MDI and hydrogen bonding with PTMEG. Comparably, all experimental elastic modulus values of PU with Br-CNF as polyol were over two times or higher than Halpin-Tsai model simulated values (**Figure 3.2c**), indicating the extreme effectiveness of strong covalent bonding between Br-CNF and MDI. This observation illustrated surface OHs on Br-CNF are more reactive to free MDI as polyol but less accessible to MDI-capped PTMEG prepolymer as chain extender. In fact, the same modulus 8.3 MPa was achieved with Br-CNF serving as either polyol or chain extender, but requiring only one sixth in the polyol role (0.3 w%)

than the chain extender (1.8 w%). The optimal molar replacement of Br-CNF hydroxyls for those in PTMEG soft segment or 1,4-BD chain extenders was 1.8 or 11 mol%, respectively.

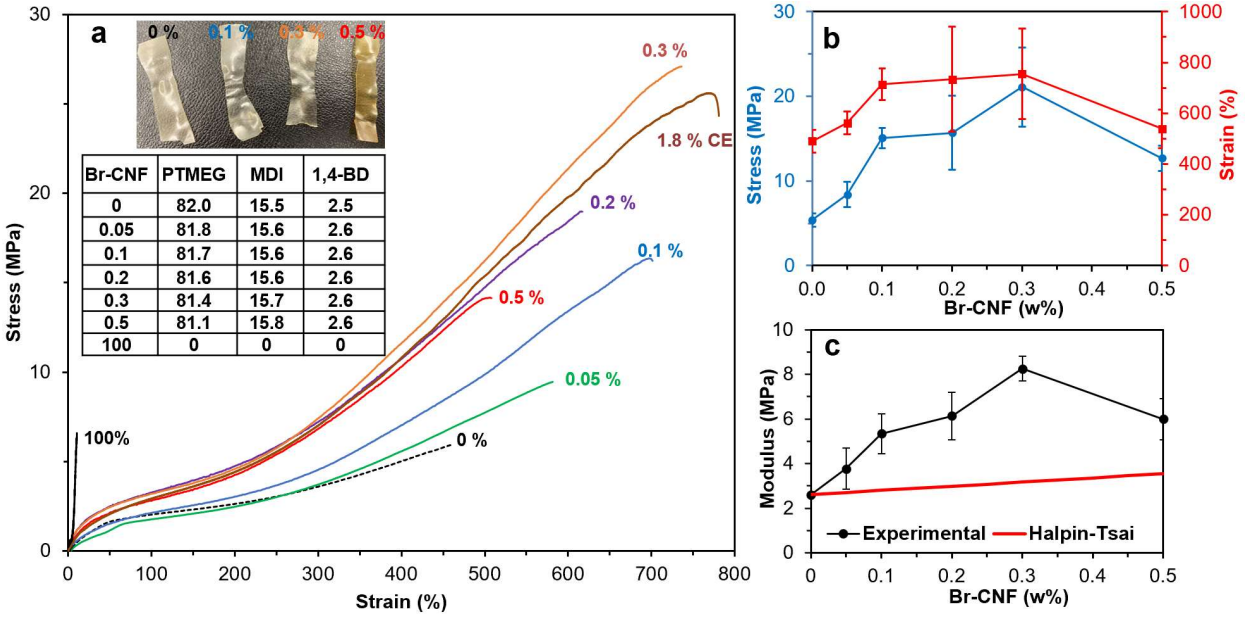

Br-CNF	PTMEG	MDI	1,4-BD
0	82.0	15.5	2.5
0.05	81.8	15.6	2.6
0.1	81.7	15.6	2.6
0.2	81.6	15.6	2.6
0.3	81.4	15.7	2.6
0.5	81.1	15.8	2.6
100	0	0	0

Figure 3.2. Tensile properties of PU synthesized with Br-CNFs as polyols replacing 0.3, 0.6, 1.2, 1.8 and 3.1 mol% OHs in PTMEG (Mn:2,900 *Da*) diol at 2.2:1:1 NCO_{MDI}:$OH_{PTMEG+Br\text{-}CNF}$:$OH_{1,4\text{-}BD}$ mole ratio: (a) representative stress-strain curves for PU/CNF films with 0.05, 0.1, 0.3, and 0.5 w% Br-CNF; photographic images of the upper portions of fractured samples and 1.8 w% Br-CNF (11 mol% of OH in 1,4-BD) as chain extender (CE) from Figure 3.3.1a for comparison; (b) tensile stress (MPa) and strain-to-failure (%); (c) Experimental and Halpin-Tsai simulated elastic modulus (MPa) of PU/CNF films (n≥3).

These findings show, for the first time, that a mere 0.3 w% Br-CNF quantity can significantly enhance the tensile modulus (3.2x) and strength (3.9x) while also improve the strain-to-failure (1.5x). In all prior work of involving cellulose or nanocellulose either as filler[21-24, 27, 28] or in PU synthesis[29-34], improvement in all three tensile properties was only reported in three, i.e., 5 w%

MCC[29], 1 w% MFC[30], and sonication assisted 1 w% CNC[32], all with the shorter PTMEG (M_n:1,000 *Da*) (Table 3.1). While those PUs synthesized with the commonly used shorter PTMEG is expected to have higher modulus but reduced strain, the MDI quantities were also double. Among them, only two documented FTIR evidence of new covalent bonding formation between MFC[30] or CNC[32] and isocyanates. Furthermore, Br-CNF is homogeneously dispersed in DMF without any pretreatment nor shear force mixing, a stark contrast to the extra and necessary processes of freeze-drying[32], solvent exchange[33,34] then aided by homogenization[31], or soniction[32-34], to disperse hydrophilic nanocelluloses. Uniquely, Br-CNF is not only efficiently synthesized, i.e., one-pot esterification and *in situ* disintegration, directly from cellulose, but also robust in reactivity to serve dual roles as either polyol or chain extender in the synthesis of PU. Most significantly, the quantity of the toxic MDI was significantly reduced to half.

3.3.4. MDI optimization. In the attempt to further reduce the diisocyanate quantity, the molar excess MDI was reduced from 10 to 0 mol% in the synthesis of prepolymer with 0.3 w% Br-CNF as polyol replacing 1.8 mol% PTMEG hydroxyls (**Figure 3.3a**). Generally, both modulus and tensile strength displayed positive correlation to excess MDI mol% meanwhile negative correlation was observed for strain-to-failure (**Figure 3.3b** and **c**). In the absence of Br-CNF, both elastic modulus and tensile stress of the PU control slightly increased from 2.5 to 2.8 MPa and 4.3 to 5.8 MPa, whereas strain-to-failure slightly decreased from 585 to 507 % with 5 mol% excess MDI, but showing no further change with 10 mol% excess MDI, indicating 5 mol% excess MDI to be adequate to cap PTMEG diols in the synthesis of PU. With 0.3 w% Br-CNF, all three tensile modulus, stress, and strain-to-failure moderately increased from 6.5 to 8.3 MPa, 13.2 to 21.1 MPa and 656 to 755 % with the increase of excess MDI to 10 mol%. More excess MDI required with Br-CNF than the control suggested that surface OHs on Br-CNF may be less accessible than those

of the PTMEG diol. It is also possible that surface Br esters determined by ^{1}H NMR may be over-estimated due to the DMF-to-acetone solvent exchange preparation that left out some less substituted Br-cellulose, leading to underestimated OHs content of Br-CNF. Further increasing Br-CNF content from 0.3 to 1 w% (**Figure S3.4**) w/o excess MDI moderately increased strength (1.2x) and strain-to-failure (1.2x) but sacrificed 20 % elastic modulus. The optimal Br-CNF as polyol w/o excess MDI was determined to be 1 w%, nearly 3-time higher than optimal 0.3 w% Br-CNF content at 10 mol% excess MDI. Thus, 10 mol% excess MDI not only further enhance the tensile properties of PU/CNF composite but also requiring significantly less Br-CNF. Unlike prior PU synthesized with a constant 2:1 NCO_{MDI}:OH_{PTMEG}[29, 30, 32, 34] ratio without consideration of cellulose OHs, this work rationally targets the OHs of both Br-CNF polyol and PTMEG diol stoichiometrically to isocyanate to significantly improve all tensile properties of PU, i.e., 3.2x modulus and 3.9x strength and 1.5x strain-to-failure, with a mere 0.3 w% Br-CNF as polyol and 10 mol% excess MDI.

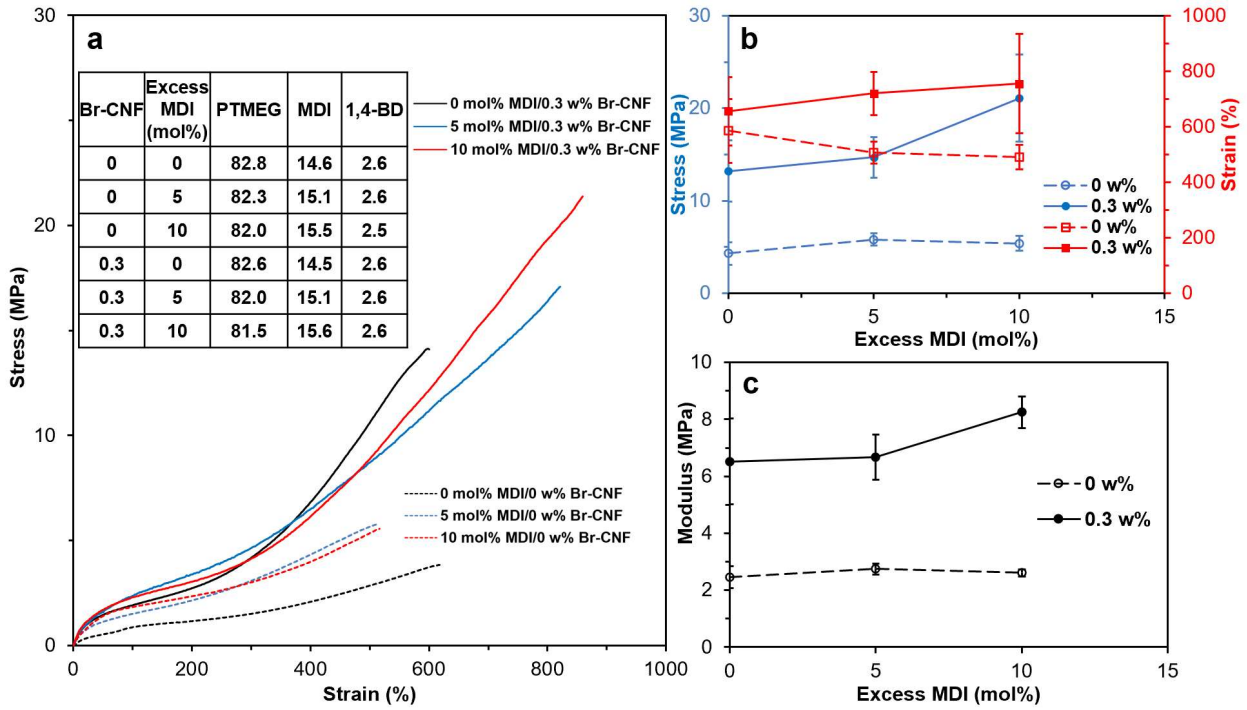

Figure 3.3. Tensile properties of PU synthesized with 0.3 w% Br-CNF polyol in PTMEG (Mn:2,900 *Da*) diol with 0 to 10 mol% excess MDI (2-2.2:1:1 NCO_{MDI}:$OH_{PTMEG+Br\text{-}CNF}$:$OH_{1,4\text{-}BD}$): (a) representative stress-strain curves with compositions in w%; (b) tensile stress and strain; (c) modulus (n≥3).

3.3.5. PTMEG chain length. While using longer PTMEG (M_n : 2,900 *Da*) than the commonly reported shorter PTMEG (M_n:1,000 *Da*) has the advantage of reducing MDI usage, lower elastic modulus and higher strain of PU are expected and was confirmed by the control PU synthesized without Br-CNF (**Figure 3.4a**). With the optimal 0.3 w% Br-CNF as polyol and 10 mol% excess MDI, the elastic modulus nearly doubled from 8.3 to 16.1 MPa while strength and strain modestly increased and decreased, respectively for the shorter PTMEG, while in contrast, the modulus increased from 2.6 to 8.3 MPa by over three times, stress nearly quadruple from 5.4 to 21.1 MPa, and strain nearly doubled from 490 to 755 % with the nearly three times longer PTMEG (**Figure 3.4b**). Therefore, while incorporating 0.3 w% Br-CNF as polyol most significantly improved the modulus of PU with shorter PTMEG, the effect on PU with the longer PTMEG was significant in all three tensile properties. The more significant reinforcement effects of Br-CNF on PU synthesized with longer PTMEG (M_n:2,900 *Da*) support the notion that both covalent bonding between Br-CNF and MDI and hydrogen bonding between B-CNF and PTMEG were maximized to give the best mechanical performance. Also, adding 0.3 w% Br-CNF as polyol would minimize negative effects of the longer PTMEG on the modulus to retain same modulus (8.3 MPa) as short PTMEG (M_n:1000 *Da*).

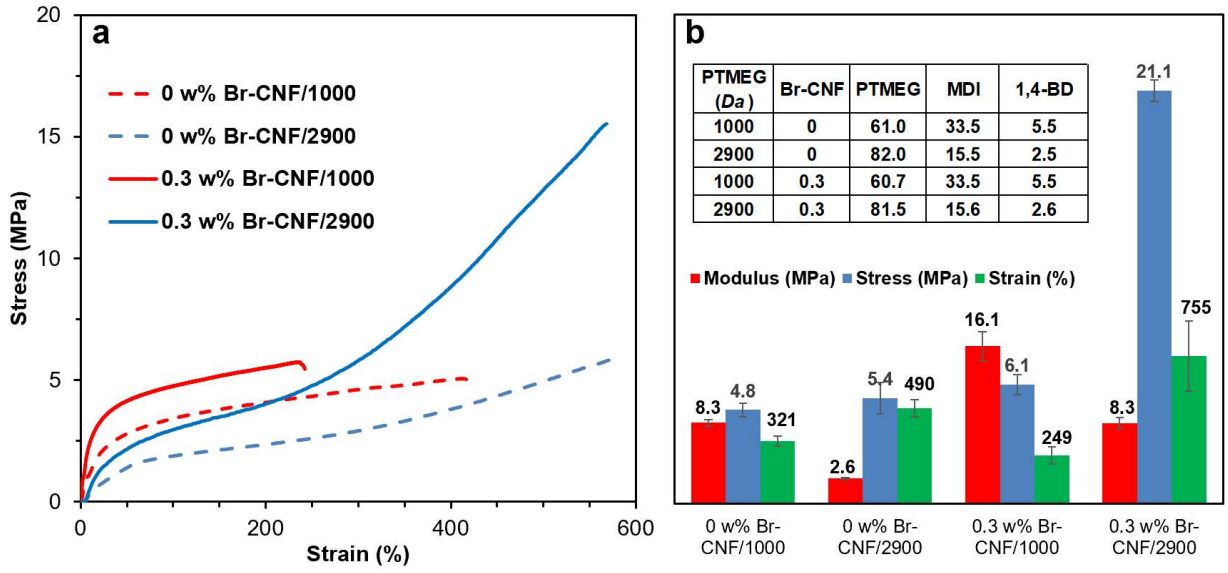

Figure 3.4. Tensile properties of PU synthesized with Br-CNFs as polyols and either 1,000 or 2,900 *Da* PTMEG at a consistent 2.2:1:1 NCO_{MDI}:$OH_{PTMEG+Br\text{-}CNF}$: $OH_{1,4\text{-}BD}$: (a) Representative stress-strain curves; (b) elastic modulus, tensile stress, and strain-to-failure (n≥3), with compositions (w%).

While the optimal 1.8 w% Br-CNF as extender led to 27 % higher tensile strength (26.7 vs 21.1 MPa), 17 % higher strain-to-failure (883 vs 755 %), and same elastic modulus (8.3 MPa) than its role as polyol, the slight strength enhancement with six times of Br-CNF is indicative of the more efficient covalent bonding of Br-CNF with MDI as polyol than as chain extender. With similar PTMEG, MDI and 1,4-BD contents, 0.3 w% Br-CNF as polyol capped by 10 mol% excess MDI with PTMEG (M_n : 2,900 *Da*) were optimal to produce the most significantly reinforced PU film with 3.2x modulus, 3.9x strength and 1.5x strain-to-failure meanwhile reducing MDI usage to 15.7 w%.

3.3.6. ATR and DSC spectra of PU/CNF composites. The presence of urethane link in PU and PU/CNF composite films were clearly evident in their ATR spectra (**Figure 3.5a**), showing C=O peaks at 1709 cm^{-1} (hydrogen bonded) and 1730 cm^{-1} (free), C-N asymmetric stretching peak at 1610 cm^{-1}, and N-H bending peak at 1530 cm^{-1}. For films with 1.8 and 5.4 w% Br-CNF as chain extender, the detection of a new carbonyl peak at 1645 cm^{-1} gave evidence to the reaction between the Br-CNF surface OHs with MDI. In those with Br-CNF as polyol, however, no new peak was observed due to the extremely low quantities up to 0.5 w%. The effects of Br-CNF from covalent bonding with MDI, either as polyol or chain extender, as well as their interactions with the soft segments were further elucidated by their thermal behaviors (**Figure 3.5b**). Glass transition temperature T_g (°C) increased from -71.9 °C to -63.7 °C with increasing 0 to 0.5 w% Br-CNF polyol, but decreased to -79.5 °C with increasing 0 to 5.4 w% Br-CNF extender. The endothermic recrystallization peak for MDI-1,4-BD-MDI hard domains remained constant at -1.5 °C and independent of Br-CNF contents and roles, indicative of no Br-CNF effects on original PU hard domain size and distribution. As polyol, the effective reaction between Br-CNF and MDI introduces new Br-CNF-MDI carrying polyisocyanate terminals among the diols, also bearing isocyanate terminals, to reduce the segmental motion of the soft segments to decrease T_g. As extender, the higher Br-CNF contents and the availability of more unreacted OHs on Br-CNF surface would hydrogen bonded with PTMEG (-OR), suppressing PTMEG phase separation into smaller soft domains thus lowered T_g. Melting temperature T_m (°C) decreased from 18.9 °C to 12.0 °C with increasing Br-CNF contents from 0 to 0.3 w% as polyol, while decreased slightly to 16.2 °C with Br-CNF as extender up to 5.4 w%. In either polyol or extender role, increasing Br-CNF contents is expected to increase the extent of covalent bonding to MDI, lowering the extent of MDI-1,4-BD-MDI hard domains to lower T_m. The stronger covalent bonding between Br-CNF

and MDI may be the reason for higher T_m reduction with Br-CNF as polyol than extender. One possible explanation for elevated T_m (14.6 °C) with increased Br-CNF as polyol from 0.3 to 0.5 w% may be that Br-CNFs extensively covalent bonded with MDI behave as crosslinkers and new hard domains to suppress mobility of the original MDI-1,4-BD-MDI hard domains.

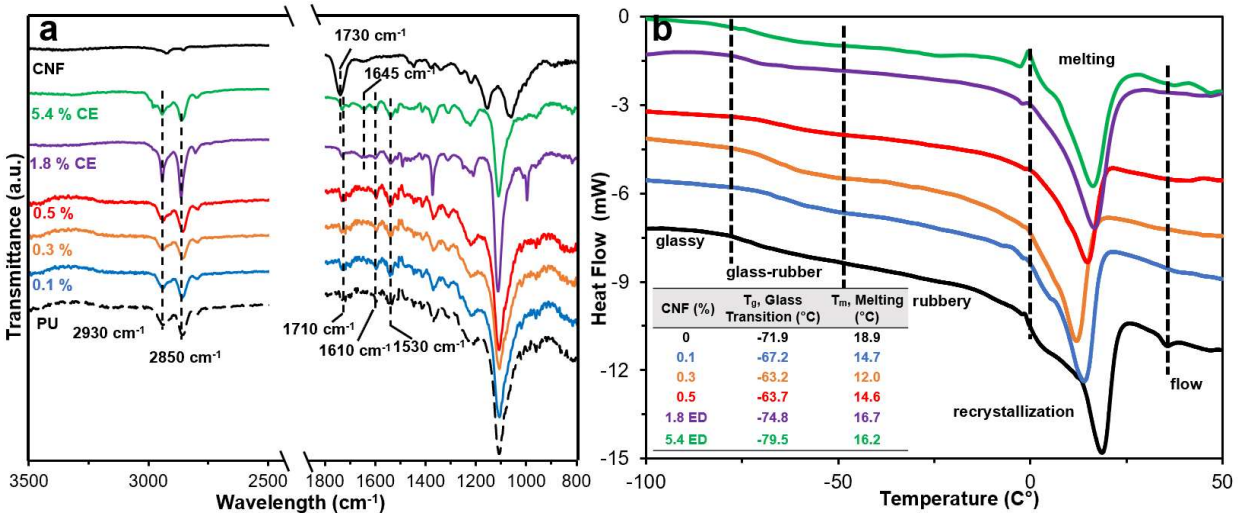

Figure 3.5. Characteristics of PU/CNF composites with Br-CNF as polyol (0.1, 0.3, 0.5 w%) or extender (1.8 and 5.4 w%): (a) attenuated total reflectance (ATR) spectra; (b) differential scanning calorimetry thermograms.

3.3.7. Cyclic tensile properties of polyurethane film with Br-CNF as polyol. To further investigate elastic and inelastic behaviors, uniaxial cyclic tensile strain/stress curves for PU/CNF films with 0, 0.1, 0.3 and 0.5 w% Br-CNF (0, 0.6, 1.8 and 3.1 mol% PTMEG OHs) as polyol was evaluated at up to 400 % strain (**Figure 3.6a**). The 1st cycle tensile stress significantly increased from 4.4 to 11.9 MPa with increasing Br-CNF contents to 0.3 w%, then lowered to 9.9 MPa at 0.5 w%. In the 1st cycle, the strain recovery for PU was 152% and increased to 223 % with 0.3 w% Br-CNF polyol (**Figure 3.6b** and **c**). The behavior of decreasing stress at 400 % with increasing number of cycles, or stress relaxation phenomenon, was observed for all three PU/CNF composites.

At the end of 5th cycle, stress at 400 % strain decreased from 8.3 to 7.0 MPa, 11.9 to 9.5 MPa and 9.9 to 8.5 MPa, corresponding to 0.1, 0.3 and 0.5 w% Br-CNF contents, respectively, in contrast to the lacking stress relaxation for PU control. Those observed stress relaxation phenomenon possibly caused by realignment of Br-CNF along loading direction indicated the existence of irreversibility with Br-CNF as polyol at high strain to 400 %. Nevertheless, the stress after five cycles of PU with Br-CNF polyols were significantly higher than PU. Both highest 11.9 MPa tensile stress and 223 % 1st cycle recovery observed at 0.3 w% Br-CNF as polyol confirmed this to be optimal PU/CNF composition to generate the most resilient film.

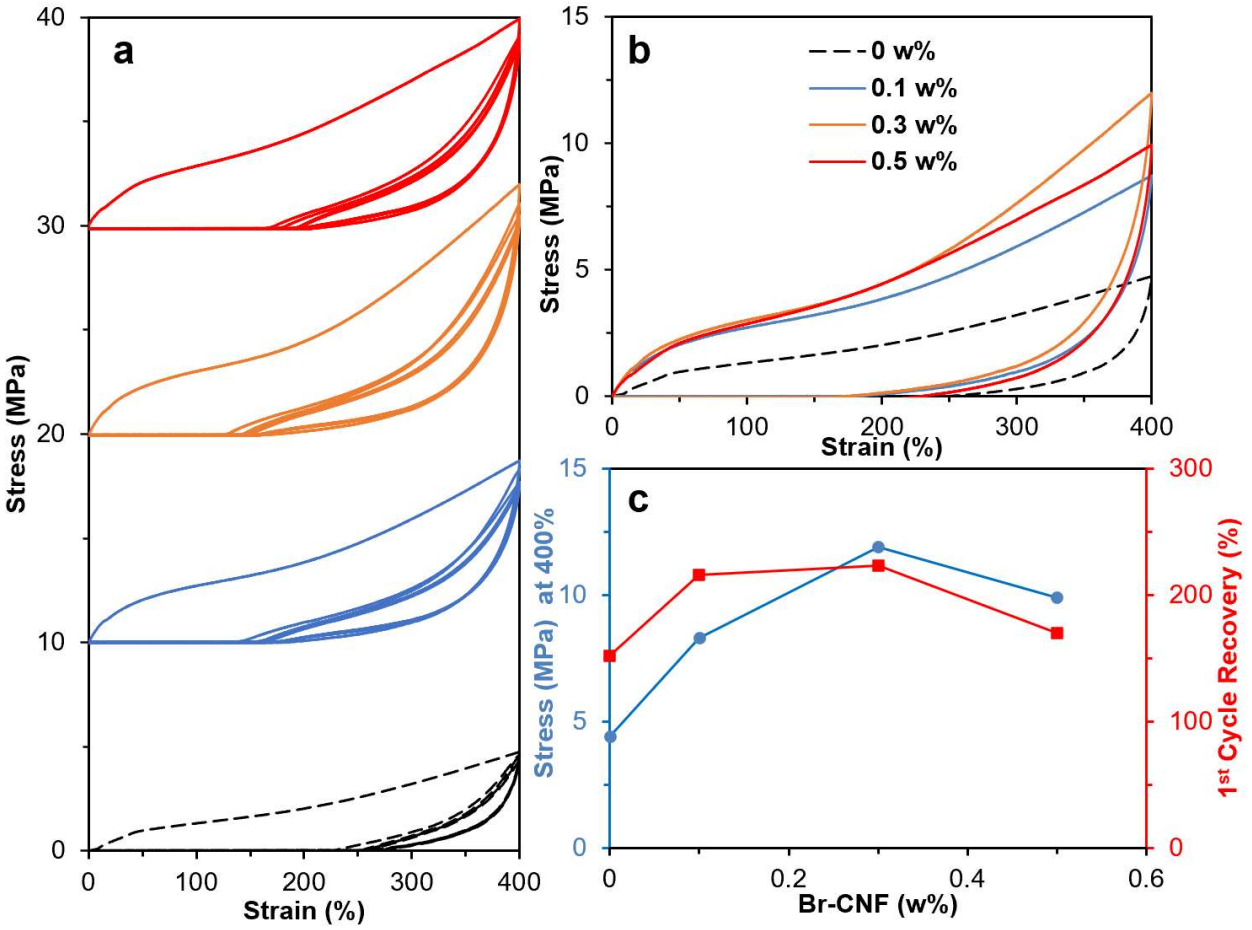

Figure 3.6. Cyclic tensile properties of PU/CNF films with Br-CNF (w%) as polyol at 400 % strain for 5 cycles: (a) cyclic stress-strain curves; (b) 1st cyclic stress-strain curves, (c) 1st tensile

stress and cycle recovery (%). All films are synthesized with at 2.2:1:1 NCO_{MDI}:$OH_{PTMEG+Br\text{-}CNF}$:$OH_{1,4\text{-}BD}$ and PTMEG (Mn=2,900 *Da*).

3.3.8. Orientation of Br-CNF in PU along loading direction. Films with 0.5 w% Br-CNF as polyol and 1.8 w% Br-CNF as extender were uniaxially stretched at up to 300 % strain to observe their morphology by optical microscopy (**Figure 3.7**). The phase separated hard (MDI-1,4-BD-MDI) and soft (PTMEG) microdomains appeared as granular black and white clusters in the PU control (**Figure S3.5a**) whereas PU containing either 0.5 w% Br-CNF as polyol or 1.8 w% Br-CNF as chain extender displayed isotropically arranged microfibers, under both transmission and cross-polar modes (**Figure 3.7a** and **d**). The same microfibers were also observed with 0.1 and 0.3 w% Br-CNF as polyol (**Figure S3.5b** and **c**). The presence of microfibers illustrated inter-fibril Br-CNF association possibly by hydrogen bonding. Upon uniaxial stretching, the microfibers appeared to align along the loading direction from strain-induced stress stiffening above 200 % (**Figure S3.4**). All microfibers were reoriented along the loading direction at 300 % strain (**Figure 3.7b** and **e**) and returned to original isotropic arrangement (**Figure 3.7a** and **d**) upon unloading. The observed full reversibility for Br-CNF microfibers from isotropic (**Figure 3.7a** and **d**) to oriented alignment (**Figure 3.7b** and **c**) upon uniaxial stretching then back to isotropic (**Figure 3.7a** and **d**) upon returning to zero strain demonstrated apparent elastic behavior at up to 300 % strain, unlike the inelastic stress relaxation observed at 400 % strain (**Figure 3.6**). The film fractured at 539 % strain also showed isotropic fibrils at fracture edge (**Figure 3.7c**), indicative of fully reversibility of PU/CNF film after releasing loading force even in fracture region. The strain induced fiber realignment in PU with Br-CNF as extender (**Figure 3.7f**) was not as clear as that with Br-CNF as polyol, supportive of the polyol role to be more effective in reinforcing PU.

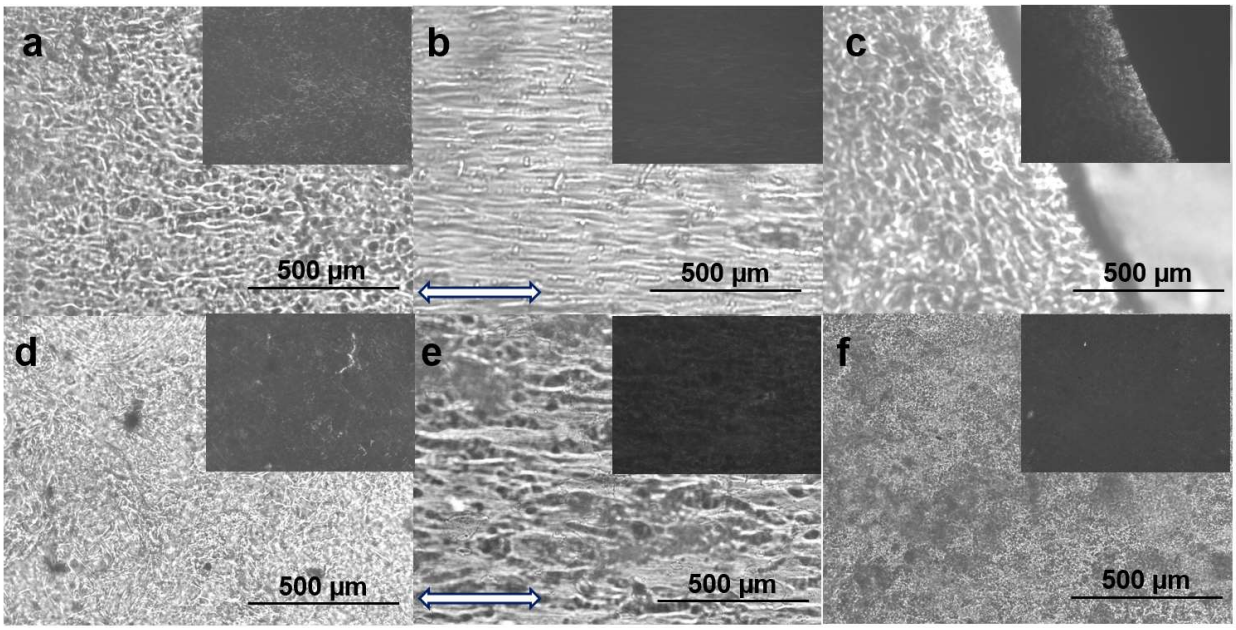

Figure 3.7. Optical microscopy images of PU/CNF films (0.4 mm thickness), with 0.5 w% Br-CNF as polyol: (a) as is, (b) under ca. 300 % strain (direction shown by arrow), (c) fractured edge; with 1.8 w% Br-CNF as chain extender: (d) as is, (e) under ca. 300 % strain (direction shown by arrow); with 5.4 w% Br-CNF as lone extender: (f) as is. Upper right insets were corresponding images under cross-polar.

3.4. Conclusion

This stoichiometrically rationalized study demonstrated for the first time that 2-bromopropionyl bromide esterified cellulose nanofibrils (Br-CNF) facilely synthesized from one-pot esterification of cellulose with 2-bromopropionyl bromide (BPB) and *in situ* ultrasonication can serve the dual role of either chain extender or polyol in the syntheses of polyurethanes. The substituted surface 2-bromopropionyl ester (3.2 mmol/g) endows Br-CNF excellent dispersibility in DMF while the remainig surface OHs (3.5 mmol/g) highly reactive to methylene diphenyl diisocyanate (MDI). Most importantly, the uniquely anisotropic (4.6 nm thick, 29.3 nm wide, ca. 1 µm long) and dual surface functional Br-CNF significantly reduced the MDI content to 15.7 % with the use of longer

PTMEG (M_n:2,900 *Da*) as the soft segment. As polyol, replacing a merely 1.8 mol% of PTMEG OHs with the surface OHs of Br-CNF (0.3 w%) optimally improved the respective elastic modulus, tensile strength, and strain impressively by 3.2, 3.9 and 1.5 times to 8.3 MPa, 21.1 MPa, and 755 %. As chain extender, replacing 11 mol% of 1,4-butanediol OHs with the surface OHs of Br-CNF (1.8 w%) also improved the respective tensile properties to 8.3 MPa, 26.7 MPa, and 883%, in fact 17% higher in strength and 17 % higher in modulus. However, 6 times of Br-CNF were required in the role as chain extender than that of polyol prepolymer. In the role of polyol prepolymer, the 0.3 w% Br-CNF of the PU synthesized is the lowest among reported to date while requiring only half of MDI. The experimental modulus exceeding those predicted by the Halpin-Tsai model gave evidence to the synergistic effectiveness of optimal covalent bonding of Br-CNF with MDI and hydrogen bonding between Br-CNF and PTMEG. Intriguingly, complete reversibility of isotropic Br-CNF under zero strain to oriented microfibril alignment at 300 % strain extends the elastic recovery of PU to beyond the typical yield point. The efficiently synthesized Br-CNF with the unique organic compatibility and reactivity endowed by the respective surface 2-bromopropionyl ester and hydroxyls have enabled rationally designed and stoichiometric synthetic strategy for the synthesis of significantly stronger polyurethane with 50% less diisocyanate. The newly synthesized 2-bromopropionyl esterified Br-CNF offer novel synthetic strategies to not only maximize their reinforcing effect on polyurethane synthesized but also demonstrate potential to broaden the applications of this functionalized nanocellulose to the syntheses of other polymers.

3.5. Supplemental information

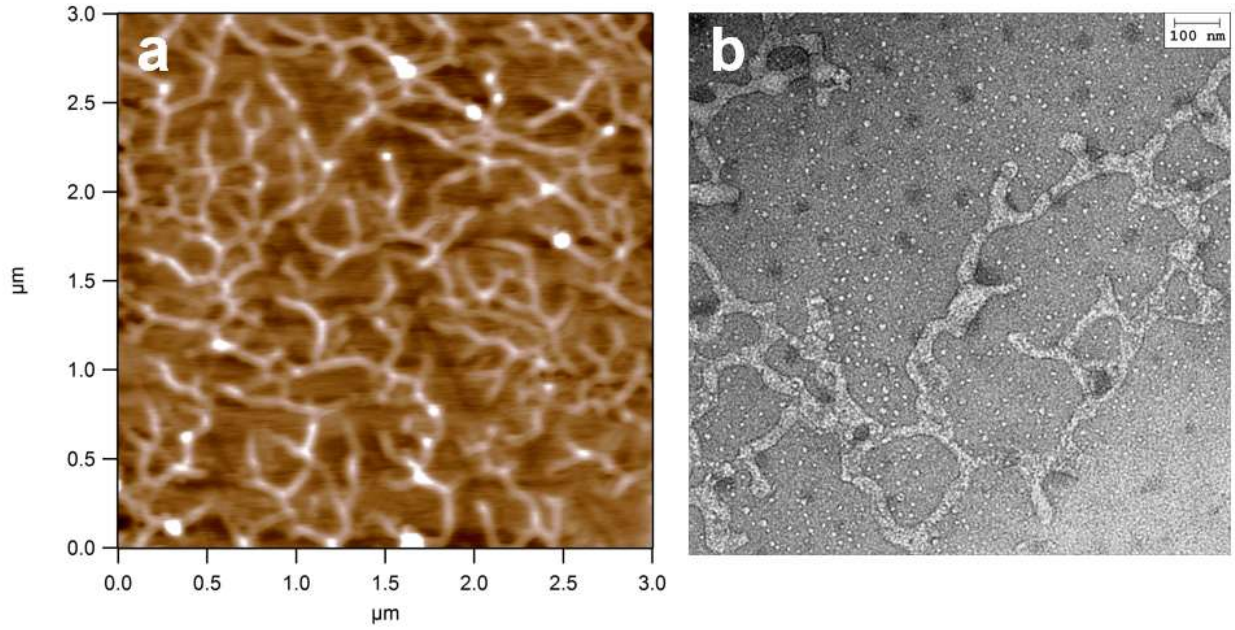

Figure S3.1. CNF Characteristics: (a) AFM height and (b) TEM images of CNFs.

The level of substitution (ρ) of Br-CNF by ^{1}H NMR. For each sample, 40 mL acetone was added to 10 mL Br-CNF dispersion in DMF (0.5 w/v%) and centrifuged (5k rpm, 10 min) to decant the supernatant, then repeated three times to prepare acetone gel. Br-CNF acetone gel (ca. 5 mg) was added into 1 mL DMSO-d_6, sonicated (10 min, Branson 2510) and vacuumed at 50°C for 1 h, then repeated three times to remove residual acetone. Br-CNF in DMSO-d_6 suspension was centrifuged (5k rpm, 10 min) and supernatant was collected for ^{1}H NMR (Bruker AVIII 600 MHz ^{1}H NMR spectrometer) characterization. Trifluoroacetic acid (50 µL) was added to DMSO-d_6 dispersion to shift all OHs peak downfield.

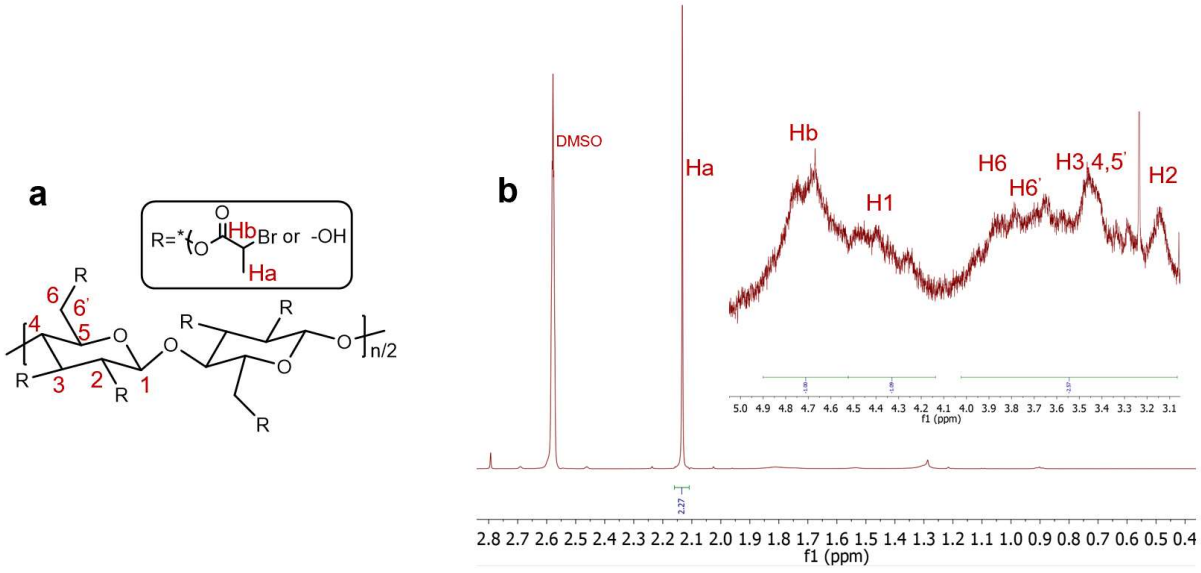

Figure S3.2. Br-CNF: (a) Structure and (b) ^{1}H NMR spectra.

The cellulose anomeric proton was the sum of the integrated areas for all anomeric H1 to H6' proton peaks averaged by 7. Br bearing esters were estimated by integration of the areas of methyl Ha divided by the respective 3 protons. The ratio of esterified C2, C3 and C6 OHs per surface AGU could be determined mathematically by the area ratio of Br ester calculated from Ha over the normalized anomic proton. The level of substitution (ρ), i.e., the fraction of OH substituted by Br bearing ester as determined by proton Ha, was calculated by dividing ratio of esterified OHs per surface AGU by 3, i.e., 3 OH per AGU to be 48 %:

$$\rho = \frac{1}{3} \times \frac{\text{integral of methyl protons (Ha, doublet)}/3}{\sum_{1}^{6'} \text{integral of anomeric protons } (H^{i})\ /7} \qquad (1)$$

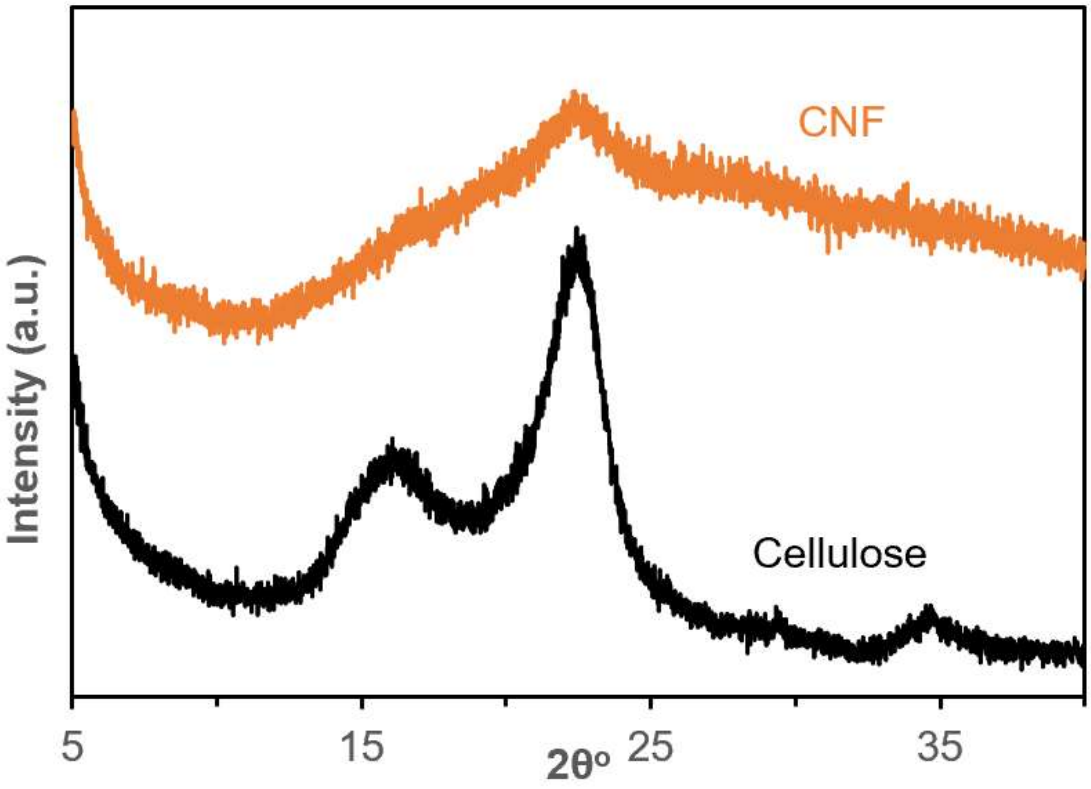

Figure S3.3. X-ray diffractograms of cellulose and Br-CNF.

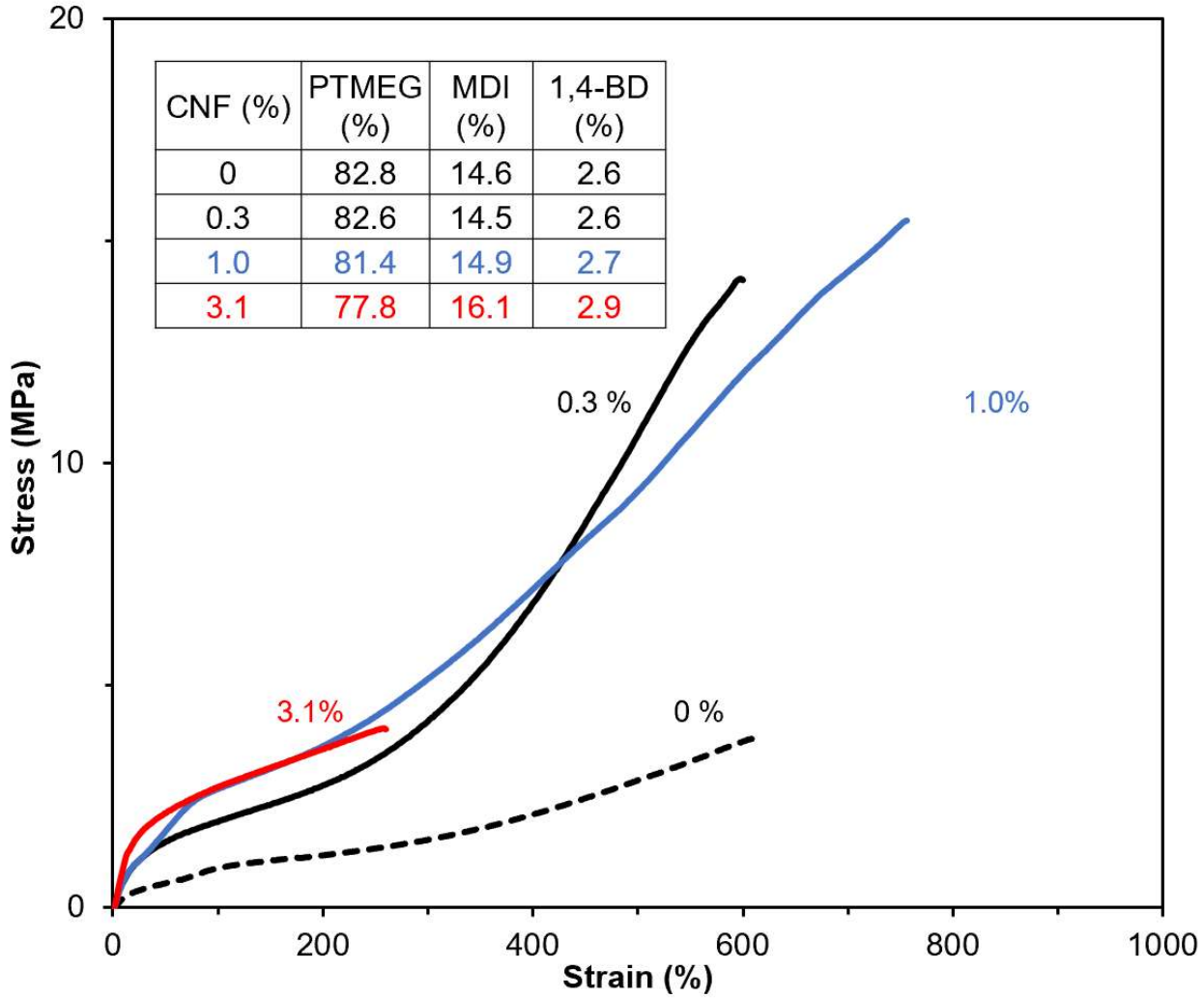

Figure S3.4. Stress-strain curves of PU synthesized with 0, 0.3, 1.0 or 3.1 % Br-CNF polyol with PTMEG (M_n=2,900*Da*) diol in 2:1:1 NCO_{MDI}: $OH_{PTMEG+CNF}$: $OH_{1,4\text{-}BD}$.

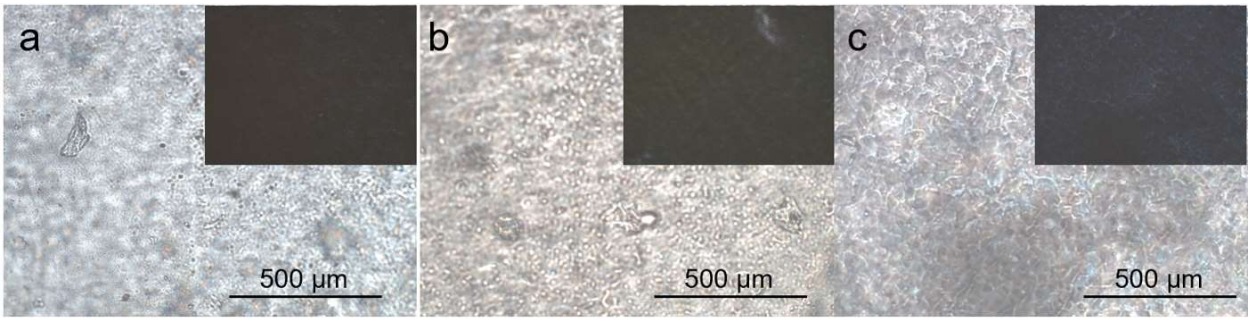

Figure S3.5. Optical microscopy images (10x) of upstretched PU films with (a) 0%, (b) 0.1%, (c) 0.3% Br-CNF as polyol. Insets on upper were corresponding images under cross-polar.

3.6. Reference

1. Zu, G.; Shen, J.; Zou, L.; Wang, F.; Wang, X.; Zhang, Y.; Yao, X., Nanocellulose-derived highly porous carbon aerogels for supercapacitors. *Carbon* **2016,** *99*, 203-211.
2. Iwamoto, S.; Kai, W.; Isogai, A.; Iwata, T., Elastic modulus of single cellulose microfibrils from tunicate measured by atomic force microscopy. *Biomacromolecules* **2009,** *10* (9), 2571-2576.
3. Fukuzumi, H.; Saito, T.; Isogai, A., Influence of TEMPO-oxidized cellulose nanofibril length on film properties. *Carbohydr. Polym.* **2013,** *93* (1), 172-177.
4. Diaz, J. A.; Wu, X.; Martini, A.; Youngblood, J. P.; Moon, R. J., Thermal expansion of self-organized and shear-oriented cellulose nanocrystal films. *Biomacromolecules* **2013,** *14* (8), 2900-2908.
5. Puangsin, B.; Yang, Q.; Saito, T.; Isogai, A., Comparative characterization of TEMPO-oxidized cellulose nanofibril films prepared from non-wood resources. *Int. J. Biol. Macromol.* **2013,** *59*, 208-213.
6. Habibi, Y.; Lucia, L. A.; Rojas, O. J., Cellulose nanocrystals: chemistry, self-assembly, and applications. *Chem. Rev.* **2010,** *110* (6), 3479-3500.
7. Bondeson, D.; Mathew, A.; Oksman, K., Optimization of the isolation of nanocrystals from microcrystalline cellulose by acid hydrolysis. *Cellulose* **2006,** *13* (2), 171.
8. Elazzouzi-Hafraoui, S.; Nishiyama, Y.; Putaux, J.-L.; Heux, L.; Dubreuil, F.; Rochas, C., The shape and size distribution of crystalline nanoparticles prepared by acid hydrolysis of native cellulose. *Biomacromolecules* **2007,** *9* (1), 57-65.
9. Dufresne, A., Nanocellulose: a new ageless bionanomaterial. *Mater Today* **2013,** *16* (6), 220-227.
10. Jiang, F.; Hsieh, Y.-L., Chemically and mechanically isolated nanocellulose and their self-assembled structures. *Carbohydr. Polym.* **2013,** *95* (1), 32-40.
11. Saito, T.; Nishiyama, Y.; Putaux, J.-L.; Vignon, M.; Isogai, A., Homogeneous suspensions of individualized microfibrils from TEMPO-catalyzed oxidation of native cellulose. *Biomacromolecules* **2006,** *7* (6), 1687-1691.
12. Isogai, A.; Saito, T.; Fukuzumi, H., TEMPO-oxidized cellulose nanofibers. *Nanoscale* **2011,** *3* (1), 71-85.
13. Jiang, F.; Han, S.; Hsieh, Y.-L., Controlled defibrillation of rice straw cellulose and self-assembly of cellulose nanofibrils into highly crystalline fibrous materials. *RSC Adv.* **2013,** *3* (30), 12366-12375.
14. Jiang, F.; Hsieh, Y.-L., Self-assembling of TEMPO oxidized cellulose nanofibrils as affected by protonation of surface carboxyls and drying methods. *ACS Sustain. Chem. Eng.* **2016,** *4* (3), 1041-1049.
15. Wang, M. S.; Jiang, F.; Hsieh, Y.-L.; Nitin, N., Cellulose nanofibrils improve dispersibility and stability of silver nanoparticles and induce production of bacterial extracellular polysaccharides. *J Mater Chem B* **2014,** *2* (37), 6226-6235.
16. Li, J.; Wei, X.; Wang, Q.; Chen, J.; Chang, G.; Kong, L.; Su, J.; Liu, Y., Homogeneous isolation of nanocellulose from sugarcane bagasse by high pressure homogenization. *Carbohydr. Polym.* **2012,** *90* (4), 1609-1613.
17. Pääkkö, M.; Ankerfors, M.; Kosonen, H.; Nykänen, A.; Ahola, S.; Österberg, M.; Ruokolainen, J.; Laine, J.; Larsson, P. T.; Ikkala, O., Enzymatic hydrolysis combined with mechanical shearing and high-pressure homogenization for nanoscale cellulose fibrils and strong gels. *Biomacromolecules* **2007,** *8* (6), 1934-1941.

18. Wågberg, L.; Decher, G.; Norgren, M.; Lindström, T.; Ankerfors, M.; Axnäs, K., The build-up of polyelectrolyte multilayers of microfibrillated cellulose and cationic polyelectrolytes. *Langmuir* **2008,** *24* (3), 784-795.
19. Aulin, C.; Johansson, E.; Wågberg, L.; Lindström, T., Self-organized films from cellulose I nanofibrils using the layer-by-layer technique. *Biomacromolecules* **2010,** *11* (4), 872-882.
20. Saito, T.; Isogai, A., TEMPO-mediated oxidation of native cellulose. The effect of oxidation conditions on chemical and crystal structures of the water-insoluble fractions. *Biomacromolecules* **2004,** *5* (5), 1983-1989.
21. Cao, X.; Dong, H.; Li, C. M., New nanocomposite materials reinforced with flax cellulose nanocrystals in waterborne polyurethane. *Biomacromolecules* **2007,** *8* (3), 899-904.
22. Santamaria-Echart, A.; Ugarte, L.; García-Astrain, C.; Arbelaiz, A.; Corcuera, M. A.; Eceiza, A., Cellulose nanocrystals reinforced environmentally-friendly waterborne polyurethane nanocomposites. *Carbohydr. Polym.* **2016,** *151*, 1203-1209.
23. Pursula, P.; Kiri, K.; Mc Caffrey, C.; Sandberg, H.; Vartiainen, J.; Flak, J.; Lahtinen, P., Nanocellulose–polyurethane substrate material with tunable mechanical properties for wearable electronics. *Flexible Printed Electron.* **2018,** *3* (4), 045002.
24. Lossada, F.; Jiao, D.; Guo, J.; Hoenders, D.; Eckert, A.; Walther, A., Outstanding Synergies in Mechanical Properties of Bioinspired Cellulose Nanofibril Nanocomposites using Self-Cross-Linking Polyurethanes. *ACS Appl. Polym. Mater.* **2019,** *1* (12), 3334-3342.
25. Wen, J.-G.; Geng, W.; Geng, H.-Z.; Zhao, H.; Jing, L.-C.; Yuan, X.-T.; Tian, Y.; Wang, T.; Ning, Y.-J.; Wu, L., Improvement of corrosion resistance of waterborne polyurethane coatings by covalent and noncovalent grafted graphene oxide nanosheets. *ACS Omega* **2019,** *4* (23), 20265-20274.
26. Wang, L.; Shen, Y.; Lai, X.; Li, Z.; Liu, M., Synthesis and properties of crosslinked waterborne polyurethane. *J. Polym. Res.* **2011,** *18* (3), 469-476.
27. Auad, M. L.; Contos, V. S.; Nutt, S.; Aranguren, M. I.; Marcovich, N. E., Characterization of nanocellulose-reinforced shape memory polyurethanes. *Polym. Int.* **2008,** *57* (4), 651-659.
28. Rueda, L.; Saralegui, A.; d'Arlas, B. F.; Zhou, Q.; Berglund, L. A.; Corcuera, M.; Mondragon, I.; Eceiza, A., Cellulose nanocrystals/polyurethane nanocomposites. Study from the viewpoint of microphase separated structure. *Carbohydr. Polym.* **2013,** *92* (1), 751-757.
29. Wu, Q.; Henriksson, M.; Liu, X.; Berglund, L. A., A high strength nanocomposite based on microcrystalline cellulose and polyurethane. *Biomacromolecules* **2007,** *8* (12), 3687-3692.
30. Yao, X.; Qi, X.; He, Y.; Tan, D.; Chen, F.; Fu, Q., Simultaneous reinforcing and toughening of polyurethane via grafting on the surface of microfibrillated cellulose. *ACS Appl. Mater. Interfaces* **2014,** *6* (4), 2497-2507.
31. Amin, K. N. M.; Amiralian, N.; Annamalai, P. K.; Edwards, G.; Chaleat, C.; Martin, D. J., Scalable processing of thermoplastic polyurethane nanocomposites toughened with nanocellulose. *Chem. Eng. J.* **2016,** *302*, 406-416.
32. Pei, A.; Malho, J.-M.; Ruokolainen, J.; Zhou, Q.; Berglund, L. A., Strong nanocomposite reinforcement effects in polyurethane elastomer with low volume fraction of cellulose nanocrystals. *Macromolecules* **2011,** *44* (11), 4422-4427.
33. Ivdre, A.; Mucci, V.; Stefani, P.; Aranguren, M.; Cabulis, U. Nanocellulose reinforced polyurethane obtained from hydroxylated soybean oil, *IOP Conf. Ser.: Mater. Sci. Eng.*, **2016**, vol. 111, no. 1, p. 012011.

34. Lee, M.; Heo, M. H.; Lee, H.-H.; Kim, Y.-W.; Shin, J., Tunable softening and toughening of individualized cellulose nanofibers-polyurethane urea elastomer composites. *Carbohydr. Polym.* **2017,** *159*, 125-135.
35. Szymańska-Chargot, M.; Cieśla, J.; Chylińska, M.; Gdula, K.; Pieczywek, P. M.; Kozioł, A.; Cieślak, K. J.; Zdunek, A., Effect of ultrasonication on physicochemical properties of apple based nanocellulose-calcium carbonate composites. *Cellulose* **2018,** *25* (8), 4603-4621.
36. Morandi, G.; Heath, L.; Thielemans, W. J. L., Cellulose nanocrystals grafted with polystyrene chains through surface-initiated atom transfer radical polymerization (SI-ATRP). *Langmuir* **2009,** *25* (14), 8280-8286.
37. Zhang, X.; Zhang, J.; Dong, L.; Ren, S.; Wu, Q.; Lei, T., Thermoresponsive poly (poly (ethylene glycol) methylacrylate) s grafted cellulose nanocrystals through SI-ATRP polymerization. *Cellulose* **2017,** *24* (10), 4189-4203.
38. Zhang, J.; Wu, Q.; Li, M.-C.; Song, K.; Sun, X.; Lee, S.-Y.; Lei, T., Thermoresponsive copolymer poly (N-vinylcaprolactam) grafted cellulose nanocrystals: synthesis, structure, and properties. *ACS Sustain. Chem. Eng.* **2017,** *5* (8), 7439-7447.
39. Yuan, W.; Wang, C.; Lei, S.; Chen, J.; Lei, S.; Li, Z., Ultraviolet light-, temperature-and pH-responsive fluorescent sensors based on cellulose nanocrystals. *Polym. Chem.* **2018,** *9* (22), 3098-3107.
40. Zhou, L.; He, H.; Li, M.-C.; Huang, S.; Mei, C.; Wu, Q., Grafting polycaprolactone diol onto cellulose nanocrystals via click chemistry: Enhancing thermal stability and hydrophobic property. *Carbohydr. Polym.* **2018,** *189*, 331-341.
41. Zhang, Z.; Wang, X.; Tam, K. C.; Sebe, G., A comparative study on grafting polymers from cellulose nanocrystals via surface-initiated atom transfer radical polymerization (ATRP) and activator re-generated by electron transfer ATRP. *Carbohydr. Polym.* **2019,** *205*, 322-329.
42. Morits, M.; Hynninen, V.; Niederberger, A.; Ikkala, O.; Gröschel, A. H.; Müllner, M., Polymer brush guided templating on well-defined rod-like cellulose nanocrystals. *Polym. Chem.* **2018,** *9* (13), 1650-1657.
43. Zhang, Z.; Sèbe, G.; Wang, X.; Tam, K. C., Gold nanoparticles stabilized by poly (4-vinylpyridine) grafted cellulose nanocrystals as efficient and recyclable catalysts. *Carbohydr. Polym.* **2018,** *182*, 61-68.
44. Le Gars, M.; Bras, J.; Salmi-Mani, H.; Ji, M.; Dragoe, D.; Faraj, H.; Domenek, S.; Belgacem, N.; Roger, P., Polymerization of glycidyl methacrylate from the surface of cellulose nanocrystals for the elaboration of PLA-based nanocomposites. *Carbohydr. Polym.* **2020,** *234*, 115899.
45. Rosilo, H.; McKee, J. R.; Kontturi, E.; Koho, T.; Hytönen, V. P.; Ikkala, O.; Kostiainen, M. A., Cationic polymer brush-modified cellulose nanocrystals for high-affinity virus binding. *Nanoscale* **2014,** *6* (20), 11871-11881.
46. Zhang, Z.; Tam, K. C.; Sèbe, G.; Wang, X., Convenient characterization of polymers grafted on cellulose nanocrystals via SI-ATRP without chain cleavage. *Carbohydr. Polym.* **2018,** *199*, 603-609.
47. Zhang, Z.; Sèbe, G.; Wang, X.; Tam, K. C., UV-absorbing cellulose nanocrystals as functional reinforcing fillers in poly (vinyl chloride) films. *ACS Appl. Nano Mater.* **2018,** *1* (2), 632-641.
48. Majoinen, J.; Walther, A.; McKee, J. R.; Kontturi, E.; Aseyev, V.; Malho, J. M.; Ruokolainen, J.; Ikkala, O., Polyelectrolyte brushes grafted from cellulose nanocrystals using Cu-mediated surface-initiated controlled radical polymerization. *Biomacromolecules* **2011,** *12* (8), 2997-3006.

49. Wang, Z.; Zhang, Y.; Yuan, L.; Hayat, J.; Trenor, N. M.; Lamm, M. E.; Vlaminck, L.; Billiet, S.; Du Prez, F. E.; Wang, Z., Biomass approach toward robust, sustainable, multiple-shape-memory materials. *ACS Macro Lett.* **2016,** *5* (5), 602-606.
50. Hatton, F. L.; Kedzior, S. A.; Cranston, E. D.; Carlmark, A., Grafting-from cellulose nanocrystals via photoinduced Cu-mediated reversible-deactivation radical polymerization. *Carbohydr. Polym.* **2017,** *157*, 1033-1040.
51. Wang, H. D.; Roeder, R. D.; Whitney, R. A.; Champagne, P.; Cunningham, M. F., Graft modification of crystalline nanocellulose by Cu (0)-mediated SET living radical polymerization. *J Polym Sci A Polym Chem.* **2015,** *53* (24), 2800-2808.
52. Abousalman-Rezvani, Z.; Eskandari, P.; Roghani-Mamaqani, H.; Mardani, H.; Salami-Kalajahi, M., Grafting light-, temperature, and CO2-responsive copolymers from cellulose nanocrystals by atom transfer radical polymerization for adsorption of nitrate ions. *Polymer* **2019,** *182*, 121830.
53. Yu, J.; Wang, C.; Wang, J.; Chu, F., In situ development of self-reinforced cellulose nanocrystals based thermoplastic elastomers by atom transfer radical polymerization. *Carbohydr. Polym.* **2016,** *141*, 143-150.
54. Morandi, G.; Heath, L.; Thielemans, W., Cellulose nanocrystals grafted with polystyrene chains through surface-initiated atom transfer radical polymerization (SI-ATRP). *Langmuir* **2009,** *25* (14), 8280-8286.
55. Risteen, B.; McBride, M.; Gonzalez, M.; Khau, B.; Zhang, G.; Reichmanis, E., Functionalized cellulose nanocrystal-mediated conjugated polymer aggregation. *ACS Appl. Mater. Interfaces* **2019,** *11* (28), 25338-25350.
56. Morandi, G.; Thielemans, W., Synthesis of cellulose nanocrystals bearing photocleavable grafts by ATRP. *Polym. Chem.* **2012,** *3* (6), 1402-1407.
57. Boujemaoui, A.; Mongkhontreerat, S.; Malmström, E.; Carlmark, A., Preparation and characterization of functionalized cellulose nanocrystals. *Carbohydr. Polym.* **2015,** *115*, 457-464.
58. Kedzior, S. A.; Kiriakou, M.; Niinivaara, E.; Dube, M. A.; Fraschini, C.; Berry, R. M.; Cranston, E. D., Incorporating cellulose nanocrystals into the core of polymer latex particles via polymer grafting. *ACS Macro Lett.* **2018,** *7* (8), 990-996.
59. Kiriakou, M. V.; Berry, R. M.; Hoare, T.; Cranston, E. D., Effect of Reaction Media on Grafting Hydrophobic Polymers from Cellulose Nanocrystals via Surface-Initiated Atom-Transfer Radical Polymerization. *Biomacromolecules* **2021,** *22* (8), 3601-3612.
60. Huang, C.-F.; Chen, J.-K.; Tsai, T.-Y.; Hsieh, Y.-A.; Lin, K.-Y. A., Dual-functionalized cellulose nanofibrils prepared through TEMPO-mediated oxidation and surface-initiated ATRP. *Polymer* **2015,** *72*, 395-405.
61. Morits, M.; McKee, J. R.; Majoinen, J.; Malho, J.-M.; Houbenov, N.; Seitsonen, J.; Laine, J.; Gröschel, A. H.; Ikkala, O., Polymer brushes on cellulose nanofibers: Modification, SI-ATRP, and unexpected degradation processes. *ACS Sustain. Chem. Eng.* **2017,** *5* (9), 7642-7650.
62. Navarro, J. R.; Edlund, U., Surface-initiated controlled radical polymerization approach to enhance nanocomposite integration of cellulose nanofibrils. *Biomacromolecules* **2017,** *18* (6), 1947-1955.
63. Guo, M.; Hsieh, Y.-L., One-pot synthesis of 2-bromopropionyl esterified cellulose nanofibrils as hydrophobic coating and film. *RSC Adv.* **2022,** *12* (24), 15070-15082.
64. Kupczewska-Dobecka, M.; Czerczak, S.; Brzeźnicki, S., Assessment of exposure to TDI and MDI during polyurethane foam production in Poland using integrated theoretical and experimental data. *Environ. Toxicol. Pharmacol.* **2012,** *34* (2), 512-518.

65. Lu, P.; Hsieh, Y.-L., Preparation and characterization of cellulose nanocrystals from rice straw. *Carbohydr. Polym.* **2012,** *87* (1), 564-573.
66. Fukuda, J.; Hsieh, Y.-L., Hydrophobic 2, 7-Octadienyl Ether-Cellulose Nanofibrils Using Butadiene Sulfone as the Dual Reagent and Medium. *ACS Sustain. Chem. Eng.* **2021,** *9* (18), 6489-6498.
67. Halpin, J.; Kardos, J., Moduli of crystalline polymers employing composite theory. J. Appl. Phys. **1972,** *43* (5), 2235-2241.
68. Van Es, M.; Xiqiao, F.; Van Turnhout, J.; Van der Giessen, E.; Al-Malaika, S.; Golovoy, A., Specialty polymer additives: principles and applications. *Malden, MA: Blackwell Science* **2001**.

Chapter 4. Surface-initiated Atom Transfer Radical Polymerization of Poly(lauryl methacrylate) on 2-Bromopropionyl Esterified Cellulose Nanofibrils as Rheology Modifier in Organic Media (Submission Ongoing)

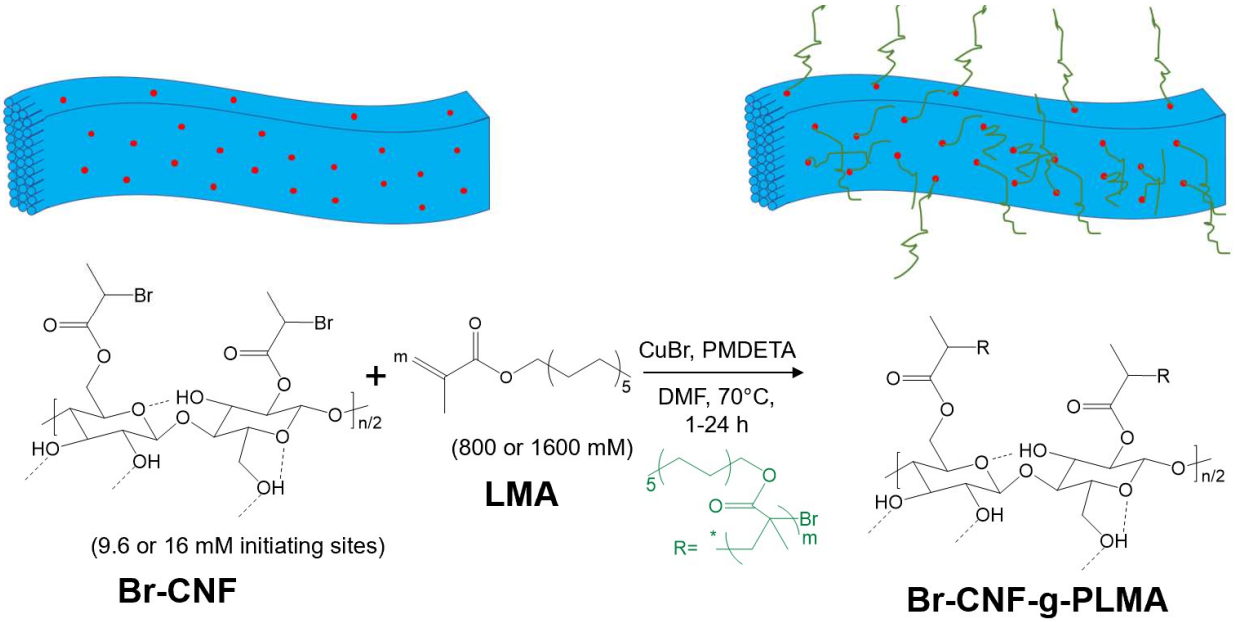

Abstract

2-Bromoproponyl esterified CNF (Br-CNF) was grafted by lauryl methacrylate (LMA) via surface-initiated atom transfer radical polymerization (SI-ATRP), for preparation of Br-CNF-g-PLMA as organic compatible and shear-thinning viscosity modifier. Polymerization of LMA brushes on Br-CNF followed the first order kinetics up to a chain length of ca. 46 repeating units. Also, lower than 37% of chain length of all graft copolymers were estimated from solution state ^{1}H NMR. Extremely high 92.7% monomer conversion was achieved at 16 mM initiator concentration, 800 mM monomer concentration, and 24 h in absence of sacrificing initiators. The hydrophobic PLMA grafts increased the WCAs of films from 69.8° to 110.6° and decreased moisture content from 9.9 % to 1.6 %. This novel Br-CNF-g-PLMA exhibited combined shear thinning behavior of Br-CNF proved by flow behavior index n< 1 and drag reducing effects of

PLMA with up to 21071x increased viscosity. Especially, Br-CNF-g-PLMA with longest side chain (DP=46) could be fully dispersed in silicon pump oil to behave as drag reducer to enhance viscosity up to 5x at varied temperatures of 25, 40 and 55 °C. This study validated the role of Br-CNF as a novel macroinitiator directly used in control radical polymerization.

4.1. Introduction

Cellulose is the most abundant natural polymer on earth with renewable annual production of 75 to 100 billion tons.[1] Nanocellulose, cellulose nanocrystals (CNC) and cellulose nanofibrils (CNF) can be produced by many top-to-down methods, such as non-crystalline region removal by acid hydrolysis[2-6], modification by oxidation[6-12], disintegration by mechanical forces[6-11, 13-16], or a combination of the latter two[7-11]. Hydrophilic nature of these nanocelluloses with surface anionic charges[2-12] or exposed hydrophilic planes[13-16] limit their applications in most synthetic polymer matrixes. Thus, chemical modifications for hydrophobic nanocelluloses[17] involved esterification, silanation, amidation, and polymer grafting. Polymer grafted by well-defined brushes is one of most applicable techniques due to controllable tuning of material compatibility and functionality for broad applications.

A variety of grafting methods including ring opening polymerization (ROP)[18-20], reversible-deactivation radical polymerization (RDRP)[21, 22], and cerium free radical graft polymerization[23-26] have been used to graft polymer brushes on CNCs[20, 21, 24, 26] or CNFs[18, 19, 22, 23, 25]. Atom transfer radical polymerization (ATRP) [27-50] is still the most widely used surface grafting techniques due to the simple initiator immobilization, precise molecular weight control, and wide range of solvent systems.[51] Surface initiated (SI)-ATRP has been applied to graft controllable lengths of functional polymer brushes on CNCs[27-46] or CNFs[47-50] to produce stimuli-responsive materials[27-31], polymer fillers[32-39, 45, 47], gold nanoparticle stabilizers[40], binders for ionic[41, 42] or organic[48] pollutants, hard

domain in thermoplastic polybutyl acrylate elastomer[43], or for kinetics studies[44, 46, 49, 50] (**Table 1**). To enable surface grafting by ATRP, these nanocelluloses were either freeze-dried[27, 28, 31-45, 50] or solvent exchanged[29, 46, 48] to DMF[27-29, 31, 35, 38-46, 50], DMSO[36], toluene[32, 37] or anisole[33, 34, 48] to react with 2-bromoisobutyryl bromide (2-BIB)[27-29, 31-46, 48, 50] to generate surface initiators. Of those where the extent of OHs converted to Br esters were determined as low as 1.4[36], 3.5[37], 7.44[44] and 9.5[34] Br w% by elementary analysis, or 26 %[29] and 43 %[50] converted OHs by NMR, which limited grafting density of Br bearing esters on those already existing nanocelluloses.

The monomer conversion for SI-ATRP on CNC with macroinitiators from 2-BIB was also less than 35 %[27, 36, 38]. One possible reason for low conversion was the less accessibility of immobilized Br initiators on nanocelluloses surfaces compared to free initiators. Thus, additional initiators, such as ethyl 2-bromoisobutyrate (EBIB)[31, 32, 34, 35, 37, 39-41, 43, 44, 46] or 2-hydroxyethyl 2-bromoisobutyrate (HEBIB)[48, 49], were included with macroinitiators to significant increase conversion up to 85 %[39] for CNC-Br and 70 %[48] for CNF-Br, both with narrow polydispersity index (PDI) up to 1.4[39] and 1.17[48] determined by gel permeation chromatography (GPC). Addition of sacrificial initiator was also used to gather chain length information and distribution without cleaving polymer chains from the macroinitiator surface under the assumptions of equal accessibility and reactivity for both sacrificial and immobilized initiators. The few ATRP surface grafting on CNFs[47-50] included those by TEMPO-oxidized,[48] enzymatically pretreated,[47] and film from vacuum filtration from TEMPO-oxidized CNF[49] is even more scarce. Polystyrene chains has been grafted on TEMPO-oxidized CNF at 70% conversion as organic pollutant absorbent improved absorbance (t = 2 h) of 1,2,4-trichlorobenzene from 70 to 91 w% compared to pure CNF.[48] However, a low conversion of 50% was reached when grafting polystyrene on TEMPO-oxidized CNF film via vacuum filtration with moderately increase of WCA from 67.6 to 92.8°.[49] Enzymatic pretreated CNF was grafted with

poly(stearyl acrylate) followed by sequential extrusion and melt-press process for enhanced water contact angle (WCA) from 43 to 107° with up to 80% monomer conversion.[47]

Table 4.1. SI-ATRPs on nanocelluloses based on reaction with 2-bromoisobutyryl bromide (2-BIB)[27-29, 31-46, 48-50], 2-bromopropionic acid[30], and 2-bromo-2-methylpropionic acid[47].

Nanoellulose[a]	Pretreatment	Solvent	Monomer	rafting Densit	DP	onversion (%	Sacrifier Initiator	PDI
CNC (SH)[27]	freeze-drying	DMF	ethylene glycol methacrylate	-	-	16.4	-	-
CNC (SH)[28]	freeze-drying	DMF	azoC6MA-co-DMAEMA	-	-	-	-	-
CNC (SH)[29]	solvent echange to DMF	DMF	N-vinylcaprolactam	26% Br/OHs	-	-	-	-
CNC (SH)[30]	NA	anisole	styrene, NIPAM	-	-	-	-	-
CNC (SH)[31]	freeze-drying	DMF	glycidyl methacrylate	-	-	85	EBIB	up to 1.4
CNC (HH)[32]	freeze-drying	toluene	butyl acylate	-	110,486	70	EBIB	1.09
CNC (SH)[33]	freeze-drying	anisole	styrene	-	-	-	-	-
CNC (SH)[34]	freeze-drying	anisole	styrene	9.5 Br %	up to 173	40	EBIB	1.1
CNC (SH)[35]	freeze-drying	DMF	styrene	-	up to 160	26.5	EBIB	1.05-1.15
CNC (SH)[36]	freeze-drying	DMSO	methyl acylate	1.4 Br %	-	30.3	-	1.46-2.06
CNC (SH)[37]	freeze-drying	toluene	methyl methacylate	3.5 Br %	-	-	EBIB	1.1,1.2
CNC (unknow)[38]	freeze-drying	DMF	cinnamoyloxy ethyl methacrylate	-	-	35	-	-
CNC (SH)[39]	freeze-drying	DMF	4-vinylpyridine	-	-	23.1	EBIB	-
CNC (SH)[40]	freeze-drying	DMF	DMAEMA	-	-	35	EBIB	up to 1.6
CNC (SH)[41]	freeze-drying	DMF	DMAEMA	-	13-26	-	-	-
CNC (SH)[42]	freeze-drying	DMF	methyl methacylate	-	-	61.4	EBIB	-
CNC (SH)[43]	freeze-drying	DMF	butyl acylate	7.44 Br %	47-101	-	EBIB	1.18,1.21
CNC (SH)[44]	freeze-drying	DMF	t-butyl acylate	-	-	36	EBIB	less than 1.1
CNC (SH)[45]	freeze-drying	DMF	DMAEMA	-	-	-	-	-
CNC (SH)[46]	solvent exchange to DMF	DMF	styrene	-	-	25	EBIB	1.09-1.19
CNF (enzymatic)[47]	solvent exchange to DMSO	)MSO/toluen	stearyl acrylate	-	-	80	2-ethyl-bromo-2-methylpropi	1.06
CNF(TEMPO)[48]	solvent exchange to DMF	anisole	styrene	-	135-278	70	HEBIB	1.09-1.17
CNF (TEMPO) membrane[49]	casting film	toluene	styrene	-	150	50	HEBIB	1.06
CNF(homogenized)[50]	freeze-drying	DMF	butyl acylate	43 % Br/OHs	up to 800	11.8	EBIB	-

[a] "SH" for sulfuric acid hydrolysis; "HH" for hydrochloric acid hydrolysis; "DMAEMA" for dimethylaminoethyl acrylate; "NIPAM" for N-isopropylacrylamide; "EBIB" for ethyl 2-bromoisobutyrate; "HEBIB" for 2-hydroxyethyl 2-bromoisobutyrate.

Recently, a novel Br-CNF (T = 4.7 nm, W = 29.3 nm width, L = ca. 1 um) was successfully defibrillated from the chemical stable 2-bromopropionyl esterified cellulose by direct ultrasonication.[52] Those Br bearing high crystalline CNFs compatible to DMF and have potential to be utilized as reinforcement or rigid backbone for polymer grafting. Specially, Br-CNFs with surface available OHs have been successfully demonstrated as reactive polyol for prepolymer synthesis to synthesize thermoplastic polyurethane (PU) whose cast films exhibited significantly improved' modulus (3.2x) and strength (3.9x) and strain-to-failure (1.5x). Unlike all above macro-initiators prepared via modification of already existing NCs,[27-50] these novel Br-CNFs with surface alkyl bromines are potential macroinitiators for direct ATRPs.

For fluid transportation, drag reducing agent could increase viscosity to turn more energy consumable turbulent flow to laminar flow without reducing speed of transporting. Poly(lauryl methacrylate) (PLMA) homopolymer, as one oil-soluble drag reducer, has been added in kerosene at 0.06 w % to reduce drag by 68 %[53]. To broad its drag reducing effects in paints or ink-printing applications, thixotropy behavior should be introduced by copolymerizing with rigid backbones already showing shear-thinning behavior. Although the thixotropy behavior of grafted CNF in organic media has not been investigated yet, shear thinning rheological behavior of mechanical treated[54], TEMPO[55, 56] or periodate[57] oxidized CNFs in aqueous dispersion expanded applications in coating[57], thickening[54], and 3D printing/bioprinting[55, 56] Thus, Br-CNF is considered as one potential candidate to be grafted with PLMA for preparation of bottle brush-like Br-CNF-g-PLMA drag reducer with shear-thinning behavior via SI-ATRP.

Br-CNF is a potential already existing macroinitiator which could be used for direct grafting without immobilization of initiators as before. SI-ATRP of LMA is proposed to graft on those DMF dispersible high surface area Br-CNF with copper bromide (CuBr) as catalyst (**Scheme 1**). N,N,N',N',N"-pentamethyldiethylenetriamine (PMDETA) is selected as the amine ligand to yield the more stable copper(I) to mediated ATRP polymerization as compared to the aliphatic amine ligand like 2,2'-bipyridine.[58] Conversion of LMA and DP of PLMA were studied by sequentially varying macroinitiator concentration ([I] =9.6 or 16 mM) and LMA monomer concentration ([M]=800 or 1600 mM) at variety of reaction times (1-24 h). The structures of Br-CNF-g-PLMA were characterized by attenuated total reflection (ATR) and solution phase proton nuclear magnetic resonance (^{1}H NMR) spectroscopy. Thermal properties were characterized by thermogravimetric analysis (TGA). Surface hydrophobicity and morphology of Br-CNF-g-PLMA copolymer were characterized by WCA measurements and atom force microscopy (AFM). Br-CNF-g-PLMA with varied DPs were further investigated as rheology modifier in toluene or drag reducer in pump oil. The rheology of toluene and pump oil dispersed Br-CNF-g-PLMA was characterized by viscometer under varied shear rates and temperatures.

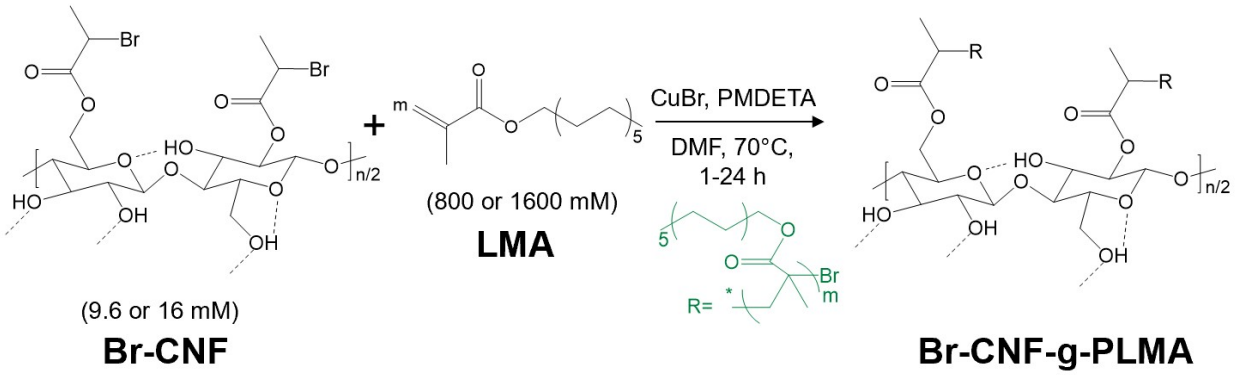

Scheme 4.1. Reaction scheme for SI-ATRP of LMA on Br-CNF to Br-CNF-g-PLMA.

4.2. Experimental

4.2.1. Materials. Cellulose was isolated from rice straw (Calrose variety) by a previously reported three-step 2:1 v/v toluene/ethanol extraction, acidified NaClO2 (1.4%, pH 3-4, 70 °C, 5 h) delignification, alkaline hemicellulose dissolution (5% KOH, 90 °C, 2 h) process and lyophilized (Labconco Lyophilizer).[59] 0.5 w/v % Br-CNF in DMF dispersion was prepared by reported combined esterification and ultrasonication with surface still available Br esters estimated to be 5.7 mmol/g cellulose[52] equivalent to 3.2 mmol/g Br-CNF. Cuprous bromide (CuBr, Spectrum Chemical), N,N,N′,N′′,N′′-pentamethyldiethylenetriamine (PMDETA, 99%, TCI), N,N-dimethylformamide (DMF, certified grade, Fisher Scientific), toluene (ACS grade, Spectrum Chemical), methanol (ACS grade, Sigma Aldrich), tetrahydrofuran (THF, ACS grade, Alfa Aesar), and vacuum pump oil (Welch® DuoSeal®) were used as received without further purification. Lauryl methacrylate (LMA, 97%, TCI) was flushed by 5 M sodium hydroxide solution to remove inhibitor then dried by molecule sieves overnight. Highly oriented pyrolytic graphite (HOPG, grade ZYB) was used for AFM characterization. For UV−vis spectrophotometry, 1 mm UV-vis standard cell quartz cuvettes (Fisher Scientific) were used.

4.2.2. SI-ATRP from Br-CNF with LMA. A total volume of 25 mL 0.3 (0.24 mmol Br) w/v% Br-CNF DMF dispersion was prepared at initiator concentration [I] of 9.6 mM. Catalyst CuBr (0.034 g, 0.24 mmol) was dissolved in Br-CNF DMF dispersion (0.24 mmol Br) in Schlenk flask under constant stirring. After 5 min degassing by sonication, the mixture was purged by nitrogen for 10 min then capped with a rubber septum. Complexing ligand PMDETA (50.1 μL, 0.24 mmol) was dissolved in monomer LMA (5.1 g, 20.0 mmol) and sonicated (1 min, Branson 2510). The LMA/PMDETA mixture was injected through a syringe into flask under 70°C oil bath ([M]o=800 mM) to initiated polymerization and terminated by adding 5 mL THF after 1, 3, 4.5, 6 or 24 h.

Final mixture was washed by cold methanol and centrifugated (Eppendorf 5804R, 5k rpm, 10 min) to decant supernatant. The methanol washing and centrifugation process was repeated three times to remove all catalyst and unreacted monomer. Final precipitate was dried under vacuum (0.5 atm) in oven (50 °C) overnight to obtain pure Br-CNF-g-PLMA in the form of an elastic gel. The [I] and [M]o were sequentially increased to 16 mM and 1600 mM, respectively, with catalyst and complexing ligand set to be equal to initiator concentrations [I] to be polymerized up to 24 h (**Table 4.1**).

The conversion (%) of LMA to PLMA was determined by percentage of PLMA mass gain on Br-CNF-g-PLMA over initial LMA mass. The degree of polymerization (DP) pf PLMA was determined by mass gain assuming unity polydispersity or equal chain lengths of PLMA as follows

$$\mathrm{DP} = \frac{m_2 - m_1}{0.2544 \times \sigma m_1} \tag{4.1}$$

Where m_1 is Br-CNF mass (g), m_2 is Br-CNF-g-PLMA mass (g), 0.2544 (g/mmol) is the molecular mass of LMA, and σ is the quantity of Br ester on Br-CNF macroinitiator or 3.2 mmol/g[52] prepared by combined tunable cellulose esterification and ultrasonication.

4.2.3. Characterization. Br-CNF-g-PLMA in toluene dispersions (1w/v%) were scanned by UV-vis spectroscopy (Thermo Scientific, Evolution 600) from 325 to 800 cm^{-1} at 4 cm^{-1}/s. A small volume (ca. 1 mL) Br-CNF-g-PLMA (1 w/v%) in toluene dispersions were deposited on clean glass slide and dried overnight in fume hood to prepare thin film for water contact angles (WCAs) measurements. WCAs of sessile drops Milli-Q water (5 μL) on Br-CNF-g-PLMA film were measured using the ImageJ Analyzer and the average values were calculated from both sides of a sessile drop reported in total of 5 images for each (n=5).

Br-CNFs (10 µL, 0.0005 w/v %) in DMF dispersion and Br-CNF-g-PLMA (10 µL, 0.0005 w/v %) in toluene dispersions were deposited on highly oriented pyrophoric graphite (HOPG), then air-dried in fume hood for 6 h and profiled by AFM (Asylum-Research MFP-3D) in the tapping mode with scan size and rate set to 5µm × 5µm and 512 Hz. For solution-state ^{1}H NMR sample preparation, Br-CNF-g-PLMA (0.01 g) gel was dispersed directly in DMSO-d_6 (1 mL) aided by sonication (Branson 2510, 10 min). Pure Br-CNF in DMSO-d_6 was prepared as reported by three times repeating solvent exchange to acetone and DMSO-d_6 followed by 1 h vacuum evaporation (0.5 atm) at 50 °C as reported.[52]

Oven-dried (56°C, overnight) Br-CNF-g-PLMA elastic gel was used for proton nuclear magnetic resonance (^{1}H NMR), attenuated total reflectance (ATR), and thermogravimetric analysis (TGA) characterizations without any further purification. For ^{1}H NMR, Br-CNF-g-PLMA (ca. 10 mg) was added into 1 mL DMSO-d_6 followed by 1 h sonication (Branson 2510). After centrifugation (5k rpm, 10 min), Br-CNF-g-PLMA in DMSO-d_6 supernatant was collected for ^{1}H NMR (Bruker AVIII 800 MHz ^{1}H NMR spectrometer) characterization. The level of substitution (ρ) of Br-CNF surface OHs to 2-bromopropoinyl groups was quantified by reported method (Chapter 3) for calculation of percent OH converted to Br initiating sites. For ATR characterization, each Br-CNF-g-PLMA gel was scanned by Thermo Nicolet 6700 spectrometer under ambient conditions from an accumulation of 128 scans at a 4 cm^{-1} resolution from 4000 to 400 cm^{-1}. TGA were performed on a TGA-50 thermogravimetric analyzer (Shimadzu, Japan) by heating 10 mg dry sample at 10 °C/min from 25 to 500 °C under purging N_2 (50 mL/min).

Viscosities of Br-CNF in DMF dispersion (0.5, 0.3 and 0.1 w/v%) and Br-CNF-g-PLMA in toluene dispersions at different concentrations were measured at 25 °C with shear rates from 1 to 220 s^{-1} using a Brookfield DV3T rheometer. Similarly, viscosity measurements for Br-CNF-g-

PLMA in toluene (4 w/v%) or oil (1, 2 and 4 w/v%) dispersions were repeated at elevated temperatures of 40 °C and 55 °C. Power law model[60] was used to calculate flow behavior index (n) of Br-CNF-g-PLMA in toluene dispersions as follows:

$$\eta = a\gamma^{n-1} \quad (4.2)$$

Where η is viscosity in mPa·s, a is flow consistency index, and γ is shear rate in s^{-1}.

4.2.4. Redispersion of Br-CNF-g-PLMA in Toluene and Pump Oil. Br-CNF-g-PLMA (1.5 g) with varied DP was added in 10 mL toluene then sonicated (Branson 2510) 1 h to prepare homogeneous dispersions at 15 w/v%. After rheology test by viscometer at 25 °C from 1 to 220 s^{-1}, 5 mL of Br-CNF-g-PLMA in toluene dispersions (15 w/v%) were diluted to 10 w/v% and rheology test was repeated. Same dilution and test procedures were repeated to obtain viscosities results for Br-CNF-g-PLMA at concentrations of 8, 7, 6, 4, 2, 1 and 0.5 w/v%. For low conversion Br-CNF-g-PLMA, only 0.2 g copolymer was added in 5 mL toluene then sonicated 1 h to prepare homogeneous dispersion at 4 w/v%. This dispersion was serial diluted to 2, 1 and 0.5 w/v% followed by same rheology test. For oil dispersion preparation, 0.4 g Br-CNF-g-PLMA was added in 10 mL toluene followed by 10 min sonication (Branson 2510) to prepare 4 w/v% homogeneous dispersion. 10 mL vacuum pump oil was added to 4 w/v% Br-CNF-g-PLMA toluene dispersion then sonicated for another 10 min. This toluene/oil dispersion was dried under vacuum (0.5 atm) in oven (50 °C) for 24 h to evaporate all toluene for preparation of 4 w/v % Br-CNF-g-PLMA in oil dispersion. 2 and 1 w/v % Br-CNF-g-PLMA in oil dispersion were prepared by serial dilution.

4.3. Results and discussion

4.3.1. SI-ATRP on Br-CNF.

4.3.1.1. Kinetics of Polymerization. SI-ATRP of LMA on Br-CNF using it as macroinitiator was conducted at 70 °C with Br-CNF macroinitiator concentration [I] of 9.6 or 16 mM, LMA monomer concentration $[M]_o$ of 800 or 1600 mM, and reaction time from 1 to 24 h (**Table S4.1**). Effects of polymerization time on monomer consumption, logarithm of $[M]_0/[M]$, and degree of polymerization (DP) for three combinations of [I] and $[M]_0$ were displayed (**Figure 4.1a-c**). The initial $[M]_0$ to [I] ratio was 83 or 50:1 ($[M]_0$=800 mM, [I]=9.6 mM or 16 mM), and polymerization was conducted at 70 °C and allowed to proceed for 24 h to reach respective final conversions of 52.0 % and 92.7 %. Conversion dropped to 41.3% at 24 h when double $[M]_0$ to 1600 mM at same [I] = 16 mM. The semilogarithmic plot of monomer consumption, i.e., ln $[M]_0/[M]$, increase linearly with time to 6 h at conversion of 48.6 % and 74.8 % for high and low [M] to [I] ratio, demonstrating first order kinetics for ATRP as control radical polymerization. Slope or apparent rate constant for high [I] scenario was 0.1829 h^{-1}, 41% higher than rate constant 0.1295 h^{-1} for low [I]. This observation indicated high [I] would help to generate more radicals for chain propagation. However, at the same [I] = 16 mM, the extreme low apparent rate constant 0.0401 h^{-1} with high $[M]_0$ = 1600 mM compared to $[M]_o$ = 800 mM might be attributed to the early achieved nonlinear region even before 1 h.

DP for surface grafted chains increased dramatically from 3 to 40, 18 to 37 and 26 to 40 with time increased from 1 to 6 h (**Figure 4.1c**), then all DPs slightly increased to between 41 to 46 at 24 h. Compared to short chains, the longer side chain length above DP = 41 potentially increased degree freedom of chain end radicals, enhancing possibility of radical termination by combination and causing only slightly increased DP. Thus, 6 h is determined as optimal propagation time for all

three scenarios for preparation of Br-CNF-g-PLMA with ca. 40 repeating units. However, when monomer conversion and highest achievable chain length were both taken into consideration, $[M]_o$ = 800 mM and [I] = 16 mM were determined as the optimal condition resulted in 92.7 % conversion at 24 h, higher than the 11.8 to 85 % conversion previously reported of ATRPs on CNCs[27, 31, 32, 34-36, 38, 39, 42, 44, 46-50] even with the aid of sacrificial initiators (Table 4. 1).

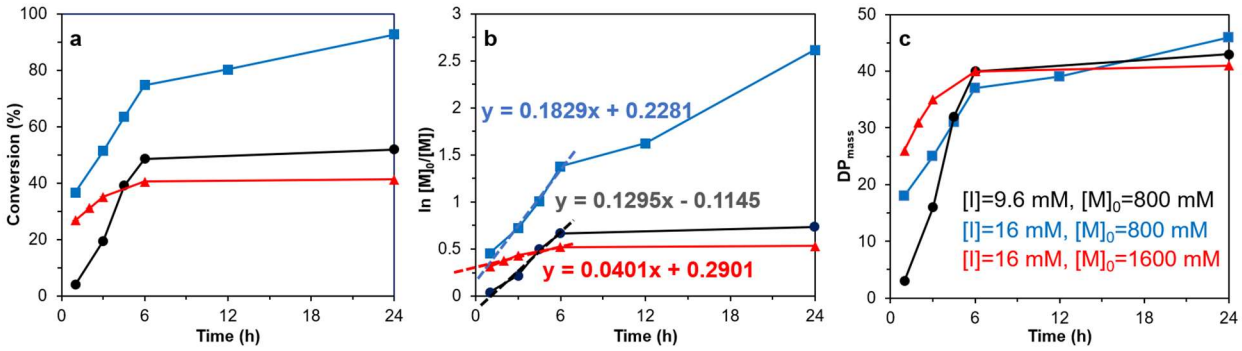

Figure 4.1. SI-ATRP of LMA ($[M]_o$=800 or 1,600 mM) on Br-CNF ([I] = 9.6 or 16 mM) at 70 °C: (a) conversion, (b) ln ($[M]_o$/[M]), (c) DP.

4.3.1.2. Mn Estimation of Br-CNF-g-PLMA. Br-CNF-g-PLMA with highest DP = 46 was suspended in pyridine, ethyl acetate, chloroform, toluene and hexane at 5 w/v% to determine the most compatible solvent (**Figure S4.1**). Transparent dispersion was prepared in toluene meanwhile translucent suspensions were observed with other four solvents, indicative of toluene as the most compatible solvent to copolymer. Five Br-CNF-g-PLMA gels with DP = 3, 16, 32, 40 (**Figure 4.1a**) and 46 (**Figure 4.1b**) were dispersed in toluene at varied concentrations of 0.5, 1, 2 and 4, 6, 8, 10 and 15 w/v % for viscosity measurement at 25 °C. M_n of Br-CNF-g-PLMA could be estimated by Mark–Houwink equation[60] under homopolymer assumption as follows

$$M_n = ([\eta]/K)^{1/\alpha} \quad (4.3)$$

Where K and α are Mark-Houwink parameters (0.73×10^{-2} ml/g, 0.69)[61] for PLMA in THF, [η] is the intrinsic viscosity determined by extrapolation of natural logarithm of relative viscosity ($\ln\eta_r$) or specific viscosity (η_{SP}) over concentration (C) to y axis. Homopolymer assumption for Br-CNF-g-PLMA is reasonable with limited Br-CNF content range from 2.7 to 7.4 w%. Parameters K and α for PLMA in THF were used in absence of any reported values in toluene. Since toluene is less polar and more compatible to the hydrophobic PLMA, K and α values (lower for better polymer-solvent interactions) may be overestimated by using less compatible THF as solvent and caused an underestimation of final M_n. The plots of inherent viscosity ($\frac{\ln\eta_r}{C}$) verse concentrations for Br-CNF-g-PLMA with corresponding estimated M_n were displayed (**Figure 4.2**).

To increase accuracy of intrinsic viscosity determination from either inherent or reduced viscosity, sufficiently dilute concentrations[62] of Br-CNF-g-PLMA in toluene system were required and only the linear regions for each DPs was selected (**Figure 4.2a** and **S2**). M_n determined by inherent viscosity ($\frac{\ln\eta_r}{C}$) moderately increased from 264 to 616 kDa with DP increased from 16 to 40, then doubled to 1381 kDa (2.2x) at DP = 46 (**Figure 4.2b**). Similarly, M_n determined by reduced viscosity ($\frac{\eta_{SP}}{C}$) moderately increased from 386 to 671 kDa with DP increased from 16 to 40, then jump to 1592 kDa (2.4 x) with DP slightly increased from 40 to 46 (**Figure S4.2**). M_n determined by inherent viscosity ($\frac{\ln\eta_r}{C}$) was considered more reliable than from reduced viscosity ($\frac{\eta_{SP}}{C}$) due to their better linear relationship. With hydrophobic LMA monomer gradually grafted on relative hydrophilic Br-CNF surface, Br-CNF-g-PLMA in DMF dispersion turned from transparent (t=0) to milky (t=1 h) to solid-liquid phase separation (t=3 h) and finally gelation ([M]o=800 mM, [I]=16 mM) with polymerization time

increased to 24 h. This observation indicated Br-CNF-g-PLMA became more incompatible to polar DMF with increasing PLMA chain lengths and precipitated chains tended to terminate than isolated chains in solution. No gelation was observed for each point (**Figure 4.2a**) thus the most possible reason for significantly increase on M_n (2.2x) when DP slightly increased from 40 to 46 (**Figure 4.2b**) was attributed to chain ends combination, in which two radicals between two grafted chain ends from different CNF surface terminated.

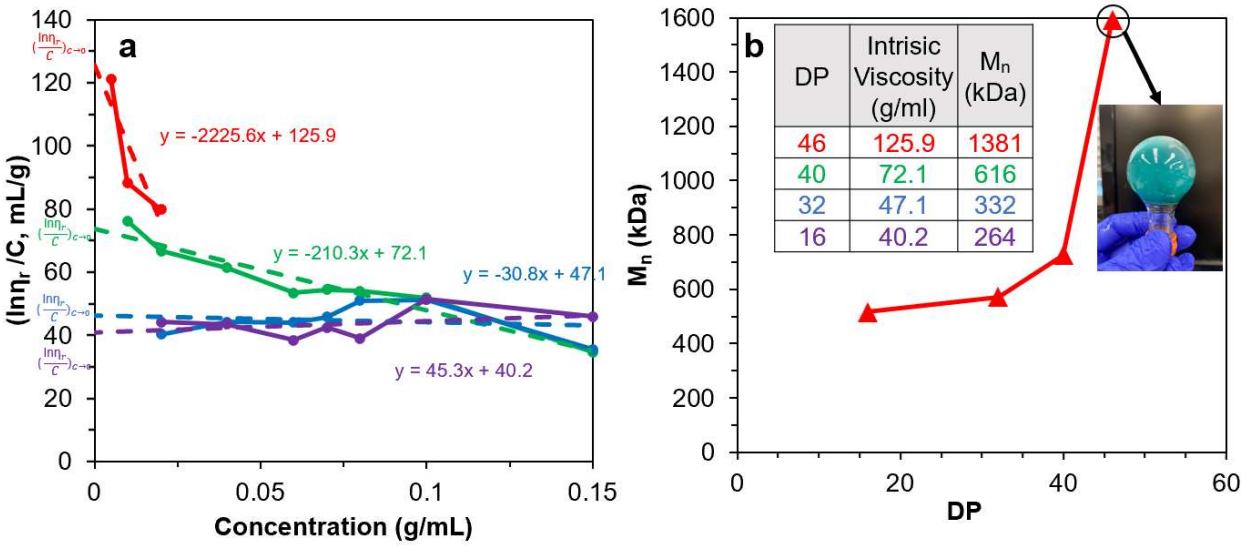

Figure 4.4.2. Plot of (a) inherent $(\frac{\ln\eta_r}{C})$ and concentration (C) for Br-CNF-g-PLMA in toluene dispersions; (b) M_n verse estimated DP by eqn (4.1) with calculated intrinsic viscosities.

4.3.1.3. ATR spectroscopy and thermal analysis of Br-CNF and Br-CNF-g-PLMA. The presence of broad peak at 1040 cm^{-1} in the FTIR spectra of Br-CNF closed to characteristic stretching peaks of C-O, C=C and C-C-O (1035 cm^{-1})[67] and confirmed existing cellulose structure (**Figure 4.3a**). This characteristic peak intensity at 1040 cm^{-1} dramatically dropped for both DP = 3 and 16 Br-CNF-g-PLMA, then disappeared on spectra of DP = 32, 40 and 46 due to relative low cellulose content of 3.8, 3.1 and 2.7 w%. Intensity of O-H stretching peak (3400 cm^{-1}) on Br-CNF spectra was stronger compared Br-CNF-g-PLMA with all DPs, indicating the decrease of relative

hydrophilic Br-CNF with the increase hydrophobic PLMA up to DP = 46. The C=O stretching peak at 1740 cm^{-1} of Br-CNF elucidated the successful conversion of cellulose OHs to 2-bromopropionyl group. Same peak (1740 cm^{-1}) appeared on all Br-CNF-g-PLMA spectra, representing C=O from esters on both side chain (PLMA) and backbone (Br-CNF). Both ester sp^3 and sp^2 C-C stretching peaks at 2860 cm^{-1} and 2930 cm^{-1} were slightly more intense on spectra of Br-CNF-g-PLMA compared to Br-CNF with chain growth of polyacrylates.

With chain growth from 0 to 46 repeating units, decreasing trend of moisture (%), char (%) and increasing trend of onset, maximum degradation temperatures were displayed (**Figure 4.3b** and **c**). After incorporating PLMA side chains, Br-CNF-g-PLMA displayed elevated onset and 1st max degradation temperatures in the ranges of 215 to 230 °C and 240 to 250 °C except for DP=3. Onset degradation temperatures reflected HBr releasing from PLMA chain end groups, which could potentially be suppressed by steric effects provided by long alkyl chain. 1st max degradation temperatures represented Br-CNF degradation and were elevated when grafted with more stable PLMA. The decreased 1st max degradation temperatures for long chain grafted Br-CNF-g-PLMA (DP = 16, 32, 40 and 46, 240 to 250 °C) compared to short chain (DP = 3, 293°C) may be due to reduced thermal stability caused by potential cellulose degradation[50] at extreme high DP. All Br-CNF-g-PLMAs showed 2nd even 3rd (DP=16, 32 and 46) max degradation at and above 317 °C, where the second is close to reported 327 °C depolymerization temperature for of PLMA (M_n= 29000) [68]. With decreased of Br-CNF content from 100 to 3.1 w%, moisture absorption of Br-CNF-g-PLMA proportionally reduced from 8.50 % to 0.05 %, accompanied with reduced char residue (%) from 9.9 to 1.7 % (**Figure 4.3d**). Nearly linear relationship between moisture (%) and Br-CNF (w%) is consistent with the still hydrophilic Br-CNF with remaining OHs of 1.6 mmol/g. Char residual (%) significantly increased from 1.7 to 9.2 % (5.4x) when Br-CNF content increased

from 2.7 to 28.2 w%, and only slightly higher for pure Br-CNF at 9.9 %. This observation indicated Br-CNF has more carbon materials compared to PLMA, which cannot be dissociated into smaller volatile fragments and remain there at 500 °C.

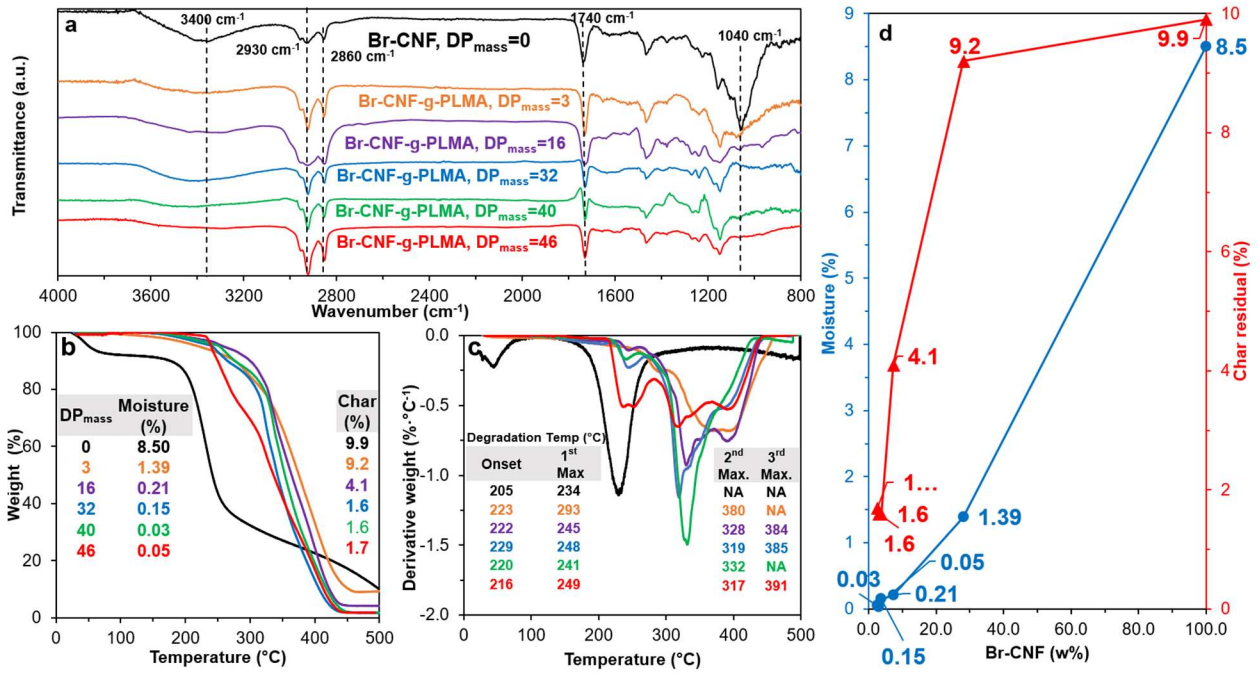

Figure 4.3. Characterizations of Br-CNF, Br-CNF-g-PLMA with DP = 3, 16, 32, 40 and 46: (a) ATR spectra; (b) TGA; (c) DTGA curves; and (d) Br-CNF portion effects on moisture (%) and char residue (%). Moisture (%) was the mass loss at 140 °C and char residue (%) was retained mass at 500 °C.

4.3.1.4. Degree of polymerization (DP) determined by solution-state 1H-NMR. The ^{1}H-NMR spectra of pure Br-CNF and Br-CNF-g-PLMA with varied DPs were displayed (**Figure 4.4a**) with corresponding protons (**Figure 4.4b**). For protons peaks on Br-CNF, the furthest downfield H6 and H6$^{'}$ peaks appeared at δ 3.63-3.89 in all five Br-CNF-g-PLMA spectra, comparable to those in δ3.71-4.06 of Br-CNF[52] and δ 3.65-3.88 range for dissolved MCC in NaOD/D_2O[63]. Multiple overlapping peaks between δ 3.29-3.58 were assigned to H2, H3, H4 and H5, matching those at δ 3.16-3.70 of Br-CNF[52] and δ 3.27-3.66 of TEMPO-CNF in D_2O[64]. The theoretical furthest

downfield cellulosic H1 proton peak existed in Br-CNF at δ 4.20-4.52 but disappeared after PLMA grafting due to potential overlapping with broad PLMA methylene H_e at δ 4.10. For proton peaks on grafted PLMA chains, chemical shift of H_e, H_c+ H_f, H_d + H_h and H_g were assigned to δ 4.05, δ 1.41-1.58, δ 0.81 and δ 1.13-1.27, matching corresponding δ 3.96, δ 1.65-1.84, δ 0.93 and δ 1.32 of homopolymer PLMA in chloroform-d_1[65]. The average ratios of integrated proton H_e:(H_c+H_f):(H_d+H_h):H_g peaks were 1:1.9:2.3:12.8 for all five Br-CNF-g-PLMAs, near to the 1:2:3:9 theoretical proton ratio to confirm these proton assignment for the PLMA grafts.

Assuming all anomeric protons of amorphous and crystalline surface AGUs of Br-CNF are detectable by ^{1}H NMR, surface AGUs was the sum of the integrated areas for anomeric H2 to H6' proton peaks, averaged by 6 or 3 anomic protons for amorphous or crystalline surface (only half exposed), respectively. H1 proton peak was excluded due to overlapping with methylene proton (Hb). LMA units could be estimated by integration of the areas of methylene H_g divided by respective 18 protons. LMA units per surface AGU could be determined mathematically by the area ratio of LMA calculated from H_g over surface AGUs calculated from H2 to H6'.

For amorphous Br-CNF, each AGU has 3 exposed OHs, DP_{NMR}, representing the # of LMA per initiating sites, could be calculated by sequentially dividing # of LMA per AGU by 3 and level of substitution (ρ=0.48) according to eqn. (4)

$$DP_{NMR,amorphous} = \frac{1}{3\times\rho} \times \frac{\text{integral of methylene protons } (H_g)/18}{\sum_2^{6'} \text{integral of anomeric protons } (H^i)/6} \quad (4.4)$$

For crystalline surface of Br-CNF, each cellobiose (two AGUs) has three exposed OHs, DP_{NMR}, representing the # of LMA per initiating sites, could be calculated by sequentially dividing # of LMA per surface AGU by 1.5 and level of substitution (ρ=0.48) according to eqn. (5)

$$DP_{NMR,crystalline} = \frac{1}{1.5\times\rho} \times \frac{\text{integral of methylene protons } (H_g)/18}{2\times\sum_2^{6'} \text{integral of anomeric protons } (H^i)/6} \quad (4.5)$$

Thus, the DP_{NMR} for amorphous and crystalline surface are the same numerical value calculated by eqn (4) or (5). Where ρ is 0.48, or 48% OHs on surface AGUs of Br-CNF were converted to Br initiating sites. DP_{NMR} calculated by ^{1}H NMR were 2, 14, 24, 31 and 29 for Br-CNF-g-PLMA, up to 37% lower than DP estimated from mass gain w% and grafting density (**Figure 4.4c**). In the polar DMSO-d_6 used for solution-state NMR, the more hydrophilic Br-CNFs were dispersed but the increasingly more hydrophobic Br-CNF-g-PLMA with greater extents of hydrophobic PLMA moiety or higher DPs became less dispersible. The less or undispersed PLMA cannot be detected by NMR thus underestimated H_g and DP_{NMR}. This is the first successful attempt to estimate chain length of nanocelluloses grafted copolymer matrix via NMR to avoid using sacrificial initiator or cleaving polymer chains from the macroinitiator surface with potential underestimation.

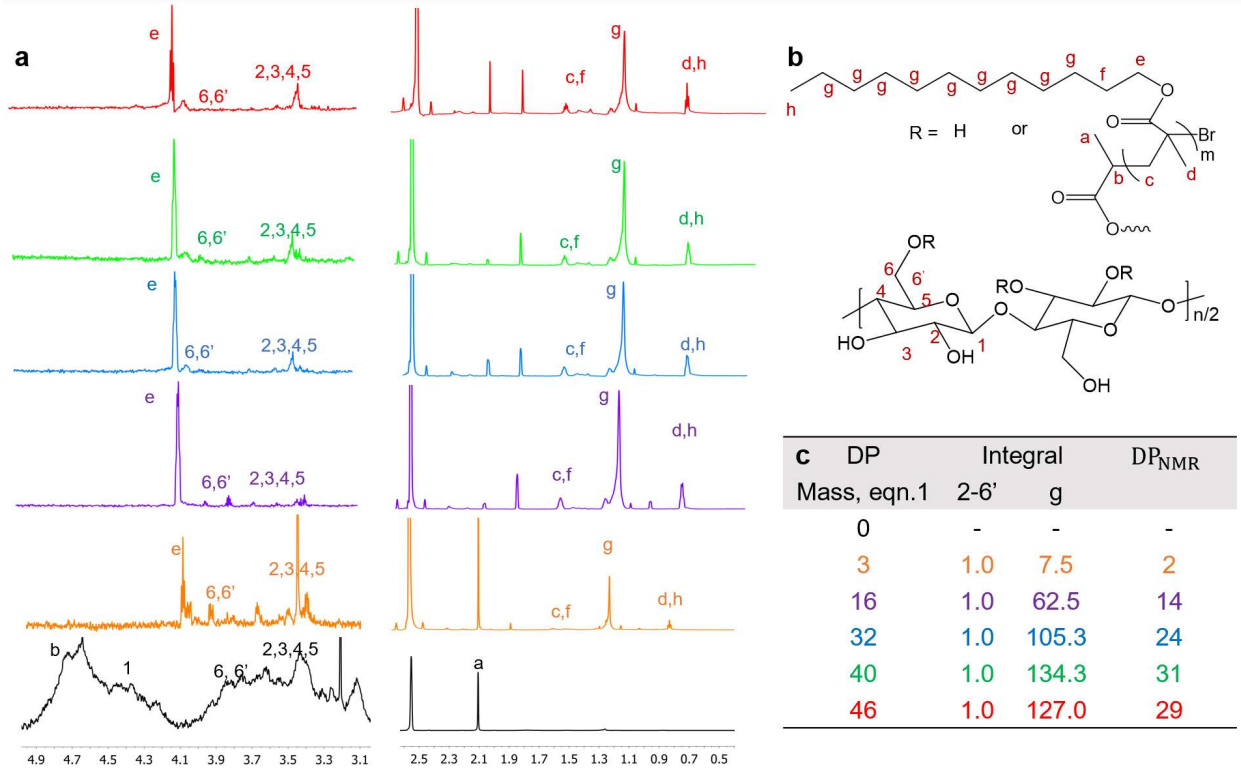

Figure 4.4. ^{1}H NMR spectra of Br-CNF and Br-CNF-g-PLMA in DMSO-d6: (a) Spectra with assigned protons; (b) Proton assignment for Br-CNF backbone and PLMA chains; (c) integral of Br-CNF protons (2-6') and methylene protons (g) on PLMA chains. DP determined by NMR based on eqn. (4) or (5)

4.3.1.5. Surface Compatibility of Br-CNF-g-PLMA. Br-CNF and Br-CNF-g-PLMA (DP=3 and 46) from SI-ATRP were further imaged by AFM on freshly exfoliated graphite. Br-CNF appeared as interconnecting nanofibrils with 4.7 nm average thickness and varying lengths in the order around 1 μm (**Figure 4.5a**). Majority of short chain Br-CNF-g-PLMA (DP=3) displayed as bead particulates with some nanofibrils (**Figure 4.5b**). Only bead particulates appeared for long chains Br-CNF-g-PLMA (DP=46) on graphite (**Figure 4.5c**). Br-CNF-g-PLMA with longer hydrophobic alkyl chains became increasingly incompatible to the moderately hydrophobic graphite surface (WCA=71.8°) to coil and aggregate. UV-vis spectra of transparent Br-CNF-g-PLMA (DP=3, 16, 32, 40 and 46) in toluene dispersions at 1 w/v% displayed increased absorbance with increased DP from 16 to 46 at all wavelengths from 400 to 800 cm^{-1} (**Figure 4.5d**). The larger Br-CNF-g-PLMA with increased DP led to higher molar attenuation coefficient in Beer–Lambert law[66], causing increased absorbance at same concentration and path length. The less compatibility between low DP =3 Br-CNF-g-PLMA and nonpolar solvent toluene may cause aggregation of short chain copolymer into large aggregates, increasing molar attenuation coefficient to higher absorbance compared to Br-CNF-g-PLMA (DP =16 and 32). The WCAs of Br-CNF-g-PLMA casted film gradually increased from 80.9° to 86.2° with DP varying from 3 to 40, then significantly increased to 110.6° when DP =46 (**Figure 4.5e**). This observation also demonstrated increased surface hydrophobicity of Br-CNF-g-PLMA with chain growing. Characterizations of Br-CNF-g-PLMA copolymer were summarized and displayed in **Table 4.2**. Br-CNF-g-PLMA copolymer with

tunable WCAs (80.9-110.6°), DP (3 -46), and M_n (264-1381 kDa) has been successfully prepared via SI-ATRP by controlling polymerization time (1-24 h) and [I] (9.6 and 16 mM) at up to 92.7% monomer conversion.

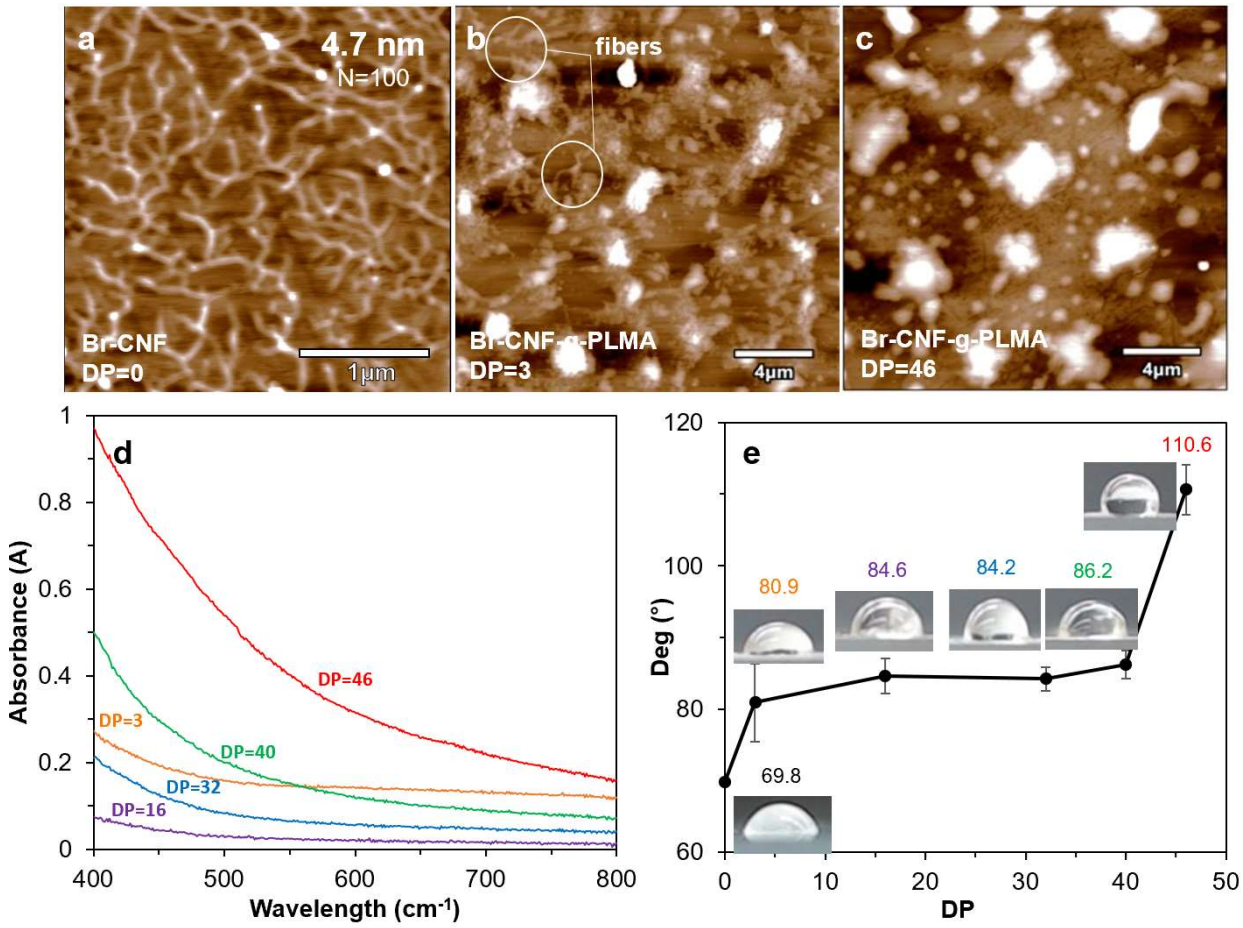

Figure 4.5. AFM morphology (a) Br-CNF in DMF; Br-CNF-g-PLMA in toluene (b) DP=3, (c) DP= 46, all from 10 μL at 0.0005 w/v% on HOPG substrate; (d) UV-vis spectra of Br-CNF-g-PLMA (1 w/v %, toluene); (e) WCAs on films cast from Br-CNF-g-PLMA with varied DP.

Table 4.2. SI-ATRPs of LMA ($[M]_o$=800 mM) on Br-CNF to Br-CNF-g-PLMA: DP_{mass}, DP_{NMR}, WCA, M_n characterizations.

Time	[I]	Conversion	Br-CNF	DP	DP_{NMR}	WCA	M_n
(h)	(mM)	(%)	(w%)			(°)	KDa
1	9.6	4	28.1	3	2	80.9	-
3		19.5	7.4	16	14	84.6	264
4.5		39.1	3.8	32	24	84.2	332
6		48.6	3.1	40	31	86.2	616
24	16	92.7	2.7	46	29	110.6	1381

4.3.2. Br-CNF-g-PLMA as Viscosity Modifier

4.3.2.1. Viscosities of Br-CNF-g-PLMA at varied shear rates. The viscosities of Br-CNF-g-PLMA dispersions in toluene at varied concentrations of 4, 6, 8 and 10 w/v% were measured at 25 °C and plotted against shear rates (**Figure 4.6**). The flow behavior index (n) of Br-CNF-g-PLMA was derived from (n-1), the slope of plot natural logarithm on both sides of the Power law model eqn (5). Theoretically, $n < 1$ indicates pseudoplastic or shear-thinning behavior of liquid. For Br-CNF grafted with short chain (DP=16), shear thinning behavior was apparent only at 10 w/v% concentration (**Figure 4.6a**) with $n = 0.7202$. For medium chain grafted Br-CNF-g-PLMA (DP=32 and 40), shear-thinning behavior existed at both 10 and 8 w/v% with corresponding n values near 0.71 and 0.84-0.87, respectively (**Figure 4.6b** and **c**). For long chain grafted copolymer with DP = 46, pseudoplastic behavior showed at all concentrations of 4, 6, 8 and 10 w/v% with lower n values between 0.38 and 0.48 (**Figure 4.6d**). The flow index n decrease with increasing either the total Br-CNF-g-PLMA concentration or proportion of Br-CNF and PLMA moieties at three DPs of 16, 32 and 40, but remained low and indifferent for Br-CNF-g-PLMA with the highest DP = 46 (**Figure 4.6e** and **f**). At lower concentrations, the coil-like Br-CNF-g-PLMA have limited interactions with each other thus Newtonian behavior should be anticipated at all shear rates. At

higher concentrations, those coil structures would stay entangled at low shear rates to generate more friction for enhanced viscosity; at high shear rates those coil structure would extend to along the shear direction to avoid shear friction for reduced viscosity. The potential coil to fiber transition between low and high shear rates introduce unique shear-thinning behavior of Br-CNF-g-PLMA in toluene, potentially serving as viscosity modifier in oil-based paints and ink printing applications. Shear-thinning phenomenon for Br-CNF-g-PLMA in toluene dispersions could be tuned by varying concentrations or side chain length of PLMA. Among all, Br-CNF-g-PLMA with the longest side chain (DP=46) has shown the most apparent shear-thinning behaviors (lowest n) at all and even lowest 4 w/v% concentration.

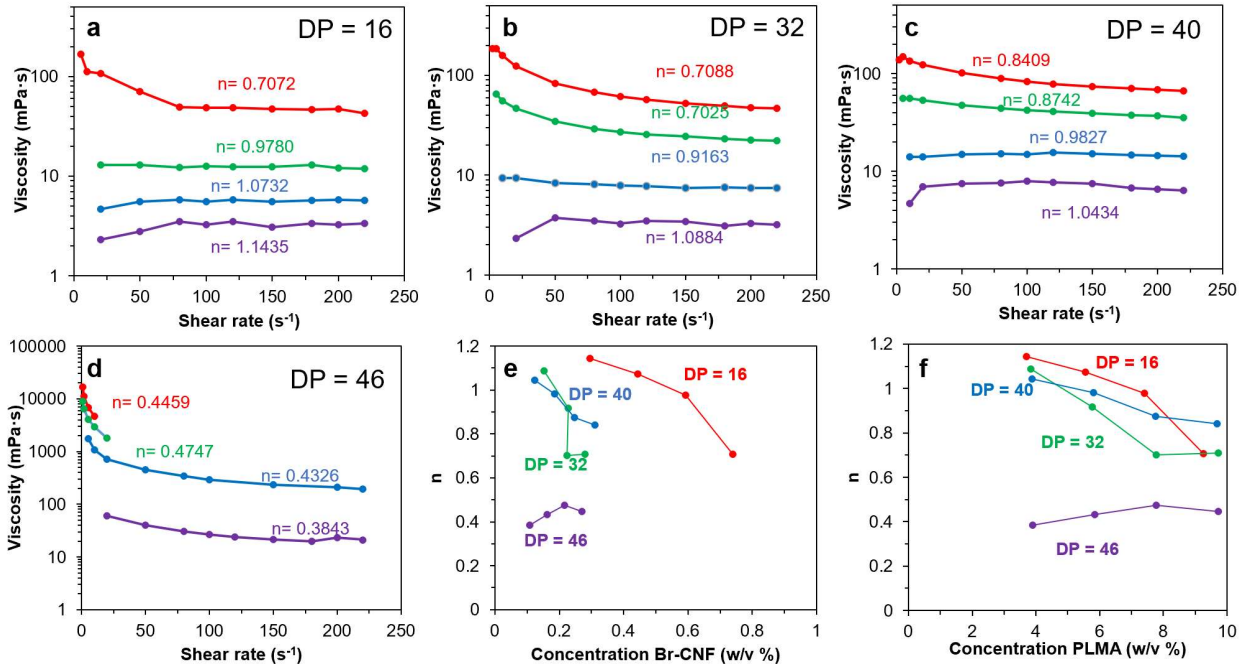

Figure 4.6. Viscosity verse shear rate of toluene dispersions of Br-CNF/PLMA with DP of: (a) 16; (b) 32; (c) 40 and (d) 46 at 4 w/v% (purple), 6 w/v% (blue), 8 w/v% (green) and 10 w/v % (red). All measurements were conducted at 25 ºC. The flow behavior index (n) value was noted for each concentration.

4.3.2.2. Concentration, chain length and temperature effects on Br-CNF-g-PLMA rheology. Rheology of Br-CNF-g-PLMA in toluene were evaluated under more expanded concentrations (0.5 to 10 w/v%), chain length (DP = 3, 16, 32, 40 and 46) and temperatures (25, 40 and 55 °C) (**Figure 4.7**). Viscosities of Br-CNF-g-PLMA in toluene at lowest 0.5 w/v% concentration were all below 1 mPa·s, slightly higher than pure toluene of 0.464 mPa·s (**Figure 4.7a**). Viscosities of Br-CNF-g-PLMA with shorter chain lengths (DP=3, 16 and 32) moderately increased to 1.51 (3.3x), 3.16 (6.8x) and 3.24 (7.0x) mPa·s as concentration increased to 4 w/v%, while viscosities of those with longer chains (DP=40 and 46) significantly increased to 6.93 (15x) and 29.7 (64x) mPa·s at 4 w/v% concentrations. When concentrations increased to 10 w/v%, significant increases (153 to 211x) of viscosities for Br-CNF-g-PLMA (DP=16, 32 and 40) were observed, while that with longest side chain (DP=46) appeared as a viscous gel with dramatically increased viscosity to 9,777 mPa·s (21,071x). The enhanced viscosity improvement with longer side chain was also observed (**Figure 4.7b**), in which viscosity significantly increase to 9.3x or 307x with increase of DP from 16 to 46 at respective 4 or 8 w/v%. The longer molecular chains on Br-CNF surface are expected to increase intermolecular attractions at any given concentration to contribute to a resistance to flow and lead to more significant viscosity enhancement effect.

Viscosities for all Br-CNF-g-PLMA with varied DP decreased with increased temperatures from 25 to 55°C at constant 4 w/v% (**Figure 4.7c**). For Br-CNF-g-PLMA with shorter chains of DP =3 and 16, viscosities moderately decreased to 0.71x and 0.84x at 55 °C, while those with longer chains of DP = 32, 40 and 46, viscosities slightly more decreased to 0.61x, 0.64x and 0.67x compared to 25 °C. Energy level of Br-CNF-g-PLMA macromolecules would increase with the increase of temperature. Thus, they are more easily able to overcome the intermolecular hydrogen bonding or Vander Waals attractive forces binding them together and reduced viscosity should be

anticipated. The temperature dependent property of Br-CNF-g-PLMA with longer side chains (DP=32, 40 and 46) makes them more applicable as viscosity modifier in paints and coating at constant and low temperatures.

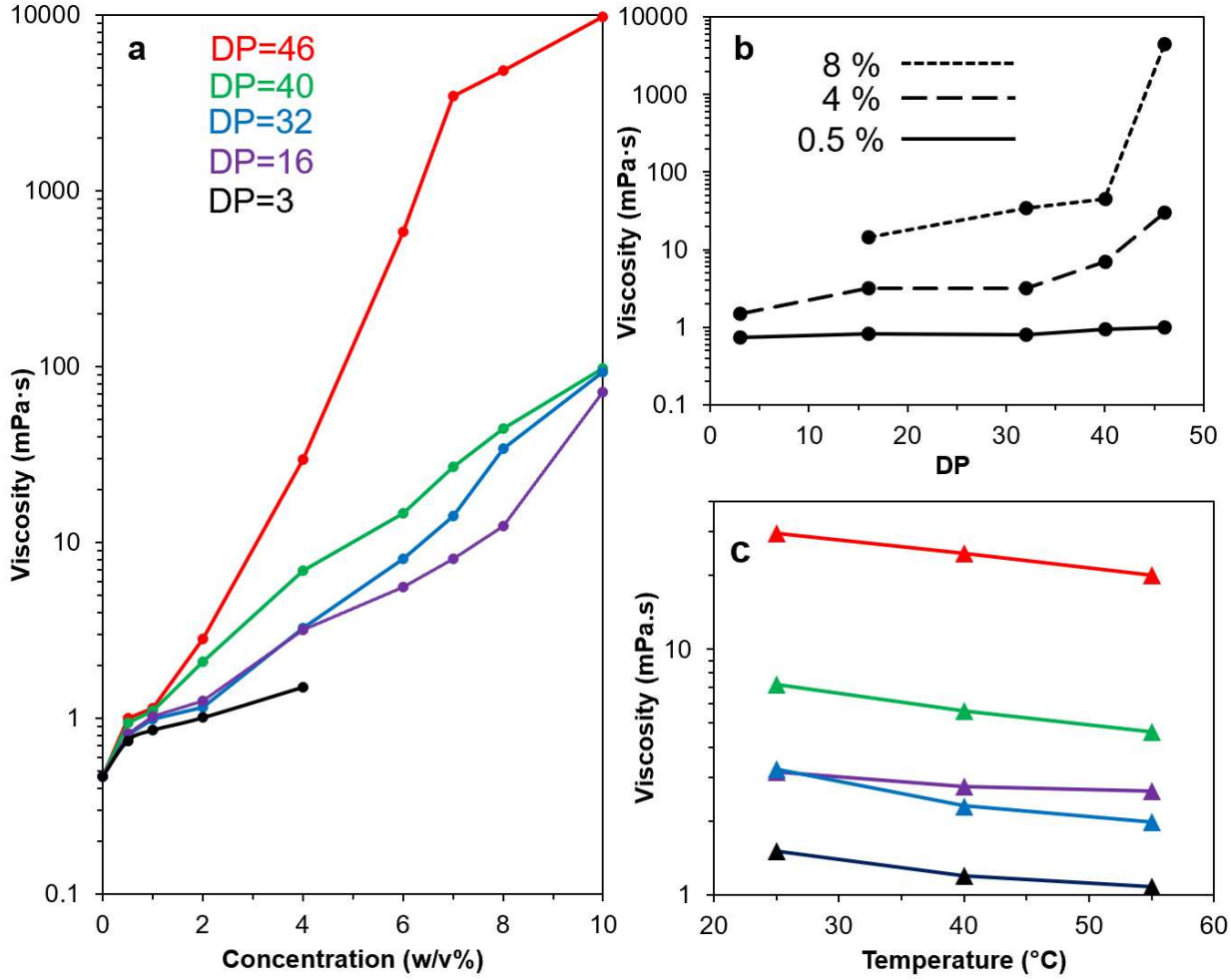

Figure 4.7. Viscosity of Br-CNF-g-PLMA in toluene as effect by: (a) concentration at varied DPs (25 °C); (b) DP at varied concentrations (25 °C); and (c) temperature at varied DPs (4 w/v%). Average viscosity at shear rates from 1 to 220 s^{-1} were used for all data points.

4.3.2.3. Br-CNF-g-PLMA as drag reducer in pump oil. To validate drag reducing effects in oil-based fluid, Br-CNF-g-PLMA (DP=46) was solvent exchanged from toluene to pump oil at 0.1, 0.3, and 0.5 w/v% to measure their viscosities over varied shear rates (**Figure 4.8a**). Viscosity

decreased to ¾, ⅖ and ⅕ for respective 0.1, 0.3, and 0.5w/v% Br-CNF-g-PLMA when shear rates increased from 1 to 220 s^{-1}, indicative of more significant shear-thinning behavior for the more concentrated dispersions. Br-CNF grafted with longest PLMA chain (DP=46) was solvent exchanged from toluene to silicon pump oil at 1, 2 and 4 w/v% to appear translucent (**Figure 4.8b**). At 25 ºC, viscosities slightly increased from 102.2 to 110.9 mPa·s at up to 2 w/v% Br-CNF-g-PLMA, then significantly increased to 256.0 mPa·s at 4 w/v%. Similar trends were also observed at elevated temperatures at 40 and 55 °C, indicating 4 w/v% was adequate concentration for Br-CNF-g-PLMA used as viscosity transducer. Newtonian behavior was observed for pure pump oil at all three temperatures while shear-thinning behavior displayed at 4 w/v% Br-CNF-g-PLMA addition (**Figure 4.8c**). Viscosity significantly increased from 104.2 mPa·s to 406.3 mPa·s (3.9x) at 1 s^{-1} and only slightly increased to 178.2 mPa·s (1.7x) at 220 s^{-1} both at 25 °C. At elevated temperature of 55 °C, viscosity dramatically increased to 5.0x or 2.2x at respective 1 or 220 s^{-1}. The more significant viscosity enhancing effect indicated potential Br-CNF-g-PLMA application as oil drag reducer at low temperature, in addition to convert turbulent flow to laminar flow for energy saving.

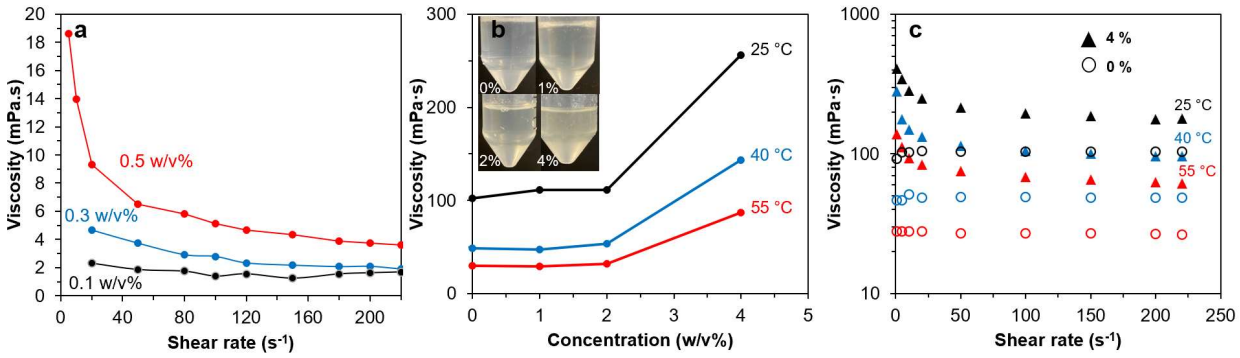

Figure 4.8. Rheology test of (a) Br-CNF in DMF, (b) Br-CNF-g-PLMA (DP=46) in oil and (c) viscosity verse shear rate at temperatures of 25 °C, 40 °C and 55°C.

4.4. Conclusion

This work successfully demonstrated surface grafting of PLMA on one-pot synthesized Br-CNF macroinitiators via surface-initiated atom transfer polymerization (SI-ATRP). Up to 92.7% conversion of LMA was achieved by tuning initiator concentration [I], monomer concentration [M]o, and propagation time to prepare Br-CNF-g-PLMA copolymer in absence of sacrificing initiators. First order kinetics for ATRP was demonstrated by linear plot of semilogarithmic monomer consumption and time with slopes determined as apparent rate constants to be 0.1829 h^{-1} and 0.1295 h^{-1}, for high [I] = 16 mM and low [I] = 9.6 mM, respectively. DP of PLMA chains on Br-CNF surface was determined between 3 to 46 by mass gain and grafting density, higher than potentially underestimated DP_{NMR} from 2 to 31 determined by solution-state ^1H NMR. M_n for DP=16 to 46 copolymer was estimated in range of 264 to 1381 kDa by intrinsic viscosity measurement with toluene as the most compatible solvent. Surface hydrophobicity of Br-CNF-g-PLMA casted films increased with increased DP, evidenced by increasing WCAs from 69.8° to 110.6° and decreasing moisture content from 9.9 to 1.6 %. This grafted copolymer was considered as novel viscosity modifier in organic media since it combined shear thinning behavior of Br-CNF and viscosity enhancing effect of high M_n PLMA. Viscosity of toluene dispersion could be tuned from 0.464 to 9777 mPa·s (21071x) with addition of 0 to 10 w/v% Br-CNF-g-PLMA (DP=46). Especially, Br-CNF-g-PLMA (DP=46, 4 w/v%) could be fully dispersed in silicon pump oil as transducer via solvent exchange from toluene to enhance viscosity up to 5 times at varied temperatures from 25 to 55°C. This study validated the role of Br-CNF as a novel macroinitiator directly used in control radical polymerization. Moreover, this simple and facile method involving grafting different functional polymer brushes via SI-ATRP, should not only have potential applications in rheology modification but also enlarge the scope of nanocomposites fabrication.

4.5. Supplemental information

Table S4.1. SI-ATRP of LMA on Br-CNF characterizations and final copolymer DP estimations under various macroinitiator concentrations and polymerization time at 70 °C. LMA conversion (%) was determined by mass gain divided by initial LMA mass. CNF (w %) was determined by mass of Br-CNF divided by mass of Br-CNF-g-PLMA.

Time	[M]	[I]	Conversion	Br-CNF	DP eqn (1)
h	mM	mM	%	w%	
1	800	9.6	4.0	28.1	3
3			19.5	7.4	16
4.5			39.1	3.8	32
6			48.6	3.1	40
24			52	2.9	43
1	800	16	36.7	6.6	18
3			51.4	4.8	25
4.5			63.5	3.9	31
6			74.8	3.4	37
12			80.3	3.1	39
24			92.7	2.7	46
1	1600	16	26.9	4.7	26
2			31.2	4.0	31
3			35.2	3.6	35
6			40.6	3.1	40
24			41.3	3.0	41

	Pyridine	Ethyl Acetate	Chloroform	Toluene	Hexane
δd (MPa)$^{(1/2)}$	19.0	15.8	17.8	18.0	14.9
δp (MPa)$^{(1/2)}$	8.8	5.3	3.1	1.4	0.0
δh (MPa)$^{(1/2)}$	5.9	7.2	5.7	2.0	0.0
Relative Polarity	0.302	0.228	0.259	0.099	0.009

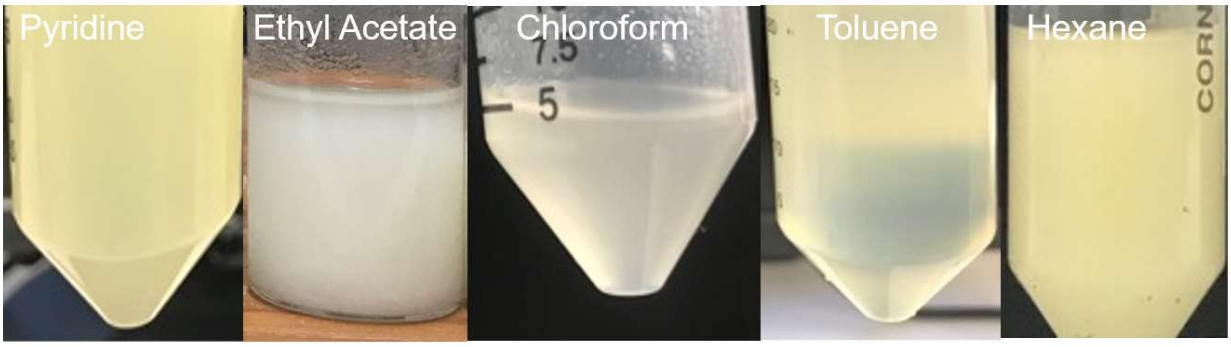

Figure S4.1. Redispersion of Br-CNF-g-PLMA (DP=46) into different solvents at 5 w/v%.

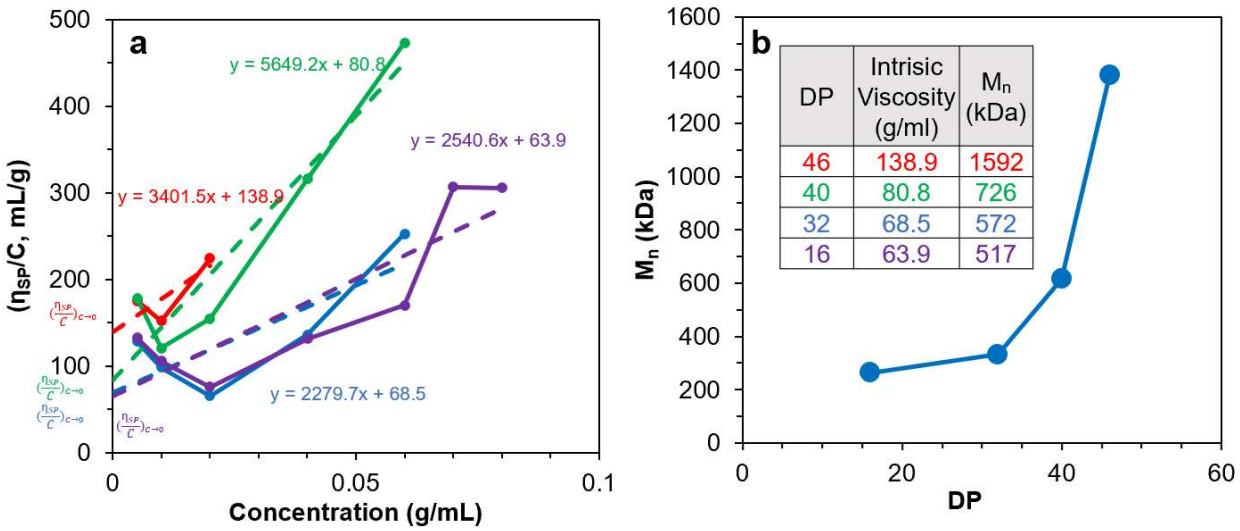

Figure S4.2. Plot of (a) reduced viscosity ($\frac{\eta_{SP}}{C}$) verse concentration; (b) M_n verse estimated DP determined by eqn (4.1). Calculated intrinsic viscosities and M_n determined by eqn (4.2) were displayed in b.

4.6. Reference

1. Chen, L.; Zhu, J.; Baez, C.; Kitin, P.; Elder, T., Highly thermal-stable and functional cellulose nanocrystals and nanofibrils produced using fully recyclable organic acids. *Green Chemistry* **2016,** *18* (13), 3835-3843.
2. Habibi, Y.; Lucia, L. A.; Rojas, O. J., Cellulose nanocrystals: chemistry, self-assembly, and applications. *Chemical reviews* **2010,** *110* (6), 3479-3500.
3. Bondeson, D.; Mathew, A.; Oksman, K., Optimization of the isolation of nanocrystals from microcrystalline cellulose by acid hydrolysis. *Cellulose* **2006,** *13* (2), 171.
4. Elazzouzi-Hafraoui, S.; Nishiyama, Y.; Putaux, J.-L.; Heux, L.; Dubreuil, F.; Rochas, C., The shape and size distribution of crystalline nanoparticles prepared by acid hydrolysis of native cellulose. *Biomacromolecules* **2007,** *9* (1), 57-65.
5. Dufresne, A., Nanocellulose: a new ageless bionanomaterial. *Materials today* **2013,** *16* (6), 220-227.
6. Jiang, F.; Hsieh, Y.-L., Chemically and mechanically isolated nanocellulose and their self-assembled structures. *Carbohydrate Polymers* **2013,** *95* (1), 32-40.
7. Saito, T.; Nishiyama, Y.; Putaux, J.-L.; Vignon, M.; Isogai, A., Homogeneous suspensions of individualized microfibrils from TEMPO-catalyzed oxidation of native cellulose. *Biomacromolecules* **2006,** *7* (6), 1687-1691.
8. Isogai, A.; Saito, T.; Fukuzumi, H., TEMPO-oxidized cellulose nanofibers. *nanoscale* **2011,** *3* (1), 71-85.
9. Wang, M. S.; Jiang, F.; Hsieh, Y.-L.; Nitin, N., Cellulose nanofibrils improve dispersibility and stability of silver nanoparticles and induce production of bacterial extracellular polysaccharides. *Journal of Materials Chemistry B* **2014,** *2* (37), 6226-6235.
10. Jiang, F.; Han, S.; Hsieh, Y.-L., Controlled defibrillation of rice straw cellulose and self-assembly of cellulose nanofibrils into highly crystalline fibrous materials. *Rsc Advances* **2013,** *3* (30), 12366-12375.
11. Jiang, F.; Hsieh, Y.-L., Self-assembling of TEMPO oxidized cellulose nanofibrils as affected by protonation of surface carboxyls and drying methods. *ACS Sustainable Chemistry & Engineering* **2016,** *4* (3), 1041-1049.
12. Saito, T.; Isogai, A., TEMPO-mediated oxidation of native cellulose. The effect of oxidation conditions on chemical and crystal structures of the water-insoluble fractions. *Biomacromolecules* **2004,** *5* (5), 1983-1989.
13. Li, J.; Wei, X.; Wang, Q.; Chen, J.; Chang, G.; Kong, L.; Su, J.; Liu, Y., Homogeneous isolation of nanocellulose from sugarcane bagasse by high pressure homogenization. *Carbohydrate polymers* **2012,** *90* (4), 1609-1613.
14. Pääkkö, M.; Ankerfors, M.; Kosonen, H.; Nykänen, A.; Ahola, S.; Österberg, M.; Ruokolainen, J.; Laine, J.; Larsson, P. T.; Ikkala, O., Enzymatic hydrolysis combined with mechanical shearing and high-pressure homogenization for nanoscale cellulose fibrils and strong gels. *Biomacromolecules* **2007,** *8* (6), 1934-1941.
15. Wågberg, L.; Decher, G.; Norgren, M.; Lindström, T.; Ankerfors, M.; Axnäs, K., The build-up of polyelectrolyte multilayers of microfibrillated cellulose and cationic polyelectrolytes. *Langmuir* **2008,** *24* (3), 784-795.
16. Aulin, C.; Johansson, E.; Wågberg, L.; Lindström, T., Self-organized films from cellulose I nanofibrils using the layer-by-layer technique. *Biomacromolecules* **2010,** *11* (4), 872-882.

17. Sun, L.; Zhang, X.; Liu, H.; Liu, K.; Du, H.; Kumar, A.; Sharma, G.; Si, C., Recent advances in hydrophobic modification of nanocellulose. *Current Organic Chemistry* **2021,** *25* (3), 417-436.
18. Lalanne-Tisné, M.; Mees, M. A.; Eyley, S.; Zinck, P.; Thielemans, W., Organocatalyzed ring opening polymerization of lactide from the surface of cellulose nanofibrils. *Carbohydrate polymers* **2020,** *250*, 116974.
19. Lönnberg, H. Ring-opening polymerization from cellulose for biocomposite applications. KTH, 2009.
20. Lizundia, E.; Fortunati, E.; Dominici, F.; Vilas, J. L.; León, L. M.; Armentano, I.; Torre, L.; Kenny, J. M., PLLA-grafted cellulose nanocrystals: Role of the CNC content and grafting on the PLA bionanocomposite film properties. *Carbohydrate polymers* **2016,** *142*, 105-113.
21. Hatton, F. L.; Kedzior, S. A.; Cranston, E. D.; Carlmark, A., Grafting-from cellulose nanocrystals via photoinduced Cu-mediated reversible-deactivation radical polymerization. *Carbohydrate polymers* **2017,** *157*, 1033-1040.
22. Chen, S.; Zhang, Z.-L.; Song, F.; Wang, X.-L.; Wang, Y.-Z., Rapid Synthesis of Polymer-Grafted Cellulose Nanofiber Nanocomposite via Surface-Initiated Cu (0)-Mediated Reversible Deactivation Radical Polymerization. *Macromolecules* **2021,** *54* (16), 7409-7420.
23. Littunen, K.; Hippi, U.; Johansson, L.-S.; Österberg, M.; Tammelin, T.; Laine, J.; Seppälä, J., Free radical graft copolymerization of nanofibrillated cellulose with acrylic monomers. *Carbohydrate polymers* **2011,** *84* (3), 1039-1047.
24. Kedzior, S. A.; Graham, L.; Moorlag, C.; Dooley, B. M.; Cranston, E. D., Poly (methyl methacrylate)-grafted cellulose nanocrystals: One-step synthesis, nanocomposite preparation, and characterization. *The Canadian Journal of Chemical Engineering* **2016,** *94* (5), 811-822.
25. Zhang, X.; Wang, Y.; Zhao, J.; Xiao, M.; Zhang, W.; Lu, C., Mechanically strong and thermally responsive cellulose nanofibers/poly (N-isopropylacrylamide) composite aerogels. *ACS Sustainable Chemistry & Engineering* **2016,** *4* (8), 4321-4327.
26. Kan, K. H.; Li, J.; Wijesekera, K.; Cranston, E. D., Polymer-grafted cellulose nanocrystals as pH-responsive reversible flocculants. *Biomacromolecules* **2013,** *14* (9), 3130-3139.
27. Zhang, X.; Zhang, J.; Dong, L.; Ren, S.; Wu, Q.; Lei, T., Thermoresponsive poly (poly (ethylene glycol) methylacrylate) s grafted cellulose nanocrystals through SI-ATRP polymerization. *Cellulose* **2017,** *24* (10), 4189-4203.
28. Yuan, W.; Wang, C.; Lei, S.; Chen, J.; Lei, S.; Li, Z., Ultraviolet light-, temperature-and pH-responsive fluorescent sensors based on cellulose nanocrystals. *Polymer Chemistry* **2018,** *9* (22), 3098-3107.
29. Zhang, J.; Wu, Q.; Li, M.-C.; Song, K.; Sun, X.; Lee, S.-Y.; Lei, T., Thermoresponsive copolymer poly (N-Vinylcaprolactam) grafted cellulose nanocrystals: synthesis, structure, and properties. *ACS Sustainable Chemistry & Engineering* **2017,** *5* (8), 7439-7447.
30. Risteen, B.; McBride, M.; Gonzalez, M.; Khau, B.; Zhang, G.; Reichmanis, E., Functionalized cellulose nanocrystal-mediated conjugated polymer aggregation. *ACS Applied Materials & Interfaces* **2019,** *11* (28), 25338-25350.
31. Majoinen, J.; Walther, A.; McKee, J. R.; Kontturi, E.; Aseyev, V.; Malho, J. M.; Ruokolainen, J.; Ikkala, O., Polyelectrolyte brushes grafted from cellulose nanocrystals using Cu-mediated surface-initiated controlled radical polymerization. *Biomacromolecules* **2011,** *12* (8), 2997-3006.

32. Boujemaoui, A.; Mongkhontreerat, S.; Malmström, E.; Carlmark, A., Preparation and characterization of functionalized cellulose nanocrystals. *Carbohydrate Polymers* **2015,** *115*, 457-464.
33. Yin, Y.; Tian, X.; Jiang, X.; Wang, H.; Gao, W., Modification of cellulose nanocrystal via SI-ATRP of styrene and the mechanism of its reinforcement of polymethylmethacrylate. *Carbohydrate polymers* **2016,** *142*, 206-212.
34. Morandi, G.; Heath, L.; Thielemans, W., Cellulose nanocrystals grafted with polystyrene chains through surface-initiated atom transfer radical polymerization (SI-ATRP). *Langmuir* **2009,** *25* (14), 8280-8286.
35. Zhang, Z.; Tam, K. C.; Sèbe, G.; Wang, X., Convenient characterization of polymers grafted on cellulose nanocrystals via SI-ATRP without chain cleavage. *Carbohydrate polymers* **2018,** *199*, 603-609.
36. Wang, H. D.; Roeder, R. D.; Whitney, R. A.; Champagne, P.; Cunningham, M. F., Graft modification of crystalline nanocellulose by Cu (0)-mediated SET living radical polymerization. *Journal of Polymer Science Part A: Polymer Chemistry* **2015,** *53* (24), 2800-2808.
37. Kedzior, S. A.; Kiriakou, M.; Niinivaara, E.; Dube, M. A.; Fraschini, C.; Berry, R. M.; Cranston, E. D., Incorporating cellulose nanocrystals into the core of polymer latex particles via polymer grafting. *ACS Macro Letters* **2018,** *7* (8), 990-996.
38. Zhang, Z.; Sèbe, G.; Wang, X.; Tam, K. C., UV-absorbing cellulose nanocrystals as functional reinforcing fillers in poly (vinyl chloride) films. *ACS Applied Nano Materials* **2018,** *1* (2), 632-641.
39. Le Gars, M.; Bras, J.; Salmi-Mani, H.; Ji, M.; Dragoe, D.; Faraj, H.; Domenek, S.; Belgacem, N.; Roger, P., Polymerization of glycidyl methacrylate from the surface of cellulose nanocrystals for the elaboration of PLA-based nanocomposites. *Carbohydrate polymers* **2020,** *234*, 115899.
40. Zhang, Z.; Sèbe, G.; Wang, X.; Tam, K. C., Gold nanoparticles stabilized by poly (4-vinylpyridine) grafted cellulose nanocrystals as efficient and recyclable catalysts. *Carbohydrate Polymers* **2018,** *182*, 61-68.
41. Rosilo, H.; McKee, J. R.; Kontturi, E.; Koho, T.; Hytönen, V. P.; Ikkala, O.; Kostiainen, M. A., Cationic polymer brush-modified cellulose nanocrystals for high-affinity virus binding. *Nanoscale* **2014,** *6* (20), 11871-11881.
42. Abousalman-Rezvani, Z.; Eskandari, P.; Roghani-Mamaqani, H.; Mardani, H.; Salami-Kalajahi, M., Grafting light-, temperature, and CO2-responsive copolymers from cellulose nanocrystals by atom transfer radical polymerization for adsorption of nitrate ions. *Polymer* **2019,** *182*, 121830.
43. Yu, J.; Wang, C.; Wang, J.; Chu, F., In situ development of self-reinforced cellulose nanocrystals based thermoplastic elastomers by atom transfer radical polymerization. *Carbohydrate polymers* **2016,** *141*, 143-150.
44. Kiriakou, M. V.; Berry, R. M.; Hoare, T.; Cranston, E. D., Effect of Reaction Media on Grafting Hydrophobic Polymers from Cellulose Nanocrystals via Surface-Initiated Atom-Transfer Radical Polymerization. *Biomacromolecules* **2021,** *22* (8), 3601-3612.
45. Morits, M.; Hynninen, V.; Niederberger, A.; Ikkala, O.; Gröschel, A. H.; Müllner, M., Polymer brush guided templating on well-defined rod-like cellulose nanocrystals. *Polymer Chemistry* **2018,** *9* (13), 1650-1657.

46. Zhang, Z.; Wang, X.; Tam, K. C.; Sebe, G., A comparative study on grafting polymers from cellulose nanocrystals via surface-initiated atom transfer radical polymerization (ATRP) and activator re-generated by electron transfer ATRP. *Carbohydrate polymers* **2019,** *205*, 322-329.
47. Navarro, J. R.; Edlund, U., Surface-initiated controlled radical polymerization approach to enhance nanocomposite integration of cellulose nanofibrils. *Biomacromolecules* **2017,** *18* (6), 1947-1955.
48. Huang, C.-F.; Chen, J.-K.; Tsai, T.-Y.; Hsieh, Y.-A.; Lin, K.-Y. A., Dual-functionalized cellulose nanofibrils prepared through TEMPO-mediated oxidation and surface-initiated ATRP. *Polymer* **2015,** *72*, 395-405.
49. Chen, J.-K.; Huang, H.-Y.; Tu, C.-W.; Lee, L.-T.; Jamnongkan, T.; Huang, C.-F., SI ATRP for the Surface Modifications of Optically Transparent Paper Films Made by TEMPO-Oxidized Cellulose Nanofibers. *Polymers* **2022,** *14* (5), 946.
50. Morits, M.; McKee, J. R.; Majoinen, J.; Malho, J.-M.; Houbenov, N.; Seitsonen, J.; Laine, J.; Gröschel, A. H.; Ikkala, O., Polymer brushes on cellulose nanofibers: modification, SI-ATRP, and unexpected degradation processes. *ACS Sustainable Chemistry & Engineering* **2017,** *5* (9), 7642-7650.
51. Khabibullin, A.; Mastan, E.; Matyjaszewski, K.; Zhu, S., Surface-initiated atom transfer radical polymerization. In *Controlled Radical Polymerization at and from Solid Surfaces*, Springer: 2015; pp 29-76.
52. Guo, M.; Hsieh, Y.-L., One-pot synthesis of 2-bromopropionyl esterified cellulose nanofibrils as hydrophobic coating and film. *RSC Advances* **2022,** *12* (24), 15070-15082.
53. Hoeng, F.; Denneulin, A.; Reverdy-Bruas, N.; Krosnicki, G.; Bras, J., Rheology of cellulose nanofibrils/silver nanowires suspension for the production of transparent and conductive electrodes by screen printing. *Applied Surface Science* **2017,** *394*, 160-168.
54. Rees, A.; Powell, L. C.; Chinga-Carrasco, G.; Gethin, D. T.; Syverud, K.; Hill, K. E.; Thomas, D. W., 3D bioprinting of carboxymethylated-periodate oxidized nanocellulose constructs for wound dressing applications. *BioMed research international* **2015,** *2015*.
55. Tang, A.; Liu, Y.; Wang, Q.; Chen, R.; Liu, W.; Fang, Z.; Wang, L., A new photoelectric ink based on nanocellulose/CdS quantum dots for screen-printing. *Carbohydrate polymers* **2016,** *148*, 29-35.
56. Salo, T.; Dimic-Misic, K.; Gane, P.; Paltakari, J., Application of pigmented coating colours containing MFC/NFC: Coating properties and link to rheology. *Nordic Pulp & Paper Research Journal* **2015,** *30* (1), 165-178.
57. Holtmyer, M. D.; Chatterji, J., Study of oil soluble polymers as drag reducers. *Polymer Engineering & Science* **1980,** *20* (7), 473-477.
58. Xia, J.; Matyjaszewski, K., Controlled/"living" radical polymerization. Atom transfer radical polymerization using multidentate amine ligands. *Macromolecules* **1997,** *30* (25), 7697-7700.
59. Lu, P.; Hsieh, Y.-L., Preparation and characterization of cellulose nanocrystals from rice straw. *Carbohydrate Polymers* **2012,** *87* (1), 564-573.
60. Voeks, J., Estimation of the parameters in the Mark-Houwink equation. *Journal of Polymer Science* **1959,** *36* (130), 333-339.
61. Mahabadi, H.; O'driscoll, K., A gel permeation chromatography calibration method for a broad molecular weight distribution polymer. *Journal of Applied Polymer Science* **1977,** *21* (5), 1283-1287.
62. Nishida, K.; Kaji, K.; Kanaya, T.; Fanjat, N., Determination of intrinsic viscosity of polyelectrolyte solutions. *Polymer* **2002,** *43* (4), 1295-1300.

63. Isogai, A., NMR analysis of cellulose dissolved in aqueous NaOH solutions. *Cellulose* **1997,** *4* (2), 99-107.
64. Jiang, F.; Dallas, J. L.; Ahn, B. K.; Hsieh, Y.-L., 1D and 2D NMR of nanocellulose in aqueous colloidal suspensions. *Carbohydrate polymers* **2014,** *110*, 360-366.
65. Iborra, A.; Díaz, G.; López, D.; Giussi, J. M.; Azzaroni, O., Copolymer based on lauryl methacrylate and poly (ethylene glycol) methyl ether methacrylate as amphiphilic macrosurfactant: Synthesis, characterization and their application as dispersing agent for carbon nanotubes. *European Polymer Journal* **2017,** *87*, 308-317.
66. Swinehart, D. F., The beer-lambert law. *Journal of chemical education* **1962,** *39* (7), 333.
67. Sills, D. L.; Gossett, J. M., Using FTIR to predict saccharification from enzymatic hydrolysis of alkali-pretreated biomasses. *Biotechnology and bioengineering* **2012,** *109* (2), 353-362.
68. Wu, M.; Wu, M.; Pan, M.; Jiang, F.; Hui, B.; Zhou, L., Synthesization and Characterization of Lignin-graft-Poly (Lauryl Methacrylate) via ARGET ATRP. *International Journal of Biological Macromolecules* **2022,** *207*, 522-530.
69. Liao, J.; Pham, K. A.; Breedveld, V., Rheological characterization and modeling of cellulose nanocrystal and TEMPO-oxidized cellulose nanofibril suspensions. *Cellulose* **2020,** *27* (7), 3741-3757.

Chapter 5. One-pot Synthesis of Bromine Esterified Cellulose Nanofibrils for Solvent Free Polyurethane Synthesis and Fabric Coating (Submission Ongoing**)**

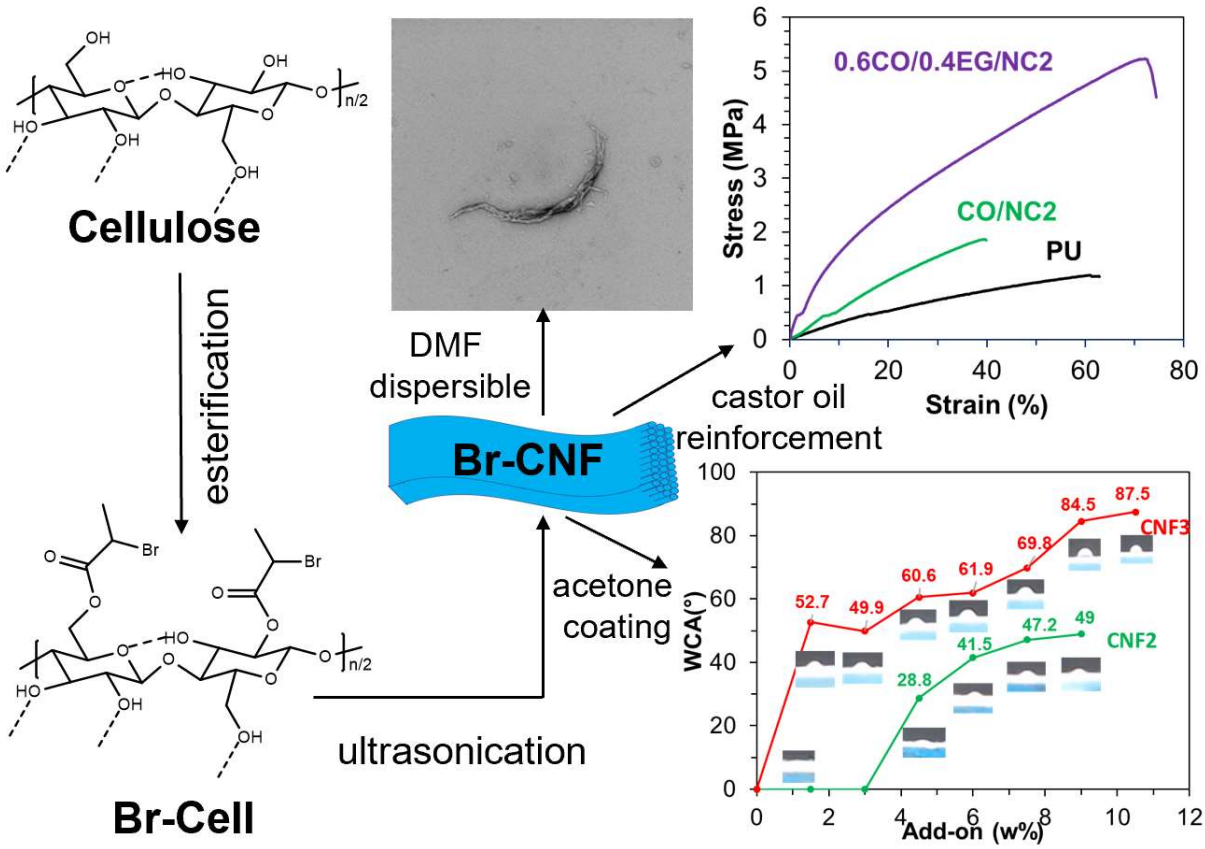

ABSTRACT

A streamlined one-pot hydrophobic cellulose synthesis coupled with direct disintegration in castor oil or acetone was investigated for prepration of organic compatible bromine esteriffied cellulose nanofibrils (Br-CNF) for polyurethane synthesis and coating applciations. Br esterified cellulose (Br-Cell) with 1.9, 3.3, and 5.4 mmol/g Br add-ons from reactions at respectivee temperatures of 23, 35, and 50°C, then defibrillated into Br-CNF1, 2, and 3 with respective DS of 0.32, 0.64, and 0.70 in yields up to 87.1 w%. Fibrous Br-CNF1 and Br-CNF2 with retaining crystallnity of 62.6% and 48.6% were characterized by AFM and TEM in ca. 300 nm in length, 7 nm in width and 2.4

to 4.0 nm in thickness. A solvent free Br-CNF2 (0.3 w%) in castor oil suspension was streamlined for synthesis of plastic PU with enhanced 2.3x modulus (modulus), strength (3.7x), and strain (1.5x) in presence of 40 mol% OHs replacement by ethylene glycol at 20 mol% excess MDI usage. Coating cotton fabric with 10.5 w% Br-CNF3 improved hydrophobicity in WCAs up to 87.5°, as well as moderately improved modulus (1.4x and strength (1.2x) for Br-CNF2 only. This one pot streamlined preparation involving Br esterification and ultrasonication enables nanocellulose preparation in variety of organic solvents to broad their applications in hydrophobic matrix or coatings, especially for oil based PU synthesis and textiles.

5.1. Introduction

Nanocelluloses, isolated from crystalline domains of cellulose, are classified to a few to tens nm wide and hundreds nm long rod-like cellulose nanocrystals (CNCs) or thinner and longer cellulose nanofibrils (CNFs). Nanocellulose and its applications gain high attraction in both research and industrial areas due to ultra-high elastic modulus (150 GPa for CNCs, 28 GPa for CNFs)[1, 2], low axial thermal expansion coefficient (10^{-7} K^{-1} for CNCs, 5×10^{-6} K^{-1} for CNFs)[3, 4], optical transparency[5, 6], unique nanoscale lateral dimensions[7, 8] and high biocompability[9, 10] Most common nanocelluloses have been produced by removing or disintegrating the non-crystalline regions via acid hydrolysis[11-14], oxidation[7, 15-18] or mechanical forces[8, 9, 19-22], thus are hydrophilic and incompatible to less polar organic media and most synthetic polymers.

Besides addition of cationic surfactant[23, 24] or quaternary ammonium salt[25, 26], chemical means such as esterification[27-40], silanation[41-44], amidation[45-48] and polymer grafting[49-57] have been reported to modify the existing hydrophilic nanocelluloses[23-36, 41-57] to generated hydrophobic nanocelluloses. Chemical modification on micro-size cellulose followed by mechanical

treatment[37-40] has been investigated as streamlined process for hydrophobic nanocellulose preparation. Direct esterification of cellulose with acetic anhydride followed by refining, cryo-crushing, and homogenization has shown to generate 10-50 nm wide and ethanol or acetone dispersible CNFs with unreported yield.[37] One-pot solventless telomerization of butadiene into 2,7-octadienyl ether (ODE), a 8-carbon diene, on cellulose followed by mechanical blending of aqueous suspensions of ODE-cellulose to generate hydrophobic ODE-nanocelluloses has been demonstrated with 27-41% yield in DMF, DMSO, and chloroform.[38]

Bromine esterification of ionic liquid dissolved cellulose[58, 59] and CNC[34, 51] by 2-bromoisobutyryl bromide (2-BIB) has been investigated to improve solubility or dispersity to less polar DMF[34, 58, 59] and anisole[51]. Recently, one novel DMF dispersible nanofibrils (Br-CNF) have been facilely produced from one-pot esterification of cellulose with 2-bromopropionyl bromide (BPB) followed by disintegration via ultrasonication at high yield of 70.9%.[39] To further demonstrate feasibility of above methodology from different cellulose stock and broad applications, pulp based Br-CNF with controllable degree of substitution are aimed to be prepared at previously determined optimized condition[39] of 5:1 bromine provider BPB to anhydroglucose unit (AGU) ratio and 6 h reaction time (6 h), but varied temperatures of 23, 35, and 50°C that have shown to most significantly alter bromine esterification, followed by optimized ultrasonication (30 min, 50% amplitude) in organic media (**Scheme 5.1a**). The effect of sonication in disintegrating bromine esterified cellulose into nanocelluloses was conducted in DMF, the most compatible with the bromine ester functionality. Castor oil, a vegetable oil, has been used as reactive polyol for polyurethane (PU) synthesis.[60, 61] However, the low compression stress of 0.118 MPa[60] for foam and tensile stress of 1.6 MPa[61] for film at 5 mol% excess isocyanates limited those application as plastics. Herein a streamlined synthesis of castor oil suspensible Br-NCs/Microfibers (MFs) mixtures was investigated followed

by reaction to methylene diphenyl isocyanates (MDI) to prepare rigid PUs (**Scheme 5.1b**). Direct sonication of Br esterified cellulose in acetone was also evaluated for coating on cotton to alter hydrophilic fabric to be hydrophobic as well as enhancing mechanical properties (**Scheme 5.1c**). The morphologies of DMF dispersible Br-CNFs were imaged by atom force microscopy (AFM) and transmission electron microscopy (TEM) to identify the optimized Br-CNFs in fibrous structure. Chemical structure of Br-CNFs casted film was elucidated by Fourier-transform infrared spectroscopy (FTIR) with thermal properties analyzed by thermogravimetric analysis (TGA) and crystallinity determined by X-ray diffraction (XRD). Degree of substitution (DS) of DMF dispersible Br-CNF was characterized by solution-state proton nuclear magnetic resonance (^{1}H NMR). Tensile stress, stain-to-failure, and elastic modulus of the Br-CNF reinforced castor oil-based PU film were tested via Instron 5566. Moreover, the wetting behavior of Br-CNF deposited bleached cotton fabric were evaluated by water contact angle (WCA) measurement. Br-Cell under varied pretreatment and reaction conditions were imaged by optical microscopy (Leica DM2500) in transmission mode and under cross-polars.

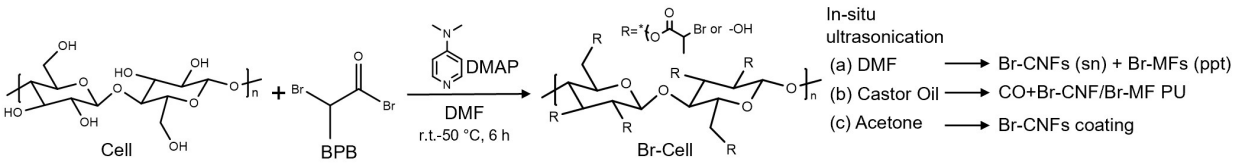

Scheme 5.1. Bromine acylation reaction of cellulose and ultrasonication for preparation of DMF, castor oil and acetone dispersible Br-CNF for characterizations, polyurethane synthesis, and fabric coating.

5.2. Experimental

5.2.1. Materials. Soft wood dissolving pulp was provided by the Forest Products Laboratory of US Department of Agriculture Forest Service (Madison, WI). 2-Bromopropionyl bromide (BPB,

97%, Alfa Aesar), 4-dimethylaminopyridine (DMAP, 99%, Acros Organics), potassium bromide (KBr, 99.9+%, Fisher Scientific), acetone (histological grade, Fisher Scientific), N, N-dimethylformamide (DMF, certified grade, Fisher Scientific), castor oil (Sigma Aldrich, hydroxyl value 150-160[62]), methylene diisocyanate (MDI, 97 %, Sigma Aldrich), ethylene glycol (anhydrous, EG, 99.8 %, Sigma Aldrich), tert-butanol (ACS reagent, Sigma Aldrich), and bleached plain-woven cotton fabric were used as received without further purification. All water used was purified by Milli-Q Advantage water purification system (Millipore Corporate, Billerica, MA). For AFM imaging, mica (highest-grade V1 mica discs, 10 mm, Ted Pella, Inc. Redding, CA) and highly oriented pyrolytic graphite (HOPG, grade ZYB) were used. For TEM, carbon grids (300-mesh copper, formvar−carbon, Ted Pella Inc.) were used.

5.2.2. Synthesis of Bromine Acylated Cellulose (Br-Cell). Bromine acylation of cellulose was performed at varying reaction temperature (23 to 50 °C) at a fixed 5:1 BPB to anhydroglucose units (AGU) in cellulose ratio for 6 h (**Scheme 5.1**). The dissolving pulp sheet was cut and ground (Thomas-Wiley Laboratory Mill model 4, Thomas Scientific, USA) to pass through 60-mesh screen. Crystallinity of pulp cellulose was determined to be 0.824 via X-ray diffractometer (XRD), and non-crystalline cellulose OH was calculated by total OHs per g cellulose (18.52 mmol/g) multiplied by one minus crystallinity, which is equivalent to 3.26 mmol/g. Ground cellulose (0.5 g, 1.63 mmol AGU) was added to DMF (30 mL) and ultrasonicated (Qsonica Q700, 50/60 Hz, 3 min, 50 % amplitude) to a homogeneous suspension. Bromine provider BPB (3.5 g, 16.3 mmol) and DMAP (0.05 g, 0.4 mmol) catalyst were dissolved in DMF (10 mL) in an ice bath under vortexing, then added dropwise to the cellulose dispersion to start the reaction and vacuum filtered to stop the reaction. The reacted cellulose solids were rinsed with acetone (×3) to remove residual BPB, DMAP and DMF, then dried at 55 °C overnight to obtain bromine acylated cellulose (Br-

Cell). The extent of reaction in Br-Cell was determined by mass gain and expressed as Br add-on (σ, mmol/g):

$$\sigma = \frac{m_2 - m_1}{135 \times m_1} \quad (5.1)$$

where m_{cell} is the initial cellulose mass (g), $m_{\text{Br-cell}}$ is the dry Br-Cell mass (g), and 135 (g/mmol) is the molar mass gain from hydroxyl to bromine ester.

5.2.3. In-situ Ultrasonication in DMF, Acetone and Castor-oil to Br-NCs. Br-Cell (0.1 or 0.5 g) was suspended in 100 mL DMF or acetone (0.1 or 0.5 w/v%) and ultrasonicated (Qsonica Q700, 50/60 Hz) at 50% amplitude for 30 min at 10-minute intervals in an ice bath. Tert-butanol wetted Br-Cell (0.5 g) was also pre-wetted with tert-butanol (0.5 mL) then sonicated as above. All ultrasonicated dispersions were centrifuged (Eppendorf 5804R, 5k rpm, 10 min) to collect the clear Br-acylated nanocellulose (Br-NC) containing supernatants and Br-Cell precipitates for further characterizations. Similarly, Br-Cell (0.25 g) was suspended in 50 g castor oil for preparation of 0.5 w% suspension and ultrasonicated at 50% for 30 min. Mass of air-dried Br-Cell precipitates was determined gravimetrically and subtracted from the initial Br-Cell mass to derive the quantity of Br-NC in the supernatant.

5.2.4. Characterizations. The morphology of dried Br-Cells was imaged by optical microscopy (Leica DM2500). Br-Cell microfibers were redispersed in DMF at 0.1 w/v% and 10 μL droplets were deposited on glass slides to measure their widths and lengths (n > 100). Their averages and standard deviations were reported. Br-NCs in DMF dispersions were imaged by AFM and TEM on different substrates. Br-NCs (10 μL, 0.0005 w/v %) were deposited on freshly cleaved hydrophilic mica or relatively hydrophobic highly oriented pyrophoric graphite (HOPG), then evaporated in fume hood for 30 min and decant excess liquid by filter paper followed by 1 min

nitrogen blowing. The dried samples were profiled by AFM in the tapping mode with scan size and rate set to 5um × 5um and 512 Hz. Br-NCs Castor oil (0.5 w%) was diluted by DMF directly to 0.0005 w/v% followed by centrifugation (5k RPM, 10 min), the supernatant (10 μL) was deposited on mica or graphite in the same manner as described above. Br-NC (10 μL, 0.0005 w/v %) was deposited onto glow discharged carbon-coated TEM grids, and excess liquid was removed after 5 min by blotting with a filter paper. The specimens were negatively stained with 2 w/v% aqueous uranyl acetate and blotted to remove excess solution with filter paper, repeated five times then dried under the ambient condition for 15 min. The samples were observed using a Philip CM12 transmission electron microscope at a 100 kV accelerating voltage. The lengths and widths of Br-CNFs were measured and calculated using ImageJ Analyzer (ImageJ, NIH, USA).

For Fourier transform infrared spectroscopy (FTIR), transparent pellets were prepared by mixing 3 mg of Br-CNF powder with 300 mg of spectroscopic grade (99.9+%) potassium bromide (KBr) after 1 min pressurization under 800 MPa barrel chamber, then scanned by Thermo Nicolet 6700 spectrometer under ambient conditions from an accumulation of 64 scans at a 4 cm^{-1} resolution from 4000 to 400 cm^{-1}. Thermogravimetric analysis (TGA) was performed on a TGA-50 thermogravimetric analyzer (Shimadzu, Japan) by heating 5 mg dry sample at 10 °C/min from 25 to 500 °C under purging N_2 (50 mL/min). The crystalline structures were determined by X-ray diffraction (XRD) using a PANalytical X'pert Pro powder diffractometer with a Ni-filtered Cu Kα radiation (λ = 1.5406 Å) at 80 kV anode voltage and 40 mA current. The samples were fixed on by double-sided tape, then diffractograms were recorded from 5 to 40° at a scan rate of 2°/min. Crystallinity index (CrI) was calculated using the intensity of the 200 peak (I_{200}, 2θ =22.5°) and the intensity minimum between the peaks at 200 and 1110 (I_{am}, 2θ = 19.0°) as follows[63]

$$\mathrm{CrI} = \frac{I_{200} - I_{am}}{I_{200}} \tag{5.2}$$

The crystallite dimensions were calculated using the Scherrer equation[64]

$$D_{hkl} = \frac{0.9\,\lambda}{\beta_{1/2}\cos\theta} \tag{5.3}$$

where D_{hkl} is the crystallite dimension in the direction normal to the (h k l) lattice planes, λ is the X-ray radiation wavelength (1.5406 Å), $\beta_{1/2}$ is the full width at half-maximum of the diffraction peak in radius determined by excel.

To prepare Br-CNF for proton nuclear magnetic resonance (^{1}H NMR), Mill-Q water (40 mL) was added into Br-CNF in DMF dispersions (10 mL, 0.50 w/v%) followed by centrifugation (5k rpm, 10 min) to decant the supernatant, and repeated three times to prepare Br-CNF aqueous suspension (ca. 0.5 w%). The suspension was quickly frozen by pouring liquid nitrogen into the container and then freeze-dried into Br-CNF powder. Br-CNF powder (ca. 5 mg) was added into 1 mL DMSO-d_6, then sonicated (10 min, Branson 2510) to partially dispersed followed by centrifugation (5k RPM, 10 min). Br-CNF in DMSO-d_6 supernatant (ca. 0.2 w/v%) was collected for ^{1}H NMR (Bruker AVIII 800 MHz ^{1}H NMR spectrometer) characterization. Around 1 mL supernatant was placed in one NMR tube with 100 μL trifluoracetic acid added to shift water absorption peak downfield to above 4.5 ppm, then water suppression mode was applied on ^{1}H-NMR spectra by selecting the water peak at δ 4.7-5.0.

5.2.5. Castor-oil Based PU Synthesis and Dip Coated Cotton Fabric. MDI (3.96 g. 15.8 mmol) was dissolved in 1 mL acetone with 10 min sonication (Branson 2510), then added to ultrasonicated Br-Cell (ca. 0.05 g) in castor oil (10 g, 26.3 mmol OHs) in 1.2:1 NCO_{MDI}:OH_{CO} ratio and sonicated for 10 min. The same process was repeated using 6 or 8 g Br-Cell in castor oil, followed by addition of 0.16 (5.3 mmol) and 0.32 (10.6 mmol) g ethylene glycol for preparation of EG replaced castor oil PU. Polyurethane films were prepared by pouring the mixture into glass petri dish and let reacted at 80°C under vacuum oven (0.5 atm). Bleached plain-woven cotton

fabric was washed by hot water (ca. 70 °C) followed by drying in oven (56°C) overnight. Each fabric was cut into 0.2 g piece (4 cm×4 cm). A drop (0.255 mL) of acetone dispersions (0.3 w%, Br-CNF2 or Br-CNF3) were padded on each fabric, evaporate for ca. 1 min and repeated five times, then dried in fume hood for 5 min before water contact angles (WCAs) measurement. WCAs of sessile drops (5 µL) on pad coated cotton fabric were measured using the ImageJ Analyzer and the average values were calculated from both sides of a sessile drop. Castor oil-based PU films and coated fabric were cut into 40 mm×15 mm× 2 mm or 40 mm×10 mm× 0.2 mm for tensile test (Instron 5566) at strain rate of 10 mm/min until breakage. All coated fabrics were tested along warp direction.

5.3. Results and discussion

5.3.1. Bromine Acylated Cellulose (Br-Cell) and in-situ Ultrasonication into Br-NCs. Bromine acylation was performed of pulp cellulose that were ground and/or sonication to study potential improved reaction. Length of pulp fibers significantly decreased from 1216 to 201 (0.17x) µm after grinding and only slightly decreased to 193 µm after being further sonicated (**Figure 5.1a**). Width of fibers stayed almost unchanged between 23.2 and 24.5 µm after sequential treatments of grinding and pre-sonication (**Figure 5.1b**). Bromine esterification of ground and sonicated cellulose at constant 5:1 BPB:AGU ratio and 6 h reaction time produced Br esterified cellulose (Br-Cell) with significantly increased Br add-ons (σ) of 1.9, 3.3, and 5.4 mmol/g at 23, 35, and 50 °C, yet similar to 2.3, 3.0, and 5.8 mmol/g of the untreated cellulose (**Figure 5.1c**). In contrast, the Br-NCs yield collected in supernatant for ground/sonicated cellulose increased from 48.2 to 87.1%, all higher than those for untreated as is cellulose from 28.6 to 43.3% with increasing temperatures. Grinding not only reduce cellulose length potentially via onset of chain scission but

also significantly increase Br-NCs yield. Esterification on ground cellulose without pre-sonication was also prepared at 35 and 50°C to collect slightly less esterified Br-Cell2 (3.1 mmol/g) and 3 (5.1 mmol/g) (**Table S5.1**), indicative of lesser effect of sonication than grinding on esterification. Moreover, more intensive esterification at 50°C led to length deduction and displayed irregular beads or bundles under cross-polar (**Figure 5.1d**) compared to relative mild esterification at 23 and 35°C. Grinding or higher reaction temperatures both help to increase Br-NCs yield by respectively decreasing length of microfiber or increasing Br add-ons. Overall, Br-Cell1-3 with Br add-ons of 1.9, 3.3, and 5.4 mmol/g has been facilely produced and easily controlled by varying reaction temperatures, then ultrasonicated in DMF (0.1 w/v%) (50 % amplitude, 30 min) to collect the Br-NC containing supernatants with 48.2 % Br-NC2, 74.5 % Br-NC2, and 87.1% Br-NCs. Thus, increasing Br esterification level on Br-Cell converts more amorphous OH to Br bearing esters, improves its compatibility to DMF and disintegration into NC by sonication.

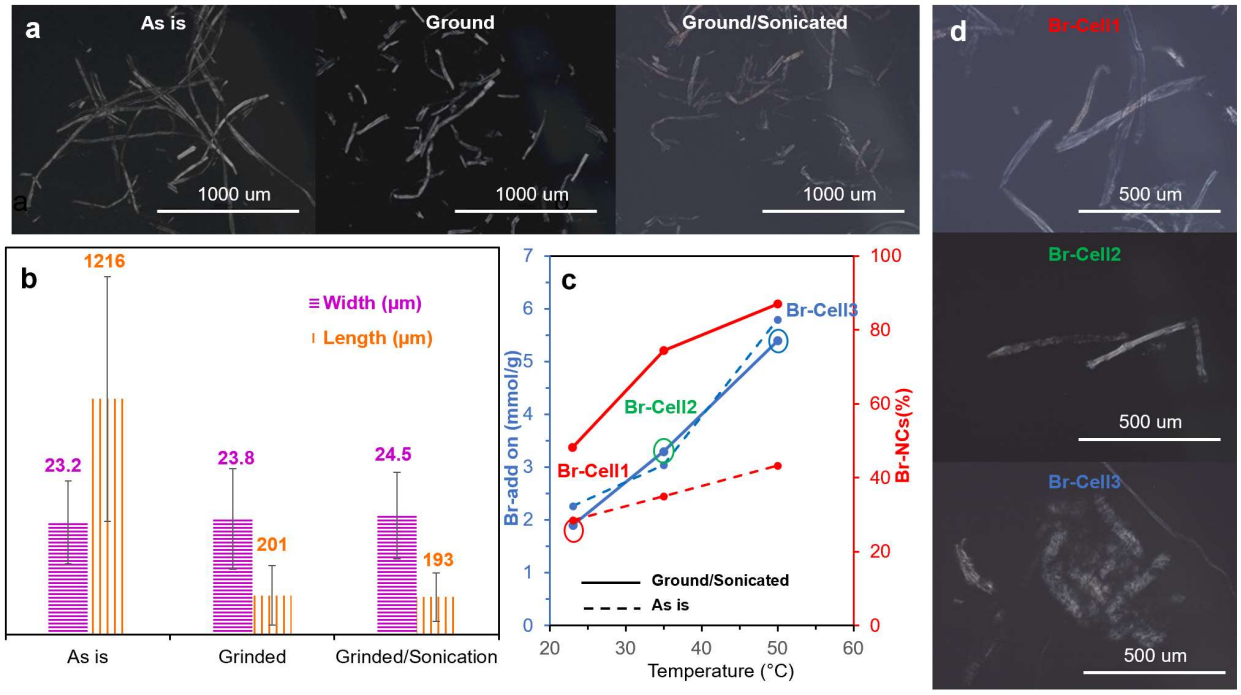

Figure 5.1. Effects of grinding and pre-sonication (3 min, 50% amplitude) on pulp cellulose: (a) optical microscopic images of cellulose; (b) microfiber dimensions; (c) Br add-on and Br-NCs (%) yield from esterification (5:1 BPB:AGU, 6 h) at varied temperatures; (d) optical microscopic images of Br-Cell1-3. All images in a and d were captured at 1 w/v% in DMF under cross-polar.

5.3.2. Br-NC Morphology. Hydrophilic mica (16.8°) and moderately hydrophobic graphite (71.8°), glow-discharged carbon grid (68.2°) with corresponding WCAs[39] were used for deposition of Br-NC1-3 with increased hydrophobicity of Br add-ons from 1.9 to 5.4 mmol/g under AFM or TEM (**Figure 5.2**). On the most hydrophilic mica substrate, the least esterified Br-NC1 displayed as fibers at 2.8 nm thickness, meanwhile the moderated esterified Br-NC2 displayed mostly as fibers (2.4 nm) but also few particulates and the most esterified Br-NC3 showed only particulates (**Figure 5.2a-c**). In contrast on relative hydrophobic graphite, only bead particulates were observed for Br-NC1, while major or partial clear fibers were observed for Br-NC2 and Br-NC3 at corresponding 4.0 and 3.4 nm thickness(**Figure 5.2d-f**). Widths of 7.0 and 6.7 nm fibrous Br-NC1 and 2 were observed on glow discharged carbon grid but only ribbon-like aggregations of Br-NC3 appeared (**Figure 5.2g-i**). The forms and sizes of Br-NCs were found highly dependent on the extent of Br-acylated cellulose and depositing substrates. Br-NC1 displayed in fibers on hydrophilic mica but particulates on hydrophobic graphite, indicating the esterification is not intensive enough to convert sufficient OHs to relatively hydrophobic esters for homogeneous deposition on more hydrophobic substrates. Br-NC2 displayed in fibers structures on mica and graphite, indicative of modest esterification on Br-Cell2 surfaces to be amphiphilic, thus compatible to both mica and graphite. Thickness of Br-CNF2 measured on hydrophobic graphite (4.0 nm) was higher than that measured on hydrophilic mica (2.4 nm), indicating esterified cellulose was more defibrillated along hydrophilic (110) planes compared to hydrophobic (200)

planes during ultrasonication. However, major bead particulates instead of fibers were observed for the most esterified Br-NC3. Those bead particulates along with ribbon-like structures under TEM (**Figure 5.2i**) could be attributed to either super hydrophobic CNFs which incompatible to graphite or dissolved cellulose aggregation. The latter one was more reasonable due to the significant reduced 0.22 CrI (**Figure 5.4b**) compared to original cellulose (0.82) . All length to thickness ratios, or aspect ratios of Br-CNFs on mica (128, 105 for Br-CNF1 and 2) and graphite (80, 95 for Br-CNF2 and 3), were all roughly equal to 100 and indicative of successfully preparation of CNFs instead of rod-like CNCs. Clear fibrous structures of Br-CNF1, Br-CNF2 and ribbon-like associated Br-CNF3 were further confirmed under TEM.

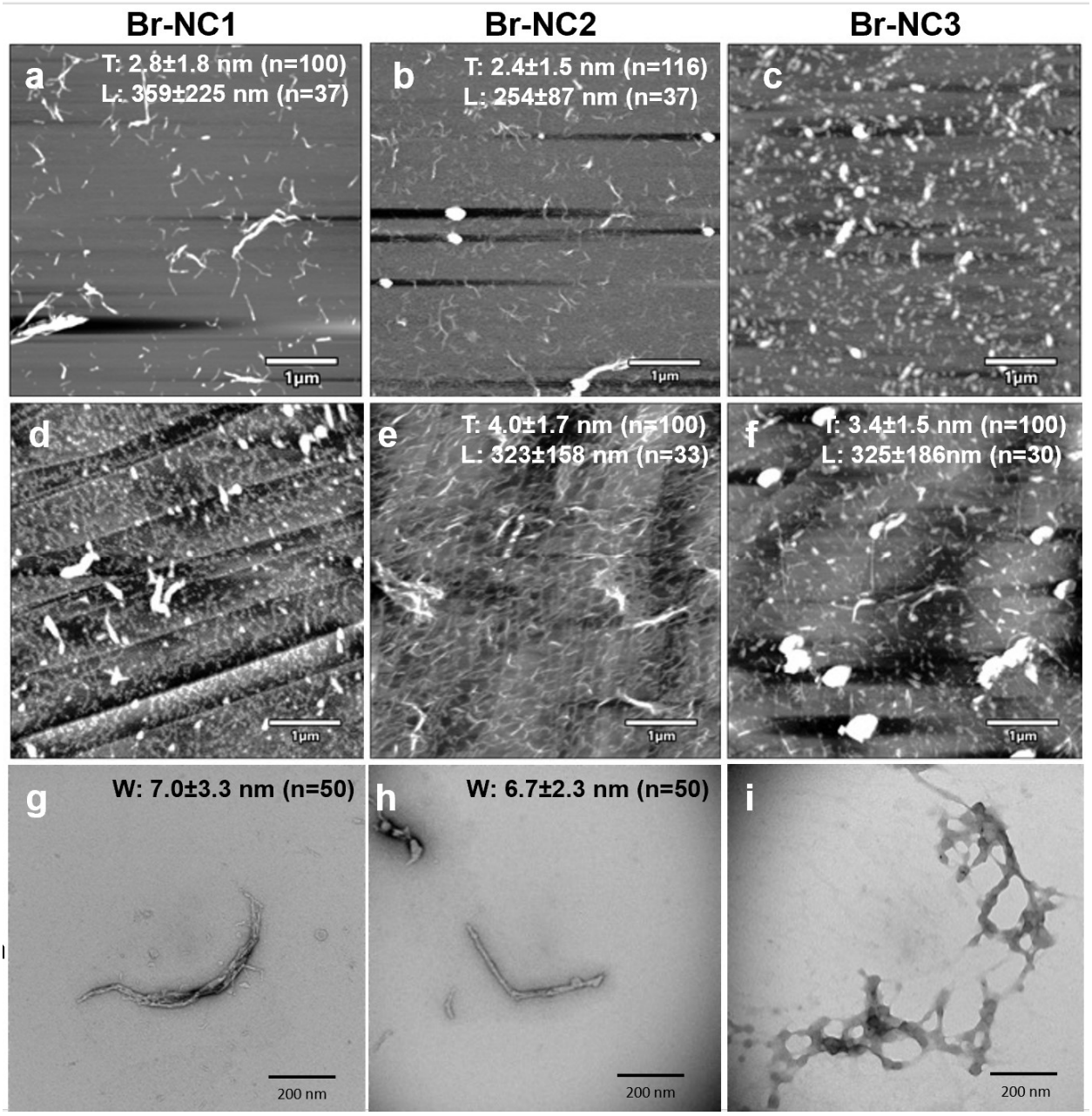

Figure 5.2. AFM and TEM height images (0.0005 w/v%) of Br-NCs from sonication (30 min, 50% amplitude) on mica (a-c), graphite (d-f) and glow discharged carbon (g-i). Br add-on and yield values for Br-CNF1-3 are 1.9 mmol/g, 48.2%; 3.3 mmol/g, 74.5%; and 5.4 mmol/g, 87.1%.

5.3.3. Structural Characterization by FTIR, TGA, and XRD. The presence of the C=O stretching peak at 1740 cm^{-1} in the FTIR spectra of all Br-Cells and Br-CNFs confirmed the successful conversion of hydroxyls to 2-bromopropionyl group on cellulose (**Figure 5.3a**). The unchanged carbonyl peak (1740 cm^{-1}) on both Br-Cells and Br-CNFs indicates no side reaction or degradation to the alkyl bromines from ultrasonication. With the increased Br add-ons from 0 to 5.4 mmol/g, the lowered intensity of absorbed water peak (1632 cm^{-1}) was expected from the more hydrophobic esters converted. Furthermore, weaker hydrogen bonding O-H stretching peak (3400 cm^{-1}) in all Br-Cells and Br-CNFs than underivatized cellulose supports the successful cellulose hydroxyl conversion to bromine esters. The reduced hydrogen bonding interactions between cellulose chains could aid the opening of bromine acylated cellulose (110) or (1-10) planes via ultrasonication to generate more NCs.

Moisture absorption of Br-Cells were reduced to between 3.77 and 4.62 % as compared to underivatized cellulose (7.28%) (**Figure 5.3b)**, consistent with effect of converting hydrophilic hydroxyls to Br-ester. The significantly higher moisture contents of Br-CNF1 (6.3 %) and Br-CNF2 precipitate (6.5 %) were observed compared to those precursors Br-Cell1 (4.1 %) and Br-Cell2 (3.8 %), which suggested that hydrophilic surfaces may be generated from the opening of cellulose (110) and (1-10) planes during ultrasonication. In comparison for the most esterified Br-CNF3, no significant moisture (%) difference was observed due to its extremely hydrophobic nature in both Br-Cell3 and Br-CNF3. Both the onset and max degradation temperatures decreased from esterification of celluloses into Br-Cell1-3 (**Figure 5.3c**) and could be attributed to the conversion of hydroxyls to less thermal stable bromine esters. Further but slightly lowered onset and max degradation temperatures of Br-CNF1-3 (203 - 213°C) than those precursors Br-Cell1-3 (204 - 225°C) may be due to the three order of magnitude smaller fiber dimensions (2.4-3.4 nm

thickness) and higher specific surfaces. Char residual (%) for all esterified celluloses and derivatives (6.5-19.4%) were significantly higher than underivatized cellulose (2.4%) due to the insertion of more thermally stable methyl groups from Br bearing esters.

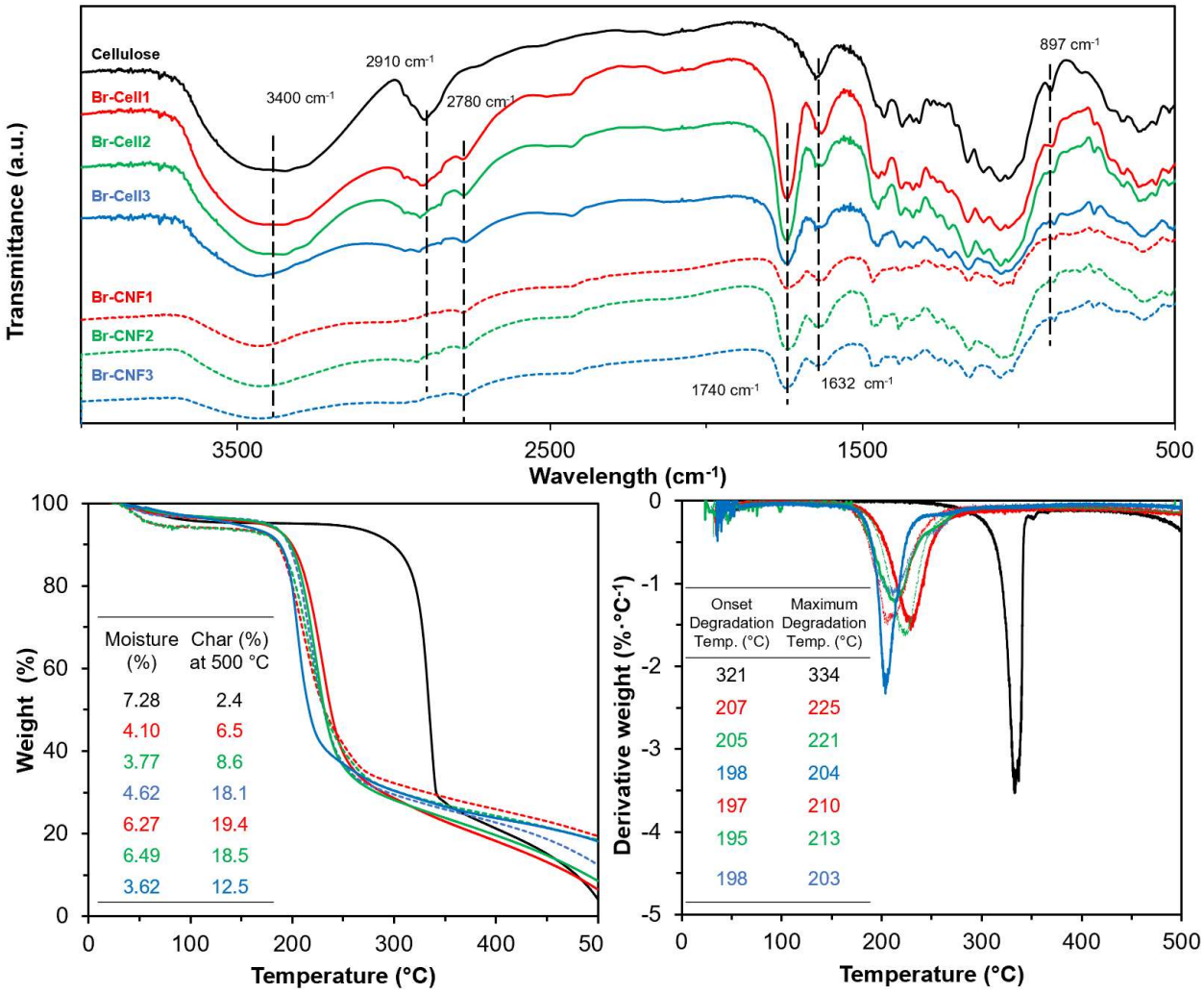

Figure 5.3. Characterizations of pulp cellulose, Br-Cell1-3 and Br-CNF1-3: (a) FT-IR spectra; (b) TGA; and (c) DTGA curves. Moisture (%) is determined as mass loss at 140 °C.

5.3.4. Crystalline structure by XRD. The deconvolution of XRD spectra of three Br-CNFs displayed 2θ peaks at 14.6, 16.5, and 22.5° corresponding to the respective (1-10) (110) (200) monoclinic Iβ lattice planes of cellulose (**Figure 5.4a**). The crystallinity of Br-CNFs lowered from 0.63 to 0.22 accompanied by increased Br add-on from 1.9 to 5.4 mmol/g, compared to the 0.69

CrI of original cellulose (**Figure 5.4b)**. All above observations indicated partial loss of cellulose crystalline region from one-pot synthesis process, and the higher esterification level led to more cellulose dissolution. Crystalline size (D_{hkl}) slightly decreased from 4.10 to 3.91 nm with 1.9 mmol/g Br add-on, but significantly decreased to 1.02 and 0.88 nm when Br add-ons increased to 3.3 and 5.4 mmol/g, respectively. Slightly decreased D_{hkl} indicated low level of bromine esterification would affect the cellulose crystalline surface without affecting crystalline size. In contrast, high level of bromine esterification may penetrate inside the crystalline cellulose to break large crystals to one quarter size.

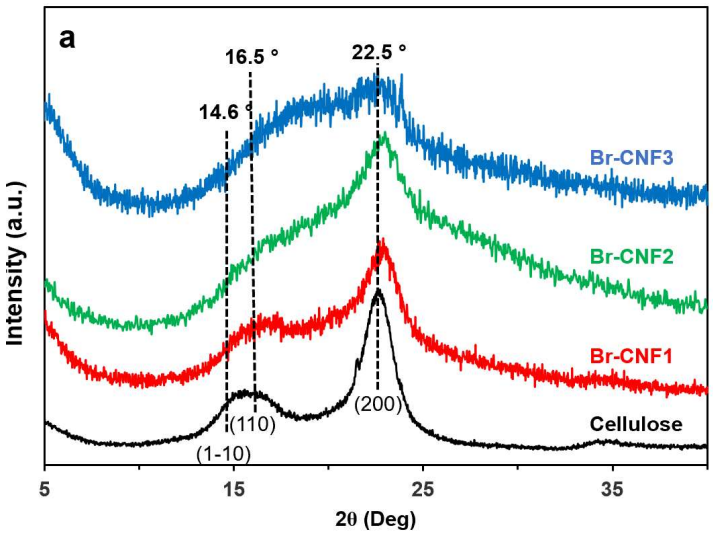

b

Samples	CrI	FWHM (degree)	$\beta_{1/2}$ (rad) [a]	D_{hkl} (nm)[b]
Cellulose	0.82	2.1	0.0366	4.10
Br-CNF1	0.63	2.2	0.0384	3.91
Br-CNF2	0.49	8.4	0.1466	1.02
Br-CNF3	0.22	9.8	0.1710	0.88

Figure 5.4. Crystalline structure of Br-CNFs: (a) XRD spectra; (b) CrI and crystal parameters. a. $\beta_{1/2}$ is the full width at half-maximum of the diffraction peak in radius. b. Crystalline dimension determined by Scherrer equation.

5.3.5. Degree of substitution of surface OH by Solution-State 1H-NMR. Solution-state ^{1}H NMR of Br-CNFs showed cellulosic anomeric protons with characteristic methyl proton (Ha) or methylene proton (Hb) peaks from the alkyl bromide groups (**Figure 5.5a**). All esterified pulp

cellulose anomeric protons peaks were assigned at δ 4.40 (H1), δ 3.30-4.01 (H3-6') and δ 3.15 (H2), matching chemical shift of δ 4.53 (H1), δ 3.42-3.97 (H3-6') and δ 3.04 (H2) on esterified rice straw cellulose in the same DMSO-d_6 solvent.[39] Two characteristic peaks were at δ 1.29 (Ha) and δ 4.51-4.86 (Hb), which perfectly matching published Ha and Hb peaks at respective δ 1.28 and δ 4.53-4.87.[39] Assuming that all anomeric protons and all Ha, Hb protons of surface AGUs (amorphous and crystalline) of Br-CNFs are detectable by ^{1}H NMR, the degree of substitution of surface hydroxyls to Br esters (DS) could be quantified. The ratio of converted C2, C3 and C6 OHs per surface AGU could be determined mathematically by the area ratio of Br esters over normalized anomeric proton. The cellulose anomeric proton was the sum of the integration of areas for all anomeric H1 to H6' proton peaks averaged by 7 then normalized by reference methylene proton Hb at δ 4.51-4.86. Br content could be estimated by integration the areas of methyl Ha divided by # of respective 3 protons. Degree of substitution (DS), the fraction of OH substituted by Br-ester, could be calculated by dividing ratio of converted OHs by 3, the number of OHs per AGU as

$$\mathrm{DS} = \frac{1}{3} \times \frac{\text{integral of methyl protons (Ha, doublet)}/3}{\sum_1^{6'} \text{integral of anomeric protons } (\mathrm{H^i})/7} \tag{5.4}$$

Due to the overlapping peaks of H1 and Hb, the integration of methyl peak (Ha) is more reliable for calculation of DS in eqn. 4. ^{1}H NMR spectra of Br-CNF1-3 accompanied with integrations values normalized by Hb were displayed (**Figure 5.5b** and **c**). The calculated DS significantly increased from 0.32 to 0.70 (2.2x) with increasing Br add-ons from 1.9 to 5.4 mmol/g, indicating 32 to 70% of surface hydroxyls were converted to esters. In preparation of Br-CNFs in DMSO-d_6 for ^{1}H NMR, Br-CNFs was first solvent exchanged from DMF to aqueous where the more hydrophilic or less esterified CNFs may remain in the aqueous phase that was decanted. Thus, the

0.32-0.70 DS values derived may represent the more hydrophobic CNF, or overestimate the overall effect of the reaction.

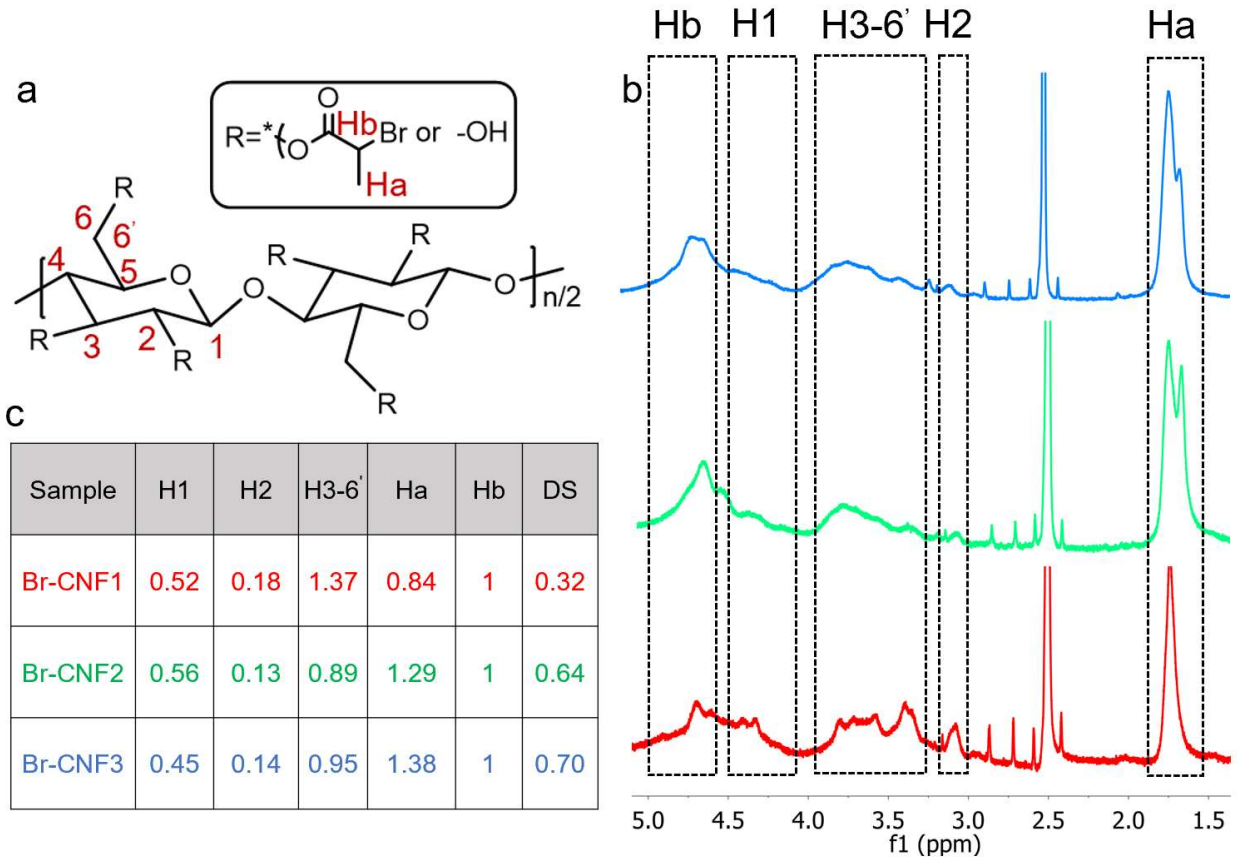

c

Sample	H1	H2	H3-6'	Ha	Hb	DS
Br-CNF1	0.52	0.18	1.37	0.84	1	0.32
Br-CNF2	0.56	0.13	0.89	1.29	1	0.64
Br-CNF3	0.45	0.14	0.95	1.38	1	0.70

Figure 5.5. (a) Structure and proton assignment of Br-CNF1-3; (b) Spectra of Br-CNF1-3; (c) Integral values of H1-6', Ha and Hb with corresponding Br-CNF; (b) Freeze-dried Br-CNF3 (ca. 0.2 w%) ^{1}H NMR spectra in DMSO-d_6.

5.3.6. Castor Oil Polyurethane Synthesis in Presence of Br-NCs. Br-Cells (0.25 g) with 1.9, 3.3, and 5.4 mmol Br add-ons were ultrasonicated (50%, 30 min) in castor oil (50 g) to produce three respective suspensions containing ca. 10 w%, 50 w%, and 70 w% Br-NC1, Br-NC2, and Br-NC3, showing also improved extent of fibrillation of Br-esterified microfibers (Br-MFs) into Br-CNFs in castor oil with increasing esterification. The whole ultrasonicated mixture of castor oil (CO) triols, in varied proportions of Br-NC and Br-MF polyols, were used to react with 20 mol%

excess of MDI isocyanate into PU (**Table S5.2**). Partial replacement of less accessible 18 carbon chain castor oil with more accessible 2 carbon ethylene glycol (EG) could enhance covalent bonding between isocyanates and hydroxyls thus increase stretchability. The composition of PU matrices was 0.3 w% of Br-NCs/MFs as well as ca. 70 w% of CO+EG and 30 w% of MDI. The colorless pure PU turned brown with ca. 0.3 w% addition of Br-CNF3. Representative strain/stress curves (**Figure 5.6a**) showed tensile properties of PU with addition of 0.3 w% Br-NC1/MFs significantly decreased compared to original PU. Comparably, modulus of 0.3 w% addition of Br-NC2 and Br-NC3 along with respective 50 and 30 w% Br-MFs moderately increased to 1.4x and 1.1x, as well as significantly increased strength to 1.4 and 1.7x (**Figure 5.6b**). The reduced mechanical performance of Br-NC1 addition was attributed to existence of large portion of Br-MFs (90 w%) which aggregated into separated phase during solvent evaporation, inducing to inhomogeneous microphase separation of hard and soft domain. PU with Br-CNF3 displayed the highest strength (1.7x) and strain (1.3x) enhancement but only slightly increased modulus (1.1x). The reinforcement effects on modulus and tensile strength for Br-NC2 and 3 were attributed to crystalline region of Br-CNF as well as synthesis of a new kind of hard segment in which Br-CNF OHs covalent bonded with MDI. The limited increased modulus may indicate low crystallinity of Br-NC3 in castor oil, which could also be illustrated by similar Br-CNF3 in DMF of 0.22 CrI (**Figure 5.5**). Thus, Br-NC2/MFs in castor oil should be further investigated for plastic PU synthesis. PU films with replacement of 20 and 40 mol% castor oil with EG (0.3 w% Br-CNF2) were prepared accordingly (**Figure 5.6a**). With mol% of EG increased from 0 to 40 mol%, Strength significantly increased to 3.3x meanwhile modulus and strain moderately improved to 1.6x and 2.3x, with mol% of EG increased from 0 to 40 mol%. The improved modulus and strength were attributed to the increased hard domain size due to the presence of MDI-EG-MDI as a new

larger hard segment. Under AFM Br-NC2 were displayed in bead particulates on hydrophilic mica but single fiber was also observed on moderately hydrophobic graphite (**Figure 5.6b**), suggesting the super hydrophobic nature of Br-NC2 which were incompatible to both relatively hydrophilic substrates. Similar modulus (2.94 and 3.62 MPa), stress (0.90 and 0.85 MPa) and strain (51 and 57%) were observed for no excess and 10 mol% excess MDI (**Figure S5.1**), both with partial replacement of 20 mol% OHs from castor oil with EG. In contrast, significantly enhanced modulus (2.3x), stress (3.5x), and slightly increased strain (1.1x) PU film was prepared with the addition of 20 mol% excess MDI. This observation indicated 20 mol% excess MDI as optimized content to react all OHs on castor oil, Br-CNFs and EG to enhance mechanical performance. With same 0.3 w% addition of Br-NCs/MFs, Br-NC2 (3.4 mmol/g Br add-on) and 40 mol% soft domain OHs replacement of EG were optimal to produce the most significantly reinforced PU plastic film with 2.3x modulus, 3.7x strength and 1.5x strain-to-failure.

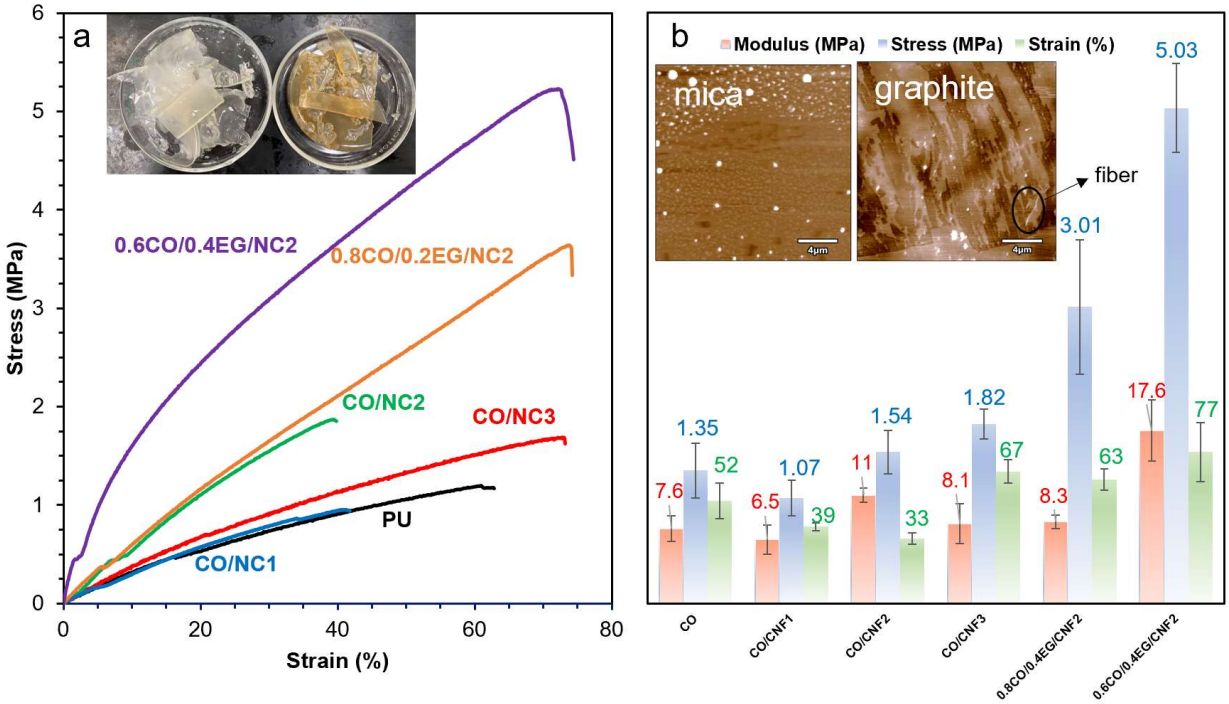

Figure 5.6. Tensile properties (n≥3) of castor oil (CO) triol/Br-NCs/MFs polyol/ethylene glycol (EG) diol PU films (40x15x2 mm) with ca. 0.3 w% Br-NCs/MFs: (a) typical stress-strain curves with photographic images of PU/Br-CNF3 (right) and PU (left) films; (b) modulus, strength, and strain. Insets are AFM images for Br-CNF2 solvent exchanged from castor oil to DMF (0.0005 w/v%) imaged on mica and graphite. NCs portion in castor oil suspension are estimated to be 10%, 50% and 70% for Br-CNF1, Br-CNF2 and Br-CNF3. An excess of 20 mol% MDI to total OHs was used for all scenarios.

5.3.7. Br-CNFs Pad Coated Bleach Cotton. Like Br-CNFs preparation in DMF, Br-Cell1-3 were suspended in acetone at 0.5 w% followed by ultrasonication (50% amplitude, 30 min) and centrifugation (5k RPM, 10 min) to collect the supernatant as Br-CNF1-3. Less than 10 w% Br-CNF1 indicated Br-Cell1 was only slightly defibrillated due to the still existing strong hydrogen bonding between cellulose chains caused by remaing large portion of surface hydroxyls. Yields of Br-CNF2 and 3 were 33.2 and 42.9 w% and further increased to 51.5 and 64.1% by prewetting Br-Cell2 and 3 in tert-butanol before ultrasonication. (**Figure 5.7a**). The OHs of tert-butanol would hydrogen bond to Br-Cell surfaces with three hydrophobic methyl groups exposed to increase compatibility to acetone, improving ca. 20% yield of Br-CNF2 or 3 containing supernatant. Br-CNF2 and 3 produced from tert-butanol pre-wetted Br-cell in acetone were pad coated on bleached cotton to measure their WCAs (**Figure 5.7b**). WCAs of Br-CNF2 coated fabric retained zero with mass add-on from 0 to 3 w%, and gradually increased to 49° at 9 w%. For cotton coated with the highly esterified and more hydrophobic Br-CNF3, WCA immediately jumped to 52.7° at merely 1.5 w% add-on then increased up to 87.5° at 10.5 w%. Mechanical properties add-ons of Br-CNF2 and Br-CNF3 coated fabrics were displayed (**Figure 5.7c** and **d**). With addition of 9 w% Br-CNF2, the elastic modulus moderately increased one third from 835 to 1149 MPa and the tensile strength

by nearly a quarter from 44.6 to 55.3 MPa, while the strain retained the same. However, significantly decreased modulus to 677 MPa (0.8x) and strength to 30.3 MPa (0.7x) by coating 10.5 w% Br-CNF3. The reinforcement effects of Br-CNF2 coating may be due to the relatively high retention of the crystalline region (CrI = 0.486), and the reduced mechanical performance could be attributed to significant loss in 0.22 CrI for Br-CNF3. Thus, significant WCAs improvement for Br-CNF3 coated fabric enable it as one potential hydrophobic coating material in textiles. Moderately mechanical reinforcement of less functionalized and high crystallinity Br-CNF2 make it could be further investigated to serve as strength enhancement additives variety of coatings or packaging applications.

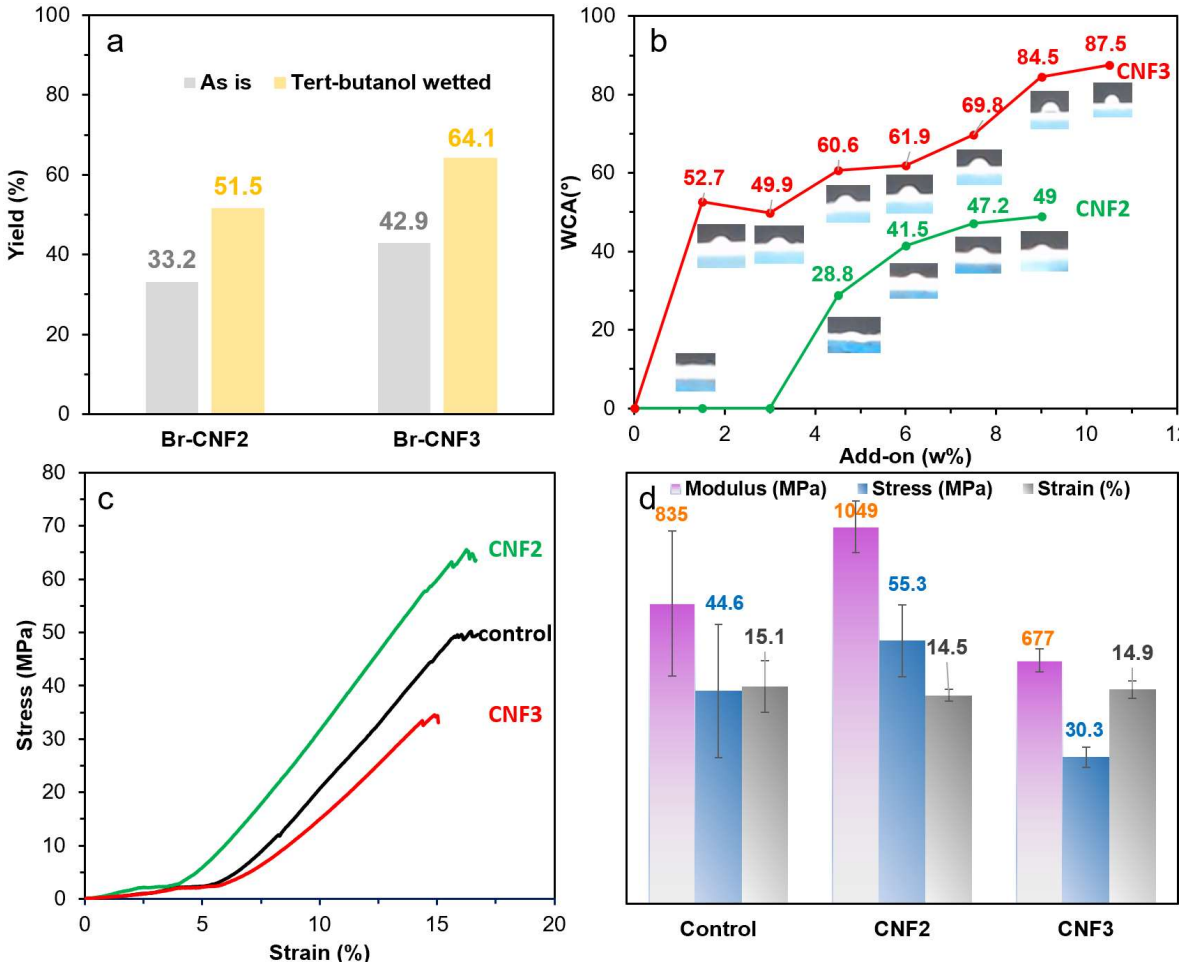

Figure 5.7. (a) Yield of ultrasonicated Br-CNF2 and Br-CNF3 from ultrasonication in acetone with or without t-Butanol wetting; (b) WCA (°) of bleached cotton fabric with add-on (w%) of Br-CNF2 and Br-CNF3 from t-Bu wetted Br-cell; (c) Representative strain/stress curves (n≥3) for cotton fabric (40x15x0.2 mm) with pad coated Br-CNF2 (9 w%) and Br-CNF3 (10.5 w%); (d) modulus, strength and strain.

5.4. Conclusion

Facile one-pot bromine acylation (1.9-5.4 mmol/g Br add-on) has been applied soft wood cellulose in DMF followed by direct ultrasonication (50% amplitude, 30 min) of microfibers suspension in DMF, acetone, or castor oil for prepration of organic compatible cellulose nanofbirls with controallble DS between 0.32 and 0.70. Three esterification levels of Br-Cell1-3 with Br add-ons of 1.9, 3.3 and 5.4 mmol/g were successfully defibrillated into 48.2, 74.5 and 87.1% yield of Br-CNF1-3 with averaged thickness and length ranging from 2.4 to 4.0 nm and 254 to 359 nm, meanwhile retaining crystallnity of 62.6%, 48.6% and 21.5%, respectively. 83% length reducation of cellulose after grinding indicated the onset of chain sission under shear force. Irregular beads or bundles for esterified cellulose at 50°C suggested the possible cellulose dissolution at elevated temperatures. Successful conversion of surface OHs to bromine esters were confirmed by the presence of C=O at 1740 cm^{-1} in FTIR and chemical shift for methyl (Ha) proton at δ=1.29 in ^{1}H NMR. Castor oil-based plastic PU was reinforced to 2.3x modulus, 3.7x strength and 1.5x strain with the addition of 0.3 w% Br-CNF2 in presence of 40 mol% OHs replacement from ethylene glycol. Dip coated bleached cotton fabric by acetone dispersed Br-CNF2 and 3 enable significantly improved WCAs up to respective 49° and 87.5° with add-on to 9 and 10.5 w%. Moderately mechanical enhanced bleached cotton (1.4x modulus and 1.2x strength,) was also prepared at 10.5

w% add-on of Br-CNF2. This paper streamlined one pot synthesis of hydrophobic esterified nanocelluloses in variety of solvents such as DMF, acetone and castor oil to broad applications in hydrophobic coating and matrix reinforcement.

5.5. Supplemental information

Table S5.1. Grinded and non-grinded pulp cellulose bromine acylation optimization (5:1=BPB: AGU and 6 h) followed by sonication (50% amplitude) and centrifugation (5k rpm, 10 min).

Grinding	Pre-sonication	Esterification		mass gain (%)	Br add-on (mmol/g)	Redispersing Solvent	Sonication Time (min)	Supernatant Portion (%)
	(50%, 3 min)	Ratio	Temp. (°C)					
Yes	Yes	2.5:1	23	14	1	-	-	-
No	No	5:1	23	30	2.2	DMF	30	28.6
No	Yes	5:1	23	28.6	2.1	DMF	30	15.4
Yes	Yes	5:1	23	25.2	1.9	DMF	30	48.2
						DMAc	30	57.7
No	No	5:1	35	41.5	3	DMF	30	35
Yes	No	5:1	35	42.5	3.1	-	-	-
Yes	Yes	5:1	35	46.2	3.3	DMF	30	74.5
Yes	Yes	5:1	50	74.1	5.4	DMF	10	56.1
						DMF	30	87.1
Yes	No	5:1	50	69.5	5.1	DMF	30	90.1
No	No	5:1	50	79	5.8	DMF	30	43.3
No	No	5:01	70	17.7	1.3	-	-	-

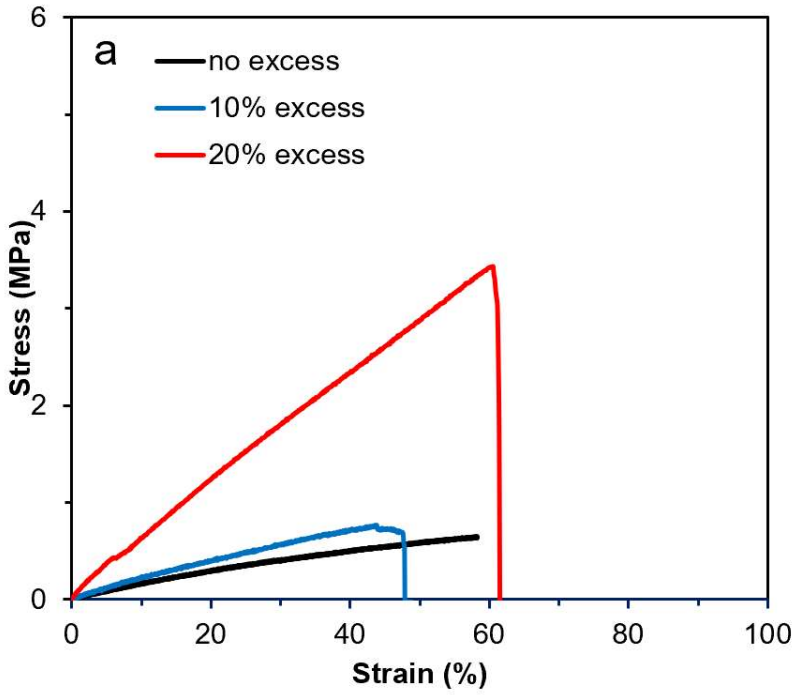

Figure S5.1. Engineering stress-strain curves (n=3) for PU/CNF films with 0.3 w% Br-CNF2 and 80/20 mol/mol% castor oil/ethylene glycol.

Table S5.2. Mole and weight composition of each component in castor oil PU matrixes. Only components with OHs were used to name each trial: "CO" for castor oil; "EG" for ethylene glycol. 20 mol% excess MDI used if not indicated.

	mol%				w%			
Trial Name	CNF	CO	EG	MDI	CNF	CO	EG	MDI
CO	0	45.4	0	54.6	0	71.8	0	28.2
CO/NC1 CO/NC2 CO/NC3	0.5	45.2	0	54.3	0.3	71.6	0	28.1
0.8CO/0.2EG/NC2	0.4	36.2	9.1	54.3	0.3	66.1	1.3	32.3
0.6CO/0.4EG/NC2	0.3	27.2	18.1	54.4	0.3	58.4	3.2	38.1
0.8CO/0.2 EG/NC2 (no excess MDI)	0.4	39.8	9.9	49.8	0.3	69.7	1.4	28.5
0.8CO/0.2EG/NC2 (10 mol% excess MDI)	0.4	37.9	9.5	52.1	0.3	67.8	1.4	30.5

5.6. Reference

1. Iwamoto, S.; Kai, W.; Isogai, A.; Iwata, T., Elastic modulus of single cellulose microfibrils from tunicate measured by atomic force microscopy. *Biomacromolecules* **2009,** *10* (9), 2571-2576.
2. Fukuzumi, H.; Saito, T.; Isogai, A., Influence of TEMPO-oxidized cellulose nanofibril length on film properties. *Carbohydrate Polymers* **2013,** *93* (1), 172-177.
3. Diaz, J. A.; Wu, X.; Martini, A.; Youngblood, J. P.; Moon, R. J., Thermal expansion of self-organized and shear-oriented cellulose nanocrystal films. *Biomacromolecules* **2013,** *14* (8), 2900-2908.
4. Puangsin, B.; Yang, Q.; Saito, T.; Isogai, A., Comparative characterization of TEMPO-oxidized cellulose nanofibril films prepared from non-wood resources. *International journal of biological macromolecules* **2013,** *59*, 208-213.
5. Zhao, M.; Ansari, F.; Takeuchi, M.; Shimizu, M.; Saito, T.; Berglund, L.; Isogai, A., Nematic structuring of transparent and multifunctional nanocellulose papers. *Nanoscale Horizons* **2018,** *3* (1), 28-34.
6. Haywood, A. D.; Davis, V. A., Effects of liquid crystalline and shear alignment on the optical properties of cellulose nanocrystal films. *Cellulose* **2017,** *24* (2), 705-716.
7. Jiang, F.; Han, S.; Hsieh, Y.-L., Controlled defibrillation of rice straw cellulose and self-assembly of cellulose nanofibrils into highly crystalline fibrous materials. *Rsc Advances* **2013,** *3* (30), 12366-12375.
8. Jiang, F.; Hsieh, Y.-L., Chemically and mechanically isolated nanocellulose and their self-assembled structures. *Carbohydrate Polymers* **2013,** *95* (1), 32-40.
9. Pääkkö, M.; Ankerfors, M.; Kosonen, H.; Nykänen, A.; Ahola, S.; Österberg, M.; Ruokolainen, J.; Laine, J.; Larsson, P. T.; Ikkala, O., Enzymatic hydrolysis combined with mechanical shearing and high-pressure homogenization for nanoscale cellulose fibrils and strong gels. *Biomacromolecules* **2007,** *8* (6), 1934-1941.
10. Ye, Y.-S.; Zeng, H.-X.; Wu, J.; Dong, L.-Y.; Zhu, J.-T.; Xue, Z.-G.; Zhou, X.-P.; Xie, X.-L.; Mai, Y.-W., Biocompatible reduced graphene oxide sheets with superior water dispersibility stabilized by cellulose nanocrystals and their polyethylene oxide composites. *Green Chemistry* **2016,** *18* (6), 1674-1683.
11. Habibi, Y.; Lucia, L. A.; Rojas, O. J., Cellulose nanocrystals: chemistry, self-assembly, and applications. *Chemical reviews* **2010,** *110* (6), 3479-3500.
12. Bondeson, D.; Mathew, A.; Oksman, K., Optimization of the isolation of nanocrystals from microcrystalline cellulose by acid hydrolysis. *Cellulose* **2006,** *13* (2), 171.
13. Elazzouzi-Hafraoui, S.; Nishiyama, Y.; Putaux, J.-L.; Heux, L.; Dubreuil, F.; Rochas, C., The shape and size distribution of crystalline nanoparticles prepared by acid hydrolysis of native cellulose. *Biomacromolecules* **2007,** *9* (1), 57-65.
14. Dufresne, A., Nanocellulose: a new ageless bionanomaterial. *Materials today* **2013,** *16* (6), 220-227.
15. Saito, T.; Nishiyama, Y.; Putaux, J.-L.; Vignon, M.; Isogai, A., Homogeneous suspensions of individualized microfibrils from TEMPO-catalyzed oxidation of native cellulose. *Biomacromolecules* **2006,** *7* (6), 1687-1691.
16. Isogai, A.; Saito, T.; Fukuzumi, H., TEMPO-oxidized cellulose nanofibers. *nanoscale* **2011,** *3* (1), 71-85.

17. Saito, T.; Isogai, A., TEMPO-mediated oxidation of native cellulose. The effect of oxidation conditions on chemical and crystal structures of the water-insoluble fractions. *Biomacromolecules* **2004,** *5* (5), 1983-1989.
18. Wang, M. S.; Jiang, F.; Hsieh, Y.-L.; Nitin, N., Cellulose nanofibrils improve dispersibility and stability of silver nanoparticles and induce production of bacterial extracellular polysaccharides. *Journal of Materials Chemistry B* **2014,** *2* (37), 6226-6235.
19. Li, J.; Wei, X.; Wang, Q.; Chen, J.; Chang, G.; Kong, L.; Su, J.; Liu, Y., Homogeneous isolation of nanocellulose from sugarcane bagasse by high pressure homogenization. *Carbohydrate polymers* **2012,** *90* (4), 1609-1613.
20. Wågberg, L.; Decher, G.; Norgren, M.; Lindström, T.; Ankerfors, M.; Axnäs, K., The build-up of polyelectrolyte multilayers of microfibrillated cellulose and cationic polyelectrolytes. *Langmuir* **2008,** *24* (3), 784-795.
21. Aulin, C.; Johansson, E.; Wågberg, L.; Lindström, T., Self-organized films from cellulose I nanofibrils using the layer-by-layer technique. *Biomacromolecules* **2010,** *11* (4), 872-882.
22. Jiang, F.; Hsieh, Y.-L., Self-assembling of TEMPO oxidized cellulose nanofibrils as affected by protonation of surface carboxyls and drying methods. *ACS Sustainable Chemistry & Engineering* **2016,** *4* (3), 1041-1049.
23. Dai, L.; Zhu, W.; Lu, J.; Kong, F.; Si, C.; Ni, Y., A lignin-containing cellulose hydrogel for lignin fractionation. *Green Chemistry* **2019,** *21* (19), 5222-5230.
24. Qing, W.; Wang, Y.; Wang, Y.; Zhao, D.; Liu, X.; Zhu, J., The modified nanocrystalline cellulose for hydrophobic drug delivery. *Applied Surface Science* **2016,** *366*, 404-409.
25. Yin, Y.; Hong, Z.; Tian, X.; Zhu, Q.; Jiang, X.; Wang, H.; Gao, W., Cellulose nanocrystals modified with quaternary ammonium salts and its reinforcement of polystyrene. *Polymer Bulletin* **2018,** *75* (5), 2151-2166.
26. Kaldéus, T.; Träger, A.; Berglund, L. A.; Malmström, E.; Lo Re, G., Molecular engineering of the cellulose-poly (caprolactone) bio-nanocomposite interface by reactive amphiphilic copolymer nanoparticles. *ACS nano* **2019,** *13* (6), 6409-6420.
27. Fumagalli, M.; Sanchez, F.; Molina-Boisseau, S.; Heux, L., Surface-restricted modification of nanocellulose aerogels in gas-phase esterification by di-functional fatty acid reagents. *Cellulose* **2015,** *22* (3), 1451-1457.
28. Wang, Y.; Wang, X.; Xie, Y.; Zhang, K., Functional nanomaterials through esterification of cellulose: a review of chemistry and application. *Cellulose* **2018,** *25* (7), 3703-3731.
29. Kang, X.; Sun, P.; Kuga, S.; Wang, C.; Zhao, Y.; Wu, M.; Huang, Y., Thin cellulose nanofiber from corncob cellulose and its performance in transparent nanopaper. *ACS Sustainable Chemistry & Engineering* **2017,** *5* (3), 2529-2534.
30. Sethi, J.; Farooq, M.; Sain, S.; Sain, M.; Sirviö, J. A.; Illikainen, M.; Oksman, K., Water resistant nanopapers prepared by lactic acid modified cellulose nanofibers. *Cellulose* **2018,** *25* (1), 259-268.
31. Geng, S.; Wei, J.; Aitomäki, Y.; Noël, M.; Oksman, K., Well-dispersed cellulose nanocrystals in hydrophobic polymers by in situ polymerization for synthesizing highly reinforced bio-nanocomposites. *Nanoscale* **2018,** *10* (25), 11797-11807.
32. Germiniani, L. G.; da Silva, L. C.; Plivelic, T. S.; Gonçalves, M. C., Poly (ε-caprolactone)/cellulose nanocrystal nanocomposite mechanical reinforcement and morphology: the role of nanocrystal pre-dispersion. *Journal of Materials Science* **2019,** *54* (1), 414-426.

33. Zhang, Z.; Zhang, B.; Grishkewich, N.; Berry, R.; Tam, K. C., Cinnamate-functionalized cellulose nanocrystals as UV-shielding nanofillers in sunscreen and transparent polymer films. *Advanced Sustainable Systems* **2019,** *3* (4), 1800156.
34. Morandi, G.; Heath, L.; Thielemans, W. J. L., Cellulose nanocrystals grafted with polystyrene chains through surface-initiated atom transfer radical polymerization (SI-ATRP). *Langmuir* **2009,** *25* (14), 8280-8286.
35. Ashori, A.; Babaee, M.; Jonoobi, M.; Hamzeh, Y., Solvent-free acetylation of cellulose nanofibers for improving compatibility and dispersion. *Carbohydrate polymers* **2014,** *102*, 369-375.
36. Tripathi, A.; Ago, M.; Khan, S. A.; Rojas, O. J., Heterogeneous acetylation of plant fibers into micro-and nanocelluloses for the synthesis of highly stretchable, tough, and water-resistant co-continuous filaments via wet-spinning. *ACS applied materials & interfaces* **2018,** *10* (51), 44776-44786.
37. Jonoobi, M.; Harun, J.; Mathew, A. P.; Hussein, M. Z. B.; Oksman, K., Preparation of cellulose nanofibers with hydrophobic surface characteristics. *Cellulose* **2010,** *17* (2), 299-307.
38. Fukuda, J.; Hsieh, Y.-L., Hydrophobic 2, 7-Octadienyl Ether-Cellulose Nanofibrils Using Butadiene Sulfone as the Dual Reagent and Medium. *ACS Sustainable Chemistry & Engineering* **2021,** *9* (18), 6489-6498.
39. Guo, M.; Hsieh, Y.-L., One-pot synthesis of 2-bromopropionyl esterified cellulose nanofibrils as hydrophobic coating and film. *RSC Advances* **2022,** *12* (24), 15070-15082.
40. Huang, P.; Wu, M.; Kuga, S.; Wang, D.; Wu, D.; Huang, Y., One-step dispersion of cellulose nanofibers by mechanochemical esterification in an organic solvent. *ChemSusChem* **2012,** *5* (12), 2319-2322.
41. Valdebenito, F.; García, R.; Cruces, K.; Ciudad, G.; Chinga-Carrasco, G.; Habibi, Y., CO2 adsorption of surface-modified cellulose nanofibril films derived from agricultural wastes. *ACS Sustainable Chemistry & Engineering* **2018,** *6* (10), 12603-12612.
42. Frank, B. P.; Durkin, D. P.; Caudill, E. R.; Zhu, L.; White, D. H.; Curry, M. L.; Pedersen, J. A.; Fairbrother, D. H., Impact of silanization on the structure, dispersion properties, and biodegradability of nanocellulose as a nanocomposite filler. *ACS Applied Nano Materials* **2018,** *1* (12), 7025-7038.
43. Lin, W.; Hu, X.; You, X.; Sun, Y.; Wen, Y.; Yang, W.; Zhang, X.; Li, Y.; Chen, H., Hydrophobic modification of nanocellulose via a two-step silanation method. *Polymers* **2018,** *10* (9), 1035.
44. Jiang, F.; Hsieh, Y.-L., Amphiphilic superabsorbent cellulose nanofibril aerogels. *Journal of Materials Chemistry A* **2014,** *2* (18), 6337-6342.
45. Johnson, R. K.; Zink-Sharp, A.; Glasser, W. G., Preparation and characterization of hydrophobic derivatives of TEMPO-oxidized nanocelluloses. *Cellulose* **2011,** *18* (6), 1599-1609.
46. Wang, L.; Okada, K.; Sodenaga, M.; Hikima, Y.; Ohshima, M.; Sekiguchi, T.; Yano, H., Effect of surface modification on the dispersion, rheological behavior, crystallization kinetics, and foaming ability of polypropylene/cellulose nanofiber nanocomposites. *Composites Science and Technology* **2018,** *168*, 412-419.
47. Li, W.; Wang, S.; Wang, W.; Qin, C.; Wu, M., Facile preparation of reactive hydrophobic cellulose nanofibril film for reducing water vapor permeability (WVP) in packaging applications. *Cellulose* **2019,** *26* (5), 3271-3284.
48. Navarro, J. R.; Bergström, L., Labelling of N-hydroxysuccinimide-modified rhodamine B on cellulose nanofibrils by the amidation reaction. *Rsc Advances* **2014,** *4* (105), 60757-60761.

49. Zhang, X.; Zhang, J.; Dong, L.; Ren, S.; Wu, Q.; Lei, T. J. C., Thermoresponsive poly (poly (ethylene glycol) methylacrylate) s grafted cellulose nanocrystals through SI-ATRP polymerization. *Cellulose* **2017,** *24* (10), 4189-4203.
50. Yin, Y.; Tian, X.; Jiang, X.; Wang, H.; Gao, W., Modification of cellulose nanocrystal via SI-ATRP of styrene and the mechanism of its reinforcement of polymethylmethacrylate. *Carbohydrate polymers* **2016,** *142*, 206-212.
51. Huang, C.-F.; Chen, J.-K.; Tsai, T.-Y.; Hsieh, Y.-A.; Lin, K.-Y. A., Dual-functionalized cellulose nanofibrils prepared through TEMPO-mediated oxidation and surface-initiated ATRP. *Polymer* **2015,** *72*, 395-405.
52. Pal, N.; Banerjee, S.; Roy, P.; Pal, K., Reduced graphene oxide and PEG-grafted TEMPO-oxidized cellulose nanocrystal reinforced poly-lactic acid nanocomposite film for biomedical application. *Materials Science and Engineering: C* **2019,** *104*, 109956.
53. Abushammala, H., Nano-Brushes of alcohols grafted onto cellulose nanocrystals for reinforcing poly (Butylene succinate): Impact of Alcohol chain length on interfacial adhesion. *Polymers* **2020,** *12* (1), 95.
54. Li, Y.; Zhu, L.; Grishkewich, N.; Tam, K. C.; Yuan, J.; Mao, Z.; Sui, X., CO2-responsive cellulose nanofibers aerogels for switchable oil–water separation. *ACS applied materials & interfaces* **2019,** *11* (9), 9367-9373.
55. Kim, M.; Schmitt, S. K.; Choi, J. W.; Krutty, J. D.; Gopalan, P., From self-assembled monolayers to coatings: Advances in the synthesis and nanobio applications of polymer brushes. *Polymers* **2015,** *7* (7), 1346-1378.
56. Syverud, K.; Xhanari, K.; Chinga-Carrasco, G.; Yu, Y.; Stenius, P., Films made of cellulose nanofibrils: surface modification by adsorption of a cationic surfactant and characterization by computer-assisted electron microscopy. *Journal of Nanoparticle Research* **2011,** *13* (2), 773-782.
57. Yang, X.; Xie, H.; Du, H.; Zhang, X.; Zou, Z.; Zou, Y.; Liu, W.; Lan, H.; Zhang, X.; Si, C., Facile extraction of thermally stable and dispersible cellulose nanocrystals with high yield via a green and recyclable FeCl3-catalyzed deep eutectic solvent system. *ACS Sustainable Chemistry & Engineering* **2019,** *7* (7), 7200-7208.
58. Sui, X.; Yuan, J.; Zhou, M.; Zhang, J.; Yang, H.; Yuan, W.; Wei, Y.; Pan, C., Synthesis of cellulose-graft-poly (N, N-dimethylamino-2-ethyl methacrylate) copolymers via homogeneous ATRP and their aggregates in aqueous media. *Biomacromolecules* **2008,** *9* (10), 2615-2620.
59. Chmielarz, P. J. E. P. L., Cellulose-based graft copolymers prepared by simplified electrochemically mediated ATRP. *Express Polymer Letters* **2017,** *11* (2), 140.
60. Zhang, L.; Zhang, M.; Hu, L.; Zhou, Y., Synthesis of rigid polyurethane foams with castor oil-based flame retardant polyols. *Industrial Crops and Products* **2014,** *52*, 380-388.
61. Zhang, C.; Xia, Y.; Chen, R.; Huh, S.; Johnston, P. A.; Kessler, M. R., Soy-castor oil based polyols prepared using a solvent-free and catalyst-free method and polyurethanes therefrom. *Green Chemistry* **2013,** *15* (6), 1477-1484.
62. Patterson, H., Quality and control. In *Hydrogenation of fats and oils*, Elsevier: 2011; pp 329-350.
63. Segal, L.; Creely, J. J.; Martin Jr, A.; Conrad, C., An empirical method for estimating the degree of crystallinity of native cellulose using the X-ray diffractometer. *Textile research journal* **1959,** *29* (10), 786-794.
64. Scherrer, P., Estimation of the size and internal structure of colloidal particles by means of röntgen. *Nachr. Ges. Wiss. Göttingen* **1918,** *2*, 96-100.